CFD Modelling of Wind Flow

Over Terrain

by Paul Stangroom, MEng

Thesis submitted to The University of Nottingham
for the degree of Doctor of Philosophy, January 2004

Abstract

The aim of this project is to show the capabilities of a RANS based numerical model in accurately analysing wind flow over real terrain regions, and assess its usage for wind energy applications. The main reasons this type of model is not widely used in the wind energy industry are due to the computational cost and the expertise required to operate such a model. These factors are assessed and various setups of the model are examined to consider the accuracy attained. The modelling process is also automated to reduce necessary user input in the process.

The models performance is tested over a number of terrain types: Flat terrain (with surface roughness), an axisymmetric hill and a real terrain region (the Askervein hill). Primary consideration is given to velocity speed-up predictions which are paramount when considering the energy availability in the wind.

A number of turbulence models have been tested for each terrain region to assess the improved accuracy obtained by using a more complicated CFD setup. The mesh discretisation has also been analysed for sensitivity to change, providing a comprehensive analysis of wind flow over Askervein.

The CFD setup process is automated to reduce the time taken in setting up a model and increase the speed of providing a full wind field assessment for all wind directions, and allowing determination of average yearly values of velocity. This improves the access to such models for non-expert users and improves the availability of the model to wind energy developers siting farms in complex terrain regions.

The model is shown to perform well for all terrain and roughness types. The turbulence properties are not well modelled, and that is a known limitation of this model type. The project demonstrates the advantages of CFD models for wind energy applications through the presented results and successful automation of the process.

Acknowledgements

The author would like to thank the following people:

Dr Nigel Wright, for his expert supervision, reassurance, patience and encouragement throughout this work.

Dr Dave Pearce and **Dr Chris Ziesler**, for insights into practical uses of CFD away from the academic environment and for PowerGen's financial support of the project.

Dr Peter Taylor, for providing experimental data from the Askervein hill project.

Dr Dave Hargreaves, for all his help in the early stages of the project and general insights into the world of numerical methods.

Dr Hervé Morvan, for detailed insights into the finer points of CFX and being the ultimate spin doctor.

Rob Smith, for computer programming hints, tips and solutions coupled with a little, often necessary, cynicism.

Laura MacHardy, for putting up with me in an office for the past years, helping in every way possible and being a shoulder to sob gently on when things (quite regularly) do not go quite according to plan.

For their moral and financial support throughout, and for their understanding about how long one of these things can take, I would like to thank my parents.

List of Figures

List of tables

List of symbols

ABL	Atmospheric Boundary Layer
A	control volume surface area
A	constant
CFD	Computational Fluid Dynamics
C, C_1, C_2	model constant
$C_{\varepsilon 1}$, $C_{\varepsilon 2}$, C_{1RNG}, C_μ	constants in turbulence transport equations
DES	Detached Eddy Simulation
DNS	Direct Numerical Simulation
D_{ij}	diffusion term in Reynolds stress equation
d	zero plane displacement height
E_{ij}	lowest order energy spectrum
e_{ijk}	alternating value
F	force
F_1	constant in k-ω turbulence model
Fr	Froude number
f	Coriolis parameter
f_1, f_2, f_μ	terms in low Reynolds number turbulence model
g	gravitational acceleration
GGI	General Grid Interface
h	height above ground; hill height
h_R	average roughness height
ip	integration point
k	kinetic energy
k^+	non-dimensional roughness height

LES	Large Eddy Simulation
L	Obukhov length scale; characteristic hill length
l	mixing length; inner layer depth
m	mass; constant
N	stratification frequency
P	pressure
P_{ij}	production term in Reynolds stress equation
PDE	Partial Differential Equation
Pe	Peclet number
Pr	Prandtl number
RANS	Reynolds Averaged Navier-Stokes
RNG	Renormalisation Group Technique
RSM	Reynolds Stress Model
Re	Reynolds number
Ri	Richardson number
R_{ij}	Reynolds stresses
R_T	term in low Reynolds number k-ε model
S	source; strain rate
S_{ij}	strain rate tensor
T_i	temperature
t	time
U	mean velocity
U_∞	free stream velocity
u_i, u_j	velocity
u'	fluctuating component of velocity

u_*	friction velocity
u^+, u^x	non-dimensional velocity scale
$\overline{u_i' u_j'}$	Reynolds stress
u, v, w	velocity components
V	volume
x_i	distance
x, y, z	directional components
y_R	sand grain roughness height
Δy_p	distance from the wall to the first node
y^+, y^x, z^+	non-dimensional distance from the wall
z	vertical height
z_0	roughness length
α	turbulence model constant
β	advection scheme variable
β^*, β	turbulence model constant
Γ	diffusion coefficient
Γ_{ij}	diffusion term in Reynolds stress equation
δ_{ij}	Kronecker delta
ε	dissipation rate of k per unit mass
ε_{ij}	dissipation term in Reynolds stress equation
ϑ	velocity scale
η, η_0	turbulence model constants
θ	hill steepness

ϕ_{ij}	pressure-strain correlation term
ϕ	latitude
κ	Von Karman constant
μ	dynamic viscosity
μ_t	turbulent viscosity
μ_T	total viscosity
ν	kinematic viscosity
Π_{ij}	strain term in Reynolds stress equation
ρ	density
ρ_0	reference density
σ_k, σ_ε	turbulent Prandtl numbers in k-ε model
σ, $\sigma*$	turbulence model constants
σ_u, σ_v, σ_w	root mean square of turbulence component
τ	shear stress
τ_0	wall shear stress
τ_{ij}	turbulent stress tensor
Φ	flow property
Ω_{ij}	rotation term in Reynolds stress equation
Ω	angular velocity
ω	dissipation rate of k per unit k
ω_k	rotation vector

1. Introduction

1.1. Energy Background

As resources of coal, oil and other fossil fuels are depleted, research continues into finding a suitable replacement source of energy. Experts predict that global oil supplies will only meet demand until production peaks sometime between 2013 and 2020, though Salameh (2003) argues that this may occur much sooner causing a serious energy gap to develop sometime between 2008 and 2010. In the author's opinion, nuclear energy must become a major energy source in the 21st century, though public concern about nuclear waste processing and its implications on future generations has led governments to invest heavily in renewable resources as alternate energy supplies. The main forms of energy available are solar, wind and hydro, though others such as biomass and wave power have developed considerably too.

Solar energy development has been primarily limited to countries with suitable space, climate and financial resource such as Mediterranean countries and the USA. The weather in northern Europe is more conducive to wind and wave energy and countries such as Denmark, Spain and the UK have invested considerably in these forms of energy due to their western Atlantic coasts.

The total energy in the wind worldwide, is estimated at three to four times the total energy consumption of the planet. How much of this resource it is feasible to exploit is hard to determine, and efforts to model and understand the full resource have been undertaken, globally by Ackermann and Soder (2002) and for northern Europe specifically by Cockerill *et al*. (2001). Methods for retrieving energy have developed and improved considerably during the last few decades, as has the understanding of wind flow.

At the end of 2002, more than 31GW of energy was being produced from the wind worldwide in over fifty countries, over 75% (24GW) of which is operating within the European Union. The annual market growth in Europe alone is around 40%. While this figure is set to reduce to about 10% by 2010, the level of investment in wind energy is considerable. The European Commission set a goal of achieving 12% of energy production from renewable sources by 2010, which will effectively double the amount of energy coming from the wind, and save 72 Mt of CO_2 per year (Zervos, 2003). The capacity is increasing fast and could even reach 60GW by 2005, enough to power 75 million homes (Salameh, 2003). While not a large scale solution to the world's energy needs, it is clear that a well managed wind resource could provide significant levels of power.

The UK has the one of the most suitable wind resources in Europe with regard to wind power availability, and significant investment in farming has already begun. Figure 1.1 show a wind map for the UK showing average wind speed above 5m/s for the entire country. Wind farms are

generally suited to regions of wind speed between 5m/s and 15m/s. The UK government has set a target to produce 10% of energy from renewable sources by 2010, and 20% by 2020 and so investment in both on- and off-shore farms is considerable. The UK government granted over 40 contracts for offshore wind farm developments in 2001 alone. Wind energy is very cheap as a resource, once the plant investment is considered, the only remaining cost is plant maintenance which, for onshore farms particularly, is minimal.

The issue of global warming is also addressed by the use of renewable energy resources. Carbon dioxide emissions are considered the biggest contributor to global warming, and power production from fossil fuel sources is one of the main supplies of this harmful gas. Governments around the world are planning to reduce the levels of CO_2 production under the Kyoto Treaty in an attempt to curb the effects of global warming. While the USA is by far the major producer of these emissions, and the only country so far not to sign the treaty, the efforts of other countries will go someway to helping solve the problem. Cynics may doubt the effectiveness of the government's plans:

> "The goal is a 10% reduction in carbon dioxide emissions. So that's a 10% cut in the 3% of CO_2 that's man-made. From a country that is home to just 1% of the world's population. Ah yes, I see how that will end the greenhouse effect" – Clarkson, 2003

but the need for new, clean, renewable energy sources is clear.

1.2. Site location

Two options exist for wind farm location, offshore and onshore. Recent investment in offshore farms has been considerable. The advantage of a fully developed wind flow away from terrain influence makes for a more predictable power rating. Pryor and Barthelmie (2001) investigated the potential power production between on- and offshore sites, finding that the amount of time at which expected power levels are maintained can be double the onshore level for an offshore farm. Removal of the farms from the sight of residents is a popular move as some dispute remains over the visual impact of turbines on the landscape. The increased cost of plant maintenance (due to saltwater corrosion of the towers) and the difficulty in retrieving the power from farms many kilometres out at sea has been a factor in much of the development.

Onshore wind farms have been in use for many years. From windmills and simple farm based turbines used to pump water, through to electricity generating wind farms, the interest and development has been strong and rapid. The ideal location for a wind farm is on open flat terrain or with very low hills, as the wind is easily predicted and the power availability is more consistent. These sites are highly visible and resistance from local residents has been considerable with complaints over visual and sound pollution, leading to difficulties in obtaining planning permission. Farms must be kept clear from major obstacles and cliffs where turbulence effects in the wind flow are more prominent. Developers are being forced to

consider more and more complex terrain regions in an attempt to appease local residents and countryside agencies. The wind field in these regions is more difficult to predict and yet accurate power predictions are imperative for the financial viability of any venture. Understanding and predicting the flow over these complex areas has been the subject of considerable research over the past few decades. Any potential wind farm location must have the site thoroughly surveyed and the wind flow analysed. Slight variations in predicted wind velocity can have dramatic effects on the wind power availability as the available power is proportional to the velocity to the power three.

Wind tunnel and numerical models are used to aid this process wherever possible but as the terrain becomes more complex, so does the complexity of any solution. Current numerical models used by the wind energy industry, such as WAsP (Mortensen and Landberg, 1993), are limited to more straightforward terrain regions and hill flows. These models are quick and easy to use and also have been validated and verified for a large number of flow situations. More complex fluid flow models are available, which are expected to enhance prediction accuracy, especially in highly complex terrain where flow separation occurs or when thermal stability effects become important, but their suitability and accuracy for use in wind farm analysis needs further validation.

Calculation of atmospheric flow over complex terrain is extremely difficult. The wind field must be resolved on very fine scales in order to

achieve a high level of accuracy within the lower part of the atmosphere. The high spatial resolution involves significant modelling challenges owing to the interaction of the surface wind with detailed feature such as ridges and steep hills (Landberg *et al.*, 2003).

1.3. Atmospheric effects

The effects of topography on the wind flow are very important. Velocity speedups and increased levels of turbulence must be considered in potential wind farm locations. High levels of turbulence and regions of flow recirculation are not beneficial and make predictions of wind power availability much more complicated. These variations of flow coupled with environmental aspects such as the migration paths of birds and insect flights all contribute against a site's suitability for wind farming. Atmospheric flows incorporate buoyancy and Coriolis forces which serve to further complicate the flow regime. These body forces may be coupled with the effects of the surface topography.

1.4. Wind flow prediction

The prediction of wind flow in complex terrain is based on theoretical and experimental techniques. Experiments are made at full scale or in the wind tunnel, whereas theoretical techniques are based on empirical, analytical or numerical methods. To gain a more complete understanding of the wind flow in any given situation, a combination of methods is used, with each approach being used to validate another.

The main numerical model currently in use for wind farm modelling is WAsP, developed in Denmark at the Risø lab. The model is limited to flows with no unsteady or non-linear effects such as separation. More complex models are available such as RANS, DES and LES, though if these are to be used in confidence by the wind energy industry, their accuracy must be determined through validation against wind tunnel and full scale data.

1.5. Thesis aims and layout

The aims and objectives of this research project are:

- To assess current atmospheric boundary layer theory, identify key issues and determine the most important flow characteristics and atmospheric conditions for predicting wind flow patterns;
- To assess current numerical modelling techniques, in conjunction with the conclusions from Aim 1 above, and determine a strategy for modelling wind flow over terrain features using advanced numerical models;
- To evaluate the model and modelling technique for use in predicting ABL flow over rough terrain and to assess the numerical model's reproduction of flow features associated with the atmospheric boundary layer, and complex terrain features
- To evaluate the model performance for flow over more complex topography, and critically assess the performance in comparison with field data, wind tunnel data and numerical data from alternative numerical models;

- To improve the model's applicability within the wind energy industry for use in wind field predictions for wind power assessments.

This introduction sets out the subject area and shows the need for more complex models in the wind energy sector. Chapter 2 considers the form of the atmospheric boundary layer and the particular aspects of wind flow over hills. It aims to give a general understanding of geophysics and pinpoint the most important aspects of the flow from a modelling point of view. It reviews the literature of experimental efforts in wind flow comprehension and in the prediction of flow over hills and other complex terrain elements.

Chapter 3 summarises the types of numerical models available for this type of work and looks in depth at RANS based CFD models which are the next stage in the evolutionary process of wind flow modelling. The use of numerical models for wind flow prediction is reviewed in depth as is the development of the turbulence models and other numerical methods used in this work. The CFD model used in this work, CFX-5, is considered and the particulars of its modelling methodology are discussed.

The results of this study are presented in Chapters 4, 5 and 6. The first of these looks at the validation of CFD for use in wind flow analysis. A flat terrain region is used to model the velocity flow over a rough terrain surface. Then the region is complicated through the addition of a three-

dimensional hill with a rough surface. A simple terrain is considered and the flow around a cosine shaped hill is considered. The results are compared with available wind tunnel data. A variety of model attributes, including boundary conditions and turbulence models, are investigated to assess the optimum configuration.

Chapter 5 analyses a more complex terrain model. A real terrain region, the Askervein hill (Taylor and Teunissen, 1987), is incorporated into the numerical model and the flow over the hill is modelled from two wind directions. The configuration and validation work from Chapter 4 is utilised to model a real wind flow. Results from the model are compared with field data, wind tunnel data and alternative numerical results for analysis of velocity profiles and speedups, turbulence characteristics and recirculation regions.

The practicality of using CFD model for wind field analysis is considered in Chapter 6. The added complexity of the model requires the user to be more of an specialist in the field of numerical work. Here, the CFD process is automated to improve the access to the model for non-expert users. The Askervein hill remains the test case and is modelled for several wind direction variations.

Chapter 7 summarises the findings of the research, the performance of the numerical model and its versatility from a wind engineering standpoint. Recommendations for future studies and developments as also discussed.

2. The Atmospheric Boundary Layer

2.1. Introduction

The concept of a boundary layer in fluid flows has been studied and classified since the late 19th century by scientists such as Froude and Prandtl, who recognised features close to surfaces and the transition from the free stream conditions to the condition of no-slip at the wall. From an geophysical point of view, the atmospheric boundary layer (ABL) is best considered as the layer of air above the Earth's surface which is directly affected by the nature of the surface itself (shape, friction, thermal), with time scales of less than a day and turbulent motion length scales of the order of the boundary layer depth (Garratt, 1992). Our knowledge of weather and terrain induced variations of the ABL has developed considerably during the past few decades and is well summarised by Garratt *et al.* (1996).

This chapter aims to summarise the aspects of the ABL which are important from a wind energy perspective, including boundary layer structure, the governing flow equations and near wall flow treatment. Wind farms are generally located in rural regions where hills and valleys are commonplace. Grass, trees and crops are the standard wall roughness condition, and they have considerable effects on the flow. Before any numerical simulation of this flow type can be confidently undertaken, an understanding of the atmospheric boundary layer must be demonstrated.

2.2. Governing equations for fluid flow

The governing equations of fluid flow are as applicable to atmospheric flows as they are to any laboratory experiment. Full derivations are available in fluid dynamics texts and so are not repeated here. Readers are directed to Wilcox (1994) for fuller details.

2.2.1. Conservation equations

Analysis of atmospheric flows and conditions must satisfy the general governing equations of fluid mechanics. The well known and documented Navier-Stokes equations in conservative form are:

$$\frac{\partial \rho u_i}{\partial t} + \frac{\partial \rho u_i u_j}{\partial x_j} = -\frac{\partial P}{\partial x_i} + \frac{\partial}{\partial x_j}\left(\mu\left(\frac{\partial u_i}{\partial x_j} + \frac{\partial u_j}{\partial x_i}\right)\right) \tag{2.1}$$

and balance the transport of fluid on the left-hand side of the equation with source and sink terms due to pressure and viscosity on the right-hand side. These equations are also known as the momentum equations.

The mass conservation equation is derived through consideration of the instantaneous density and the general mean form is:

$$\frac{\partial \rho}{\partial t} + \frac{\partial}{\partial x_j}\left(\rho u_j\right) = 0 \tag{2.2}$$

though it is more commonly found for incompressible flow:

$$\frac{\partial u_j}{\partial x_j} = 0 \tag{2.3}$$

2.2.2. Coriolis

The rotation of the Earth has consequences on atmospheric flows. The resultant forces are known as the Coriolis forces and in the wider sense, add an extra term to the governing flow equations. The Coriolis parameter relates the angular velocity, Ω, to the latitude, ϕ, and is positive in the northern hemisphere and negative in the southern.

$$f = 2\Omega \sin\phi \tag{2.4}$$

The momentum equation now has an extra term, fu_i:

$$\rho \frac{\partial u_i}{\partial t} + \rho u_j \frac{\partial u_i}{\partial x_j} = -\frac{\partial P}{\partial x_i} + f u_i + \mu \frac{\partial}{\partial x_j}\left(\frac{\partial u_i}{\partial x_j} + \frac{\partial u_j}{\partial x_i} \right) \tag{2.5}$$

In boundary layer studies, the Coriolis forces are not normally considered as they only have an effect in the outer layer, and the complicated and variable influence makes them difficult to consider accurately. However, without Coriolis forces, a horizontally homogeneous boundary layer is not possible and it must grow. At the top of the boundary layer, the Coriolis force must balance the applied pressure gradient to counteract the boundary layer growth, which can be considerable as investigated by Stubley and Riopelle (1988). So, numerical models which consider atmospheric conditions must consider the effect of Coriolis forces on the flow by applying the correct boundary condition at the top of the domain.

2.2.3. Variation of pressure and temperature

The fundamental static equation of the atmosphere is based on the hydrostatic assumption that the atmosphere is free from vertical acceleration and mean flow:

$$\frac{\partial P}{\partial z} = -\rho g \tag{2.6}$$

As density is a function of height only, it naturally follows that:

$$\frac{\partial^2 P}{\partial x \partial z} = \frac{\partial^2 P}{\partial y \partial z} = 0 \tag{2.7}$$

and so the horizontal pressure gradients are independent of height.

Temperature variation in the vertical is one of the most important factors of geophysical science (Sutton, 1953). The diurnal cycle of heating and cooling the Earth's surface means the ABL is rarely in a state of thermal equilibrium, and the temperature variations cause density variations which alter the gravitational forces. If there is no mean motion in the vertical direction, the gravitational force is balanced by the pressure gradients as in the hydrostatic equation above. As this changes from an equilibrium state, a net buoyancy force is created which affects the mean velocity profile, directly as a source term in the momentum equation and indirectly by affecting the turbulent shear stress. In stably stratified flows (described later) the forces can give rise to internal wave motions, which serve to further complicate the flow regime.

2.3. Turbulence and flow description

As flow speed increases, the structure of the flow breaks down and eddies form. As these get stronger, the flow becomes more random and turbulent. Turbulence is an eddying motion which, at the high Reynolds numbers involved, has a wide variety of eddy sizes and a corresponding variety of frequencies. Its motion is always rotational and can be thought of as a tangle of vortex elements which are highly unsteady. Turbulence takes energy out of the flow, so its effects must be modelled.

The turbulent nature of the ABL is one of its most important features. This turbulence differs from that created within a wind tunnel due to thermal effects co-existing with wind shear, and due to the ABL turbulence interacting with a mean flow that has been affected by the Earth's rotation. However, its structure shows many similarities to the two dimensional layers created in a wind tunnel. Both have a distinctive inner and outer region. The inner layer is primarily dependent on surface features and not rotation as is the case for the outer layer. The transition between the layers is not rapid, and is characterised by an overlap region.

Townsend (1961) made an important hypothesis regarding turbulence which has been part of the basic understanding of the ABL. The turbulent motion of the inner layer consists of an active part which produces the shear stress, and whose statistical properties are universal functions of height and stress, and an inactive and effectively irrotational part

determined by the turbulence in the outer layer. The hypothesis states that the inactive turbulence does not interact with the active, or contribute to the shear stress in any way. It is large scale and arises in the upper parts of the boundary layer, with its energy being dissipated close to the surface (Hogstrom *et al*., 2002). Stull (1988) highlights the effect the active turbulence has on allowing the boundary layer to respond to surface forcings. The strict definition by Townsend that the inactive, large scale turbulence has no effect on the flow near the ground has been challenged by a number of authors including McNaughton and Brunet (2002) who show evidence of an interaction between the two types. They conclude that while the hypothesis has been universally accepted, it is not universally applicable. It is obvious however that the understanding of atmospheric turbulence has been greatly aided.

2.3.1. RANS Equations

Atmospheric turbulence is considerable, and exists over a number of length and time scales. The standard Navier-Stokes equations were derived originally for laminar flow. In most areas of fluid mechanics the flows of practical importance are almost always turbulent. Turbulent fluid motion is highly random, unsteady and three dimensional. Reynolds (1895), suggested a statistical approach where the values of velocity, u_j, at any time can be split into a mean component and a fluctuating value, with U_j as the mean velocity, and $u_j^{'}$ representing the turbulent variations.

$$u_j = U_j + u_j^{'} \tag{2.8}$$

The Navier-Stokes momentum equations applied to laminar flow:

$$\frac{\partial \rho u_i}{\partial t} + \frac{\partial \rho u_i u_j}{\partial x_j} = -\frac{\partial P}{\partial x_i} + \frac{\partial}{\partial x_j}\left(\mu\left(\frac{\partial u_i}{\partial x_j} + \frac{\partial u_j}{\partial x_i}\right)\right) \tag{2.9}$$

are transformed using the mean and fluctuating components and making use of the fact that the mean values of the fluctuations $\overline{u_j'} = 0$:

$$\frac{\partial \rho U_i}{\partial t} + \frac{\partial}{\partial x_j}\rho\left(U_j U_i + \overline{u_j' u_i'}\right) = -\frac{\partial \overline{p}}{\partial x_i} + \frac{\partial}{\partial x_j}\left(\mu\left(\frac{\partial U_i}{\partial x_j} + \frac{\partial U_j}{\partial x_i}\right)\right) \tag{2.10}$$

which can be re-arranged as:

$$\frac{\partial \rho U_i}{\partial t} + \frac{\partial}{\partial x_j}\rho\left(U_j U_i\right) = -\frac{\partial \overline{p}}{\partial x_i} + \frac{\partial}{\partial x_j}\left(\mu\left(\frac{\partial U_i}{\partial x_j} + \frac{\partial U_j}{\partial x_i}\right) - \rho\overline{u_i' u_j'}\right) \tag{2.11}$$

giving extra source terms on the right-hand side of the momentum equation, known as the Reynolds stresses, defined as:

$$\tau_{ij} = -\rho\overline{u_i' u_j'} \tag{2.12}$$

2.3.2. Closure

The appearance of these unknown Reynolds stress terms gives rise to a problem of closure. The equations governing the fluid flow (the Navier Stokes equations) are no longer solvable directly, and are renamed the Reynolds Averaged Navier-Stokes (RANS) equations which give a more accurate representation of real fluid flow. Previously there were four unknowns with four equations of motion, and the set could be solved. Now ten unknowns are present, yet the number of equations has not changed. Turbulence models must be introduced for the solution of the flow problem, and these are detailed in Chapter 3 in the section on turbulence modelling.

2.3.3. The mixing length

To understand the turbulent motions in the flow, Prandtl (1925) introduced the idea of a mixing-length, which is analogous to the mean free path in the kinetic theory of gases. If we consider a small discrete volume of fluid (an eddy), breaking away from an original level, z, and being carried to a new level, $z+l$, where it mixes with the mean flow. The distance travelled by the fluid before it becomes part of the mean flow, l, is known as the mixing length, the hypothesis for which is that the length is unique and characterises the local turbulence intensity at any level, but can be a function of position or velocity.

2.4. ABL structure and depth

The depth of the ABL varies considerably with atmospheric conditions and time of day. This variability makes its simulation using numerical models and wind tunnel simulations quite difficult. A set up must be chosen which best represents the atmospheric conditions required. The layer has two main sections. The outer region, sometimes known as the Ekman layer, is dominated by Coriolis effects due to the rotation of the Earth. This layer reaches out to 3-5km above the Earth's surface, but can also reduce to less than 1km at night when the thermal effects are minimal. The inner region, dominated by surface effects also varies considerably in height, normally between a hundred meters up to over a kilometre.

Figure 2.1 shows the structure of the ABL above the ground surface with approximate heights for each region. Directly above the ground is the viscous sublayer described in detail in section 2.7. The flow is complex as all the effects of the terrain shape, and surface roughness initiate here. Above this, the dynamic sublayer is a fully turbulent region, close enough to the ground that buoyancy and Coriolis forces can be ignored, but far enough away that the individual roughness elements, and the viscosity of the air have no effect. Under neutral conditions, the dynamic sublayer occupies the entire surface layer which is approximately 10% of the ABL depth. A region of overlap, called the inertial sublayer links this inner region with the outer region, or Ekman layer, where the flow is nearly independent of the nature of the surface and mainly determined by the freestream.

This layout is relevant to neutral conditions described in section 2.5. When the ABL is unstable, the outer region is characterised by thermal convective turbulence causing the depth to be quite variable, but in general is thicker than for a neutral layer. For stable ABL, the depth can range between 10m and 500m.

The height of the neutral ABL can be defined as the height where the wind direction reaches that of the geostrophic wind (Clarke and Hess, 1973), the height at which the wind magnitude first reaches the geostrophic value (Wyngaard, 1983) or where the stress approaches zero (Plate, 1971). From

a traditional fluid mechanics point of view, the definition of Wyngaard is most usual as the geostrophic wind is equivalent to the free stream, but the three main methods highlight how difficult it is to truly define the height of the boundary layer. The variance in height is dependent on the time of day, exact weather conditions and surface effects. Zilitinkevich and Baklanov (2002) used the Richardson number and other methods to calculate the height of the stable boundary layer, with limited success, and there are many other methods for depth calculation, reviewed by Martano and Romanelli (1997) and by Vogelezang and Holtstag (1996).

Ground roughness has a considerable effect on the height of the layer. Aynsley *et al.* (1977) defines the boundary layer height as the point at which the mean wind speed becomes independent of the ground. As would be expected, this height increases as the surface roughness becomes more intrusive. Aynsley *et al.* (1977) defines four main terrain roughness categories in table 2.1.

Category	**Description**	**Inner layer height, (m)**	**Roughness length, z_0 (m)**
1	Open sea, ice, desert	250	0.001
2	Open country, low scrub, scattered trees	300	0.03
3	Suburban areas, small towns, well wooded areas	400	0.3
4	Numerous tall buildings, city centres, industrial areas	500	3

Table 2.1 – Surface roughness and ABL height for varying terrain types From Aynsley et al. (1977)

The depth of the boundary layer is a function of the surface roughness and the free stream wind speed, which is controlled by the driving pressure

gradients. Significant research has concentrated on this, and is well summarised by Aynsley *et al.* (1977). For a strong wind at a typical rural site, as might be expected for an onshore wind farm location, the total daytime boundary layer depth is approximately 1km.

2.5. Stratification and stability

If a fluid is considered to be made up of parcels of various densities, the tendency due to gravity is for the parcels to arrange themselves with the higher densities below those of lower density, and the fluid is described as stratified. If heavy parcels are found below the lighter ones, the fluid is stable, though if the parcels are located the other way around, the system tries to overturn itself, and the fluid is unstable. If there is little or no variation in temperature with height and hence little variation of density, the fluid is considered neutral and so there are no stratification effects.

If we consider vertical stratification, so that the fluid is in equilibrium horizontally, and a parcel of fluid at height, z, above the ground, has a density, ρ_z. If this fluid parcel is displaced to a new height, $z+h$, where the ambient density is ρ_{z+h}, the parcel will be subject to a buoyancy force:

$$F = (\rho_{z+h} - \rho_z)gV \tag{2.13}$$

From Newton's law, $F = ma$:

$$(\rho_{z+h} - \rho_z)gV = \rho_z V \frac{d^2h}{dt^2} \tag{2.14}$$

The stratification in the atmosphere is only weak, and the density variations are relatively small compared to the average fluid density, so the reference

density ρ_z on the right hand side of the above equation, can be replaced by a reference value ρ_o. This leads to:

$$\frac{d^2h}{dt^2} - \frac{g}{\rho_0}\frac{d\rho}{dz}h = 0 \tag{2.15}$$

and a stratification frequency, N, can de defined as

$$N^2 = -\frac{g}{\rho_0}\frac{d\rho}{dz} \tag{2.16}$$

if N^2 is positive, the solution has an oscillatory appearance. The heavy parcel is displacement downwards, where its inertial force causes it to continue down past other parcels of equal density and it becomes surrounded by heavier parcels. Thus it is propelled upwards due to imposed buoyancy forces, and oscillations about its ideal position occur. When N^2 is negative, there is no stratification frequency as such. The parcel is displaced upward, having been surrounded by heavier fluid, and it continues up, further away from its initial location.

The changes in density which affect atmospheric fluid can be caused in two ways:

- Pressure changes
- Internal-energy changes

In the first case, pressure, temperature and density all vary. Heavy parcels of fluid located above lighter ones will compress those below causing P, ρ and T to all increase. In this way, the lower packets become heavier and no location (dynamic) changes need occur. In the second case, changes occur due to heat flux, moisture variation and other atmospheric conditions. So

variations remain despite the compression found in the first scenario and these cause density differences to occur which drive the vertical motion.

The sign of N^2 can not be taken as a measure of the stability of the fluid. Above ground, during the day, the lower atmosphere is heated by the warmer ground and is in a state of turbulent convection. This convective layer covers regions of both positive and negative temperature gradient and Stull (1988) details the need for nonlocal methods to determine the stability of the flow.

2.5.1. Froude number

The Froude number, *Fr*, is a measure of the importance of boundary layer stratification. It compares the level of stratification of a fluid flowing past an obstacle with the height of the obstacle, *h*, and the free stream velocity of the fluid, U_∞. For a full derivation, the reader is directed to Cushman-Roisin (1994):

$$Fr = \frac{U_\infty}{N \cdot h} \tag{2.17}$$

where *N* is the stratification frequency described above. Flows can be assumed neutral for $Fr = 0$, stable for positive *Fr* and unstable where *Fr* is negative. It is simply a variation on *N* which considers changes in height above the surface. The Froude number relies on a knowledge of density variation within the fluid, which is not straightforward to measure. Ding *et al.* (2003) raise the point that $\frac{U_\infty}{N \cdot h}$ is not strictly a Froude number due to

the physical implications, but should be considered as a ratio of the buoyancy time scale ($\frac{1}{N}$) and the eddy overturning time scale ($\frac{U_\infty}{h}$).

2.5.2. Richardson number

The thermal stability of the flow is measured by the Richardson number, which can also be used with reference to the turbulence. From a thermal perspective the stability of the flow indicates the level of heat transfer within the fluid. It is effectively a variation of the Froude number described above relating the stability of the flow to temperature rather than density, as it is much simpler to measure temperature changes within a flow.

$$Ri = \frac{\frac{g}{T}\left(\frac{\partial T}{\partial z}\right)}{\left(\frac{\partial U}{\partial z}\right)^2} = \frac{1}{Fr^2} \tag{2.18}$$

In neutral conditions, $Ri = 0$, and thermal effects are negligible so buoyancy effects can be ignored. In stable conditions, buoyancy acts against the turbulent kinetic energy (*Ri* is positive), whereas in unstable conditions, both shear and buoyancy terms act to produce turbulent kinetic energy. A critical value (Ri_c) exists at a value of 0.25 (Derbyshire and Wood, 1994) where the flow changes from turbulent to laminar. Between 0.25 and zero, the turbulence is generated by wind shear and is very mechanical. Below zero the turbulence is a mixture of both mechanical and convective turbulence investigated thoroughly by Gallego *et al.* (2001) using advanced dynamical systems techniques.

The Richardson number is not always a useful parameter for the characterisation of the stability of the surface layer however, as it is an unknown function of height. Equivalent functions relating to the bulk flow and flux components are available (see Kaimal and Finnigan 1994) but the parameter most recognised for surface layer flow is the ratio of height, z, to a scaling length *L* (the Obukhov length):

$$\frac{z}{L} = -\frac{\frac{g}{T}\left(\overline{w'T'}\right)_0}{u_*^3/kz} \tag{2.19}$$

where $\left(\overline{w'T'}\right)_0$ represents the temperature flux at the surface. The negative sign gives the ratio the same sign as *Ri*, and this relationship is more useful as *L* can be assumed constant through the surface layer.

2.5.3. Convection

When a parcel of air near the surface is heated, it rises through the atmosphere. The distance the parcel rises will depend upon how the ambient temperature varies with height. The rising air loses heat as it expands with the fall in ambient pressure, so its temperature drops. If the temperature of the surrounding air does not fall as quickly with increasing height, the air pocket will quickly become colder than the surrounding air, lose its buoyancy, and sink back to its original position. When it reaches the upper region of the boundary layer, forces present due to the Earth's rotation, and other outer layer effects will push it back towards the ground where it will be heated again. This convective boundary layer grows

through the morning as the suns rays heat the surface and the surface heats the surrounding air. It can reach heights of 1km during the afternoon. In the convective boundary layer, the steepest gradients of speed and temperature are at the surface and the actual profiles remain constant for the upper 90% of the layer (Kaimal and Finnigan, 1994). In heavy cloud cover, the convective layer does not really grow as the heat from the sun is blocked from heating the surface.

2.5.4. Effects on velocity profile

Wind velocity in a field survey is measured at various heights in order to determine a profile shape. Stull (1988) considers the effects of stability on the velocity profile. When plotted on a semi-log graph (see figure 2.2) the standard profile for neutral conditions appears in a straight line. When the conditions vary, so the wind profile deviates from the straight line.

2.5.5. Stability conditions

The structure of the land based ABL turbulence is influenced by the daily heating and cooling of the Earth, and by the presence of cloud formations. Neutral flow, which is more readily produced within a wind tunnel, can be approximated to windy conditions with complete cloud cover, whereas stably stratified flow occurs mostly at night in response to surface cooling, and unstable flow occurs when strong surface heating produces thermal instability and hence a convective layer (Garratt, 1992). An understanding of the different turbulent effects for each condition is shown by Nieuwstadt

and Duynkerke (1996) though they highlight that the full understanding of turbulence in the ABL has not yet been produced, and while some conditions are well understood (clear, dry ABL), for others (e.g. cloudy ABL) the situation is more complicated and consequently less clear. Absolutely neutral conditions are very rare, typically occurring during the transition between stable and unstable conditions. Near neutral conditions however occur during overcast skies and moderate to high wind speeds (Petersen *et al.*, 1987).

For flows considered in this work, the assumption of neutral stability is made. This is valid for atmospheric flows for wind power consideration, as high wind speeds and strong stratification effects (stable or unstable) do not occur together as strong wind conditions mean there is sufficient mixing in the boundary layer that thermal effects can be ignored (Parkinson, 1987). So for wind farm considerations, the flow is almost always neutral. A truly steady state, neutrally stratified, barotropic ABL rarely exists (Weng and Taylor, 2003) so modelling it as such is an approximation, though it does allow the isolation of the influence of shear production on atmospheric turbulence (Nieuwstadt and Duynkerke, 1996).

2.6. Surface layer

Simulations of boundary layer flows around buildings and over topography are based on considerations of the inner regions of the boundary layer which reaches a maximum height of a few hundred metres from the ground surface. The region is fully turbulent and sufficiently close to the surface

that the effects of Coriolis and buoyancy forces due to density stratification are negligible. It is also far enough from the surface that the viscosity of the air and the characteristics of individual roughness elements also have little effect on the motion. In neutral stability conditions, the inner region is occupied entirely by the dynamic sublayer (Brutsaert, 1982).

2.6.1. Logarithmic velocity profile

It is widely accepted that the mean vertical profile of velocity varies logarithmically in the dynamic sublayer. The profile law was developed in the early 20th century and introduced as a meteorological concept by Prandtl in 1932. Various derivations exist, through dimensional analysis (Monin and Yaglom, 1971), and the original mixing length theory as shown here. It is known (Parkinson, 1987) that the momentum flux at the surface layer is:

$$\overline{u'w'} = -l^2 \left| \frac{\partial U}{\partial z} \right| \frac{\partial U}{\partial z} \tag{2.20}$$

where l is the mixing length. Since this is approximately constant with height in the surface layer:

$$\overline{u'w'}(z) = \overline{u'w'}(z=0) = u_*^2 \tag{2.21}$$

Substituting this into the mixing length equation ($l = \kappa z$, where κ is the Von Karman constant, reviewed by Hogstrom (1996) to have a value $\kappa = 0.40 \pm 0.01$), and taking the square root gives:

$$\frac{\partial U}{\partial z} = \frac{u_*}{\kappa z} \tag{2.22}$$

Which when integrated over height from $z = z_0$ to any height z, gives the logarithmic equation:

$$\frac{U}{u_*} = \frac{1}{\kappa} \ln \frac{z}{z_0} \tag{2.23}$$

This is the standard logarithmic velocity profile, used to describe fluid flow over rough surfaces, and requires the use of two unknown scaling parameters, the friction velocity, u_*, and the aerodynamic roughness length, z_0. The profile applies equally to flows over complex terrain as it does to flat terrain for which is derivation is based (Besio *et al.*, 2003), though the effects of the topography will undoubtedly affect the profile shape.

The effects of stability on the velocity profile as described in section 2.5.4, allow an extra term to be introduced into the profile for ABL flows:

$$\frac{U}{u_*} = \frac{1}{\kappa} \left[\ln \frac{z}{z_0} - \psi \right] \tag{2.24}$$

where Ψ is a stability-dependent function, positive for unstable conditions and negative for stable conditions (Petersen *et al*., 1998).

2.6.1.1. Friction velocity

The friction velocity is a scaling velocity of the surface shear stress and is defined by the relationship:

$$u_* = \sqrt{\frac{\tau_0}{\rho}} = \left[- \left(\overline{u'w'} \right)_o \right]^{1/2} \tag{2.25}$$

and depends on the nature of the surface and the mean velocity value. While defined strictly in terms of surface values, in practice it is evaluated

at a convenient height within the surface layer where the vertical variation can be assumed to be negligible with height. It originates from the derivation of velocity profile where the shearing stress is approximately equal to the square of the mean velocity.

2.6.1.2. Aerodynamic roughness length

Terrain roughness is defined by Petersen *et al*. (1998) as the collective effect of the terrain surface and its roughness elements, leading to an overall retardation of the wind near the ground. To model the roughness as a single layer, the point of interest must be 'far away' from the individual roughness elements.

The roughness length characterises the surface roughness. It is the height above the surface at which flow begins. The existence of roughness elements prohibits fluid flow at the exact surface, though turbulent motions do begin to occur. Actual velocity flow starts at a height, z_0, above the ground (Monin and Yaglom, 1975). The value of the roughness length is usually a small percentage of the actual height of the roughness elements, but varies considerably depending on the layout and type of roughness. Full details are found in section 2.8.

2.6.2. Power law velocity profile

Some flow situations lead to mathematical difficulties in solving the logarithmic velocity profile, so it can be easier to describe the mean profile by a simple power function of height:

$$U = az^m \tag{2.26}$$

where m and $a = \left(U_1 / z_1^m\right)$ are constants for given conditions of surface roughness and turbulence, and most turbulence studies point to $m = 1/7$. There is no theoretical justification of the power law (Brutsaert, 1982) but it is known to fit mean wind profiles well when suitable parameters are defined. The work here will continue to use the logarithmic profile due to its more widely accepted use and more easily defined parameters.

2.6.3. Alternative profiles

Various alternatives to the standard profiles are presented in the literature. The most common of which is the Deaves and Harris (1978) model (D&H) which is designed specifically for strong winds. Its advantage over the two profiles above, is its applicability to all regions of the boundary layer, from right at the surface through to the top of the layer. It is in fact the only one of the three which "recognises" the top of the ABL (Cook, 1997). There is some added complexity in the profile in the form of an extra parameter, *h*, the ABL height. The profile equation is:

$$U = \frac{u_*}{\kappa}\left[\ln\frac{z}{z_0} + 5.75\left(\frac{z}{h}\right) - 1.88\left(\frac{z}{h}\right)^2 - 1.33\left(\frac{z}{h}\right)^3 + 0.25\left(\frac{z}{h}\right)^4\right] \qquad (2.27)$$

The D&H model has been shown to perform well for high speed wind flows and its use for wind energy prediction is quite suitable.

Other groups have considered alternative profiles (Wilson and Flesch, 2004 for example), each time finding a model that fits better with certain types of data. The results of these efforts are ultimately subjective, and depend on the data used for comparison, and the values measured. When specific conditions exist that the standard profiles are known to be poor at predicting, then one of these alternative options may be suitable, but for numerical modelling of the lower layers, this is unlikely.

2.6.4. Profile summary

The velocity profiles represent the flow in the boundary layer, though some debate occurs about which is most suitable. Neither of the standard laws (logarithmic and power) is valid throughout the entire overlap region of the boundary layer. The logarithmic profile is more suited to the lower region, while the power law is better above the overlap. Buschmann and Gad-el-hak (2003) compare both profiles with numerous datasets, and come to no statistically significant conclusion of preference to either law. Indeed in some boundary layer studies (Ishihara, 1999), profiles for both laws are stated with the logarithmic law in the surface layer and the power law for the rest of the boundary region. For this work, the surface layer is of most importance so it is logical to use the standard logarithmic velocity profile

or the D&H model, though the simplicity of the logarithmic profile makes it preferable.

2.7. Sublayer similarities

In the viscous sublayer, the universal logarithmic profile is no longer valid and there are as many different types of flow as there are surfaces. Close to the surface, the flow is not fully turbulent though many of the effects are still present. Except for very smooth surfaces, the nature and placement of the roughness elements will significantly affect the flow regime as the flow will continue to exist within the roughness. Figure 2.3 shows how the mean profile changes in the lower region of the ABL. The upper boundary of the layer is given by:

$$h = 30\frac{\upsilon}{u_*} \tag{2.28}$$

Within the lowest part of the sublayer, the velocity profile is linear and this is known as the laminar sublayer. Above this, a transitional layer exists between the linear profile and logarithmic profile. Consideration of this transition must be made for any boundary layer simulations of the lower layer and this is discussed in section 3.3.

2.8. Terrain characteristics

The influence of the terrain and surface roughness are considerable in the inner region of the boundary layer. The roughness of an area is determined by the size and distribution of the roughness elements it contains. The

variation in terrain height, due to hills, valleys or buildings has effects on the flow creating features such as separation, recirculation and variable pressure gradients. Full details of the complex effects in turbulent flows can be found in Piquet (1999) or Antonia and Krogstad (2001).

2.8.1. Aerodynamic roughness length

For flow over a rough surface, the height z above the ground is measured from the true ground surface, i.e. at the base of the roughness elements. The height of the roughness elements above this point is h_R, and is the mean height of *all* the roughness elements on the surface.

Due to the complexity of surface roughness, and the infinite number of setups that can occur, a method of defining any roughness configuration by a single parameter was developed, and led to the value, y_R, which is known as the equivalent sand grain roughness. Numerous texts (Nikuradse (1932), Schlichting (1955), White (1979)) discuss this system of representing roughness, and provide tables with values of y_R for certain roughness arrangements, though for the most part these relate to man made roughness elements.

The roughness length, z_0, is the height above ground where the velocity is theoretically zero, so although turbulent exchanges occur, there is no flow velocity. It can be determined from figure 2.2 as the intercept point on the y-axis. The spatial variation of z_0 has been under consideration for many years, as with naturally occurring roughnesses it will change (Taylor,

2001). For most flows z_0 can be considered constant for simplicity, unless significant roughness variations are present. The measurement of z_0 has been a subject of considerable research for many years and methods of finding accurate values are well summarised by Barthlemie *et al.* (1993) and Wieringa (1993) who presents a table (2.2 below) of suitable values for varying roughnesses. Chamberlain (1965) performed much more specific evaluation of z_0 for grass structure, presenting values of z_0 and u_* for a range of different low grass types and seem to be slightly smaller than those from Wieringa (1993), though the true value of z_0 is fairly subjective.

Roughness Type	z_0 **(m)**
Sea, sand, snow	~0.0002
Concrete, desert, flat tides	0.0002-0.0005
Flat snow field	0.0001-0.0007
Rough ice field	0.001-0.012
Fallow ground	0.001-0.004
Short grass	0.008-0.03
Long grass, heather	0.02-0.06
Low crops	0.04-0.09
High crops	0.12-0.18
Pine forest	0.8-1.6
Town	0.7-1.5

Table 2.2 – Roughness length values from various surface types Wieringa (1993)

Kustas and Brutsaert (1986) showed values of z_0 up to 5m for very complex terrains, though these are irregular distributions of very large elements such as within a city centre, or a big forest with large clearings (Wieringa, 1996).

2.8.2. Mean roughness height

For smooth walled flows, the mean velocity varies from zero at the wall to U_∞ in the free stream. Roughness on the surface varies the development of the profile and was investigated considerably by Schlichting (2000), who considered the flow along pipes with varying roughness configurations. He proposed three flow regimes based on friction velocity, u_*, and roughness element size, h_R:

Hydraulically smooth – Re < 5

Transitional – 5 < Re < 70

Fully rough – Re > 70

$$\text{where } \mathrm{Re} = \frac{\rho u_* h_R}{\mu} \tag{2.29}$$

Flows in either the completely smooth, or completely rough regimes are independent of Reynolds number, whereas flows in the transitional region will exhibit characteristics from both extremities. Snyder and Castro (2002) examined these critical Reynolds numbers showing some variation dependent on roughness type and concluded that the critical value for hydraulically smooth flows should be nearer 1 than the value of 5 presented by Schlichting (2000), which is also backed up by the work of Calder (1949).

For atmospheric flows this is more suitably considered in terms of the roughness length, z_0, which is used to characterise a rough surface which may have considerable spatial variation in exact roughness height. The relationship between z_0 and h_R has been the subject of considerable

research for naturally occurring roughnesses. The original ideas for rough surface evaluation had been limited to pipe flows (Schlichting, 2000, White, 1999), where the roughness height is reasonably simple to determine. In naturally occurring roughness areas the value of z_0 is more easily found through measurements of the velocity profile. Xian *et al*. (2002) show good understanding of the increase of z_0 with the increasing size and coverage of roughness elements in their work on desert roughness.

Paeschke (1937) was probably the first to consider how to relate z_0 to the height of the roughness elements, and his results for rough snow, various grassy surface and certain crop formations gave the ratio as:

$$h_R = a \times z_0 \tag{2.30}$$

where a=7.35.

This relationship has been confirmed by various groups though the published value of a has varied slightly from group to group, as seen in table 2.3.

Researchers	***a***
Tanner and Pelton (1961)	7.6
Perry and Jouber (1963)	7.5
Chamberlain (1966) *(artificial grass)*	7.5
Chamberlain (1968) *(bluff elements)*	8.0
Parkinson (1986)	20.0
CFX (2000)	30.0
Britter (1982)	10.0-33.3

Table 2.3 – Comparison of roughness parameters for environmental flows - from Brutsaert (1982)

For grassy surfaces over hills, which are considered in this project, the value of z_0 is in the region of 0.01m to 0.05m, a representative number can be considered as 0.03m. If a value of 7.5 is used in the above expression, this would consider grass to have average height of 0.225m, which is expected. The more extreme values given above would then indicate grass to have a height of around 0.9m which is more unlikely and not representative of the surface under consideration.

Interestingly, Neff and Meroney (1998) go on to provide a solution to very rough, forest lined surfaces, by recommending a 'crew-cut' of the forest top to provide a much smoother effective roughness and allowing higher wind speeds for wind farm development.

2.8.3. Zero plane displacement height

For denser roughness configurations where lower sections of the roughness do not even experience turbulent exchanges, and no flow effects occur, a new variable can be introduced which takes this into account. The zero plane displacement height, d, is the location above the ground, where turbulent exchanges begin to occur. It effectively displaces the ground surface by a distance into the roughness. The variable is incorporated into the logarithmic profile as follows:

$$\frac{U}{u_*} = \frac{1}{\kappa} \ln\left(\frac{z-d}{z_0}\right) \tag{2.31}$$

This is an empirical version of the original profile (Equation 2.23) for modelling flow over very rough surfaces (Sutton, 1953).

The density of the elements often does not allow flow. For a very dense canopy, such as thick forest, the flow will be expected to skim over the top of the elements and so the value of d will approach h_R, whereas for sparsely arranged elements, the value of d will approach zero, as flow will occur right up to the boundary. The value of d within the velocity profile, does not alter the shape of the profile, it only shifts the profile in the positive z-axis by a value of d. Flow is still affected by the amount of roughness protruding above the zero plane displacement height and it is from this height that the aerodynamic roughness length must be defined.

The aerodynamic roughness length, z_0, is the height, above d, where the velocity is theoretically zero, so although turbulent exchanges occur, there is no flow velocity. Velocity flow occurs at a height of $d+z_0$ above the ground surface. The original profile is used for surfaces which are covered with low-level vegetation, where z_0 is a suitable representation of the roughness height and is often only a few centimetres. The modified equation was developed for areas of ground covered in crops, trees and buildings. Figure 2.4 helps to demonstrate the physical properties of the roughness characteristics h_R, z_0 and d which are not related to the flow.

- h_R is the average height of the roughness elements
- d is a measure of the density of the elements.

- z_0 is the roughness length, a distance above d, where some flow properties occur (turbulent exchanges), and is the point where the flow velocity is zero.

In most studies of naturally occurring roughness, it has been considered reasonable to assume $d = \frac{2}{3} h_R$ (Garratt, 1992). Though if the roughness is known to be particularly dense, for example a forest canopy, then the value can be increased up to the limit of $d = h_R$, though here we would be assuming the top of the canopy is smooth. This approach is suitable for modelling forest canopies, dense bush areas and other very thick surface roughnesses. Figure 2.5 shows flow over a forest canopy and the effective locations of d and z_0.

The above discussion relates to the bulk atmospheric flow. A separate flow can occur within the canopy region (within d) but this does not have any effect on the mean flow occurring above the canopy, as is depicted in figure 2.5.

2.8.4. Roughness change

Changes in surface roughness have a significant effect on the flow. A number of roughness change models have been developed which attempt to predict the length of the adaption period, where the flow re-adjusts to the new roughness. It is still an area of research and so the models in this work will consider constant surface roughness (which is an acceptable

simplification). Deaves (1980) performed some of the earliest numerical modelling of boundary layer variation due to changes in roughness, which helped develop empirical formulae for interpolating velocities and stresses within the flow. More recently, Cheng and Castro (2002) have produced some interesting approximations of the effects on near-wall flow, while Wright *et al*. (1998) considered how the ABL adapts to the new roughness and analysed the overlap region. Three main methods exist for the determination of roughness change effects. The Karman-Pohlhausen is the simplest idea, which assumes 2-D flow and no transition region. The second method, similarity theory, requires the use of a mixing length model, though it is widely accepted as a good base. Finally, linear perturbation methods assume the flow is split into two regions, the inner layer is where all the perturbation effects occur while the outer layer is independent of roughness. Wu and Meroney (1995) have performed extensive wind tunnel based research on the area.

2.9. Influence of topography

As already discussed, the main influences on the inner section of the ABL are surface conditions. Roughness and stability effects have also been discussed, but the shape of the topography will probably have even more of an effect on the wind flow. Steep terrain causes dramatic speed ups in velocity as the stratification layers are compressed. Flow continues along these layers, but at much higher speeds. In extreme cases, when the stratification layers are pushed very close together, the fluid will move around the side of the obstacle rather than flow over the top. On the lee

side of obstacles, the stratification layers expand and the flow slows down. Hilly terrain is that which is sufficiently gentle to ensure mostly attached flow. Typical horizontal dimensions of hills are a few kilometres or less (Petersen *et al.*, 1998).

2.9.1. Flow over hills

Wind farm placement is ideal in regions of flat terrain, where the wind profile is fully developed and well understood. As these regions become less available for farming, developers must consider more complex terrain regions where hills are present. The influence of hills can be beneficial to the power availability as the flow speed increases to the top of the hill. Issues can arise on the lee slopes of hills due to flow separation and recirculation. So clear understanding of the effects and issues regarding hill influence is important. The changes in surface elevation induce large scale changes in the pressure field of the hill region, which cause internal gravity waves, further affecting the local flow field. The main areas of importance for consideration are hill shape, length scale, and the turbulent effects caused by the topography changes.

2.9.1.1. Shape

As the wind flows over the hill, the parcels of air (as in section 2.5) must move in the vertical direction. This motion is accompanied by a gravitational restoring force. Seminal work by Jackson and Hunt (1975) split the flow field for wind flow over a hill into three (initially two) layers.

The lowest of which (the inner layer) was characterised by roughly equilibrium conditions so a simple mixing length model could be used. The shear stress divergence is roughly balanced by the inertial terms, and the thickness of this layer is generally very small compared with the hill height. Above this, the outer layer has a bottom part which is essentially inviscid but rotational and stress perturbations have little effect. At greater heights the outer flow is characterised by irrotational perturbations (Castro *et al.*, 2003). A historical review of the development of understanding of flow over hills is presented by Wood (2000).

Classification of hill height and shape was also initiated by Jackson and Hunt (1975) in their model for flow over hills. They defined a characteristic length, L, which is the distance from the hill top to a point upstream where the elevation is half of its maximum (see Figure 2.6). Considering an inner layer of depth, l, where the turbulent transfer is important,

$$\frac{l}{L}\ln\left(\frac{l}{z_0}\right) = 2\kappa^2 \tag{2.32}$$

which is based on low hills with no significant mean flow separation. This idea was further developed by Jensen *et al.* (1984) who assumed a logarithmic variation in the velocity speedup, ΔU, giving:

$$\frac{l}{L}\ln^2\left(\frac{l}{z_0}\right) = 2\kappa^2 \tag{2.33}$$

which provided improved estimates of $\Delta U_{\max}$ and predicts a significantly smaller lower layer. Work on 3D classification by Mason and Sykes (1979) defined two further characteristics based on the hill geometry:

- hill length, $\frac{L}{z_0}$
- hill steepness, $\frac{h}{L}$

If the hill is large enough to disturb the whole of the ABL (the hill height, $h \approx 500m$), then buoyancy driven flow patterns are important at any time of day. For hills much smaller than the ABL ($h \approx 100m$), buoyancy effects are only important when the ABL is stably stratified. Hills with a length scale of the order of kilometres are free of buoyancy effects for most of the day and when winds are strong. As the length scales of hills are under 10km (over this would describe a mountain), we can also ignore the Coriolis forces of the Earth (Kaimal and Finnigan, 1994).

Wind flowing over hills experiences very consistent effects. Figure 2.6 shows the change in wind profile at the hill top though a description of the effects is useful. Close to the surface, there is a slight deceleration at the upwind foot of the hill. If the hill is steep enough, this deceleration may cause a small separation bubble. The flow accelerates up to the hilltop where the maximum velocity occurs. The flow then decelerates down the lee slope. If the hill is steep enough, a large separation bubble forms on the lee slope, within which the flow is in the opposite direction to that above it. The depth and length of this bubble depends on the shape of the hill.

Athanassiadou and Castro's (2001) investigation into flow over rough hills showed flow separation occurring for hills with a slope of 20° (steepness ~ 0.7) though not for slope of only 10° (steepness ~ 0.3). With or without the separation bubble, a large wake region extends behind the hill, with a significant velocity deficit, and this can extend for many hill heights behind the hill top. For a perfectly axisymmetric hill, the upwind separation bubble is replaced by a region of lateral flow divergence as the streamlines pass around the hill (Kaimal and Finnigan, 1994). For hills with low slopes (steepness < 0.3) the thickness of the separated region is comparable with the thickness of the inner region as found with the Askervein hill (Taylor and Teunissen, 1987). The level of acceleration up to the hill top is quite significant even for small slopes as the shear in the approaching wind flow amplifies the acceleration (Jackson and Hunt, 1975), for example, if the slopes of the hill is about 1/5, the speed up can be a factor of about 0.5 (Belcher and Hunt, 1998).

Wood (1995) examined the onset of separation, considering a critical steepness for the lee slope at which separation would exist:

$$\theta_{crit} = \frac{\ln\left(\frac{l}{z_0}\right)^2}{\left(\ln\left(\frac{h}{z_0}\right)\right)^2\left(1+4.2\Big/\ln\left(\frac{l}{z_0}\right)\right)} \tag{2.34}$$

The value of θ_{crit} is a fairly subjective however, and Wood's paper does not predict the onset of separation on the Askervein hill, yet a noticeable region was found during the field experiment (Cook, 2003).

2.9.1.2. Turbulent effects

The turbulence in the flow is greatly changed by hills (Belcher and Hunt, 1998). The main turbulent effects result from local equilibrium, rapid distortion and turbulence memory. Equilibrium occurs when production and dissipation of turbulence are in equilibrium, with advection and transport playing a minor role. This gives a representation of turbulent fluxes by eddy diffusivities, such as the momentum flux ($-\overline{\rho u' w'}$) would be proportional to the mean shear (dU/dz) as is found in the surface layer over flat terrain.

Rapid distortion is the opposite of this and occurs when the mean flow is changing too quickly for the turbulence to come into any sort of equilibrium with it, and this is highly dependent on the upstream anisotropy (Zeman and Jensen, 1987). The turbulence derives its energy from the mean flow. The turbulence memory is the time it would take for the turbulence to attain equilibrium, assuming the strain rates were held constant. It is estimated by comparing the kinetic energy of the flow (k) with its dissipation rate (ε or ω), and is the basis for certain turbulence models used in numerical simulations (see Chapter 3). For flow over hills, a region of local equilibrium is found at the bottom of the inner layer, while rapid distortion is prominent in the inner layer. Athanassiadou and Castro (2001) performed laboratory experiments to measure the implications of

rapid distortion on the flow over rough hills finding flow separation regions where the distortion was high, due to steep slopes over hills.

Shear and blocking effects due to complex terrain features acting on the turbulence were investigated by Tampieri *et al*. (2003) concluding that current turbulence theory does not cover all the effects a terrain change may have on the flow. This highlights the complexity of turbulence and the limits of our understanding. Atmospheric effects such as gusting and wind direction changes only serve to increase the problem. Further details about turbulent flow over hills can be found in Belcher and Hunt (1998).

2.9.2. Studies of flow over hills

Considerable research has concentrated on understanding wind flow over hills, beginning with the work by Jackson and Hunt (1975) who seemed to set a challenge to fellow researchers to help produce full comprehension of the flow. The review by Taylor *et al.* (1987) is an invaluable reference of the early work in the area and summarises clearly the field experiments undertaken and some of the wind tunnel approaches used. Performing full field experiments is costly and so while data is available, it is rarely comprehensive (Ding *et al.*, 2003). The field surveys of most use are those at Brent Knoll, Black Mountain (Bradley, 1980), Sirhowy Valley (Mason and King 1984), Blashaval Hill (Mason and King, 1985), Nyland Hill (Mason, 1986), Askervein Hill (Taylor and Teunissen, 1986), Kettles Hill (Salmon *et al.,* 1988) and Cooper's Ridge (Coppin *et al.,* 1994).

While considering the flow over real terrain is extremely beneficial, it must be supported by a clear knowledge of the idealised wind flow over hills. For this reason early theoretical and more current wind tunnel work has considered the flow over 2-D cosine shaped hills, 3-D axisymmetric cosine hills, and combinations of hills, both rough and smooth (Jackson and Hunt, 1975, Britter *et al.*, 1981, Hunt *et al.*, 1988, Weng, 1997, Miller and Davenport, 1998, Neff and Meroney, 1998, Taylor, 1998, Ishihara *et al.*, 1999, Athanassiadou and Castro, 2001, Takahashi *et al.*, 2002 as examples). Each study helps further the knowledge.

Modelling a single hill helps develop the knowledge of how a single topography change affects the wind flow. Modelling combinations of hills (Meroney *et al.*, 2002 for example) helps understand the effects of real terrain regions and how the flow over one hill will affect the next. The work by Miller and Davenport (1998) shows that velocity speed ups in complex terrain are reduced compared to those found on isolated hills. The effect of having a number of hills in series dulls the terrain effect, making the hills act almost like a very rough surface.

2.9.3. Terrain data

In the United Kingdom terrain data is available in a variety of forms, from contour maps, to elevation models and surface data models. Full details of terrain modelling techniques and models can be found through a number of sources on the internet. The most common digital terrain models for UK land coverage are as contour data or elevation data over a set grid layout.

Grid data is available at 50m intervals for all UK regions, thanks to the Ordnance Survey (http://www.ordnancesurvey.co.uk). Contour data is also available for varying locations.

2.9.3.1. Accuracy

The linear terrain data is only available at 50m intervals at the time of modelling, though more accurate data is becoming available for large parts of the country at the time of writing (5m intervals). Thus for the models used here, the terrain accuracy is not as high as would be liked. Field survey data is available at 2m contour levels, so even more accurate, but contour data is not suitable for use in this project as will be discussed in Chapter 5, due to methods for incorporating data into numerical models.

2.10. Measurements of the ABL

The work in this project considers the comparison of numerically simulated results for flows over hills with those measured in field surveys and those produced in a wind tunnel. It is important to consider, for each measurement device, what exactly is being measured and what level of accuracy can be given. Chapter 3 will discuss the accuracy of the numerical models. One of the main problems of field studies is that they are often hindered by the general sparseness and ambiguity of the data sets (Ding *et al.*, 2003) so choosing a good field survey with which to validate a model is very important. Wieringa (1996) makes an excellent point that the location of field data retrieval masts has a hugely significant effect on

what data is being collected. Thankfully most survey data specific to flow over hills has been collected at masts positioned specifically for the experiment, though Wieringa (1996) points out that the use of this data for any purpose other than predicting wind flow over hills may not be suitable. As an example, building planners require historical wind data collected over 20 years, whereas airport tower staff are only interested in 2 minute averaged data sets.

2.10.1. Cup anemometers

Cup anemometers are the most common devices used to measure mean wind profiles. They are dependable, inexpensive and reasonably accurate. They depend on moving parts coming into equilibrium with the flow, so the response time is typically too long for turbulence work (Kaimal and Finnigan, 1994).

The most commonly used system is a three-cup anemometer (shown in figure 2.7), the advantage of which is that it can accept winds from any direction. Only those obstructed by the measuring tower can be deemed unfavourable. The device is used in conjunction with a wind vane to measure the direction of the flow. There is a tendency for these anemometers to overspeed, partly due to their non-linear response to wind speed and partly from sensitivity to the vertical wind component. This overspeeding error is generally 5-10%.

For wind profile measurement, the devices are usually placed on a single tower at heights which double with each change (1, 2, 4, 8, 16m etc), though for applications measuring single height values the World Meteorological Organisation (WMO, 2003) recommends a height of 10m in an unobstructed area taken over a period of about 10 minutes. The WMO also suggest that a clear fetch of 10 obstruction heights is sufficient open space, while Wieringa (1996) points out that the unobstructed fetch should match the measuring period (i.e. for 5m/s wind speed over 10 minute period, this means an upwind fetch of more than 2km).

Cup anemometers have a start speed of 0.5m/s so are more accurate with higher wind speeds. Papadopoulos *et al.*, (2001) measured the effects of turbulence and flow inclination on the performance of a series of cup anemometers in a real flow field, finding differences between cups of up to 2% and errors of up to 5% in the measurements of the mean flow. The limitation of these errors is imperative and calibration techniques are evolving. The power curve of wind turbines must be verified to strict international standard, as even small errors in the wind speed measurement can produce significant errors in the power produced.

2.10.2. Sonic Anemometers

A sonic anemometer determines instantaneous wind speed and direction by measuring how much sound waves travelling between a pair of transducers are sped up or slowed down by the effect of the wind. They have no moving parts and can measure velocity up to twenty times per second.

They are more accurate than the cup version and can measure extremely slow winds accurately. The advantage of no moving parts means the device does not need to come into equilibrium with the flow and measurement can be much faster, so it is well suited for measuring instantaneous changes in velocity and hence turbulence. While these devices can not be considered to be perfectly accurate, the errors are generally very small. The largest errors are associated with unstable, deep, convective boundary layers, and the smallest with neutral layers (Wilczak *et al.*, 2001). A typical sonic anemometer is shown in figure 2.8.

2.10.3. Gill Anemometers

Several gill anemometers were used during the field survey, which measure the three orthogonal vectors of the wind, along wind component, U, across wind component, V, and vertical wind component, W, using three propeller anemometer sensors are mounted at right angles on a common mast as seen in figure 2.9.

Each sensor measures the wind component parallel with its axis of rotation. Propeller response as a function of wind angle approximates the cosine law, allowing true wind velocity and direction to be calculated. The anemometer is designed for maximum sensitivity at lower wind speeds.

This type of anemometer retains many of the issues discussed for the cup anemometer is regard to coming into equilibrium with the flow. The extra

accuracy provided by having all three primary wind components recorded separately is invaluable.

2.10.4. The wind tunnel

Boundary layer wind tunnels are a common apparatus for analysing the atmosphere, and their use has been very successful in accurately reproducing wind flows over terrain. Large scale wind engineering, involving consideration of the ABL as influenced by thermal effects, surface roughness, Coriolis and other effects is more statistical than deterministic in character, as it is seldom possible to find the necessary meteorological data to assemble well defined boundary conditions. For this reason, the results of atmospheric studies performed in wind tunnels can be used for design purposes and to provide data for CFD calibration (Gosman, 1999).

The advantage of the wind tunnel is its controlled, reproducible environment that allows the investigation of the individual effects of specific parameters and their variations. Boundary layer wind tunnels have been used in many wind engineering applications and have undergone rigorous validation against field data. They will remain the main tool of the wind engineer for many years to come. Numerical models can be used alongside wind tunnels to provide solutions to wind engineering problems.

There are some issues in need of consideration for wind tunnel modelling. Separated flow regions cause problems in the use of hot-wire anemometers, the main method of flow measurement. Pulsed-wire anemometers are a suitable alternative and have been used successfully (Britter *et al.*, 1981). Scaling issues are also important. To maintain an accurate representation of the real flow, it must be ensured to be aerodynamically rough, which occurs when $u_* z_0 / \upsilon > 5$ (Schlichting, 2000). When the real terrain is reduced to a scale suitable for a wind tunnel, the surface roughness shrinks too much to satisfy this condition. The alternative options are to work with an aerodynamically smooth version (which would incorrectly model the near-wall turbulence, and hence separation), or to increase the roughness disproportionately (in which case, the surface layer would be occupied almost entirely by the magnified roughness elements) (Finnigan *et al.*, 1990). Other errors in wind tunnel simulations are described by Farell and Iyengar (1999) who show 10% deficits in shear stress prediction amongst other problems such as the evaluation of roughness length. In a later paper, Iyengar and Farrell (2002) show errors of u_* calculation in excess of 15% from measuring Reynolds stresses with a cross-wire probe, and significant errors in calculating the roughness length in simulated ABL flows. This problem of determining roughnesses reminds wind tunnel users that due consideration must be given to errors if z_0 is one of the parameters used to determine the scale of the simulation.

Over a typical grass covered hill about 100m in height, the surface layer is roughly 10m in depth, and it is this region where the wind gradients are the

largest so this is the area of most interest. Wind tunnel methods are constantly being developed for new modelling techniques and consideration of more complex flow effects such as vertical Reynolds stress distributions and velocity power spectra (Cermak *et al.*, 1995).

The stability of the boundary layer within a wind tunnel is simulated by the heating or cooling of the ground and the airflow to simulate the heating of air by the ground surface (Ohya, 2001). The turbulence in the ABL is one of the most important features and is important to reproduce it as accurately as possible. This turbulence differs from that created by the wind tunnel as there are both thermal and shearing effects, and as the mean flow has been affected by the Earth's rotation (Garratt, 1992).

Neutral flow, in which buoyancy effects are absent, is readily produced in a wind tunnel, and may be closely approximated to the atmosphere in windy conditions with a complete cloud cover (Garratt, 1992). However, thermally stratified flow and the Coriolis force generated by the Earth's rotation are beyond the capability of a wind tunnel. Strictly speaking, while the wind tunnel cannot simulate the Coriolis force, it can treat thermal stratification in a limited sense, though with significant difficulty and great expense (Derickson and Peterka, 2004).

Blockage issues in wind tunnel measurements have been analysed and presented by Parkinson and Cook (1992) who used a wind tunnel section with slatted walls and open area ratios up 0.55 as an optimum, allowing

blockages of up to 30% of the test section without any considerable effects on the wind flow. This is impressive as numerical models must keep the blockage to as low as 4% of the test section (Baetke and Werner, 1990).

The advantages of wind tunnel studies are clear and the accuracy of the results are generally excellent. Errors are present as with any study, though these are kept to a minimum through consideration of the flow regime and the measuring requirements. They will continue to be the tool of choice for wind engineers for many years. The advent of numerical models does not change this and the two methods of modelling wind flow work well together in efforts to validate and understand the flow of wind.

2.11. Summary

The structure and size of the ABL have been detailed in this chapter. Flow effects have been considered with respect to weather conditions, terrain influence and roughness layout to show a clear understanding of the processes occurring within the ABL. It is clear that from a numerical modelling point of view, the main areas of importance that must be considered for an accurate simulation are:

- Roughness layout
- Velocity profile (particularly in viscous sublayer)
- Terrain model accuracy
- Flow stability and stratification
- Turbulence

Chapter 3 will consider how these will be numerically modelled.

3. Numerical Modelling

3.1. Introduction

"It is the mark of an educated mind to rest satisfied
with the degree of precision that the nature of the
subject admits, and not to seek exactness when
only an approximation is possible."

Aristotle (384 BC)

Chapter 2 discussed the theory of the ABL and the sections of environmental flows which are important to consider when attempting to model the flow. This chapter considers the models and codes used to simulate wind flow, looking at their accuracy and ease of implementation. Numerical models use computers to perform large numbers of calculations of the fluid flow and to simulate the flow patterns and fluid structure. A large variety of numerical models are available, ranging from simple linear solvers through to direct numerical solutions. Their use for ABL flows varies in quality, with the linear models being easy to put into practice albeit with limited accuracy, and the more complex models being much more difficult to compute, though producing much more precise solutions.

3.1.1. Linear models

The most renowned linear model is WAsP (Wind Atlas Analysis and Application Program), developed by the RISØ wind engineering laboratory in Denmark in 1987, based on the concept of linearised flow models introduced by Jackson and Hunt (1975). The model was developed initially for neutrally stable flow over hilly terrain (Mortensen and Landberg, 1993) and has been developed considerably with numerous releases. It contains simple models for turbulence and surface roughness (based on Charnock, 1955), providing a quick and accurate method of analysis for mean wind flows (Miller and Davenport, 1998). The model is best suited to more simple geometries and is known to poorly predict flow separation and recirculation (Botta, 1992), though its strength lies in predicting flow over simpler regions, as proved by the good results for the prediction of offshore flow fields in Lange and Hojstrup (2001). As significant numbers of wind farms are now being placed offshore, this is an application where linear codes are more suitable due to the low solution times. This high speed solver has made it one of the most common models in use for wind farm location and analysis. As wind farms are being placed in more complex terrain regions, the model is beginning to find its limitations which results from the linearity of the equation set (Pearce and Ziesler, 2000). For this reason, over complex terrain, 3-D full RANS solvers appear to be more appropriate (Alm and Nygaard 1993, Montavon, 1998) as WAsP can be suspiciously different from other model results for complex areas (Nielsen, 1999). Walmsley *et al*. (1990) show errors of up to 15% from codes like WAsP and MS-Micro, though codes such as this

remain the dominant models for use in the wind power sector due to the level of validation work available for them. Yamaguchi *et al.* (2003) modelled a coastal region of Japan, showing good agreement for non-linear models with the experimental data, while the linear model tended to overestimate the mean wind speed and underestimate the turbulence.

3.1.2. Direct Numerical Simulation

Direct numerical simulation of the Navier-Stokes equations for a full range of turbulent motions for all scales (large down to dissipation) is the goal for numerical simulation of fluid flow. It is the most accurate way to model fluid flow numerically (Murakami, 1997). The only approximations made would be those necessary numerically and would be chosen so as to minimise discretisation errors. When properly carried out, DNS results would be comparable in every way to quality experimental data (Ferziger, 1993). The main advantages are the clear definition of all conditions (initial, boundary and forcing) and the production of data for every single variable. However from a practical viewpoint, only simple geometries and low Reynolds numbers will be modelled and while DNS is unsurpassed in its ability to predict turbulence, it is unlikely to become a practical engineering tool (Speziale, 1998).

The computational requirements for DNS are considerable. It has revolutionised the study of turbulence (Speziale, 1998) but its use as an engineering tool will be a long time coming. As an example, high Reynolds number flows with complex geometries could require the

generation of 10^{20} numbers. Even if the facilities were available, it is questionable whether satisfactory results would be achieved with this level of detail from an engineering standpoint (Speziale, 1998). However, basic computations using DNS (such as those by Le *et al.*, 1993) provide very valuable information for verifying and revising turbulence models (Murakami, 1998).

3.1.3. Large Eddy Simulation (LES)

The complex nature of turbulence and the wide range of length and timescales (Speziale, 1998) mean that, at high Reynolds number, direct numerical simulation is not possible in the foreseeable future (Ferziger, 1993).

LES developed from the pioneering paper by Smagorinsky (1963), detailing the physics of smaller turbulent scales serving mainly to remove energy from the larger ones, so that their effect could be modelled instead of being resolved (as would be the case in DNS). The small scales are thought to be more universal in nature, based on the work of Kolmogorov (1941). Thus, the larger scales which contain most of the energy, and are known to be significantly affected by the flow configuration, should be computed while the smaller scales are modelled.

Considerable research concentrates on using LES for more and more complex flows. For example, Murayama *et al.* (1999) modelled the turbulent boundary layer over a rough surface showing good agreement for

mean wind field and turbulent spectra, though the high frequency wind fluctuations decreased and were less well simulated. Rodi (1997) gives a detailed comparison of RANS models with LES for flows over bluff bodies concluding that while LES showed significant improvements in accuracy over the RANS simulations, the required computational time (in 1997) outweighed any advantages. Allen and Brown (2001) performed LES simulation of turbulent flow over rough hills in two dimensions and produced good results, showing the increased accuracy available from LES particularly for turbulence predictions. Using LES for flow over hills might give useful insights, although careful resolution of the inner region is costly and decisions must be made between model accuracy and solution cost (Belcher and Hunt, 1998). For a more detailed consideration of LES, the reader is directed to Jacobsen (1997) and for consideration of its use in wind engineering to Murakami (1997).

3.1.4. Non-linear models

Computational Fluid Dynamics (CFD) is the analysis of any system involving fluid flow by means of computational simulation. A CFD code solves all aspects of numerical fluid modelling using the Reynolds Averaged Navier-Stokes (RANS) equations, a set of non-linear equations presented in Chapter 2, hence this type of modelling also being known as RANS modelling. This work considers the use of a widely available CFD code (CFX-5) to model wind flow over terrain and the code is discussed in detail throughout this chapter. For more details on CFD topics not presented in this chapter the reader is directed to a number of reference

texts: for an introduction to CFD, Versteeg and Malalasekera (1996) provide clear details; for consideration of the numerics involved, Hirsch (1988) and Chung (2002); and the CFX-5 User Manual (2003) provides full details of the software used in this project.

3.1.5. Detached Eddy Simulation

LES, even with quality wall treatment models, is far from affordable in aerodynamic calculations, and will be for decades (Spalart, 2000). This has led to the proposal of detached eddy simulation (DES), where the whole boundary layer is modelled using a RANS model and only separated regions (detached eddies) are modelled by LES. Developed for external flows such as flow over an airfoil, it is also suitable for use in modelling wind flow over hilly terrain. For simple flow situations where no flow separation occurs, the simulation reduces to a standard RANS model and as the flow becomes more complicated, so does the model, as LES attributes are introduced. This hybrid model allows the use of the simpler CFD type models for most of the flow regions, and offers the advantages of LES in the more complicated regions. DES is computationally demanding but is a promising method for strongly separating flows (Landberg *et al*., 2003)

3.1.6. Summary

While DNS is the ideal method of modelling fluid flow, the computational facilities are unlikely to become available in the foreseeable future. The inherent difficulties in developing reliable Reynolds stress models leaves

LES as the preferred approach, but until computational facilities are available which can handle the level of calculation required for complex flows, RANS based CFD codes remain the most practical tools. LES will eventually become the model of choice (Rodi, 1997), but many of the developments in validation and verification of RANS models will benefit the users of LES. Hybrid models such as DES do allow more use of the LES formulation, but require some expertise to incorporate them effectively. In view of the current situation in numerical modelling, industry demands accuracy from RANS/CFD models but not perfection (Spalart, 2000). Errors in wind energy estimates are strongly related to the distance over which the prediction is made. Numerical models predict ideal conditions which are relatively rare and yet are compared to data which has been averaged over a number of years (Ayotte *et al.*, 2001), and this can explain many of the errors between numerical results and field data.

A number of research groups develop in-house codes designed specifically to simulate certain flow types. These often produce exciting and accurate results, but their use in more general fields is limited and the amount of validation data is low. Manwell *et al*. (2000) summarise some of the more useful codes developed at the University of Massachusetts which incorporate specific models to analyse the effect of wind turbines on the flow field and the appropriate algorithms. In this project the commercially available CFD code CFX-5 is used. It is a general application code designed for a wide range of uses. This is the most common type of code

found in industry, so from a wind engineering perspective, it is important to consider its ability to model the flow field.

The methodology of using non-linear CFD codes is now discussed in depth and all the consideration required for a wind engineering model of the atmospheric boundary layer are looked at.

3.2. Turbulence modelling

"Big whorls have little whorls,

Which feed on their velocity,

And little whorls have lesser whorls

And so on to viscosity"

Lewis F. Richardson (1881-1953)

Turbulence is a difficult concept to comprehend and understanding of its effects has mainly been developed by engineers and fluid mechanists who seek to work out a definition. Kolmogorov (1941) imagined the whole cascade of energy down through smaller and smaller scales until finally a limit is reached when the eddies become so tiny that viscosity takes over. This is a reasonable approximation of the physics of turbulence.

3.2.1. Closure problem

The use of the RANS equations (section 2.3.1) leads to six unknown terms, called Reynolds stresses (equations 2.10-2.12). From a mathematical point of view, there are now eleven unknown variables (u_i, p, $-\overline{u_i' u_j'}$, ε) and only

four equations with which to solve them, so the equation set is now not closed. The instantaneous Navier-Stokes equations had only four unknowns, so are in theory solvable directly (Direct Numerical Simulation). To close the RANS equations extra models must be used to account for the turbulence in the flow. A number of models are available ranging from those based on the eddy viscosity concept to full second order closure models with simulate the effect of each Reynolds stress on the flow. These models do not model the turbulence itself (despite the name) but attempt to consider the effects the turbulence will have on the mean flow. Easom (2000) performed a detailed analysis of turbulence models for wind engineering applications, and some of the more commonly used models are also well summarised by Murakami (1998).

3.2.2. The Boussinesq approximation

Work in the late 19th and early 20th century theorised a correlation between the transfer of momentum and the transfer of heat and matter in turbulent motion. Reynolds (1895) pioneered some of the early work, though Taylor (1921 and 1938) developed the mathematics significantly in the early part of the 20th century. It was Boussinesq (1877) who suggested that the Reynolds stresses related directly to the mean strain. This is based on the idea that viscous and Reynolds stresses have similar effects on the mean flow.

Reynolds averaging the Navier-Stokes equations, considering the instantaneous velocity as having mean and fluctuating parts ($u = U + u'$), had transformed the conservative equations:

$$\frac{\partial \rho u_i}{\partial t} + \frac{\partial \rho u_i u_j}{\partial x_j} = -\frac{\partial P}{\partial x_i} + \frac{\partial}{\partial x_j}\left(\mu\left(\frac{\partial u_i}{\partial x_j} + \frac{\partial u_j}{\partial x_i}\right)\right) \tag{3.1}$$

into an averaged set:

$$\frac{\partial \rho U_i}{\partial t} + \frac{\partial}{\partial x_j}\rho\left(U_j U_i + \overline{u_j' u_i'}\right) = -\frac{\partial \overline{p}}{\partial x_i} + \frac{\partial}{\partial x_j}\left(\mu\left(\frac{\partial U_i}{\partial x_j} + \frac{\partial U_j}{\partial x_i}\right)\right) \tag{3.2}$$

which is rearranged as:

$$\frac{\partial \rho U_i}{\partial t} + \frac{\partial}{\partial x_j}\rho\left(U_j U_i\right) = -\frac{\partial \overline{p}}{\partial x_i} + \frac{\partial}{\partial x_j}\left(\mu\left(\frac{\partial U_i}{\partial x_j} + \frac{\partial U_j}{\partial x_i}\right) - \rho\overline{u_i' u_j'}\right) \tag{3.3}$$

For incompressible fluids, the Reynolds stress is related to the mean velocity gradient, and turbulent viscosity μ_t is defined as,

$$\tau_{ij} = -\rho\overline{u_i' u_j'} = -\mu_t\left(\frac{\partial u_i}{\partial x_j} + \frac{\partial u_j}{\partial x_i}\right) \tag{3.4}$$

The turbulent viscosity is a term used to model the additional viscosity resulting from the turbulence in the flow ($\mu_{Total} = \mu + \mu_t$). The modelling can now be completed if this turbulent viscosity can be found from other variables. Gatski *et al.* (1996) provides full derivation of the eddy viscosity concept. Flows which have sudden changes in mean strain rate, however, are often poorly simulated by models based on the Boussinesq approximation. These sudden changes in mean strain rate cause the Reynolds stresses to adjust at a different rate to the mean flow processes, so the Boussinesq approximation must fail (Wilcox, 1994). Some of the most common flow situations where this occurs are for flow over curved

surfaces, three-dimensional flows and flows with boundary layer separation, all regularly found in wind engineering.

3.2.3. Prandtl's mixing length model

One of the earliest turbulence models (Prandtl, 1925) reasons that the turbulence at any point can be represented by single velocity and length scales.

$$\mu_t = \rho C_\mu l^2 \left(\frac{\partial \overline{u}}{\partial y} + \frac{\partial \overline{v}}{\partial x} \right) \tag{3.5}$$

The idea of this model is very straightforward, however it requires knowledge of a length scale, *l,* which is available for simple flows only. This mixing length is effectively the distance travelled by a small parcel of fluid before losing its momentum (Section 2.3.3). This model also fails to account for the transport of turbulence quantities such as diffusive and convective transport (Versteeg and Malalasekera, 1996), which are important for wind engineering flow fields that include regions of flow separation. Consequently more complex models are required which include these effects.

The extension of this model for three dimensional flows leads to

$$\mu_t = \rho C_\mu l^2 \left(2\overline{S}_{ij} \overline{S}_{ij} \right)^{1/2} \tag{3.6}$$

$$\text{Where} \quad S_{ij} = \frac{1}{2} \left(\frac{\partial \overline{u}_i}{\partial x_j} + \frac{\partial \overline{u}_j}{\partial x_i} \right) \tag{3.7}$$

and is the basis of the Smagorinsky (1963) sub grid scale (SGS) model used in LES modelling.

3.2.4. One equation models

Due to the limitations of the mixing length model, one equation models were introduced (Kolmogorov, 1942 and Prandtl, 1945) which can account for the transport of turbulence by solving a differential transport equation relating to it.

$$\mu_t = \rho C_\mu k^{1/2} l \tag{3.8}$$

$$\rho \frac{\partial k}{\partial t} + \rho \overline{u_j} \frac{\partial k}{\partial x_j} = \tau_{ij} \frac{\partial \overline{u_i}}{\partial x_j} - \rho\varepsilon + \frac{\partial}{\partial x_j}\left[\frac{-\upsilon_t}{\sigma_k}\frac{\partial k}{\partial x_j}\right] \tag{3.9}$$

$$\text{where, } \varepsilon = C^* \frac{k^{3/2}}{l} \tag{3.10}$$

This is a simple contraction of the Reynolds stress equation developed by Hinze (1976). The equations for fluid flow are now closed, if a suitable length scale can be defined. For this reason these 'one-equation' models are limited to simple flows where a length scale is known.

3.2.5. The *k-ε* model

Seminal work by Kolmogorov (1941) argued that small scale turbulence can be characterised by two numbers, the energy dissipation per unit mass, and the kinematic viscosity (Gatski, 1996). Two-equation models were subsequently introduced which not only account for the transport of turbulence, but calculate an empirical length scale from a second transport equation. A number of these two equation models are available, but the widely used 'industry standard' version is known as the *k-ε* (k – epsilon)

model developed originally by Hanjalic and Launder (1972), where k is the kinetic energy per unit mass:

$$k = \frac{1}{2}(\overline{u'^2} + \overline{v'^2} + \overline{w'^2}) \tag{3.11}$$

and ε is the dissipation rate of kinetic energy as heat by the action of viscosity. These are used to define a velocity and a length scale at any point and time, which is representative of large scale turbulence:

$$\text{Velocity scale } \vartheta = k^{\frac{1}{2}} \tag{3.12}$$

$$\text{Length scale } l = \frac{k^{\frac{3}{2}}}{\varepsilon} \tag{3.13}$$

Which leads to the eddy viscosity being defined as follows:

$$\mu_t = C_\mu . l . \vartheta = C_\mu \rho \frac{k^2}{\varepsilon} \tag{3.14}$$

where k and ε are the subject of the transport equations:

$$\rho \frac{\partial k}{\partial t} + \rho \overline{u_i} \frac{\partial k}{\partial x_j} = \tau_{ij} \frac{\partial \overline{u_i}}{\partial x_j} - \rho\varepsilon + \frac{\partial}{\partial x_i}\left[\left(\mu + \mu_t / \sigma_k\right)\frac{\partial k}{\partial x_i}\right] \tag{3.15}$$

$$\rho \frac{\partial \varepsilon}{\partial t} + \rho \overline{u_i} \frac{\partial \varepsilon}{\partial x_j} = C_{\varepsilon 1} \frac{\varepsilon}{k} \tau_{ij} \frac{\partial \overline{u_i}}{\partial x_j} - C_{\varepsilon 2} \rho \frac{\varepsilon^2}{k} + \frac{\partial}{\partial x_i}\left[\left(\mu + \mu_t / \sigma_\varepsilon\right)\frac{\partial \varepsilon}{\partial x_i}\right] \tag{3.16}$$

with C_μ=0.09, σ_k=1, σ_ε=1.3, $C_{\varepsilon 1}$=1.44 and $C_{\varepsilon 2}$=1.92

The model can not be integrated through the near wall region as a singularity occurs at the wall surface, so wall functions must be introduced (Patel *et al.*, 1985). The *k-ε* model is the most widely used of all turbulence models and has been verified and validated for a wide variety of flows. It has relatively low computational costs and is numerically more stable than the more advanced and complex stress models. It is most

successful in flow where the normal Reynolds stresses are less important. In wind engineering this is not valid though, and the *k-ε* does not generally perform well (Versteeg and Malalasekera, 1996).

Easom (2000) discusses the performance of the model with regard to flow around a cube which shows how important the normal stresses are for wind flows. The *k-ε* model predicts isotropic stress by definition in its calculation of turbulent kinetic energy (Equation 3.11). This is certainly not the case and in wind engineering the flow is definitely anisotropic. In different regions of the flow, differing normal stresses will dominate the regime (Murakami and Mochida, 1988). Therefore the use of simple eddy viscosity terms is inadequate to describe fully the complex flow field which may occur.

3.2.6. Modifications to the standard *k-ε*

Hanjalic (1994) identified some major deficiencies in two equation eddy viscosity models. They include the inability of the linear stress-strain relationship to cope with wake flows, buoyancy, Coriolis, curved flows and other effects. To combat these issues significant work has concentrated on adapting the model for particular flow types, some examples of which are given here.

3.2.6.1. The *k-ε* RNG model

The *k-ε* RNG model is an alternative to the standard *k-ε* model and was proposed by Yakhot and Orzag (1986). It is based on renormalisation group analysis of the Navier-Stokes equations, full analysis of which can be found in Gatski (1996), and further clarification for some of the terms is shown by Sukoriansky *et al.* (2003). The transport equations for turbulence generation and dissipation are the same as those for the standard model, but the model constants differ and the constant $C_{\varepsilon 1}$ is combined with the function $C_{\varepsilon 1RNG}$.

$$\rho\frac{\partial\varepsilon}{\partial t}+\rho\overline{u}_j\frac{\partial\varepsilon}{\partial x_j}=\left(C_{\varepsilon 1}-C_{\varepsilon 1RNG}\right)\frac{\varepsilon}{k}\tau_{ij}\frac{\partial\overline{u_i}}{\partial x_j}-C_{\varepsilon 2}\rho\frac{\varepsilon^2}{k}+\frac{\partial}{\partial x_i}\left[\left(\mu+{\mu_t}/{\sigma_\varepsilon}\right)\frac{\partial\varepsilon}{\partial x_j}\right] \tag{3.17}$$

where:

$$C_{\varepsilon 1RNG}=\frac{\eta\left(1-{\eta}/{\eta_0}\right)}{1+\beta\eta^3} \tag{3.18}$$

$$\eta=\left(2E_{ij}\cdot E_{ij}\right)^{1/2}\frac{k}{\varepsilon},\ \eta_0=4.377,\ \beta=0.012$$

This extra term in the equation improves the performance for separating flow and recirculation regions. The renormalisation group formulation is complicated and the interested reader is directed to the full analysis by Yakhot and Orzag (1986) who report very good predictions for flow over a backward facing step.

As a variant of the standard *k-ε*, the computations are only slightly more time consuming, and yet the improvement for complex flows have led to a number of commercial CFD codes incorporating the model as a

recommended option. However, is it still based on the isotropic eddy viscosity concept, and so while it may provide improved results in certain applications, it may also reduce the accuracy in others (Versteeg and Malalasekera, 1996).

Models	C_μ	$C_{\varepsilon 1}$	$C_{\varepsilon 2}$	σ_k	σ_ε
k-ε	0.09	1.44	1.92	1.0	1.3
k-ε RNG	0.085	1.42-$C_{\varepsilon 1RNG}$ (Eqn. 3.18)	1.68	0.7179	0.7179

Table 3.1 – Model constants for the k-ε models

Kim and Patel (2000) compared turbulence models in regions of complex terrain with separation and recirculation patterns in the wind field. Their comparisons of laboratory and field data with those produced from various two-equation models showed that the *k*-ε RNG model gave the best agreement with respect to flow profiles and lengths of the separated flow region, and conclude this to be the best model for prediction of wind flow under neutral conditions, which was backed up by Jeong *et al.* (2002).

3.2.6.2. The low Reynolds number *k*-ε model

The main difference from the standard model here becomes apparent in the near wall region. The higher Reynolds number model reduces the computational requirements by making use of the universal behaviour of near wall flows. This model effectively integrates to the wall surface in the low Reynolds number region of the flow. The standard model is thus revised to force the near wall conditions to be correct. Now the viscous stresses take over from the Reynolds stresses close to the wall, achieved by

using wall damping functions which alter the model constants. Patel *et al.* (1985) gives the common formulation of such models.

$$\rho\frac{\partial\varepsilon}{\partial t}+\rho\overline{u_j}\frac{\partial\varepsilon}{\partial x_j}=\left(C_{\varepsilon 1}f_1P-C_{\varepsilon 2}f_2\varepsilon\right)\frac{\varepsilon}{k}+E+\frac{\partial}{\partial x_i}\left[\left(\mu+{\mu_t}/{\sigma_\varepsilon}\right)\frac{\partial\varepsilon}{\partial x_j}\right] \tag{3.19}$$

$$\mu_t=\rho C_\mu f_\mu\frac{k^2}{\varepsilon} \tag{3.20}$$

where

$$f_\mu=\exp\left(\frac{-3.4}{\left(1+{R_T}/{50}\right)^2}\right) \tag{3.21}$$

$$R_T=\frac{\rho k^2}{\mu\varepsilon} \tag{3.22}$$

The functions f_μ, f_1 and f_2 are chosen specifically for each version of the model, but in general, f_2 is chosen to consider the change with Reynolds number of the component in the decay law of isotropic turbulence, and f_1 to return the correct behaviour of dissipation near the wall, while f_μ incorporates the transition from turbulent to viscous momentum transport as the wall is approached (Apsley, 1995).

Rahman and Siikonen (2002) have developed the model by adjusting the turbulent Prandtl number σ_k to provide more substantial turbulent diffusion in the near wall region. This development improved the applicability of the model to arbitrary topologies, and the capability for evaluating separation and re-attachment. It accounts better for near wall and low Reynolds number effects.

3.2.7. Non-Linear *k-ε* models

The standard *k-ε* model works well when the normal Reynolds stresses are not important, for example in thin shear layers. While this gives acceptable results for mean flow, the same can not be said for the prediction of turbulent effects. In fully developed channel flow for example, the standard *k-ε* model (or any isotropic eddy-viscosity model) predicts the normal stresses to all be equal (to $2k/3$) which is in contradiction of experiment (Apsley and Castro, 1997).

Several groups (Pope, 1975, Rodi, 1976 and Saffman, 1977) have developed anisotropic two equation models, based on original work by Lumley (1970) who tried to remove the isotropic eddy viscosity assumption ($u'u' = v'v' = w'w'$). Pope's (1975) model gave the advantage of increased numerical stability due to the stress-strain term relationship being retained within the differential equation, and was shown to remove the fundamental weaknesses of the Boussinesq approximation (inability to capture stress anisotropy, and excessive production of turbulence for impingement zones). Due to the higher orders of expansion the model was limited to 2-D flows as the solution of the 3-D form is too complex and alternative models have become more suitable. Speziale (1987), Suga (1996) and Craft *et al.* (1996) have all revised the model for application to 3-D flows. It should be noted that the algebraic expressions for the Reynolds stresses are unable to model fluid transport effects, consequently

these models have not been rigorously applied to wind engineering, though Easom (2000) has done some valuable work on this.

3.2.8. Summary of *k-ε* models

Various low Reynolds number *k-ε* models appear in the literature. The most commonly considered models are those from Launder and Sharma (1974), Lam and Bremhorst (1979), Chien (1982) and Lien and Leschziner (1994), and further examples can be found in the review by Patel *et al.* (1985) and in work by Rodi and Mansour (1993).

The inadequacies of the *k-ε* model are well documented, primarily regarding the overestimation of turbulent kinetic energy, *k*. Various modified versions are available and the two mentioned above are the most common examples, for which reasonable understanding of performance in a variety of situations is available. Others of interest include work by Ishihara (1999) who developed a model proposed by Shih *et al.* (1995), and a version proposed by Durbin (1993), which have both performed well for flow over hills and cliffs. Vu *et al.* (2002) modified the standard *k-ε* model for consideration of flow over urban canopies, and while the model was successful, the study served to demonstrate how sensitive the flow can be to obstructions in the flow (in this case buildings) and roughness effects. Castelli *et al.* (2001) considers the use of *k-ε* model for neutral boundary layers compared to the Mellor-Yamada (1974) (MY) model. The MY model gives unsatisfactory results for the production of *k* when applied to gentle topography, assumed to be due to the boundary layer approximation,

but found that all models predicted the mean flow well, though for kinetic energy, the k-ε was superior. The MY model has been used for atmospheric flows, but tends to overestimate values of ε and neglects pressure distributions due to buoyancy and shear (Kim *et al.*, 2003). The model was improved by Nakanishi (2001) using LES data, but the main issues still remain, and Castelli *et al*. (2001) present results for neutral flow over complex terrain, showing the standard k-ε model to better predict the turbulent kinetic energy than the MY model.

In a similar mould, the MMK (Murakami, Mochida, Kondo) k-ε model (Tsuchiya *et al.*, 1997) modifies the expression for the eddy viscosity approximation leaving the main k and ε transport equations unchanged. Tests with the model have been conducted for flow over a 2-D square rib, a 3-D cube and a low-rise building, and report improved performance compared to the standard k-ε model. The model is effectively a modification to force the standard k-ε into agreement with wind engineering flows as the additions to the equations are not derived in any way from the Navier-Stokes equations (Easom, 2000).

Huser *et al.* (1997) modified the standard k-ε model for complex terrain flows for consideration of pollutant dispersion with some promising results, though the adjustments made to the standard version may result in more errors than the improvements produce. Lun *et al.* (2003), after comparing various two-equation models, conclude significantly that the correct parameterisation of the surface roughness is almost as important as

the choice of turbulence model, and also confirms the limitations of linear models in predicting flows over complex geometries. Other work on the popular *k-ε* model considers alterations to the constants to improve the models performance in neutral flow (Xu and Taylor, 1997), and Apsley and Castro's (1997) development of a limited length scale version for neutral and stable flows.

3.2.9. The *k-ω* model

Developed initially for the aerospace industry, where flow separation performance is particularly important, *k* is still the turbulent kinetic energy but the term for *ε* is replaced by *ω*, which is the dissipation rate per unit kinetic energy rather than per unit mass. The *ω* equation is mathematically more robust than the *ε* equation and it can be integrated up to the wall without the need for damping wall functions, which are major advantages.

- Eddy Viscosity

$$\mu_t = \rho \frac{k}{\omega} \tag{3.23}$$

- Turbulent kinetic energy

$$\rho \frac{\partial k}{\partial t} + \rho U_j \frac{\partial k}{\partial x_j} = \tau_{ij} \frac{\partial U_i}{\partial x_j} - \beta^* \rho k \omega + \frac{\partial}{\partial x_j}\left[\left(\mu + \sigma^* \mu_T \right) \frac{\partial k}{\partial x_j} \right] \tag{3.24}$$

- Dissipation rate

$$\rho \frac{\partial \omega}{\partial t} + \rho U_j \frac{\partial \omega}{\partial x_j} = \alpha \frac{\omega}{k} \tau_{ij} \frac{\partial U_i}{\partial x_j} - \beta \rho \omega^2 + \frac{\partial}{\partial x_j}\left[\left(\mu + \sigma \mu_T \right) \frac{\partial \omega}{\partial x_j} \right] \tag{3.25}$$

where α, β, β_*, σ and σ_* are closure coefficients (Wilcox, 1994).

Modelling flow right up to the wall and the removal of wall functions is indeed an advantage of this model in many flow situations. The model has also been shown to reproduce reattachment points better than the *k*-*ε* model for flow over a cube (Easom 2000). However, the sensitivity of this model to free stream values has been well documented (Menter, 1992 and Wilcox, 1994) and partially solved by Menter (1994) (see below).

The idea of the wall condition for k (k_w=0) is straightforward, but the boundary condition for ω is questionable as it becomes infinite for a perfectly smooth wall. The smooth wall is also generally too expensive to compute in 3D so the rough wall condition is more suitable but has been found to be highly sensitive to the roughness height (Thivet *et al.,* 2002), which for environmental flows is difficult to specify. For rough walls:

$$\omega_w = \frac{N\upsilon_w}{k_s^2} \tag{3.26}$$

where $N = 2500$.

Despite this, there is evidence to suggest that the *k*-*ω* model is more computationally robust for integration to the wall, and has need for less empirical dampening that other two equation models (Wilcox, 1994).

A two layer model was developed by Menter (1994) which uses the *k*-*ω* model in the inner layer and the *k*-*ε* model in the outer layer (defined as the baseline model – BSL). This avoids the free-stream sensitivity issue and retains the advantages of the *k*-*ω* model which is superior in terms of numerical stability.

$$\rho\frac{\partial k}{\partial t}+\rho U_j\frac{\partial k}{\partial x_j}=\tau_{ij}\frac{\partial U_i}{\partial x_j}-\beta^*\rho k\omega+\frac{\partial}{\partial x_j}\left[\left(\mu+\sigma^*\mu_T\right)\frac{\partial k}{\partial x_j}\right] \tag{3.27}$$

$$\begin{aligned}\rho\frac{\partial \omega}{\partial t}+\rho U_j\frac{\partial \omega}{\partial x_j}&=\alpha\frac{\omega}{k}\tau_{ij}\frac{\partial U_i}{\partial x_j}-\beta\rho\omega^2\\&+\frac{\partial}{\partial x_j}\left[\left(\mu+\sigma\mu_T\right)\frac{\partial \omega}{\partial x_j}\right]+2\left(1-F_1\right)\sigma_{w2}\frac{\rho}{\omega}\frac{\partial k}{\partial x_j}\frac{\partial \omega}{\partial x_j}\end{aligned} \tag{3.28}$$

the constants for which can be found in Menter (1994).

Detailed reviews of other two equation models used for wind engineering applications are given by So *et al.* (1991), Shih and Lumley (1993) and Murayama (1999). While a number of developments and improvements are made to the two-equation models, there is no agreement on a standard by which to measure the level of improvement. It is also unclear whether the improvements apply to all applications of the model (Menter, 1994). One of the main disadvantages has always been the isotropic consideration of turbulence in the *k* equation.

The two sensitivity issues leave the *k*-*ω* model unsuitable for use in atmospheric flows as the roughness height will vary spatially in most situations (its exact value is generally unknown) and the free stream can vary considerably due to turbulent and Coriolis effects.

3.2.10. Reynolds Stress model

Work by Rotta (1951) developed the theories of Kolmogorov (1941) and revolutionised the turbulence modelling techniques by managing to close

the Reynolds stress transport equations. This early model was improved significantly by Launder *et al.* (1975) who are often credited with producing the first full model.

This alternative to eddy viscosity models is the differential Reynolds stress model (RSM). This is the most complex of the classic turbulence models with differential transport equations being solved individually for each of the Reynolds stress components. The six equations for stress transport are solved along with a model equation for the scalar dissipation rate ε (Versteeg and Malalasekera, 1996). These models naturally include the effects of streamline curvature, sudden changes in strain rate or buoyancy (Leschziner, 1990).

The transport equations for the Reynolds stresses ($R_{ij} = \frac{\tau_{ij}}{\rho} = \overline{u_i' u_j'}$) take the form:

$$\frac{DR_{ij}}{Dt} = \underbrace{P_{ij}}_{\text{Production}} + \underbrace{D_{ij}}_{\text{Diffusion}} - \underbrace{\varepsilon_{ij}}_{\text{Dissipation}} + \underbrace{\Pi_{ij}}_{\text{Strain}} + \underbrace{\Omega_{ij}}_{\text{Rotation}} \tag{3.29}$$

which sums the rate of change of R_{ij} with its transport by convection on the left hand side of the equation, and on the right hand side, the rate of production, the transport by diffusions, the rate of dissipation, the transport due to pressure-strain interaction and the transport due to rotation.

The production term is retained in its exact form:

$$P_{ij} = -\left(R_{im} \frac{\partial U_j}{\partial x_m} + R_{jm} \frac{\partial U_i}{\partial x_m} \right) \tag{3.30}$$

But extra models are required for the diffusion, dissipation rate and pressure strain correlation. Launder *et al.* (1975) and Rodi (1976) give full details of the models, though the equations are quoted here.

The diffusion term is modelled by equating the gradients of the Reynolds stresses as proportional to the rate of their transport by diffusion.

$$D_{ij} = \frac{\partial}{\partial x_m} \left(\frac{\mu_t}{\rho \sigma_k} \frac{\partial R_{ij}}{\partial x_m} + R_{jm} \frac{\partial U_i}{\partial x_m} \right) \tag{3.31}$$

The dissipation rate assumes isotropy of the smaller dissipative eddies, and is set so that it affects only the normal Reynolds stresses and each in equal amounts.

$$\varepsilon_{ij} = \frac{2}{3} \varepsilon \delta_{ij} \tag{3.32}$$

The Kronecker delta, δ_{ij} is used here, where:

$$\delta_{ij} = 1 \text{ if } i = j \text{ and } \delta_{ij} = 0 \text{ if } i \neq j$$

The most difficult term in the Reynolds stress model transport equation is that for the pressure-strain interactions. Their effect on the stresses is caused by two marked pressure fluctuations: due to two eddies interacting with each other, and due to the interaction of an eddy with a region of flow with different mean velocity. The term is used to redistribute the energy to the normal Reynolds stresses, making them more isotropic, while reducing the Reynolds shear stress.

$$\Pi_{ij} = -C_1 \frac{\varepsilon}{k}\left(R_{ij} - \frac{2}{3}k\delta_{ij}\right) - C_2\left(P_{ij} - \frac{2}{3}P\delta_{ij}\right) \tag{3.33}$$

The rotational term is given by

$$\Omega_{ij} = -2\omega_k\left(R_{jm}e_{ikm} + R_{im}e_{jkm}\right) \tag{3.34}$$

where, ω_k is the rotation vector, and e_{ijk} is the alternating symbol.

The equation for kinetic energy is needed in the above formulation

$$k = \frac{1}{2}\left(R_{11} + R_{22} + R_{33}\right) = \frac{1}{2}\left(\overline{u'^2} + \overline{v'^2} + \overline{w'^2}\right) \tag{3.35}$$

The six transport equations are solved along with a model for the dissipation rate:

$$\frac{D\varepsilon}{Dt} = \frac{\partial}{\partial x_m}\left(\frac{\mu_t}{\rho\sigma_\varepsilon}\frac{\partial\varepsilon}{\partial x_m}\right) + C_{\varepsilon 1}\frac{\varepsilon}{k}2\frac{\mu_t}{\rho}E_{ij}\cdot E_{ij} - C_{\varepsilon 2}\frac{\varepsilon^2}{k} \tag{3.36}$$

If information regarding the appropriate inlet distributions for R_{ij}, k and ε is unavailable, crude approximations can be calculated using the following assumed relationships

$$k = \frac{3}{2}\left(U_{ref}T_i\right)^2,\ \varepsilon = C_\mu^{3/4}\frac{k^{3/2}}{l},\ k = \overline{u'^2},\ \frac{1}{2}k = \overline{v'^2} = \overline{w'^2}$$

which interestingly indicates the problem of retrieving turbulence data from the k equation when using two equation models, as the normal stresses are not identical.

For near wall flows, the presence of the wall acts to suppress the normal component of turbulence (Hunt and Graham 1978) which reduces mixing, so impeding heat and momentum transfer. Durbin (1991) aimed to remove the use of wall functions and model the flow effects up to the wall surface.

For flows with complex terrain, this is justified as the near wall turbulence is not of a universal form. The idea for using wall functions is not ideal, particularly for regions with large surface curvature, but the computational requirements of integrating through the log layer is too expensive (Durbin 1993).

As with two equation models, modifications can be made to the Reynolds stress model, and these are often directly linked to the subject area of the research team. For example, Shih *et al.* (1995) redeveloped the model for flows important to jet propulsion, based on the constraints from rapid distortion theory, which does not produce any non-physical Reynolds stresses for the mean flow field.

3.2.11. Two Layer Models

The computational expense of the RSM can be reduced by using two layer models. The near wall region is modelled by a simpler two equation model where the viscous effects are dominant and universal, while using the Reynolds stress model through the rest of the boundary layer when the flow effects become more anisotropic. This process was presented by Hsieh and Chang (1999) using the low Reynolds number model from Speziale and Gatski (1994), showing that this approach retains the performance of the two equation model in the near wall region while yielding the improved accuracy of the Reynolds stress model in the rest of the boundary layer. This has only been tested for simple isothermal flows,

and its generalisation to complex flows is questionable due to the near wall treatment as with all two equation models.

The exact production term and the inherent modelling of stress anisotropies theoretically make Reynolds stress models more suited to complex flows, however practice shows that they are often not superior to two-equation models. Reynolds stress models can be suited to flows where the strain fields are complex, and reproduce the anisotropic nature of the turbulence itself.

3.2.12. Discussion

Of the models presented, the standard k-ε model is most widely used and validated. Its main advantages are the low computational costs and better numerical stability in comparison to the more complex models. Where Reynolds stresses are less important, this model performs well, however in complex wind engineering this is rarely the case. Many other models are available and can be used to model fluid flow, the ones presented here are the most common and are available for the numerical model. Where the flow regime is simple, such as for low hills, the standard k-ε performs adequately and its use is encouraged over more complicated and costly models (Beljaars *et al*., 1987).

The wall treatment in the k-ω and low Reynolds number k-ε models is of concern when modelling rough walled flows as they integrate values right up to the wall. The other models described use wall damping functions to

account for flow changes very close to the wall. The comparisons to be made during this work will consider the standard k-ε model due to its wide usage and the awareness of its inadequacies, the k-ε RNG model due to the improvements for flows with recirculation regions and flow separation, and the Reynolds stress model, to provide an understanding of how accurate classic turbulence models can be when compared to wind tunnel and full scale data.

3.3. Turbulent wall boundary conditions

At the wall, the fluid is stationary, and turbulent eddying motions have ceased. In the absence of Reynolds shear stress effects, the fluid is dominated by viscous shear. It can be assumed that the shear stress is approximately constant and equal to the wall shear stress, τ_w, throughout the layer. This layer is very thin ($y^+<5$) and a linear relationship between u^+ and y^+ is found, hence the region is sometimes referred to as the linear sublayer, but in general the laminar sublayer.

Outside this layer is a region where viscous and turbulent stresses are both important ($30<y^+<500$). The shear stress varies slowly with distance from the wall, and is assumed to be constant and equal to the wall shear stress.

$$u^+ = \frac{1}{\kappa}\ln y^+ + C = \frac{1}{\kappa}\ln\left(Ey^+\right) \tag{3.46}$$

For rough walls, the modifications detailed above are necessary. The logarithmic relationship now present lead to this being called the log-law layer.

3.3.1. CFX methodology

For flow over topography, the effects due to the wall are the most important, so the method used to represent them is critical to the CFD simulation. An economical yet accurate method of determining the effects on the momentum and turbulence transport equations must be used. This is essential in wind engineering applications where the flows are very turbulent with complex geometries and significant wall roughness.

The flow properties close to the wall are changing rapidly, from conditions of no slip at the wall, to those within the boundary layer. These high gradients would require a very fine grid close to the wall to resolve the values. To reduce the large computational power requirements for such a situation, wall functions were developed to account for this section of the flow regime, which also avoid the need to account for viscous effects within the turbulence model (Easom, 2000). Based on the universal behaviour of near wall flows (assuming that the shear stress in the near wall region is constant and that the length scale of a typical eddy is proportional to the distance from the wall), they result in the logarithmic velocity profile near the wall.

$$u^+ = \frac{U_t}{u_\tau} = \frac{1}{\kappa}\ln\left(y^+\right) + C \tag{3.37}$$

where:

$$y^+ = \frac{\rho \Delta y_p u_\tau}{\mu} \tag{3.38}$$

and:

$$u_\tau = \sqrt{\frac{\tau_\omega}{\rho}} \tag{3.39}$$

where Δy_p is the distance from the wall to the first node.

The computations above are derived for smooth walls. In topography affected wind flows, the walls are almost always rough. While the logarithmic profile still exists, it moves closer to the wall. The roughness effects can therefore be accounted for by modifying the expression for u^+

$$u^+ = \frac{1}{\kappa}\ln\left(\frac{y^+}{1+0.3k^+}\right) + C \tag{3.40}$$

where

$$k^+ = y_R \frac{\rho}{\mu} u^x \tag{3.41}$$

and y_R is the equivalent sand grain roughness.

The problem with this formulation is that it becomes singular at separation points, where the near wall velocity, U_t, approaches zero. In the logarithmic region, an alternative velocity scale, u^x can be used instead of u^+:

$$u^x = C_\mu^{1/4} k^{1/2} \tag{3.42}$$

which does not go to zero is U_t goes to zero, as k is never completely zero in turbulent flow. Now, the following explicit equation for wall shear-stress is obtained.

$$\tau_\omega = \tau_{visc}\left(\frac{y^x}{u^+}\right) \tag{3.43}$$

where

$$\tau_{visc} = \frac{(\mu U_t)}{\Delta y_p} \tag{3.44}$$

$$y^x = \frac{(\rho u^x \Delta y_p)}{\mu} \tag{3.45}$$

and is described as a scaleable wall function approach. One of the main drawbacks to the standard wall function approach is the dependence on the location of the node nearest the wall and the sensitivity to near wall meshing. Mesh refinement does not necessarily always increase accuracy (Grotjans and Menter, 1998). The idea behind this scalable wall function approach assumes mathematically that the surface coincides with the edge of the viscous sublayer ($y^x = 11.63$) which is the intersection between the logarithmic and linear near wall profile. The computed values of y^x are therefore not allowed to fall below this layer, so all grid points are outside the viscous layer and the fine grid inconsistencies are avoided.

Schlichting (1955) and White (1979) worked on the idea that any roughness configuration can be considered by a single variable. A general roughness layout will vary in height, shape and distribution. The sand grain roughness model allows any roughness to be considered as a layer of sandgrains. The equivalent height of the sand grains must be determined for each roughness setup. Guidelines are given by Schlichting (2000) and White (1999), but their work concentrated on man made roughness elements in pipes. CFX (2000) recommend using $y_R = 30 \times z_0$ for environmental flows, which for grass with a z_0 of 0.03m (a common value)

would indicate a roughness height of 0.9m which seems excessive. Morvan (2003) suggests y_R is more equivalent to the average roughness heights for environmental situations and this leads back to work by Brutsaert (1982) indicates nearer $y_R = 7.5 \times z_0$. Hence the same notation as used in section 2.8.2.

In ABL theory, the concept of a zero plane displacement was introduced, which helps consider the thickness of the roughness set up (Chapter 2). In CFD care must be taken with the modelling of very thick roughnesses. The zero plane displacement can only be incorporated into the velocity profile, not into the roughness setup. Therefore, if used, it will merely raise the zero point of the velocity profile further (vertically) into the roughness configuration. Thus the roughness is not correctly modelled, and inconsistencies in the boundary condition representation will occur. A solution to this requires that measurements above the ground surface take into account the existence of the zero plane displacement, if any comparisons with other datasets are to be made. So the standard logarithmic profile is always used, but measurements for very thick roughnesses where *d* would be appropriate will no longer be taken at heights *z* above ground, but at heights *z-d*.

3.3.2. Summary

The considerations required for the wall boundary condition are therefore:

- The roughness configuration as detailed in section 2.8
- The turbulence model wall functions
- The location of the first grid node

The configuration of the roughness is specific to each situation, regarding values of z_0 and d. The choice of a suitable turbulence model is imperative as described in section 3.2. The location of the first grid node is dependent on the settings of the mesh, which is described below.

3.4. Discretisation

Once the flow domain and boundary conditions have been defined, two processes occur. Discretisation of the domain into a number of elements (grid or mesh generation) and the transformation of the partial differential equations (PDEs) which describe the fluid flow into discrete algebraic operations involving the values of the unknown variables at each node in the domain.

3.4.1. Equations

The equations governing the fluid motion are PDEs, made up of combinations of the flow variables (e.g. velocity and pressure) and the derivatives of these variables. Computers cannot directly produce a solution as they can only recognise binary data. They can however store numbers and manipulate them over and over. Hence the PDEs must be

transformed into equations that contain only numbers. This process is known as numerical discretisation. Each term within the PDE is transformed into a numerical equivalent that the computer can be programmed to calculate.

Three methods exist for this discretisation process:

- Finite difference method
- Finite volume method
- Finite element method

Each of these produce equations for the values of the variable at a finite number of points in the domain under consideration. A set of initial conditions is required to start the calculation, as are the boundary conditions of the problem so that values of the variables at each boundary are known, or can be calculated.

The finite difference method and the finite volume method both produce solutions to the numerical equations at a given point based on the values of neighbouring points, whereas the finite element method produces equations for each element independently of all other elements. It is only when the finite element equations are collected together and assembled into global matrices that the interaction between elements is taken into account.

The finite element method splits the flow domain into a finite number of sub-domains known as elements. This method takes care of the derivative boundary condition when the element equations are formed, and then the

fixed values of the variables must be applied to the global matrices. This contrasts with the other two methods which can easily apply the fixed-values boundary conditions by inserting the values into the solution, but must modify the equations to take account of any derivative boundary conditions. See Zienkiewicz and Taylor (1989) for a fuller explanation and Tamura (2003) for a summary of current research using the method.

The philosophy of the finite difference method is to replace the partial derivatives appearing in the Navier-Stokes equations with algebraic difference quotients, yielding a system of algebraic equations (based on the a Taylor-Series expansion) which can be solved for the flow variables at the specific, discrete grid points in the flow. A comprehensive explanation can be found in Smith (1985) and research is again summarised by Tamura (2003).

The work in this thesis is based on a version of the finite volume method. Here, the region of interest is divided into small sub-regions called control volumes. The equations are discretised and solved iteratively for each control volume. As a result, an approximation of the value of each variable at specific points throughout the domain can be obtained. In this way a full picture of the behaviour of the flow can be derived. The flow equations are integrated over the fixed control volume to create volume and surface integrals. The surface integrals are the integrations of the fluxes and the volume integrals represent the source and accumulation terms.

Full details of these methods are available in a number of texts, including Hirsch (1989), Versteeg and Malalasekera (1996), Wesseling (2001) and Chung (2002). The three methods are based on similar methodology, modified slightly for certain types of PDE (found in Smith, 1985). In engineering applications, finite difference and finite volume methods are predominant (Wesseling 2001).

The finite volume scheme was originally developed as a special finite difference formulation. The PDEs representing the conservation principle for a flow variable over an infinitesimally small control volume are discretised to express the same principle over a finite control volume (Patankar, 1980). Physical and control volume boundaries are also matched. The main difference between the finite difference and finite volume techniques is the integration method for the control volumes. The differential equations are integrated over each control volume, resulting in a discretised expression for the exact conservation of the relevant properties for each finite cell size.

Values and properties of the flow variables are evaluated at the nodes. The gradients and fluxes at the control volume faces are calculated using an approximate distribution of properties between nodes. So the interpolated values at the control volume faces and the source terms and fluxes are substituted into the integral form of the PDEs representing the flow field for each volume. The process is repeated for each node in the domain and modifications are used for those associated with boundaries. This process

results in a system of algebraic equations which can be solved iteratively to obtain the distribution of the flow properties at all node locations (Versteeg and Malalasekera, 1996).

3.4.2. Grid

Two different grid types exist, structured and unstructured. For both meshes the basic idea is the same, and the domain is divided into a large number of mesh elements which tessellate to fit to the full domain. The difference between structured and unstructured meshes is the labelling of the elements and their usage in the equation solving. Structured meshes are defined due to the consistent labelling of the elements in rows, columns and levels. The equations are solved for each element in relation to the surrounding elements. In most cases a structured mesh will be made up of cuboid elements aligned in rows and appropriately classified. Unstructured meshes do not use this method of annotation. The cells are not defined by their surrounding cells and the method of solution differs. Traditionally, unstructured meshes are made up from tetrahedral elements, and are used in wind engineering applications as they give a better fit to the more complex terrain regions.

In CFX the discretisation scheme is a finite element based finite volume method originally developed by Schneider and Raw (1987). The domain is split up into a number of unstructured elements with nodes at the vertices where the properties again are stored. However the solution process takes the form of a finite volume method. Figure 3.1 shows a 2D view of an

unstructured grid in CFX-5. The triangular elements are clearly visible with the nodes at the vertices. A control volume is then created from surfaces defined by the midpoint between the node and surrounding nodes and element boundaries. The level of accuracy of the mesh is therefore defined by the number of nodes in the domain rather than the number of volume cells which is often quoted when using traditional finite volume methods.

Close to the wall, profile gradients of the flow variables are changing rapidly. In a structured mesh, this is dealt with by setting a level of expansion for the cell sizes, very small cell heights at the wall surface, which expand out as the cells become nearer the free stream. In unstructured meshing this is not so straightforward. Here an inflation layer of prismatic elements is created which are very small in height, but relatively long and wide. This helps to model changes in the vertical direction while maintaining the required level of resolution in the direction of the flow.

The generation of an accurate and suitable mesh is the most important stage in the verification of a CFD simulation (AIAA, 1998). Grid independence is a widely used term to describe a model setup where, if more volume cells (nodes) were added to the mesh, and hence each volume cell became smaller, this would have no significant effect on the results. The ability to create a grid independent solution is reliant on the computational resources available. The size of the mesh is limited by the

memory allocation on the computer used for the simulation. Confirmed grid independence is rarely achieved except for flows over simple geometries where turbulence is low. This is not a common situation for wind engineering and so is unlikely to be achieved. A more useful analysis is of the sensitivity of a mesh to change. The objective is to try and measure the spatial discretisation errors in the solution. By systematically increasing the number of cells and comparing flow profiles, the errors should reduce each time, arriving at zero when the solution is grid independent. This gives an understanding of the level of error in the results which can be linked to the mesh generation stage and effectively the computer used in the simulation process (AIAA, 1998). A high level of resolution for the grid is essential to separate errors resulting from spatial discretisation with those due to numerical issues (Baetke and Werner, 1990). Baetke and Werner's work (1990) also considers the domain requirements for modelling flow over obstacles. The amount of blockage created by obstacles in the flow should be less than 3%, so reducing the domain size to effectively improve grid resolution is not a suitable solution in most cases.

3.4.3. Method

The primary step in the finite volume method is the integration of the governing flow equations over a control volume to form a discrete equation at its node. Consider the mean form of the conservative equations for mass and momentum:

$$\frac{\partial \rho}{\partial t} + \frac{\partial \rho U_j}{\partial x_j} = 0 \tag{3.47}$$

$$\frac{\partial \rho U_i}{\partial t} + \frac{\partial \rho U_i U_j}{\partial x_j} = -\frac{\partial P}{\partial x_i} + \frac{\partial}{\partial x_j}\left(\mu\left(\frac{\partial U_i}{\partial x_j} + \frac{\partial U_j}{\partial x_i}\right)\right) \tag{3.48}$$

These equations are integrated over the control volumes using the Gauss divergence theorem to convert volume integrals to surface integrals:

$$\frac{\partial}{\partial t}\int_v \rho dv + \int_s \rho U_j dn_j = 0 \tag{3.49}$$

$$\frac{\partial}{\partial t}\int_v \rho U_i dv + \int_s \rho U_i U_j dn_j = -\int_s P dn_j + \int_s \mu \frac{\partial U_i}{\partial x_j} dn_j + \int_v S_{U_i} dv \tag{3.50}$$

where s and v are surface and volume integrals and dn_j are the differential Cartesian components of the outward normal surface vector. The surface integrals are the flux integrations, and the volume integrals represent source terms. To solve these continuous equations numerically, they must be approximated using discrete functions. By considering the layout of a volume cell, the surface fluxes must be represented at the integration points (ip) which are located at the centre of each surface segment in a 3D element (see figure 3.1). The discrete form of the integral equations is:

$$\rho V\left(\frac{\rho - \rho^o}{\Delta t}\right) + \sum_{ip}\left(\rho U_j \Delta n_j\right)_{ip} = 0 \tag{3.51}$$

$$\rho V\left(\frac{U_i - U_i^o}{\Delta t}\right) + \sum_{ip} \dot{m}_{ip}\left(U_i\right)_{ip} = \sum_{ip}\left(P\Delta n_i\right)_{ip} + \sum_{ip}\left(\mu \frac{\partial U_i}{\partial x_j}\Delta n_j\right)_{ip} + \overline{S_{U_i}} V \tag{3.52}$$

$$\text{with } \dot{m}_{ip} = \left(\rho U_j \Delta n_j\right)_{ip}^o \tag{3.53}$$

V is the control volume, the summation is over all the integration points of the finite volume, Δn_j is the discrete outward surface vector and the superscript ^{o} refers to the old time level (Schneider and Raw, 1987). The solutions for these discrete equations are stored at each of the mesh nodes. Some of the terms require solutions or gradients to be evaluated at the integration points and at the surfaces, so the variation of the solution within an element must be considered. CFX uses linear 'shape' functions which take into account the shape of the volume cell and calculate the resulting distribution of the flow quantities across it.

3.4.4. Differencing

For a control volume with cross-sectional face area A, volume ΔV and average value, $\overline{S}$, of a source S over the control volume, where Γ is the diffusion coefficient all relating to the property Φ, this gives:

$$\int_{\Delta V} \frac{d}{dx}\left(\Gamma \frac{d\Phi}{dx}\right) dV + \int_{\Delta V} S dV = 0 \tag{3.54}$$

Discretisation of this equation across the control volume gives:

$$\underbrace{\int_{\Delta V} \frac{d}{dx}\left(\Gamma \frac{d\Phi}{dx}\right) dV}_{generation} + \int_{\Delta V} S dV = \underbrace{\left(\Gamma A \frac{d\Phi}{dx}\right)_d}_{flux.leaving} - \underbrace{\left(\Gamma A \frac{d\Phi}{dx}\right)_u}_{flux.entering} + \overline{S}\Delta V = 0 \tag{3.55}$$

which states that the diffusive flux of Φ leaving the downwind face minus the diffusive flux entering the upwind face is equal to the generation of Φ. The values of Φ and the diffusion coefficient are defined and evaluated at node points. To calculate the gradients and fluxes, an approximate distribution of the properties between nodes is used. The calculation of this

distribution is dependant on the interpolation scheme involved, which can be selected to match the physical characteristics of the property.

The diffusion term is usually dealt with by a second order centred differencing scheme, as it affects the distribution of a transported quantity along its gradients in each direction.

The convection term is influenced by the flow direction as properties are effectively convected downstream. In this case, the size of the grid cells and the accuracy and properties of the differencing scheme becomes more important. So here a differencing scheme which only considers upstream values is used.

Theory states that the numerical results obtained with any of the available differencing schemes should be indistinguishable from the exact solution for an infinite number of cells. As the grid points move closer together the change in variables between neighbouring points becomes less and less, and the actual details of the distribution profile assumptions become less important. In reality, a finite number of cells is one of the major limitations of any numerical analysis and so the differencing schemes each have unique properties for their interpolation techniques, and their usage determines the accuracy of the solution obtained.

A differencing scheme for a CFD model should have certain properties which help produce realistic results. These are known as conservation,

boundedness, transportiveness and accuracy and are briefly described below.

3.4.4.1. Conservation

This is to ensure full conservation of the fluid properties throughout the domain. It is very important and achieved using consistent expressions for fluxes though the cell faces of the adjacent volumes in the finite volume scheme. It is an important consideration when different schemes are used to discretise the diffusion and convection terms (Versteeg and Malalasekera, 1996).

3.4.4.2. Boundedness

This property is representative of the stability and requires that for a problem without sources, any solution is bounded by the maximum and minimum boundary values of the flow variables. For example, if the boundary temperatures of a problem are 0°C and 50°C, then the interior values of temperature should be between 0°C and 50°C (Versteeg and Malalsekera, 1996).

3.4.4.3. Transportiveness

The transportiveness is a measure of the ability of the differencing scheme to recognise the direction of the flow. Processes contain effects due to convection and diffusion. For diffusion, changes at one location, affect the variable in a similar amount in all directions around it, whereas for convection the influence of change is purely in the direction of the flow.

The relative strengths of the scheme can be measured by the Peclet number, *Pe*, (though non convective flows do not require this property).

$$Pe = \frac{\rho u}{\Gamma/\delta x} \tag{3.56}$$

where δx is the characteristic length or cell width. For pure diffusion with no convection, $Pe = 0$, and for no diffusion and pure convection, *Pe* tends to infinity. For pure diffusion, the fluid is stagnant, and the contours of the constant will be concentric circles as the diffusion process spreads equally. As *Pe* increases, the contours change shape from circular to elliptical and are shifted in the direction of the flow (see figure 3.2). Influencing becomes increasingly biased towards the upstream direction at large values of *Pe*, so that nodes downstream from the original are strongly affected, whereas those upstream experience weak influence or no influence at all. This relationship between the size of the Peclet number and the directionality of the influencing (the transportiveness) is shown in the differencing scheme (Versteeg and Malalasekera, 1996).

3.4.4.4. Accuracy

The approximation accuracy of the convection and diffusion terms can be judged by the truncation terms of the Taylor series expansion, hence the 'order' notation of the scheme. The following differencing schemes are the most popular high and low order versions and are considered in terms of their suitability for dealing with convection. For notation, the subscript *P* is for a general node, with the neighbouring nodes identified by *U* and *D* for neighbouring nodes in the upstream and downstream directions. The

face between U and P has subscript u and between P and D, subscript d (see figure 3.3).

3.4.4.5. Advection Term

The value of any term at the upwind face is calculated from the value at the upwind node as follows:

$$\phi_u = \phi_U + \beta \frac{\partial \phi}{\partial x_i} . \Delta \vec{r} \tag{3.57}$$

where $\vec{r}$ is the vector from the upwind node to the face. Choices for values of β lead to differencing schemes. Most schemes are based on expansion approximations such as the Taylor series of continuous function (Shaw, 1992), the order of the scheme is defined by the level of truncation of the Taylor series. First order schemes are truncated after the first order terms, and in the same way, the second order accurate schemes are truncated at the second order terms.

3.4.4.6. The upwind differencing scheme

When flow is in the positive direction, the downstream cell face is simply given as

$$\phi_d = \phi_D \tag{3.58}$$

so β is zero.

The scheme satisfies conservativeness, boundedness and transportiveness, and accuracy is considered as first order in terms of Taylor series truncation. The major drawback with this scheme is found when the flow is not aligned with the grid, and the resulting error is known as false diffusion and dominates the physical diffusion for Pe>2. It is however, a very robust or numerically stable scheme and guaranteed not to introduce non-physical overshoots and undershoots.

3.4.4.7. Numerical advection correction scheme

Here a value of β is chosen between 0 and 1 and the diffusive properties of the upwind differencing is reduced. The final term in equation 3.57 is called the numerical advection correction and is equivalent to an anti diffusive flux which is added to the upwind scheme. For β=1 this scheme is formally second order accurate. This scheme is less robust than the upwind scheme and can display non-physical overshoots and undershoots in the solution.

3.4.4.8. High resolution scheme

This computes β locally to be as close to 1 without violating boundedness principles, and the method is based on Barth and Jesperson (1989). This scheme is both accurate and bounded and described as second order differencing. Any numerical model should be solved using this scheme for validation accuracy (AIAA, 1998).

3.4.4.9. Discussion

There are a number of other differencing schemes used in numerical models, which are detailed by Versteeg and Malalasekera (1996) and clearly summarised by Easom (2000). The methodology shown here is the process used in the numerical model here, CFX-5.

3.4.5. Solving the equations

The momentum transport equations have some solution issues. Firstly the convection terms which are derived from the acceleration of a fluid parcel, are non-linear. Secondly the four equations are coupled as every velocity component appears in each equation and in the continuity equation. The most complex issue is that of pressure, which appears in each of the momentum equations, but does not have its own equation.

Segregated solvers solve the momentum equations first, using a guess for the pressure and an equation for the pressure correction is obtained. This method requires a large number of iterations and needs the selection of

relaxation parameters of the variables. To improve this, a coupled solver is used which considers the hydrodynamic equations (for *u, v, w, p*) as a single system. In this way all the equations are solved for all the control volumes, at the same time, so considerably fewer iterations will be required. The discretised equations are given in implicit form, which means a set of simultaneous equations are generated consisting of many individual equations. Computing these is computationally expensive and significant research has investigated the efficiency of solution techniques for CFD. The non-linear equations are linearised and assembled into a solution matrix and then solved using an algebraic multigrid method.

The iterative process results in a known level of error which reduces through each iteration. When these errors are reduced to an acceptable level, the solution is converged. The required level of convergence will depend on the engineering situation under analysis. Aerodynamic studies require deep levels of convergence to get accurate predictions of lift and drag coefficients, whereas rough convergence is adequate if the models are simply considering the approximate flow features. Residuals errors of the order of 10^{-4} are usually accepted as an indication of convergence, but a truly converged solution is one where the solution is no longer changing with successive iterations (FLUENT, 2002).

3.4.6. Multigrid methodology

CFX uses a multigrid method to solve the discrete set of equations. The exact solution of the equations is approached through several iterations. Iterative solvers on their own decrease rapidly in performance as the number of volume cells increases. The solver is only efficient at reducing errors which have a wavelength of the order of the mesh spacing. So for dense meshes, the shorter wavelength errors will disappear quickly, but errors with longer wavelengths will remain. The multigrid method uses a series of coarser meshes based on the original such that the longer wavelength errors appear as shorter errors relative to the coarser mesh spacing and so are removed.

Algebraic multigrid is the methodology used to prevent the need to create numerous meshes for the domain and was developed by Raw (1995). A discrete set of equations for the coarser mesh is derived by summing the equation set of the finer mesh. The result is a virtual coarsening of the mesh spacing during the iterations which is then re-refined to obtain an accurate solution (Raw, 1995). Thus errors for a number of wavelength orders are removed in the solution stage and convergence is more easily achieved.

3.4.7. Discretisation effects

All numerical schemes are subject to error, either due to truncation of the expansion series or as a result of the differencing scheme used. Knowing how these errors occur can help the user to create a more accurate solution.

3.4.7.1. Numerical diffusion

This is occurs when flow is not well aligned with the mesh elements. The flow must move from one side of an upstream node, into two or more downstream nodes, and this has an effect on the whole flow domain where the features are smeared out. The effects are most pronounced in areas of flow recirculation where the flow of values in and out of the volume cells will move into numerous adjacent cells. By using unstructured mesh elements, flow can not be aligned with the mesh. Thus while the accuracy will not be as good as for flow where the mesh is perfectly aligned with the flow, the numerical diffusion errors will at least be consistent throughout the domain and the control volumes will not show additional inaccuracies in areas such as recirculation. The use of second order differencing schemes reduces this error.

3.5. Computational resources

The accuracy of any numerical analysis is usually determined by the level of computational resource available for the project. As with any expermental project, it is imperative to describe the techniques used, so in this case it is important to declare the equipment used.

All the simulations in this work have been performed on a dual processor PC (2 x Pentium III 1000 Mhz chips) with 1GB of RAM. The amount of RAM determines the density of the grid which can be used, and through this project it has been found that this amount of RAM allows the usage of a maximum of 300,000 nodes in the unstructured mesh. The processors determine the speed of solution of the project, though the time taken is of less importance from a research perspective and this will vary dramatically from machine to machine.

3.6. Literature review

Considerable literature is available on the numerical modelling of wind flow over terrain, particularly with regard to 2D hills. This section considers the more pertinent work in the area mainly considering the use of turbulence models and their suitability for these flow types and the modelling of complex terrain and the issues which arise from doing so.

3.6.1. Flow modelling using the k-ε model

The standard *k-ε* model is well known to have problems accurately predicting turbulent kinetic energy in wind engineering flows. Zhang (1994) produced good predictions for mean velocities and pressure fields, but the underprediction of *k* for recirculating flows introduced significant numerical errors into the predictions. This problem with kinetic energy prediction is common and is the main reason behind the large number of variations on the standard *k-ε* model, as researchers aim to improve model performance. Richards and Hoxey (1993) have presented alternate model constants for the *k-ε* model which are more appropriate for wind engineering situations, having been compared with full scale data from a 6m cube.

Byrne and Holdo (1998) investigated the effects of increased complexity in flows over geometry using the standard model, but it failed to accurately reproduce the downstream velocity and turbulence profiles, which is concluded to occur due to mis-representation of the inlet turbulence structure. Kobayashi *et al.* (1993) showed results for an anisotropic *k-ε* model which showed improvements in the prediction of kinetic energy production, but retained the inaccuracies of predicting the reattachment length. Abe *et al.* (1993) modified the standard low Reynolds number model for separating flows which replaces the friction velocity with a velocity scale and re-evaluates the transport equations. The improvement for separating flows is considerable.

Some research groups have attained good results with the basic model though, including Murakami and Mochida (1988) who show good results for the standard k-ε model for flows around a cube when comparing velocity and pressure fields, and Bergeles (1985) who was one of the first modellers of flow over hills using RANS techniques. Early work in 2-D showed promising results for the k-ε model compared with laboratory results.

The continual modification of the model is not always useful from a development point of view. With the RNG and low Reynolds number variants, a large amount of validation work has been performed to assess the model's performance (for example Kim *et al.,* 1997 and 2000), and increasing amounts of validation are being performed for non-linear variants, the Shih model (Ishihara and Hibi, 2000) and the Durbin model (Lun *et al.,* 2003). Researchers need to consolidate their efforts into producing validated and accepted variants of the model and defining the situations for which they are suitable (Speziale and Gatski, 1994). Easom (2000) has made a good start at this for bluff body flow around a cube.

3.6.2. Use of the Reynolds stress model

The use of the Reynolds stress model has been more limited due to the extra computational expense involved. Leschziner (1990) continues the argument for the use of Reynolds stress models as opposed to eddy-viscosity models for complex engineering flows, justifying it with results

from a variety of complex flow situations investigated at UMIST over the preceding years. With the rapid developments in computer speed and memory, groups are often moving directly into LES modelling without making significant use of the Reynolds stress models. Hanna *et al.* (2002) performed LES for flows within obstacle arrays and found substantial improvements over CFD models for simulating the relatively high turbulence intensities in the atmospheric boundary layer.

Baskaran *et al.* (1987) modelled the development of a boundary layer over a curved hill using a number of different variations of the k-ε model and the Reynolds stress model. All models predict the pressure field well, but it is the flow on the lee of the hill where the discrepancies arise. The k-ε models significantly over-predict the pressure recovery in the recirculation region, though the RNG model slightly reduces this discrepancy. The best predictions however come from the Reynolds stress model. Work by Kim and Boysan (1999) also shows the advantages of the Reynolds stress model for environmental flows around buildings in an urban environment, but they conclude that LES will become the method of choice for modelling atmospheric flows once computers are available to deal with the level of calculation involved.

3.6.3. Modelling flow over hills

Modelling complex terrain requires an understanding of the surface characteristics involved. To improve this, considerable research has been performed on isolated terrain features such as ridges and hills. Numerical

modelling has concentrated on 2-D and 3-D symmetric hills and real terrain similar to the situations considered by wind tunnel studies and for where site data is available, so that comparisons can be made between the methods.

Deaves (1975) gave the first considerations to the numerical approach for modelling the flow, showing fairly good agreement with some experimental results, though the models used have developed somewhat since then. In a later paper, Deaves (1980) modelled wind flow over 2D hills showing speed-up ratios proportional to the maximum windward slope of the hill.

Carpenter and Locke (1999) investigated wind speed over multiple 2-D hills comparing numerical results with those from a wind tunnel, aiming to quantify the effects of steep hills and landform on wind speeds and turbulence, and gauge the ability of engineering computer programs to predict these effects. The group tested a number of configurations including different shaped hills, multiple hills and irregularities in the windward slope of a hill as is common for this type of study. Their wind tunnel work is similar to many performed over the years (Counihan, 1974, Bowen and Lundley 1977, Pearse, 1981 and 1982, Gong and Ibbetson, 1989, Ferreira, 1995 and 1997, and Neff and Meroney, 1998 as examples). The CFD package used for comparison operated using a standard k-ε turbulence model, and demonstrated its limitations while providing a good basis for future work in the area. Other literature on previous use of CFD

for analysis of wind speeds over hills includes further important work by Ferreira (1997) and Selvam (1989). The CFD results from Carpenter (1999) showed reasonable agreement for velocity predictions where there was little or no separation, though the root mean square predictions were of poor quality and were not presented.

Kim *et al.* (1997) performed a numerical and experimental investigation of flow over 2-D hilly terrain, noting that because of the difficulties and costs of experiments associated with the investigation of all possible situations, a more reliable method is required to predict the complex wind flows over hilly terrain. They used a variety of meshing techniques finding that a non-orthogonal grid predicted a smaller separation zone than an orthogonal equivalent for three different turbulence models. The difference is attributed to the false diffusion owing to the discretisation scheme employed in the computation. The orthogonal grid was also found to be more stable in terms of numerical convergence, though the k-ε model with the non-orthogonal grid seemed preferable in predicting the attached flow because of the significant savings in grid generation and computational time compared to the low-Reynolds number model which required a denser grid system in the wall region.

In a later paper, Kim *et al.*, (2000) numerically modelled wind flow over real terrains, for which site data was available, and found good agreement for wind speed prediction. They deemed the numerical model suitable for reliable prediction of local-scale wind flow over hilly terrain with regions

of flow separation. They also noted the RNG version of the k-ε model performed much better than the standard version of the model.

Apsley and Castro (1997) performed both 2-D and 3-D simulations of wind flow over hills with modified k-ε models yielding satisfactory results. Lateral spatial variations were a problem, and were underestimated by eddy-viscosity models, though these simulations were for strongly stratified flow. In a similar paper, Castro and Apsley (1997) modelled 2D flows comparing numerical predictions with laboratory data. Using a modified k-ε model the mean flow is well predicted, but the kinetic energy values are low. Their simulations modelled separation regions well, when the region was steady, but for hills with lesser slopes, where the region is intermittent, the results were less satisfactory

Eidsvik and Utnes (1997) used the standard k-ε model, and considered a number of flow parameters in depth, concluding that some flow features associated with flow over hills can not be predicted in detail by two equation turbulence models, though for the most part, the important features were quite realistically predicted, including separation. They also remind readers that boundary and initial conditions for real stratified flows over hills may not always be known with sufficient resolution for detailed predictions, so the main use for some numerical modelling may be to estimate quantatively and understand how the flows can be, which is backed up by their 1996 paper where the k-ε model was used without any

variation from the standard model, producing accurate results for wind flow over mountainous terrain.

Kim *et al.* (2000) use both the standard *k*-ε and the RNG variant for modelling wind flow over hilly terrain choosing a number of real locations for which field data is available. Results for separated flow over a valley showed that the *k*-ε RNG model gave better results than the standard model, as is expected. Earlier work (Kim *et al.* 1997) had concentrated on 2D modelling comparing the standard *k*-ε with a low Reynolds number version. The near wall treatment of the low Reynolds number model did not produce enough improvements in the results to justify the extra grid resolution and computational expense.

Simulations of flow over a cliff and a hill using three versions of the *k*-ε model are presented by Lun *et al.* (2003), using the standard model, the Durbin model and a non-linear version by Shih. Their results highlight the effects of surface roughness on the flow separation point and the re-circulation. The revised models are shown to improve the prediction of kinetic energy, with the Durbin model able to predict mean flow properties best, except in regions of recirculation where the Shih model is much better. Maurizi's work (Maurizi, 2000) for flow over 2D valleys highlights the need for higher order turbulence closure models by presenting the inaccuracy of the *k*-ε model and two of its modified variants. A coupled approach to include a Reynolds stress transport equation is suggested,

though the project results show the advantages of the RNG improvement to the model when predicting flow separation.

Uchida and Oyha (2001) considered the stratification effects for flow over a 2D hill finding vortex shedding behind a recirculation bubble for certain levels of stability. Unsteady effects were only noticed under very strong stratification conditions where buoyancy plays a significant role. Their 1999 paper (Uchida and Ohya, 1999) considered the effects of different grid types on the flow over complex terrain and found no significant difference in numerical results, showing that the numerical effects from spatial discretisation errors are minimal.

Numerical studies of the turbulent flow over a hill with flow separation are scarce except for attempts made by Coelho and Pereira (1992) who presented results using standard k-ε model and a Low Reynolds number model, and Ishihara *et al.* (2000) who drew on earlier results to produce some accurate simulations, detailing the reattachment lengths and bubble heights.

Coelho questioned the adequacy of the turbulence model assumptions used in different regions of the flow as well as the numerical accuracy of the flow predictions, due to the complexity of the flow which presents strong pressure gradients, streamline curvature with effects on the turbulence, a detachment line which is not fixed and very high velocity gradients in the near wall region on top of the hill.

The numerical work by Ishihara *et al.* (2000) follows from an earlier wind tunnel experiment performed by the same group (Ishihara *et al.,* 1999), using the standard k-ε model and a non-linear version proposed by Shih (1995) to simulate wind flow over a steep 3-D hill. The latter model was very successful in predicting the velocity profiles, particularly within the recirculation region. The standard k-ε model failed to reproduce the updraft formed behind the hill and this model overestimates the turbulent kinetic energy in the separated region.

They found, as anticipated, that the standard k-ε model underestimates the kinetic energy and hence the stress. In contrast, the predictions from Shih's model manage to reproduce the anisotropy of the normal stress. However improvement upstream from the hill is small. Disagreement seems to be attributed to inadequate modelling of the turbulence transport terms, which is a major approximation in the Reynolds stress algebraic equation models. Ishihara *et al*. (2000) also noted vortices within the separation region helping to maintain it.

Lee *et al.* (2002) considered the effects of multiple hills in alignment with the flow direction, analysing the turbulence structure at the separation point on the hill top. The numerical simulations used in the study were compared with wind tunnel data, and while mean flow variables compared well (except at the hill top region), the separated regions were not well reproduced by the numerical model.

Montavon (1998) modelled highly complex mountain terrain in 2-D with a RANS solver. Some good agreement between field data and the numerical results, though the field work is from a severe windstorm and so the data is prone to error. The predictions in 2D show promise for future work for highly complex terrain, but the increased complexity of 3D flow could be too much for standard models.

Mesoscale models have been used to model wind flow (such as Finardi *et al.,* 1998). The models miss some of the sub grid flow characteristics, but give reasonable predictions of the wind flow. Their advantages have been consolidated in work by Derickson and Peterka (2004) who use a multi-scale model capable of simulating all scales from continental-scale down to micro-scale through a process of grid-nesting whereby the results from a continental scale model are used as the boundary conditions for a mesoscale model which is nested in its centre, and so on down to micro-scale. Hence all effects from Coriolis, stratification and turbulence are considered making this a powerful hybrid tool for wind power site assessment and while further validation work is necessary, the advantages are clear.

Kim *et al.* (2000) are convinced mesoscale models of atmospheric flow are not suitable for the purposes of wind power prediction or wind loading assessment. They are based on the hydrostatic assumption that the pressure field and gravity in the vertical are balanced. This is appropriate for length

scales of the order of hundreds of kilometres, but to address local wind effects it is not (Kim *et al.,* 2000). These models are also not able to resolve topographic variations in the vertical direction which are important in the prediction of local wind patterns such as recirculation and flow separation on surfaces of varying roughness (Atkinson, 1995). Further work will be needed by groups using the model to solve these issues.

3.6.4. The Askervein hill

Of the main field experiments conducted in recent years, many contain significant uncertainties and some do not provide the type of information that is needed to carry out a meaningful simulation. Many of them are also carried out on such gentle slopes that there is little or no flow separation (Taylor *et al.,* 1987). This more gentle terrain is suitable for simulation with models such as WAsP and those by Jackson and Hunt (1975) which solve linear equations (Kim *et al.,* 2000).

The Askervein hill project (Taylor and Teunissen, 1987) was a comprehensive field survey and remains the benchmark for numerical simulation of wind flow over terrain. Detailed data is available from the numerous masts located over the hill surface. Modelling of the Askervein hill has been undertaken by various groups. Castro *et al.* (2003), found limitations with the k-ε model and highlighted the need for accurate mesh generation. Recirculation regions on the lee of the hill were intermittent and only truly captured with a time-dependent simulation and third order differencing of the advection scheme. The challenge of modelling

Askervein is considerable (see Walmsley *et al.*, 1986). The recirculation region on the lee slope is caused by the downstream hilly region according to Kim and Patel (2000) which is corroborated by Teunissen *et al.* (1987). The lee slope of the hill is tricky to model, linear models have shown good prediction for the upwind flow and the flow at the hill summit (Mason and King 1985) but the poor prediction in the lee and the effects of other nearby hills make their model results less useful. Raithby *et al.* (1987) pioneered CFD modelling of the hill though had problems with grid resolution (considering computational power in 1987, this is not surprising), which is the main source of the resulting errors. Beljaars *et al.* (1987) applied a spectral finite difference model to the hill. The theory for the model is linear and so has the same limitations a WAsP, but the simplicity of the calculations and the boundary conditions is an advantage. Their model works well over Askervein, but has limitations in the lee of the hill as non-linear effects dominate the flow regime.

3.7. Summary

This chapter has discussed the CFD modelling process in relation to the ABL and considered previous work in this area. Modelling techniques for the turbulence terms created through averaging the Navier-Stokes equations have been discussed at length. Grid generation, discretisation and differencing have shown how the non-linearity of the situation and how the governing issues must be adapted for the situation in reality. These considerations are all taken into account in the following results chapters.

4. Flow over a 3D hill

4.1. Introduction and aims

One of the primary aims of the project (section 1.5) is to assess the numerical model's reproduction of flow features associated with the atmospheric boundary layer, and complex terrain features. The work is split into two main experiments. The first considers flow along two, separate, flat, rough surfaces to verify that the inlet velocity profile is maintained. The second looks at modelling wind flow over a 3D hill with a rough surface, and the work will investigate the effects of surface roughness on the flow and the effects of surface height variations.

4.2. Flat surfaces

The standard logarithmic velocity profile for flow over a rough surface contains the variable z_0, the aerodynamic roughness length. The relationship between z_0 and the actual roughness height, h_R has been determined in literature through experiment (see section 2.8). This relationship needs to be tested for the current numerical model, CFX-5. Modelling wind flow over flat terrain with constant surface roughness will show whether the profile is maintained through the fluid domain. The CFD domain is simple for this test, and is effectively a virtual wind tunnel with no test section. A Reynolds stress turbulence model is employed, with a second order advection scheme to create the most accurate prediction of results. The domain was 2km in length, allowing any changes to become

apparent. The mesh contained approximately 125,000 nodes, allowing an accurate determination of the velocity profile.

4.2.1. Grassy surface

The first of the roughness conditions is that equivalent to long grass, approximately 30cm in length. The domain conditions are for air at atmospheric pressure, with a standard logarithmic inlet velocity profile:

$$\frac{U}{u_*} = \frac{1}{\kappa} \ln\left(\frac{z}{z_0}\right) \tag{4.1}$$

where z_0 is taken at a value of 0.03m as is characteristic for long grass (Chamberlain, 1965). The friction velocity, u_* is 0.32m/s (taken from Ishihara and Hibi, 2002) and κ is given as 0.41 (inline with Hogstrom, 1996). The rough surface is modelled with the relationship:

$$y_R = 7.5 \times z_0 \tag{4.2}$$

as discussed in section 3.4 with regard to Brutsaert (1982).

Figure 4.1 shows a comparison of the inlet and outlet velocity profiles for the domain. While some small differences are found in the lowest 4m of the domain, the errors are small, and above this point, the profiles are identical. Only the lowest 10m of the domain are presented, as it is in this region that changes resulting due to surface roughness variations would be visible (Wu and Meroney, 1995). The average error between the two profiles is just 0.79% which shows excellent agreement and the suitability of the logarithmic profile to be used with this roughness setup.

4.2.2. Forest surface

The second roughness condition is equivalent to that of a forest covered canopy region. Here the modified version of the logarithmic velocity profile would normally be used

$$\frac{U}{u_*} = \frac{1}{\kappa}\ln\left(\frac{z-d}{z_0}\right) \tag{4.3}$$

with u_*=0.654 m/s (Taylor and Teunissen, 1987), κ=0.41, d=1.5m, z_0=0.3m and using the same relationship for y_R as above. This is characteristic of a forest covered region with 3-4m high trees (Brutsaert, 1982).

4.2.2.1. Extreme roughness in CFD

Concerns exist about numerically modelling very large roughness configurations, as the surface roughness must not be larger than the first volume cell next to the wall (as discussed in section 3.3). Also there is no clear method of incorporating the large value of d into the CFD roughness model. The model considers the surface roughness in relation to z_0, and there is no clear definition on how d affects this value of sandgrain roughness height. If the definition of $y_R = 7.5 \times z_0$ is used along with the modified logarithmic profile, then inconsistencies are present, as the surface roughness is not the same as that defined by the velocity profile.

To resolve this the roughness must be considered in a slightly different manner. Traditionally for a canopy roughness, the velocity profile contains

the zero plane displacement height. This serves to raise the velocity profile above the ground surface so that velocity flow begins at $d+z_0$ (see section 2.8). The problem with CFD is that d can be a significant distance and will almost certainly take up the entire first cell, if not the first few.

A solution to this issue is to remove d from the velocity profile, and consider the roughness as a normal sandgrain roughness. Then, when measuring from the CFD results, the ground must be considered as having a height value of d and not zero. Therefore the ground has effectively included the lower part of the canopy, where no flow is occurring.

From a theoretical point of view this is may not be strictly accurate, as the flow effects within the canopy are not completely understood. However, from a CFD viewpoint, it is considered that no flow occurs below d, so this approach is valid from a numerical standpoint.

It is important to remember that $z=d$ and not $z=0$, when retrieving data from the CFD solution. While the velocity profile used in the wind tunnel experiment contains the zero plane displacement height, the profile used in the CFD does not, and the above approach is considered.

4.2.2.2. Results

Figure 4.2 shows the comparison between the inlet and outlet velocity profiles. Again, some errors can be seen in the lowest few metres of the boundary layer, though above 3.5m, the profiles appear to be identical. In

this case, the error is under 1.14% which again shows good enough agreement for this roughness setup to be used in further tests.

4.2.3. Summary

The lowest few metres of the boundary layer are where the largest changes of flow are occurring. It is very complicated and difficult to model. The slight differences in profile are not unexpected and spatial discretisation errors may have some influence on the results. These straightforward tests on the maintaining of the velocity profile through the fluid domain confirm the suitability of the logarithmic profile and the roughness layout. The amount of error resulting from the boundary condition implementation is minimal.

4.3. Flow over a hill

Considerable ABL research has concentrated on flow over 2D and 3D hills, as summarised in Chapters 2 and 3. Separated flow regions on the lee of these axisymmetric hills are expected and generally well predicted through measurements inside a wind tunnel or using a numerical model. A good method of assessing a numerical model being used for ABL modelling is to consider its predictions of this flow field, and this stage of the project considers validation of the CFD code against wind tunnel results.

Work by a wind engineering research group in Japan used a steep cosine shaped hill for modelling work in both wind tunnel and numerical

modelling experiments. The hill has a maximum slope of 32° and a significant recirculation region has been identified. The group performed two sets of experiments, firstly with a grass covered hill (Ishihara *et al.*, 1999) and secondly with a forest covered hill (Ishihara and Hibi, 2002). The hill shape and size was identical for each case, but the different roughness configurations were of particular interest to this research project. Comparisons with each configuration can demonstrate the accuracy of modelling flow over rough surfaces using a CFD package.

4.3.1. Hill description

The modelled hill was circular, with a cosine-squared cross section and the shape

$$z(x,y) = h\cos^2\left(\pi\frac{\sqrt{\left(x^2+y^2\right)}}{2L}\right) \tag{4.4}$$

where $L = 100mm$ and $h = 40mm$, giving a maximum slope of about 32°, conducive to flow separation. Figure 4.3 shows a cross section of the hill.

For the grass covered hill, the velocity profile is represented by the standard logarithmic profile (equation 4.1), using $u_* = 0.212m/s$ and $z_0 = 0.01mm$, in the surface layer, and by the power law

$$\frac{U}{U_{ref}} = \left(\frac{z}{z_{ref}}\right)^{0.135} \tag{4.5}$$

through the rest of the boundary layer. As described in section 2.6, the logarithmic and power law profiles are used to describe the ABL profile as

they fit well with the data. The logarithmic profile is more commonly used in the lower part of the ABL, but often fits adequately throughout the whole layer, though the power law may be a more exact representation of the upper flow field. The simulated boundary layer in the wind tunnel has a scale of 1/1000, giving an equivalent full scale z_0 of 0.01m, characteristic of a grass covered hill (Mason and King, 1985).

Velocity and turbulence profiles were measured at various locations along the centre line of the hill, and these are used for comparison with the current numerical model.

A second study by Ishihara and Hibi (2002) modelling flow over the same hill, but with an alternate roughness layout. The velocity profile which fits the data is the modified logarithmic profile (equation 4.2), with $u_* = 0.32m/s$, $z_0 = 0.3mm$ and $d = 3mm$. Again with a scale of 1/1000, the full scale z_0 is 0.3m, d is 3m, making this characteristic of a forest covered hill (Brutsaert, 1982). The effective height of the trees is equivalent to approximately 6-8m. This second hill was the subject of a numerical study by Ishihara and Hibi (2002) using the standard k-ε turbulence model and the alternative non-linear version of Shih *et al.* (1995). The size of the computational domain used was 60h in length, 20h in width and 22.5h in height, and contained just under 80,000 nodes laid out $70 \times 32 \times 35$ in the x, y and z directions respectively.

To validate the current model against the data from Ishihara and Hibi's work, the domain size and hill shape are recreated as defined in the 2002 paper. The work is split into two sections: results for the grass covered hill and results for the forest covered hill.

4.3.2. Grid Sensitivity

A widely used term in numerical modelling is 'grid independence'. When spatial discretisation errors are zero, the grid is said to be independent, and if more nodes are added to the domain, no improvement in the accuracy of the results will occur. It is extremely difficult to obtain a truly grid independent result (see section 3.4.2). An understanding of the sensitivity of a grid to change is a useful alternative. The accuracy of the grid is not solely dependent on the number of nodes, but more importantly their location. The areas of complexity in the flow, such as separated regions, and for all flow near a wall, should have a large number of nodes per unit area, compared to regions where flow changes are minimal.

An important issue in the modelling of the ABL is the treatment of the flow equations in regions close to the wall. This near wall formulation helps to determine the prediction accuracy of shear stress, and has a large influence on boundary layer development, including the onset of separation, which is very important here. Near the wall, strong gradients in the dependent variables are present and viscous effects are great. The problems in the numerical simulation process are how to account for the effects and how to resolve these strong gradients.

At the base of the domain, where the velocity profile will be changing rapidly, and near wall turbulence will have large effects, it is necessary to employ an inflation mesh. This is a section of unstructured mesh made up of prismatic elements, which are very thin in the vertical direction, but much longer in the wind flow direction. These help account for the large changes in gradient, without using excessive computational resource. In areas of the domain where the flow is of particular interest, and large changes are expected, mesh controls can be used which concentrate large numbers of nodes at specific points or on specific regions. In this case, controls are used on the lee slope of the hill to analyse any flow separation.

Mesh sensitivity is checked by comparing meshes of varying size and analysing how different certain results are. For example velocity profiles can be considered or single point values of any flow variable. If the results are very similar then sensitivity is low, and the simulation may be approaching grid independence, though if the differences are large, then further work needs to be done on improving the mesh. As computational resources are limited, it is not simply a case of adding more cells, but a more delicate process of increasing the density of cells where large changes in the flow pattern are occurring and removing cells from areas where there is less change.

In this case four grids of varying density have been used. Two fairly coarse grids were used initially to confirm the simulation was running

correctly, then a mid density grid and finally a very dense grid, the number of nodes for each grid are shown in table 4.1. All four were set up in a similar manner. An inflation layer is imposed on the base, and mesh controls are added to increase the density near the ground surface.

Grid	Number of nodes
1	20,000
2	45,000
3	115,000
4	200,000

Table 4.1 – Grid sensitivity tests - node quantities

4.3.3. Results

Figure 4.4 shows the results of the grid independence tests in the form of velocity profile comparisons half way up the upwind slope. The results from the denser meshes are much closer together than the results of the coarser ones, showing that as the node spacings are reduced, the differences between the results are considerably reduced. The average differences in the profiles are shown in table 4.2 below

Grids compared	Percentage difference
Grid 4 – Grid 3	0.42%
Grid 4 – Grid 2	2.3%
Grid 4 – Grid 1	7.3%

Table 4.2 – Grid sensitivity results

It is not prudent to compare with wind tunnel data at this point. There is likely to be some error between the numerical results and tunnel data. It is possible that comparisons with the wind tunnel could indicate that the coarse mesh gives a better simulation of the flow but this conclusion would be false. The denser the mesh, the more accurate the CFD simulation is at

predicting the physics inputted through the domain and boundary conditions.

From these results, the full tests will be run with the setup from grid 3. The extra accuracy obtained from using grid 4 is not considered enough to utilise the extra computational resources necessary.

4.3.4. Mesh plots

A vertical cross section of the mesh on the lee slope of the hill is presented in figure 4.5 showing the inflation layer over the surface, and the dense array of mesh elements expanding away from the surface. Figure 4.6 shows an angled view of the hill configuration showing the same cross section, and the arrangement of the surface elements, over the hill.

4.4. Turbulence models

The most appropriate turbulence models for a CFD wind flow analysis were described in detail in Chapter 3. Comparing the performance of each of the models is important from a practical engineering consideration. The most complex model may not be the most appropriate for use in a situation, as the increased computation times can outweigh the benefits gained from using more complex models. CFD analyses are intended to be accurate, but there will always be errors involved, as in any experiment. If a 2-equation model gives results to an acceptable degree of accuracy, then it is more appropriate to use this to cut down the computation time and hence

simulation cost. One of the aims of this chapter is to assess the performance of two-equation models when simulating flow over terrain.

The turbulence models chosen for comparison are the standard k-ε model and the k-ε RNG model. The standard k-ε is a two equation model considered as the industry standard, and able to give good predictions of mean flow properties, though its use in more complex situations has lead to the development of more complex improved versions. The renormalisation group technique (RNG) (Yakhot and Orzag, 1986) provides additional accuracy to the standard model without significantly increasing the computation time, and is recommended for use where regions of flow separation exist.

Where suited, the Reynolds stress model (RSM) is considered. The RSM is the most complex of the models and solves transport equations for each of the Reynolds stresses, as detailed in section 3.2.10, so as to better simulate anisotropic turbulence. The simulation time is considerable and its use is therefore expensive. While it is interesting to compare the performance of this model, the computational resources available in this work mean considerable extra time is necessary for solution. It is used in this chapter for modelling the flow over a forest hill, where the more complex flow type may require its increased accuracy. The wind engineering industry currently concentrates on using two equation models due to the more robust nature of the solutions.

4.5. Grass covered hill

Ishihara and Hibi (1999) presented velocity and turbulence profiles at seven locations along the streamwise hill axis, showing a small recirculation bubble on the lee slope of the hill. The flow separates on the lee slope near the top, and reattaches just on the downwind hill foot. The separation bubble is relatively shallow, though slightly higher than on the smooth cone reported by Castro and Snyder (1982). This is due to the surface roughness being relatively small. Short grass is not expected to have a significant impact on the flow regime. The separation bubble in this case is caused more by the geometry of the hill itself. The maximum perturbations in velocity were found at a height of 40mm beyond the hill, as a result of the high pressure-gradient variation, and separation bubble.

The velocity profiles over the hill were found to reproduce the effects of hill influence as described in Chapter 2. A slight reduction in wind speed was observed at the upwind foot of the hill, though not enough to cause separation. Over the hill, the flow accelerates up to a maximum speedup ratio of 1.5, similar to the 1.6 value observed by Mason and King (1985) for the flow over the Blasheval hill which has a similar surface roughness, though more complex hill shape.

The turbulence structure in the lee of a three dimensional hill is not well understood, and Ishihara and Hibi (1999), present profiles of normal stress components, measured by split-fiber and X-wire probes. The X-wire probe

underestimates the lateral and vertical velocity components when the longitudinal component is small, and so, as anticipated, the results from the X-wire probe are less than that from the split-fiber, and only seem to be reliable 60mm above the ground (h=40mm) where the turbulence intensity is much smaller. Some increase near the ground is found in the profiles of σ_u and σ_v, though in σ_w the change is much less prominent.

The X-wire probes were calibrated against a Pitot tube in the free stream using a least-squares fitting precedure, which resulted in an average difference of less than 1%. The split-fiber probes were used as the X-wires can not give reasonable accuracy when the turbulence intensity is larger than 0.3. These were also calibrated against Pitot tube measurements, showing variations of less than $\pm 1.5\%$. The accuracy of the wind tunnel experiments is excellent and acceptable for comparison with the CFD data.

4.5.1. Numerical results

Velocity profiles over the hill surface are presented in figure 4.7 showing comparisons between the two turbulence model runs and the two measuring methods from the wind tunnel. On the upstream slope of the hill, the numerical model predicts the velocity profile well. There is a slight underprediction near the ground from both models, though this is more pronounced in the standard k-ε model. At the hilltop, the maximum velocity speedup is well predicted by both models. The recirculation region on the lee slope of the hill is predicted well by both models. The RNG variant is shown to overpredict the strength of the bubble, while the

standard model predicts the size better. The depth of the bubble is better predicted by the RNG model though, but it is clear from all results that the numerical model overpredicts the strength of the pressure gradients, and the switch between recirculation and normal flow is much more severe in the numerical results.

The recirculation bubble predicted in the CFD is effectively asymmetric, as can be seen in figures 4.8a and 4.8b which shows a plan view of the hill with streamlines flowing over the hill (Figure 4.8a), and the recirculation region clearly marked (Figure 4.8b). This is not necessarily unexpected and flows over axisymmetric obstacles often show signs of anisotropy, see Easom (2000) or Prevezer (2002) for example. This does however indicate that the flow is unsteady. Figures 4.9a and 4.9b show angled views of the hill, with the streamlines (4.9a) and with the recirculation (4.9b) showing how complex the flow regime is on the lee slope of the hill. Figure 4.10 shows a side view of the recirculation region on the lee of the hill, which is quite large as shown by the overprediction in the velocity profiles.

4.6. Forest covered hill

The second hill configuration, from Ishihara and Hibi (2002), considers the flow over a forest canopy, comparing wind tunnel results with those produced from a numerical model, using the standard k-ε model and a non-linear version by Shih *et al.*, (1995). Results were presented for the same location as recorded in their 1999 paper for the grass covered hill. A much larger recirculation region is produced than found in the preceding section,

though this is expected as the forest canopy is a much rougher flow configuration. The streamwise velocities predicted by the standard *k*-*ε* model were higher than found in the experiment, while those obtained using Shih's model were in much better agreement, showing the improvement of a non-linear *k*-*ε* model.

4.6.1. Results

The flow over a steep hill with a forest canopy produced a large region of flow recirculation on the lee of the hill, separating just after the hill top, and reattaching a short distance past the hill. Figure 4.11 shows a side view of the hill, with the recirculation region clearly visible in blue. The blue surface is an iso-surface which encapsulates all sections of the flow that have a negative streamwise velocity component.

Vertical velocity profiles along the central plane of the hill are presented in figure 4.12. On the upwind slope of the hill, the numerical model predicts the velocity well for all three turbulence models. At the hill top, the predictions again are excellent and very close to those from the wind tunnel. In the recirculation region on the lee slope, all three models predict a significant recirculation region. The *k*-*ε* RNG model, designed for recirculating flows, seems to overpredict the size of the bubble, an effect particularly noticeable downstream of the hill. The standard *k*-*ε* model and the RSM model both predict the recirculation region well. The influence of the hill and roughness is less profound with the standard *k*-*ε* model, and with the overprediction of the RNG model, this leaves the RSM model

showing the closest results to the wind tunnel experiment. In the three locations immediately downstream of the hill top ($x/h = 1.25$, 2.5, 3.75), the RSM predicts the lower region of the flow with impressive accuracy. Where the largest changes are occuring ($z/h = 1$) the model still fails to perfectly reproduce the experiment, but in general the results are promising. The numerical model is unlikely to predict the exact same flow in the lee of the hill as the wind tunnel, due to errors in both methodologies. This part of the flow is complex and the results shown here are very satisfactory.

To understand how the fluid particles enter and exit the separated region of flow, particle traces are presented of the flow over the hill. Figures 4.13a and 4.14a show plan and 3-D views of the streamlines over the hill. The effect of the hill on the flow is to push the streamlines around the side of the hill, a stratification effect described in chapter 2 for steep hills. The streamlines are then pushed up into the recirculation region by the strong pressure-gradient, before being pushed out the far end. Clear 3-D rotational effects are visible within the region, helping to show how much more helpful a 3-D simulation is compared to a 2-D test for the same hill. Figures 4.13b and 4.14b show the same plots with the recirculation bubble marked in blue, which shows the rotational effects occurring at the edge of the region where the pressure-gradient is strongest.

Previous 2-D studies by Ishihara and Hibi (2000) (see figure 4.15) on flow over a 2-D hill show closed velocity streams in the vertical cross section, as

the circulating flow must be formed to satisfy the continuity equation. In the 3-D flow, the existence of spanwise flow, allows satisfaction of the continuity equation without circulating flow, as is shown by the open streamlines. Figure 4.16 shows a similar plot from this study, again showing the open streamlines, which are also demonstrated by the horizontal streamlines shown in figure 4.13.

4.7. Summary

The work in this chapter has shown a numerical simulation of flow over terrain for two ideal situations. The flow over a flat terrain region with constant surface roughness was presented showing errors of approximately 0.7% in velocity profile maintenance, and for less intrusive roughness, this reduced to only 0.5%, which is an acceptable level of accuracy.

The second situation considered flow over a cosine-squared axisymmetric hill which constant roughness, under two different situations with three different turbulence models. For the grassy terrain configuration, the velocity profile comparison showed good agreement with the experimental data. The recirculation region showed significant asymmetry, indicating some unsteadiness in the flow. The streamline figures help indicate the magnitude of this. The size of the recirculation region has also been over predicted.

For forest covered terrain, the results of velocity profile comparisons were very good and the recirculation bubble was well captured. The Reynolds

stress model was used in this case, as the flow configuration is more complicated. The size of this region was over-emphasised by the k-ε RNG model, and slightly by the RSM, while the standard k-ε gave surprisingly good estimations of velocity, justifying its use in wind flow analyses.

The performance of the numerical model, while not perfect, is promising. The 3D hill in this case has steep slopes and large roughness, promoting a complicated flow regime which is difficult to predict numerically. The next step is to test the model with a real atmospheric flow condition over real terrain to assess its performance, but the CFD setup and the choice of boundary conditions and models has been verified.

5. The Askervein hill

5.1. Introduction

The aim of this chapter is to model the wind flow over a real terrain area and compare the results of a numerical simulation with those taken from full scale field data and those from a wind tunnel experiment.

The Askervein hill project was part of a collaborative study of boundary layer wind flow over low hills conducted through the International Energy Agency Programme of R&D on Wind Energy Conversion Systems. The main field experiments were conducted during September and October 1983 on the Askervein hill, which is located on the west coast of South Uist, an island towards the southern end of the Outer Hebrides off the North West coast of Scotland (see figure 5.1). Preliminary measurements were also carried out during the same period in 1982, in preparation for the full field experiments.

Approximately fifty towers were erected and instrumented for wind measurement during the experiments. Mostly these were simple 10m masts with cup anemometers, though there were also two 50m towers, a 30m tower and a 16m tower. Thirteen 10m towers were instrumented solely for turbulence measurement. Full details of the experimental setups and participants in the project can be found in the main field reports

(Taylor and Teunissen, 1983 and 1985), here only the areas relevant for a comparison with a CFD simulation of the hill are considered.

Askervein has been chosen for comparison as, although the experiments were performed during the early 1980s, they remain the most comprehensive of their type. It is an excellent example of the type of hill which is suitable for wind farm placement, and accurate numerical modelling results will help validate the use of CFD models for wind farm placement analysis. Other full scale experimental data is available for hills such as Kettles (Salmon *et al*., 1988), Blasheval (Mason and King, 1985) and Nyland (Mason 1986), but Askervein is considered as the benchmark for modelling.

A number of wind tunnel simulations have also been performed of the Askervein hill, and the results of this chapter will be compared with an example set from Parkinson (1987) to give an insight into the relative accuracy of the two main types of modelling (wind tunnel and numerical). There are advantages and disadvantages to all types of modelling, which will be discussed, and so it is extremely important to compare all three types to lead to more impartial and clear conclusions.

5.2. Askervein

The Askervein hill is 116 m high (126m above sea level) and has an essentially elliptical shape. Figure 5.2 shows a contour plot of the hill and surrounding area and figure 5.3 gives a more detailed view of the hill. The hill has a 2km major axis and a 1km minor axis. The major axis is oriented along a generally NW-SE line.

Long grass and heather cover the surface of the hill. A flat uniform fetch of 3-4km lies to the SW with a similar roughness configuration before joining the sea, after some sand dunes and low cliffs (5m). Some low buildings are present in the area, but for simplicity the whole region can be considered to have constant roughness. The validity of this statement will obviously have to be considered during the analysis of the results, and Zeman and Jensen (1987) observed some spatial variation over the hill surface, indicating that the best agreement with field data is made when z_0 was reduced by a factor of three within a hundred metres before the hill top. The prominent wind directions are from the South and South-West directions, which is one of the reasons the hill was chosen for study as the only other hills are present on the lee side of the hill, to the North and East. While the wind will come from a variety of directions, the presence of these hills means that only a certain number of directions can be modelled with the knowledge that the attacking velocity profile is fully developed has not been affected by other obstacles within the flow. Castro *et al.* (2003) confirm that for wind flow from the S and SSW, the flow over Askervein is unaffected by the presence of other hills in the region. The

wind strength was moderate to strong during the field experiments according to data from the nearest meteorological station (Benbecula). This is helpful from a modelling point of view as the wind flow can be assumed neutrally stable, as high wind speeds and strong stratification effects (either stable or unstable) do not occur together (Parkinson, 1987).

A reference site (RS) was located approximately 3km SSW of the hill, upstream relative to the prominent wind directions. Here, measurements were made of the unperturbed wind flow prior to any influence from the hill. Other points of importance are the hilltop (HT), 126m above sea level, and a second reference location defined as the centre point (CP). During the experiments, the majority of the instrument towers were placed in linear arrays cutting through CP and/or HT along the major and minor axes of the hill. Their locations are marked on a more detailed contour plot in figure 5.3.

5.3. CFD Setup

Setup of the CFD simulation can be split into three main sections, which consider the most important areas as they occur in the pre-processing stage. Firstly the domain is created which details the topography to be modelled and the size of the boundary layer. Then the boundary conditions are investigated to best reproduce the atmospheric boundary layer, and finally a suitable mesh is produced after the relevant tests have been performed.

5.3.1. Domain

The first challenge for setting up the numerical model was the incorporation of the terrain data. Terrain data for Askervein is available from the Ordnance Survey in the form of either contour maps, or grid point locations (www.ordnancesurvey.co.uk). The pre-processor in CFX5 lends itself to the incorporation of grid points much better than with contour data. Once point data is incorporated, the points can be linked up into curves, and then surfaces. The necessity to first make curves means that having point data in linear arrays is preferable in accuracy terms than having long linked up curves such as contours. Consideration is required for the inputting of data. The OS tile available contains some 50,000 point values, detailing a large terrain area. This full terrain was not all required, so was cut down to approximately one quarter size. However, the remaining 10,000 points can not be inputted by hand, so a program was written to process the point values into a macro file comprehendible by the numerical model.

The point data is to an accuracy of 50m, i.e. the data points are 50m apart. Obviously this is not ideal as significant terrain detail can be present within 50m section, but this is the best data available. More detailed contour mapping is available, and 2m contours were produced for the field experiments (Taylor and Teunissen, 1983), but the numerical model requires point format data. This is unfortunate as errors may be produced due to this lack of data, making it difficult to resolve whether errors are a

result of the numerical model, or the lack of available data and other simplifications.

Once the points were inputted, and a terrain surface had been created, the hill was placed on a virtual disc shape, so that the whole area could be rotated within the domain. This simplified any setup manipulations required for the investigation of alternate wind directions. The idea is analogous to a wind tunnel setup.

This disc is then mounted in a box shaped domain 10km in width, 10km in length and 1km in height. This uses the assumption that the boundary layer over the hill is approximately 1km in height, and idea backed up by in the work by Parkinson (1987) and the conclusions in the project reports (Taylor and Teunissen, 1985). The use of a domain this size produces a blockage ratio of approximately 2%, which is quite acceptable for CFD modelling (Baetke and Werner, 1990).

5.3.2. Boundary Conditions

The velocity profile at the reference site (RS) is considered fully developed for the roughness configuration over the hill, and this profile is therefore used for the inlet profile into the fluid domain.

Values in the field reports are given at various heights for the velocity profile at RS. These values fit well to the standard logarithmic profile as in section 3.2. For ease of reference, this equation is presented here again:

$$\frac{U}{u_*} = \frac{1}{\kappa} \ln\left(\frac{z}{z_0}\right) \tag{5.1}$$

A surface roughness of long grass and heather is not hugely dense, and so it is unnecessary to add the value d to the expression here. This is more suitable when forests or towns are present (see Section 2.8.3).

The value of z_0 was measured during the field experiment and found to range between 0.01m and 0.05m but a suitable approximation is 0.03m (Taylor and Teunissen, 1983). To better fit the profile, representative values of u_*, the friction velocity, and z_0, the roughness length, are derived from velocity profiles at the reference site (RS). Approximately 15 mast readings are available from heights at 3m up to 49m. Fitting a trend line through these points allows values of u_* and z_0 to be determined for a best fit line.

There was a tendency for these RS profiles to depart slightly from a simple logarithmic profile above $z = 30m$ which is considered to be the result of the effects of a slightly stable thermal stratification and baroclinicity rather than local terrain homogeneities (Mickle *et al.*, 1988). However the researchers were unable to correlate the degree of departure with measurements of stability, and this effect is not considered here.

5.3.3. Thermal effects

Analysis of the temperature differences on one of the RS towers combined with the velocity differences, allow a gradient Richardson number to be calculated between 4.9 and 16.9 m levels using the following equation:

$$Ri = \frac{g.dz.d\theta}{T(dU)^2} \tag{5.2}$$

The values are tabulated in the project reports. The gradient Richardson number is widely used as a thermal stability parameter in the ABL (Garratt 1992). In unstable conditions *Ri* will be negative, and hence positive in stable conditions. When buoyancy is zero, $Ri = 0$ and the conditions are of neutral stratification or effectively forced convection. The field survey results have Richardson numbers on average, far below 0.01, so the flow condition can be classified as near-neutral though slightly stable. Figure 5.4 shows the trend line running through the field data from field run MF01-D, with the corresponding profile equation, which shows z_0 as 0.0265m. This deviation from the declared field value of 0.03m does not necessarily indicate any instability in the flow, rather just highlights the spatial variation in z_0. Thus, to simplify the numerical modelling and so remove any need for thermal effect consideration, the flow over the Askervein hill can be assumed neutral as was concluded in the reports (Taylor and Teunissen, 1985).

5.3.4. Wall Roughness

It is assumed for simplicity that the whole domain has a constant surface roughness, so the beach, cliffs and sea are ignored. This removes the

necessity to find and test a suitable roughness change model for the boundary layer.

The wall roughness in CFX-5 is based on the sand-grain roughness height, as described in section 3.3. So, the roughness height,

$$y_R = 7.5 \times z_0 \tag{5.3}$$

A number of full scale experiments were performed, each with differing flow properties. Those with varying wind direction are easy to group together, but each of these will have a slightly differing wind strength over the experimental time. Thus each set of velocity values is normalised with the value at RS so comparisons can easily be made of the relative difference in velocity from the reference site.

At the roof of the domain, a free-slip wall boundary is imposed. This allows for the fact that the boundary layer may not be 1km in height. If a symmetry plane is used, the height of 1km is imposed on the layer, whereas the wall option allows the log profile to develop. Most of the data from Askervein is measured at a height of 10m, and the maximum is less than 200m, so any effects from this assumption will be minimal, and undetected in the measuring section.

The height of the domain is chosen as 1km so as to keep the blockage ratio low. The aim of this simulation is to model the inner region of the boundary layer, which is only a few hundred meters in height, so in theory, the domain could be reduced, but the blockage must be kept to

approximately 3% to minimise any effects it might have on the flow. The whole domain is now being modelled as if it were an inner layer, the extra height is purely to reduce the blockage.

The numerical model develops all unknown variables, and no initial values are given for the kinetic energy or its dissipation rate. This tests the numerical model further as engineers in a basic site survey will only have values of velocity to use in the setup of a simulation. Thus if numerical models are to be used in industry with confidence, it should be demonstrated that the rest of the flow values can be reproduced.

5.4. Mesh

Limitations in the computational facilities used in these experiments obviously limit the quality and density of the mesh used. The numerical model CFX-5 uses an unstructured computational mesh, consisting primarily of tetrahedra, as described in section 3.4.2

The mesh setup for the Askervein hill is similar to that used in Chapter 4 for flow over a cosine shaped hill. Close to the rough wall, many of the flow variables are changing rapidly, and it is imperative that any mesh attempts to consider these high gradients. Thus an inflation layer is used over the ground surface of the domain which consists of a number of prism shaped elements that are thin in the vertical direction, and much more substantial in the longitudinal and cross wind directions.

Mesh controls are also used to concentrate cells close to the hill surface and to the ground surface upwind from the hill. These mesh controls set a minimum cell size over the area they control, and impose an expansion factor so that the cells gradually increase in size up to the main domain parameters, hence preventing extremely large changes in cell size, which would reduce the accuracy of the simulation. Some changes in size can not be ruled out though and further control over the mesh is limited. The computer used in the simulations is has a limit of approximately 300,000 nodes due to memory constraints. The largest concentrations of nodes or cells are therefore over the hill surface and ground region.

5.4.1. Mesh Sensitivity

Mesh sensitivity tests have been performed on three different sized grids to consider how the velocity profile changes at certain locations within the domain. Grids of 200,000, 250,000 and 300,000 nodes have been tested. Each grid has the same basic setup but increased cell sizes for decreased volume cell totals.

Figures 5.5a and 5.5b shows velocity speed-up ratios at 10m for tower lines AA and B respectively, with the wind coming from the south (180°). The main interest in this project is the spatial variation in velocity and turbulence characteristics, rather than the vertical profiles. From an engineering point of view, a regional wind map which accurately represents the wind flow is of most use to a wind farm planner. Vertical

profiles can be determined more easily than horizontal profiles which are much more affected by the terrain shape and surface roughness.

It is clear that the values produced by the denser meshes are closer together than the values from the coarser meshes. This shows that the denser mesh is getting closer to predicting the ideal flow. The densest mesh also predicts the smoothest transition in velocity value over the hill.

5.5. Turbulence model

From an engineering standpoint, practicality is of equal importance to scientific accuracy, so two turbulence models are considered. The Reynolds stress model provides the highest level of computational accuracy available for a RANS simulation, and so is considered to see the extent to which CFD simulations can model the effects of turbulence on the flow. The results and conclusions from Chapter 4 establish that the most suitable two-equation turbulence model for use in this work is the k-ε RNG model. This type of model is relatively quick and easy to solve, and provides adequate accuracy for the flow setup.

The two models in use for this stage are widely available, and considered to be superior for wind flow modelling. They are not expected to predict turbulence perfectly, but to give an indication of the levels of turbulent effects within the flow. Indeed to calculate turbulence information from the k-ε RNG model, the velocity profile gradients must be used in conjunction with the eddy viscosity to calculate each of the Reynolds

stresses (as detailed in the following section). The RSM calculates each of the Reynolds stresses within the flow independently and so is hoped to produce a more accurate understanding of the turbulence.

Turbulence models are used to predict the effects of turbulence on the flow, not to calculate the actual quantities of turbulence itself. This again highlights the author's views that CFD can and should be used in conjunction with wind tunnel and full scale experimentation. All three are useful tools for wind field analysis, and each has its own area of 'expertise'. The advantages of numerical modelling lie in speed of setup and simulation, and quantity of data production. While the wind tunnel may be able to better model the effects of turbulence, the results of the CFD tests would indicate to the tunnel users where best to position their measuring equipment so as to speed up the process. This again aids the site surveyors to position their measuring masts in the most suitable locations to consider any terrain area for wind farm development.

So while it is important to try and model the turbulence as accurately as possible, from an engineering point of view the accuracy is relative. General indications of the effects are important, even if the actual values are unattainable.

5.6. Wind Directions

The wind rose for the nearest site to Askervein is presented in figure 5.6, and shows the range of wind directions experienced by the hill and

surrounding areas. It is also clear that the dominant wind directions are between the southerly and westerly directions as reported in the field reports. The Benbecula Met. Office station is located a few miles north of the Askervein hill, but is representative of the conditions found on the hill surface (Taylor and Teunissen, 1983).

Results from a number of wind directions were recorded during the study. In this chapter the hill is modelled from a single wind direction and the mesh setup accuracy is tested. Once this is completed, the hill can be rotated on the virtual disc and the simulation is run from a second wind direction. Further work in Chapter 6 considers the automation of this process to rotate the hill and re-run the simulation without further user input.

One of the main wind directions is from the south (180°) and so this is the initial setup, partly also due to the orientation of the terrain data. A wide variety of wind directions were also found during the field tests as can be seen in table 5.1. As the time taken to recreate the setup is considerable, two wind directions are considered in this chapter, 180° as described, and 210° due to the large amount of field data available and that wind tunnel data and numerical results from other authors is also available for this location. Further wind directions are considered in Chapter 6.

The work here is compared with numerical results from Beljaars *et al.* (1987) and Walshe (2003). Beljaars *et al.* used the widely referenced code

MS3DJH which is a linear code similar to WAsP and MS-Micro which are widely used in the wind energy sector. The results from Walshe (2003) are from WAsP itself. Comparisons with these codes aim to show the advantages obtained in using non-linear CFD codes for modelling wind flow over more complex terrain. The Askervein hill is not a particularly complex terrain feature and is classified as a low hill (Jackson and Hunt, 1975), so the linear codes predict the velocity speed-ups well, but the non-linear CFD results presented in this chapter aim to better capture some of the more complex effects. These alternate numerical results are only available for the wind direction 210°, which is unfortunate, but nonetheless gives an important comparison between the two primary modelling types.

Direction (°)	Number of runs	Number of hours
100	4	20
135	3	13
145	1	4
165	2	6
170	1	1.5
180	4	11.5
210	8	26
220	2	7
240	3	6
265	10	17
280	5	6
305	1	3.5
Total	**44**	**121.5**

Table 5.1 – Directional grouping of wind flow during experimental runs over the Askervein Hill

5.7. Velocity statistics

This section presents results of velocity predictions over the hill from both wind directions. Vertical profiles, in comparison with the field data, are presented first, though the more important predictions from a wind energy point of view are the lateral variations in velocity, and the speed-ups associated with changes in terrain characteristics, so these are also presented , in comparison with

5.7.1. Vertical profiles

Vertical velocity profiles for the hilltop (HT) location are presented in figures 5.7a and 5.7b. Figure 5.7a shows the profiles of the RNG and RSM models and the field data for the 180° wind direction, and figure 5.7b shows the same plot for the 210° wind direction.

In general both turbulence models capture the field data profile shape well. However, neither manages to predict the extent of the speed-up caused by the hill geometry, which will become more evident in the speed-up results presented below. The RSM model predicts a slightly higher velocity magnitude to the RNG model, though k-ε models are known to underpredict some of the wind flow effects, so this is not unexpected. The peak of the field dataset occurs at a height of 140m (14m above the hill surface), whereas the numerical results predict the maximum speed-up to occur at a height of approximately 145m (almost 20m above the surface). The shape of the profile is promising, though it is somewhat disappointing that the magnitude of velocity speed-up has not been captured.

The profile shape for the 180° wind direction shows a smooth transition from the peak velocity through to the rest of the profile. This is less visible for the 210° results and the profile shape here is much sharper. This may be as a result of the mesh distribution in this area for the alternate wind direction, or may result from increased surface steepness in the 210° direction.

5.7.2. Speed-up results

Some of the discussion in this section refers to actual mast locations from the Askervein project. These are displayed in figure 5.3. The letters refer to the mast line involved in the study (BSE, ANE, etc.) and the number refers to the mast location on that line (BSE30, AANE40, etc.).

A considerable variety of weather and wind conditions was experienced during the Askervein project in 1983, and consequently each experimental run has a different free stream wind speed and hence differing conditions over the hill. The stability remained near-neutral, but this variation in speed means that comparisons between each of the runs need to be made through velocity speed-up ratios rather than actual wind speeds. The reference site (RS) is used as a base point and the speed-up ratios are calculated in relation to the velocity, so:

$$Speed\ Up\ Ratio_{TOWER} = \frac{\overline{U}_{TOWER}}{\overline{U}_{RS}} \tag{5.4}$$

Full scale data are available for each of the 10m masts positioned along lines AA and B. Wind tunnel data is also available for these masts for certain wind directions as collected by Parkinson (1987). The masts along line A were used for turbulence data collection. Due to the similarities in terrain geometry between lines A and AA, comparison along one of them is sufficient for the velocity analysis.

As each of the runs has a different mean velocity, the wind profile at RS will also be different. The use of speed-up ratios means that the relative change is being examined rather than the actual values, so effectively, any reasonable logarithmic velocity profile could be incorporated i.e. the value of u_* is not so important, yet the value of z_0 is relevant to the surface roughness so must remain in the region of 0.03m. Excessive values of u_* are not valid, this is just to highlight that perfect profile deduction is of less importance in this case.

Figure 5.8 shows plots for the 180° wind direction for lines AA and B, comparing the full scale data with the k-ε RNG and Reynolds Stress turbulence models. No wind tunnel data is available for this wind direction.

For the line AA, the wind effectively approaches the hill from left to right on the graph. The full scale data show a steady speed as the wind approaches the upwind slope. A small slow down in speed is noticed (as expected) before the wind speeds up as the flow goes up to the top of the

hill. The highest velocity occurs just behind the crest of the hill and there is then a sharp drop in velocity as the flow goes down the lee slope and beyond. This sharp drop off is considered to be due to flow separation on the lee slope of the hill (Teunissen *et al.,* 1987).

Both turbulence models simulate the upwind flow well, remaining within a few percent of the full scale data. However, as the flow reaches its peak, the numerical data predicts the sharp change to occur slightly later than found at full scale. The numerical results also predict the flow to drop further below the full scale results.

For the line B results, the flow can be considered as passing normal to the line of towers. While strictly the flow is around 30° off this line, is it easier to understand the graph features if it is considered thus. Two significant peaks in velocity speed-up are clearly visible, one at HT as expected, and the second 20m down the hill from CP. Along the crest of the hill a noticeable drop in ratio is found. This point (BSE30) is positioned just below the high point of the hill crest, and the results from line AA show clearly that the higher velocities are not reached until right on the hill top section, or even after it, so it is understandable that this point is lower in velocity. As the points on the lower slope are considered (BSE80-BSE170) a visible slow down in velocity is found. The wind speed remains above that of RS, though while these are the lower slopes, they are still elevated above RS so this is also explained.

Again both the numerical model runs are very close to each other, with the RSM slightly underpredicting the results from the RNG model. Neither model captures the peak velocity at BSE60, and resulting from this, both models underpredict the flow on the lower slopes. The full scale data also shows a smoother decline in ratio.

Fig 5.9 shows the same plots for the 210° wind direction. For the line AA, wind flow is parallel to the line, and when considering the graph, flow is effectively from left to right. The full scale data shows similar effects to those from the 180° graphs. A noticeable dip just before the hill, then a regular increase in velocity ratio up to the hill top before peaking just after the top and a very sharp drop off in ratio which levels out around AANE40.

The RNG model results slightly underpredict the full scale data right across the data set. The sharp drop on the lee slope is well predicted, though a little late, but the model certainly improves on the wind tunnel results for the same data. The underprediction is much more noticeable with the RSM simulation. Not until the lee slope of the hill do the RSM results approach even the RNG model data. While this is not ideal, it is encouraging to know that the underprediction is fairly consistent.

The results from Walshe (2003) show consistent underprediction on the upwind slope which are similar to the RNG model, but the linear code does not predict the steep drop-off on the lee slope of the hill, and predicts results well above the CFD, wind tunnel and field data. The results from

Beljaars *et al.* (1987) overpredict the values on the upwind slope and even more so on the lee slope. It should be noted that numerical models have improved considerably since 1987 and computational power is somewhat more impressive, so these results are very good considering the year in which they were obtained. Both model types predict the general effects of the hill well, but the non-linear CFD code predicts the more sudden changes in wind velocity much better.

For the line B, wind flow is almost exactly normal to the tower line and hence the graph. Peak values are again noticeable at HT and at BSE60, and a low point along the crest at BSE30, again explainable from the geometry layout. The wind tunnel data gives good comparison with the full scale data, though there is not so much of it, highlighting one of the advantages of a CFD model.

The RNG model again slightly underpredicts the full scale data, and does not capture the severity of the BSE30 drop-off. In general the results are well modelled. Again though, the RSM results are considerably below the full scale and RNG data. It is interesting to note the RSM almost copies the RNG exactly, but a set distance (ratio) below it.

Results from Beljaars *et al.* (1987) are not presented for line B, though Walshe (2003) does show results from the WAsP simulations. WAsP undepredicts the wind speed-ups along all of line B, similar, or worse than

the RSM, particularly on the lower slopes, highlighting the deficiencies of the linear code.

For velocity predictions, it is clear that the use of the Reynolds Stress turbulence model gives no clear advantage over the k-ε RNG model. Considering the extra time taken for computing the RSM model, if the velocity is of primary importance, then the RNG model is more suitable. Turbulence comparisons are presented in the next section, where the RSM model is mathematically more robust.

5.8. Turbulence statistics

A further test of the numerical model in predicting wind flow is the consideration of turbulence values within the flow. In general, the mean wind layout is more straightforward to predict, but turbulence provides the model with much more of a challenge.

In this section, changes in turbulence characteristics predicted by the CFD models are compared with full scale data and, where possible, wind tunnel data. These comparisons show the extent to which the CFD model predicts the effects of turbulence and how the Reynolds Averaged Navier-Stokes (RANS) equations (and resulting turbulence model equations) relate to the measured full scale data.

During the field experiments, turbulence characteristics were measured along tower lines A (9 towers) and AA (4 towers) at 10m heights and also at RS and HT for various heights up to 50m. Cup and Gill anemometers were the primary measuring tool, though sonic anemometers were positioned at RS and HT. The relative accuracy of each type is as discussed in section 2.10.

The main parameters used for comparison are the root mean square of the relevant turbulence component, denoted σ_u, and the relative change of these turbulent quantities, denoted $\frac{\Delta\sigma_u}{(\sigma_u)_{REF}}$, where $\Delta\sigma_u$ is the difference in σ_u from its upstream value.

Reynolds stresses are easily retrieved from the post-processor for the Reynolds stress model as each is individually calculated. For the *k*-ε RNG model however, the Reynolds stress must be determined from the kinetic energy. The Boussinesq approximation allows the stresses to be determined from the relevant velocity gradient and turbulent stress (as detailed in section 3.5). By definition, the *k*-ε RNG model considers the sum of the primary Reynolds stresses to be twice the value of the kinetic energy, and as it calculates turbulence as isotropic, each of the Reynolds stresses are also identical in magnitude. Thus, by calculation of the kinetic energy, the Reynolds stress is determined as follows:

$$\text{Kinetic Energy} = \frac{1}{2}\left(\overline{u'u'} + \overline{v'v'} + \overline{w'w'}\right) \tag{5.5}$$

For isotropic k-ε based models, $\overline{u'u'} = \overline{v'v'} = \overline{w'w'}$ (5.6)

$$\text{So, Kinetic Energy} = \frac{1}{2}\left(3 \times \overline{u'u'}\right) \quad (5.7)$$

5.8.1. Horizontal profiles

Figure 5.10a shows the relative change in stream wise turbulence component at 10m heights along tower line AA for the wind direction 210°. Comparisons are made between the k-ε RNG and Reynolds stress model runs, the wind tunnel data and the full scale readings. Full scale data is available for only four of the towers along line AA, and the wind tunnel data for eight of the tower locations. The full scale data is measured using cup and gill anemometers which are known to have errors, either by cup over speeding, or other undetermined factors. At 10m heights, the anemometers should lie with 5% of the true value (Mickle *et al.*, 1987). CFD results are presented for all tower locations to show comparisons between the turbulence models, to show the complete horizontal profile shape as predicted by the CFD simulations, and to again highlight the advantage of CFD for data production and retrieval. The data sets compare favourably and a consistent profile is found. Upstream of CP, the turbulence levels rise slightly (approximately 10%), before a reduction in turbulence leading up to CP. Once the flow passes the top section, a sharp rise in turbulence is found, to approximately 1.4 times the upstream value. Upstream from CP, the RNG model fits closer to the wind tunnel data than the RSM, but downstream of the hill crest the RNG seems to over predict the steep change in turbulence levels. Of the full scale data available, all

data sets compare well, but as data is not available for the more extreme sections of the flow regime, few conclusions can be drawn from this apart from demonstrating that the CFD compares favourably with the wind tunnel.

Figure 5.10b shows the same data for line A across the hill. Full scale data is available for all nine towers on this line allowing a much better comparison of data sets. Upstream of the hill (on the left hand side of the graph), all the data sets show similar features, and are close in prediction. The turbulence level is fairly constant, until just before the flow reaches HT where there is a small drop of approximately 15% before a very steep rise. Each dataset shows this dramatic increase in turbulence in a very different manner, which indicates that the turbulence is particularly strong, and shows how difficult it can be to truly capture the shape. The full scale value has risen to over double the upstream level by the time the flow reaches a point 20m downstream of HT (ASW20). The turbulence level then drops down from this point on. The wind tunnel data set predicts this peak to be sooner, at (ASW10), and to reach only 1.75 times the turbulence level. Surprisingly in this case, it is the k-ε RNG model which seems to better capture the turbulence, and finds a peak level of 1.5 at ASW20, as found in the field experiments. The Reynolds stress model shows no clear peak in turbulence, though is seen to find a high point at ASW40.

Figures 5.11a and 5.11b shows the same plots for the 180° wind direction. Again for line AA, only four field data masts have turbulence data, and in

this case there is no wind tunnel data for comparison. For the data present, the numerical models predict the full scale well, though the data masts are only present in the region where little activity is occurring, so little can be drawn from this. The main turbulence region begins at AASW20 after a drop off of approximately 20% in turbulence value. The peak of the k-ε RNG model is larger than that predicted by the Reynolds stress model, but both models show similar shape, and have peaks and troughs occuring in the same location, which is promising.

For line A, all field data is again present and shows similar characteristics to those found in fig 5.10b. A decrease in turbulence levels, by about 15% is found leading up to the hill top. In this case, the field data begins to rise at exactly HT, rather than just downstream as found for the 210° case. The peak is not as large either, but reaches a level of 1.7 times the upstream value. The numerical model results begin to rise in the same location as for the 210° case, at tower ASW10, though neither turbulence model captures the effects found in the field data.

The difference in quality of data between lines A and AA can be partly explained by the local topography. The peak at HT, and the lead up is much steeper than for the equivalent at CP, and also the recirculation sections detailed later in this chapter were positioned on the lee slope at HT, indicating much more complex turbulent regions in this sector. The field data was also measured using cup and gill anemometers, which do not

produce the most accurate readings of turbulence, and their results must be considered to have significant errors.

5.8.2. Hilltop (HT) Profiles

Figure 5.12 show vertical profiles of each of the primary Reynolds stresses, compared with the kinetic energy profile from the Reynolds stress model. It is clearly visible that the cross stream and vertical Reynolds stress components are essentially equal, and half the value of the stream wise stress. This is consistent with the kinetic energy profile being almost identical to the stream wise Reynolds stress, as shown in section 3.2.10.

If these findings were applied to the calculation of the Reynolds stresses for the *k-ε* RNG turbulence model, the relation between kinetic energy and Reynolds stress changes. Instead of equation 5.7, we find:

$$\text{Kinetic Energy} = \frac{1}{2}\left(\overline{u'u'} + \frac{\overline{u'u'}}{2} + \frac{\overline{u'u'}}{2}\right) = \overline{u'u'} \qquad (5.8)$$

Which would give a different profile for Reynolds stress comparison. This can not be taken as fact as it is derived from results of a separate model, but highlights the difference in values of Reynolds stress components and the extra accuracy gained from using the Reynolds stress turbulence model.

5.8.3. σ_u Profiles

Full scale data is available for vertical profiles of σ_u, the stream wise Reynolds stress. Figures 5.13a and 5.13b shows plots of σ_u measured by cup anemometers, compared with values from both turbulence models for each of the wind directions. Figure 5.13a also shows results from the sonic anemometer tower positioned at HT.

The CFD profile is as expected from fluid mechanics theory and the understanding of the RANS equations. A small increase in turbulence to a height of approximately 10 above ground level, followed by a slow decline in turbulence level until a height of 40m above ground where the turbulence level becomes fairly constant. In the case of the full scale data from the cup anemometers, the profile is much more unexpected. The turbulence level remains high until 5m above ground level, and is followed by a considerable sharp decrease until a height of 15m , where it begins to rise again. If a subjective curve were drawn through the points, the profile would seem to return to a constant level at a height of approximately 40m above ground, as found in the CFD profile. So while the profiles are quite different in shape and magnitude, the heights at which the profiles change most are similar for each data set. The other full scale data set is from the sonic anemometers which are considered much more suitable for turbulence measurement. Here the turbulence seems to have a peak 2m from the ground surface, and a sharp reduction in turbulence until about 6m from the ground. Unfortunately these anemometers were positioned at 2m, 4m, 6m and 47m from the ground, so no data is available between the 6

and 47m points where some considerable changes would be expected. The 47m measurement seems to be in agreement with the values from the cup anemometer data as height above the ground is increased.

In figure 5.13b, very similar effects are noticeable. The CFD data sets seem to agree with general fluid theory for RANS modelling, and the full scale data again has a rise in turbulence once a height of 15m above ground is reached. Here the CFD data sets show a much smoother transition to free stream turbulence levels than found for the 210° wind direction. In all cases, the CFD underpredicts the full scale data by between two and three times.

The CFD results do agree well with the findings of Mickle *et al.* (1988) who discussed a three layer setup to the inner boundary layer. They considered changes in σ_u , showing that $\Delta\sigma_u$ increased to about 5m from the ground surface, decreased from 5m to 25m, and was constant above 25m. It is encouraging that while the specifics of this pattern are not reproduced, the levels 5m and 25m above ground are clearly visible on the numerical model results.

The CFD results predict the effects of the topography on the RANS equation model of fluid flow. The turbulence model and RANS equations are not a perfect representation of the flow, and have considerable simplifications. LES, DES and DNS simulation techniques are much more accurate methods. The profiles produced by the RANS model are therefore

a simplified result, and can not be expected to produce perfect turbulence characteristics. Turbulent effects are inherently difficult to simulate, and even the Reynolds stress model (the most advanced available in this RANS simulation) is unable to predict the full level and effect of the turbulence involved here.

5.8.4. Kinetic Energy Profiles

Vertical profiles of kinetic energy at HT are presented in figure 5.14. Figure 5.14a shows profiles for the 210° wind direction and figure 5.14b shows the same profiles for the 180° wind direction. The comparisons in this case are between the two turbulence models. Both models predict the same profile shape, showing a sharp rise in kinetic energy to a height of 10m above ground before reducing to near constant levels at a height of approximately 30m above ground. The RSM model predicts higher levels of energy than the RNG model. This is considerably more pronounced in the 210° wind direction, and the results from the 180° wind direction show a much smoother transition from the peak values to the base level further up the profile. This indicates an improved mesh layout for the 180° wind direction, which was also visible for the velocity profiles at HT presented earlier in this chapter.

5.8.5. Summary of turbulence results

The spatial variation in turbulence is well predicted by the numerical model, which compares favourably with the wind tunnel and full scale data. Flow regions with large changes in turbulence are not well predicted and the magnitude of turbulence is not captured, as can be seen by the vertical profiles at HT. Numerical models simplify the flow to a level which can be solved by mathematical formulae. Thus many of the more complicated flow effects are not taken into account, and small errors are commonplace. The lack of terrain data, the quality of mesh and the validity of the boundary conditions are three main sources of error which will have contributed in part to the results of this section.

From a wind energy viewpoint, the confidence which can be associated with modelling the spatial variation in turbulence and wind speed is promising. CFD should be used alongside the wind tunnel and full scale testing to produce a fast, accurate representation of the flow which can be viewed before the more costly wind tunnel and full scale experiments are undertaken.

5.9. Recirculation

The research groups performing the Askervein hill project detected separated flow regions on the lee slope of the hill (Cook, 2003), which was suggested to be a reason behind the sharp changes in speed-up-ratio drop off as found on the lee slope of the hill for various runs (Teunissen e*t al.* 1987). This region was located in numerical studies using the k-ε model by

Castro *et al.* (2003), for time-dependent simulations of the hill. This suggests that the flow over the hill exhibits some unsteady characteristics. The regions were found to be present during some of the field tests but not all. The CFD simulations performed here have only considered steady flow, and while future work could go on to consider the unsteady aspects, it is still interesting to consider whether the current modelling locates this flow separation.

While the mesh and boundary conditions are the same for each of the CFD simulations, the different turbulence models will predict differing separated regions, both in size and location. The turbulence close to the wall is the most intense and it is this which helps to cause the flow separation and recirculation, so the more accurate Reynolds stress model should simulate the flow effects more accurately. The k-ε RNG model will give a good indication of the recirculation region, though it is unlikely that the results will be as precise. The field survey results do not give details of these sections, so there is no real data for comparison, but fluid mechanics theory would predict some flow separation on the lee of a hill with this configuration and slope.

5.9.1. Wind from 180°

The k-ε RNG model locates a separated flow section on the lee slope of the hill as can be seen in figure 5.15a which shows a plan view of Askervein with the separated flow section in white. The region is small, and located outside the area of the flow measured by the project towers. Figure 5.15b

shows the same view for the Reynolds stress model, and a much smaller recirculation region is visible. While flow separation is expected in the domain, the size of the pocket is likely to be fairly small, particularly if it is unsteady and therefore occurring only under certain conditions, so the results from the Reynolds stress model are considered more likely.

5.9.2. Wind from 210°

Figure 5.16a shows the *k*-*ε* RNG results and 5.16b the results from the Reynolds stress model simulation. The RNG model from this wind direction predicts a large recirculation region on the lee slope of the hill. The region has a peculiar shape and seems not to be completely formed. The Reynolds stress model shows a significantly smaller region, similar in size to that found from the 180° wind direction. This is a much more likely scenario, and highlights the improved accuracy gained from using a Reynolds stress model over the *k*-*ε* and its modifications. The first order discretisation results from the Reynolds stress model show no evidence of recirculation, it only appear with a second order solution, which demonstrates the requirements of second order discretisation for accurate CFD analysis. First order solutions do not tend to locate separation and other wind flow effects.

5.9.3. Conclusions to recirculation results

The results of this section confirm that flow separation does indeed occur over the Askervein hill. The fluctuation of the recirculation region can not

be considered here, and further work on unsteady flow would be needed for full analysis of this phenomenon.

The Reynolds stress model predicts more expected recirculation regions and the results for the 210° flow case under the k-ε RNG model are particularly surprising. While the exact turbulence values did not match particularly well with the field data, the CFD shows its strength with the analysis of other flow effects. The full scale work did not measure flow separation conditions due to time and equipment constraints, but this is not an issue for the numerical model.

5.10. Cross stream velocity

Turbulent flow exhibits many effects within the fluid domain, including recirculation and eddying effects. Large changes in cross stream velocity close to the ground occur primarily due to the geometry of the hill, and partly to the turbulent effects in the near wall region. Monitoring the cross stream velocities helps to give an indication of the topographic effects within this flow.

5.10.1. Wind from 180°

Figures 5.17a and 5.17b shows plan view contour plots of the Askervein hill analysing the cross stream velocity for flow over the hill passing through HT. The k-ε RNG turbulence model predicts results very close to those from the Reynolds stress model, both in magnitude and general trend.

While the shape of the actual figure looks slightly different in downstream direction, when the magnitudes are considered, the figures are very similar, showing excellent agreement.

5.10.2. Wind from 210°

Figure 5.18 shows the cross stream velocity vector plots for the wind direction 210°. 5.18a shows results of the *k*-*ε* RNG model, 5.18b from the first order discretisation of the Reynolds stress model and 5.18c the second order discretisation of the Reynolds stress model.

The *k*-*ε* RNG model results show large regions of cross stream velocity in the downstream section of the domain. This is in a similar region to the very large separation section found during the same simulation, and can be attributed to that. The large velocity continues until approximately one hill length downstream before returning to normal. This is not as would be expected and the results from this are considered incorrect.

The second order Reynolds stress model gives much more expected results. On the upstream section of the domain, the results are the same as for the *k*-*ε* RNG model. As the flow clears the hill top, similar effects are found to those in figure 5.9 with the alternate wind direction. The first order Reynolds stress model predicts the cross stream velocity better than expected and while the full magnitudes are not obtained, the general shape is clearly visible, and gives a good indication of the expected trend, even though it is unable to pick up any flow separation.

5.10.3. Conclusions to cross-stream velocity results

It is clear from this section of the results that the Reynolds stress model gives a much improved indication of the topographic effects within the flow than the k-ε RNG model. This is expected and the simulations show flow effects as expected over the Askervein hill. The k-ε RNG model is well known to not be as accurate as the Reynolds stress, and the results here are not to conclude that it is a bad model, but merely to highlight the advantages of using a Reynolds stress model, even under first order discretisation when considering complex topographic effects on the flow.

5.11. Discussion and Conclusions

A numerical simulation of the Askervein hill has been performed and the results presented. Spatial variations in the velocity and turbulence characteristics show very good agreement with the full scale data and wind tunnel data where available.

Vertical profiles of velocity at the hilltop show good predictions of the wind speed over the hill. The magnitude is not fully captured, but the shape agreement is good and shows acceptable predictions of wind speed in the vertical direction.

Vertical profiles of kinetic energy and Reynolds stresses show good agreement with fluid theory, though they do not capture the magnitude and

shape of the full scale profiles. The theory that the inner boundary layer is split into three sections is visible within the vertical profiles, and clear changes in turbulence characteristics are available at 5m and 25m above ground for the HT position, as shown by Mickle *et al*. (1988).

The horizontal profiles of turbulence show quite dramatic changes on the lee slope of the hill where the flow is changing considerably. Rapid distortion occurs when the mean flow, from which the turbulence is deriving its energy, is changing too quickly for the turbulence to come into any kind of equilibrium with it (Kaimal and Finnigan, 1994). So the large changes in horizontal velocity on the lee slopes of the hills, as seen in figures 5.7 and 5.8, are having considerable effects on the turbulence within the flow, as is visible in figures 5.9 and 5.10. The errors in velocity prediction propagate into the turbulence comparisons.

The vertical profiles of kinetic energy and σ_u are as expected from fluid mechanics theory. The numerical model is solving the RANS equations for momentum and continuity, which are the governing equations of fluid mechanics. The turbulence model in use is to close these equations and to provide some understanding of the physics involved in turbulent motions. This method of solving the flow contains many approximations and so is unlikely to produce exact results.

Other sources of possible errors include the quality of the terrain data. Only 50m data is available for most regions of the UK, and indeed

Askervein, and this is used for the geometry setup. Significant geometry changes can occur within this grid and for more accurate analysis, a denser set of grid data would be required.

The surface roughness over the whole area is assumed constant. This is certainly not true 4km upstream of the hill where low cliffs and a seafront are present, but as the inlet velocity profile is taken from RS, this is a good approximation. It is unlikely however that the profile at RS is completely developed. Zeman and Jensen (1987) decided on a z_0 of 0.01m for the hill itself based on interpretation of the visual evidence and comparisons between model predictions and the observations. This is somewhat subjective and though roughness lengths are not expected to be significantly different, it does imply further difference between the numerical setup and the full scale scenario.

Considering these simplifications, the results of the model are encouraging, and it is demonstrated that CFD can be used confidently to model aspects of the atmospheric boundary for flow over hills. CFD will never be relied on solely to produce results for a wind flow analysis, and it is an extremely useful tool for engineers to use for analysis of the main flow characteristics for any given terrain region. Once the CFD results are analysed, a more educated wind tunnel setup, or indeed full scale experiments can be arranged.

6. Automation

6.1. Introduction

The previous two chapters have shown scientific evidence of the ability of CFD to accurately model wind flow over topography, to produce consistent approximations of the velocity speedups and Reynolds stresses. From an industry or engineering standpoint this is very important, as quality is imperative. Practicality though, is extremely important too, and if CFD is to be used in general engineering for wind farm placement studies, or any other engineering where wind flow over topography is important, it must be demonstrated that CFD can be used quickly and easily without significant and ongoing user input to the process. Automation has been extremely important for engineers right through the last century and into this one, and allows non-experts to use advanced methods.

The expertise of university research groups in obtaining CFD results of significant quality and their extra scientific knowledge about numerical modelling means that they are more suited to the development of practical CFD application. Automation of the CFD process is reasonably straight forward, once a good knowledge of the science is available.

The aim of this chapter is to automate the CFD modelling process so that once a site is chosen, all twelve wind rose directions can be modelled and a full wind map can be obtained quickly and easily, without recreating each

part of the CFD process, and with as little user activation as possible. Obviously some user input will be necessary, as CFD is a science where experience and judgement are extremely important, and the set-up of such an automated run must be carefully monitored. However the aim here is to remove user input once the simulation is set up, so that a dedicated machine can be left running for as long as is necessary and when complete, all required data will be available in any chosen location.

6.2. Method

The first stage requires consideration of how to automate the process simply. The terrain area will normally be a rectangular grid format, as this is the most commonly available DTM type (see section 2.9.3), which would need aligning with the required wind direction. One method would be to rotate the terrain area to the required angle, and reform the whole domain with the required set-up. This however is time consuming from a mesh generation point of view and also would produce changes in grid density through the domain.

The best method would be to have an identical mesh over the hill for each wind direction, which itself could be rotated. This would provide an already 'grid sensitivity checked' mesh over the hill, which could be rotated as necessary. The unstructured meshes being used in this project lend themselves to this method, whereas hexahedral meshes could be subject to numerical errors as discussed in section 3.4.7 depending on the orientation of the mesh with the bulk flow.

In Chapter 5, the Askervein terrain tile was placed on a virtual disc, which can easily be rotated without changing the domain geometry. This currently still requires the creation of a new mesh when the disc is rotated. This disc is now extruded as a cylinder with its own mesh, which can now be rotated to each of the required wind directions for any study and the modelling process performed for each one. For full wind flow analysis, all twelve wind rose directions would need modelling so that a balanced idea of how the flow is changing over the hill can be established. Care must be taken in considering the upstream effects for each wind direction as these will change. In the case of Askervein, the majority of wind directions have a simple flat upstream fetch leading out over the sea, though for others there are a series of hills which would interfere with the upstream profile. While it may not be necessary to model all of the upstream topographic components, they must be considered when defining the inlet profile for the relevant simulation.

With the domain setup consisting of two sections, some method must be incorporated for joining the sections and meshes together. The flow must be conserved across the boundary and the incorporation of any boundary must not affect the flow in any way.

6.2.1. General Grid Interfaces

When the two domain regions come into contact, an interface must be created which conserves the flux across the regional boundary. In other

industrial applications, these regions may have differing fluids, so allowing heat to transfer across, or may be parts of the same domain, with different mesh setups (for example, a join between a box section with a hexahedral mesh and a tubular section with a tetrahedral mesh). In CFX the interface is known as a general grid interface, or GGI. Initially developed for the turbo machinery industry where rotating sections of a geometry need to be linked with stationary components, their success has led to their use in many other industry sectors.

One common use is for nesting meshes. For example, when modelling a terrain area where a very dense mesh is needed to account for the topographical changes and effects on the wind flow, but where a larger domain is needed to simulate some of the other boundary layer effects, it is useful to be able to incorporate a coarser mesh to reduce computational dependence as used by Derickson and Peterka (2004). The GGI is a link between the two different meshes and allows transference of values across control volumes whose faces do not necessarily match.

The methodology is based on creating the two separate meshes and then joining them by importing them into a new model. In CFX a control surface method is used where the flux is conserved over a 2-D region. Control volumes (CVs) on each side of the interface share this 2-D region and the flow is discretised in terms of nodal and control surface (CS) variables. See figure 6.1 for a 2-D view of the GGI setup.

The control volumes on the right hand side (RHS), linked to the CS will receive the flux from those on the left hand side (LHS) in proportion to the amount of area of the CS which they occupy. In turn, those CVs on the LHS will receive the flux from the RHS relevant to the amount of the CS which they occupy. As all values are known at the nodes, and a linear relationship exists across the CS, this is a mathematically ideal situation.

The GGI in this case allows a mesh to be created for the wider domain area (which will not be as dense as the mesh over the hill), and a second mesh to be created for the disc shape, which can be rotated to the required wind direction governed by the wider domain. Figure 6.2 shows the domain set-up. Effectively the virtual disc becomes a rotating cylinder with its own mesh.

With this set-up, a series of macro type files can be created, all very similar, which:

- rotate the cylinder to the required location,
- re-create the mesh*,
- set-up the definition file for the CFD run
- start the solver.

*while the mesh is identical, it is necessary to recreate it each time the geometry is changed.

Once the results file is created, a postprocessor session file retrieves all the necessary data from the results, which is ready for analysis upon

completion of each of the simulations. The cylinder is then rotated to the next direction, and the whole process continues. If the twelve wind rose directions are being monitored for example, a single session file can rotate the cylinder 30° each time, and so the set-up is even simpler. A batch file controls the whole process.

Thus, once the user has set-up the batch run (including all session files and has created and tested a suitable mesh), no further input is necessary until the results are ready to be looked at. Monitoring of the process is simple within CFX and it is clear that the whole process needs to be regularly checked to monitor on the progress of each of the simulations.

Results can be obtained for any number of variables as with any CFD simulation. One of the aims of this section of work is to obtain information about the full wind map over Askervein. The wind rose obtained from the Met. Office (see Figure 5.6) gives the data for the twelve wind rose directions. Six of those are being modelled here, so a reasonably accurate wind map can be obtained. As these are the most prominent wind directions over the hill, and account for 70% of the wind flow, the results can be used to deduce reasonably accurate yearly mean values, which are of use to developers (Petersen *et al.*, 1998).

6.3. Wind directions

The wind directions important to the Askervein hill project, listed in Chapter 5, will be used for the automated project here. It is not appropriate

to use the twelve wind rose directions due to the location of other hills in the area which will affect the flow over Askervein (Taylor and Teunissen, 1987). The seven wind directions to be used here are all clear of interference from topography changes, and allow comparison with full scale and wind tunnel data. Figure 6.3 shows a contour plot of the hill, indicating the wind directions.

It should be noted that the mesh during this section of the project will not be perfect and mesh sensitivity is not analysed. The results are not going to be used for significant scientific comparisons, though analysis of the results will consider the velocity speed-up ratios and take into account the percentage and RMS error values between the data sets. The aim here is to produce an automation process which can be used by engineers in industry. Once the automation process is a success, further work could go on to consider the mesh set-ups and other CFD issues.

The main reason for the lack of mesh accuracy is that the GGI interface uses up a considerable amount of computer memory and so the limitations of the computer in use for this project mean that the process is of importance, not so much the results. The reduction in meshing capability due to the GGI being present is found to be approximately 30%, and sometimes as much as 50%. Thus for most situations where this process is going to occur, a powerful dedicated machine would improve the simulation accuracy. The mesh sensitivity tests performed in Chapter 5

show that a mesh with 200,000 nodes is still fairly sensitive to grid density changes.

6.4. Set-up process

The domain size from Chapter 5 is used ($10km \times 10km \times 1km$) with the hill towards the front end of the domain area (Figure 6.2) The disc itself is approximately 6km in diameter. The domain now consists of a box and a cylinder (with the disc effectively extruded through the domain) each with its own mesh. It is important to have the meshes on the interfaces of each domain as similar as possible, to reduce the chance of any adverse effects due to the presence of a GGI (Morvan, 2003).

The setup process can be seen in figure 6.4 with the rotation and setup stages clearly visible. The cylinder and box are used solely to create the meshes, so only one box is ever needed. All the boundary conditions, domain settings, flow variables, and solver considerations are performed in section 2 of the loop, when creating the definition file.

Automation would be improved if the mesh itself could be rotated rather than being recreated each time the cylinder is rotated, but this is not currently an option within the CFX code. The system in place here, by rotating the DTM surface, alters the co-ordinates of each of the measuring towers. This co-ordinate change is noted and has been transformed to a new system. Though the transformation is not inherently difficult or technical, an alternate method would be to rotate the box part of the

domain around the cylinder, thus maintaining the original co-ordinate system.

6.5. Results

The automation of wind flow modelling using CFD was successfully performed, with careful attention being paid to the process and methodology

Results are presented for each of the seven wind directions. Comparisons for wind speedups over the hill are given for the lines AA and B. Although the scientific accuracy of these results is not under examination, just the process of automation, it is promising to find that for a relatively small mesh, the results being produced are generally close to the full scale values. If a more powerful machine were dedicated to the process, improved accuracy would be expected. RMS and percentage error values of the results are also given showing the accuracy of the CFD simulations compared to the wind tunnel and full scale data.

6.5.1. Speed-up Ratios

Figures 6.5-6.18 show velocity speed-up ratios of the wind at the 10m towers along lines AA and B for each of the seven wind directions. Table 6.1 shows the RMS and percentage errors between the data sets.

Wind Direction	RMS Errors	
	CFD vs. Full Scale	Wind Tunnel vs. FS
135	0.035737	
165	0.141357	0.140712
180	0.115337	
210	0.129706	0.052785
235	0.188795	0.095233
265	0.150933	0.064343*
295	0.317503	0.104262*
Average	0.162767	0.096243

Wind Direction	Percentage Errors	
	CFD vs. Full Scale	Wind Tunnel vs. FS
135	6.65	
165	9.32	8.9
180	7.32	
210	8.57	6.27
235	15.3	6.75
265	11.68	4.78*
295	26.18	7.33*
Average	12.15 (9.81)	7.31

* second field data set compared, not wind tunnel data. So wind tunnel label is the second set of field survey data. Errors between WT and FS does not include errors between the two field data sets, only the WT errors.
** average values in brackets do not include the 295° wind direction.

Table 6.1 – RMS and % errors between data sets

With the wind approaching from 135° (Figures 6.5 and 6.6), the flow is effectively normal to line AA and parallel to B (Figure 6.2). The predictions along line B are generally good, with the CFD slightly underpredicting the flow pattern and not showing the more dramatic changes in speed-up ratio. Some discrepancy is noted between HT and CP where the two data sets fluctuate slightly. Along line AA the CFD predicts

a much smoother set of speed-ups, which compare reasonably well with the full scale data at the hill top, but less well on each of the slopes. With the wind coming from so wide an angle, this wind direction is the only one of the seven modelled here which may be affected by the location of other hills in the region, which would account for the differences in values. The percentage error between the data sets is only 6.65% though and so this should be viewed as successful.

With the flow direction at 165° (Figures 6.7 and 6.8), wind tunnel data is available for comparison alongside the full scale data. For both lines AA and B, the wind tunnel and CFD data are very closely matched, with the percentage error being just 4.64%. Again the full scale data values between HT and CP show some significant change along the crest of the hill which neither the CFD nor wind tunnel experience in such magnitude. The CFD underpredicts the full scale data on the upwind slopes, but improves on the lee side. Clear underprediction can be seen for the values along line B.

With the wind coming from the south (Figures 6.9 and 6.10), excellent comparisons are found on the upwind slope of the hill between the CFD and full scale data on line AA. The CFD over predicts the full wind speed at the top of the hill, though there is a lack of full scale data at this point as the mast AANE10 has no reading for that set. Along line B, for which the flow is close to normal, the CFD predicts well the general trend of velocity speed-ups, with a 7.32% error on average, though this time anomalies

along the hill crests are seen in both data sets. The full scale predicts higher than the CFD around CP, but further along the crest at HT, the data sets have inverted.

At 210° (Figures 6.11 and 6.12), the wind is almost parallel to AA and normal to line B. Excellent predictions are again noticed along line AA where the CFD and wind tunnel results both agree well with the full scale data. In this case, the CFD slightly underpredicts the speed-up ratio for the top of the hill, but stays within 8.6% of the full scale values on average. Along line B the wind tunnel has better agreement than the CFD results with the full scale, though again the discrepancies along the hill crest are present. The CFD predicts a generally smoother velocity speedup, though this is understandable as the CFD simulation is set-up as a simplified flow situation with few boundary layer effects presents and a less complicated environment.

At 235° (Figures 6.13 and 6.14), again the flow is normal to B and parallel to AA. Excellent predictions are found on the upwind slope of the hill for both the wind tunnel and CFD. On the lee slope for line AA, both the full scale and wind tunnel show a steep drop off in the velocity, which the CFD is unable to capture with its current setup. The steep drop off is found, but it is predicted to occur slightly further down the slope than was found during the experiments. It is from this direction that flow separation is most likely to occur and what was indeed noticed by the participants during the field survey, and this goes some way to explaining the steep change in

velocity, and some of the velocity differences along the hill crest. Line B shows the CFD predicting well on the lower slopes of the hill (right hand side of the graph) but again shows discrepancies between all three data sets along the hill crest.

With the wind coming from 265° (Figures 6.15 and 6.16), almost due west, the graphs show the CFD compared to two different field survey results, which have the wind coming from 263° and 268° respectively. These slight changes in wind direction should not have a large effect on the flow over the hill, and indeed on the upwind slope, both field data sets and the CFD and very close in their predictions. On the lee slope (along line AA) both full scale data sets show extreme drops in wind speed, which is not predicted by the CFD. Numerical models in general are known not to predict large changes in velocity, and again this could be a flow separation bubble which is found in the full scale, but not well predicted by the numerical model.

Results along line B are more interesting as the two field data sets are well separated, showing that the field results can change dramatically depending on the time of day of the survey with the weather conditions at that time. The CFD predictions are much closer to the 263° data set than to the 268°. Again there are the discrepancies along the hill crest, but the interesting point occurring from these graphs is the large differences between the full scale data sets which are on average, 8.43% apart. The CFD is within 5% of one, yet almost 12% from the second.

With the wind coming from 295° (Figures 6.17 and 6.18), almost parallel to line B, normal to line AA, and almost opposite to 135°, the CFD results are again compared to two field survey data sets, from 285° and 305°. Along line B the field data sets are very close to each other, and the CFD dramatically over predicts the speed-up ratios. Even the general trend of results is not well picked up, as the field results show a sharp drop just before the wind reaches CP, which is barely noticeable in the CFD data, though a drop is noticed just after the wind leaves HT, for which no field data is available. It is possible then that the CFD predicts this drop to occur 20m earlier than found at full scale, but without further full scale data, it is impossible to say.

Along line AA, the two field data sets are even less well matched though neither shows the large changes in speed-up ratio predicted by the CFD. Indeed this is by far the worst dataset, with the CFD predicting speedup ratios as low as 0.25 and none of the field data falls below 0.9. There is a lack of field data, but this still can not explain the CFD result.

The consistent swapping over of trendlines along the hill crests between HT and CP is unexpected. It occurs for all seven wind directions and could be due to a number of factors including topography effects. The DTM only has data points every 50m and there may well be some other topography not captured by the DTM which is affecting the flow.

6.5.2. Yearly mean values

Table 6.2 shows yearly predicted values of velocity at HT and CP. The wind rose obtained for Benbecula, the nearest Met. Office measuring station, (Figure 5.6), showed the prominent wind directions over the Askervein hill, and so a yearly mean is calculated as data is available for 70% of the wind directions. All twelve directions could be if required, but this gives a very good indication of the values available and the type of results that can be obtained with this type of analysis. Very quickly it can be determined, to a reasonable level of accuracy, whether the site is suitable for a wind farm. Full yearly mean profiles could be determined if necessary to allow various turbine heights to be considered.

Location	Yearly Mean Value (10m)
HT	12.65 m/s
CP	12.05 m/s

Table 6.2 – Yearly mean values

This demonstrates the advantages of using CFD. Wind roses are available for a large number of areas of the country, and yearly average values and a full wind map of a region can be created using CFD. In full scale experiments, measuring masts would have to be erected and monitored for the full year to create the same data, which would be expensive and time consuming. The limitations of the CFD model means that the full scale data would of course be more accurate, but nevertheless the CFD provides valuable information to planners, engineers and architects about the wind conditions of a region.

6.5.3. GGI Checking

GGI's are not widely used in CFD outside of turbo machinery applications as it is not uncommon to find 'jumps' in values across the GGI. Due to the large number of time steps involved in simulating flow over the Askervein geometry, these jumps are not noticeable. Figure 6.19 shows views of the GGI for the 235º wind direction, with vertical and cross stream velocity vector plots, confirming that the GGI has no effect on the wind flow through the domain. The GGI is designed for rotating machinery with very different (and revolving) meshes on either side of the GGI, and it is in these situations that effects have been identified by CFX users. In this case the cylinder does not rotate, and the meshes are very similar, so the chance of any effects occurring has been reduced as much as possible.

6.5.4. Time Taken

The time taken for the process (computer facilities are detailed in section 3.5) was approximately 24 hours for set-up and simulation of each wind direction, so in this case, for seven wind directions, a total of one week dedicated computer time. The GGI dramatically increases the number of iterations required, which explains the extra computation time.

The set-up for the batch run is more difficult to measure in terms of time, as the geometry was already configured here from use in Chapter 5. A best guess would approximate the total set-up time, including all the following parameters:

- Incorporation of DTM

- Pre-processing of model, including initial simulation to confirm domain and mesh suitability
- Set-up of batch file and creation of all necessary session files

could be completed in about a week, allowing for errors and problem solving.

6.6. Conclusions

The automation of the simulation process has been successfully completed and the industrial application of CFD for wind flows with varying direction can now be implemented straight forwardly.

Care must be given to ensure that enough computational power and memory is available to cope with the GGI within the domain and as a 'rule of thumb' the following points should be noted if the process is to be undertaken:

- The geometry either side of the GGI must match identically.
- The mesh on each side of the GGI must be as consistent as possible, even if the mesh through the rest of the domain is quite different.
- File names should be clear with obvious locations to simplify the batch file creation, and to ease problem solving.
- While no user input is required during the simulations process, it is useful to check on the solvers every few hours to ensure that the residuals are decreasing and that the process has not come to a halt.
- Separate session files are necessary for post processing each wind direction and it is important to accurately consider how the (x, y, z) point locations have changed with the cylinder rotation.

Significant advantages have been seen over field surveys and wind tunnel experiments. The versatility of numerical models is highlighted in the manipulation of the geometry and the retrieval of data. While the wind tunnel geometry can also be manipulated, it is much more arduous to obtain such amounts of data so quickly, and full scale experiments would require significant lengths of time spent on site. The numerical method is also cheaper as man hours are reduced and with more powerful computer equipment, the simulation run time would be minimised.

Within a relatively short time period, yearly mean values have been deduced with a model that is accurate (on average) to within 10%. Improved meshes would no doubt improve this accuracy level. Further data could be produced as necessary with items such as local wind roses easily deduced, based on wind roses of the surrounding areas. As discussed for the yearly mean values, the accuracy from the tests performed here is limited by the number of wind directions considered. To produce a local wind rose with any real confidence would require all 12 wind rose directions to be considered. Hence these results are not reproduced here.

CFD is a useful tool to aid the wind analysis process. Anomalies that are encountered during a CFD simulation could then be tested either at full scale (on-site) or in a wind tunnel, to see if reasoning can be found.

7. Conclusions

7.1. Project summary

This research shows a complete numerical simulation of wind flow over the Askervein hill. The CFD process and methodology has been thoroughly examined, including the mesh sensitivity and surface configuration for real flows over terrain. The most suitable turbulence models for wind flow analysis have been examined and compared for real situations with full scale and wind tunnel data. This shows the most suitable setup for using RANS models in atmospheric wind flow applications and has been validated against both wind tunnel and full scale data showing good levels of accuracy. The use of RANS models has been newly automated for practical engineering use, so that wind energy surveys of real terrain regions can be quickly and simply performed by non-expert CFD users. As such, the study represents one of the most detailed CFD studies of wind flow over terrain, and the Askervein hill in particular.

7.2. Conclusions

1. Current atmospheric boundary layer theory has been assessed, discussed and presented. The key issues have been identified as:

- Surface characteristics – roughness, terrain features, model accuracy;

- Atmospheric conditions – stratification issues, buoyancy, stability;
- Resulting flow profiles – velocity and turbulence;

2. Available numerical modelling techniques have been considered in depth, and suitable methods for modelling the ABL have been determined with regard to:

- model type (linear/CFD/DES/LES/DNS);
- mesh considerations;
- discretisation schemes;
- turbulence models;

3. The model and methodology has been evaluated in depth, with particular consideration towards accuracy. Grid sensitivity tests show resulting errors of less than 1%. The terrain data available has more limited accuracy, though without obtaining more accurate data and testing the setup further, it is impossible to associate a figure with the resulting errors. This is assumed to be one of the main sources of error, and the fact that the CFD results are within 7% of full scale data is promising. Improved terrain models should reduce this further, and this is a consideration for future work. Further errors involved may result from the near wall treatment due to the use of wall functions and the treatment of surface roughness, but these are minimal.

4. The investigations show that some of the more simple two-equation turbulence models can adequately predict the flow velocity over complex

terrain regions including areas of recirculation which are common in real terrain. The extra accuracy gained from using a Reynolds stress model does not match the extra time and hence cost taken in the simulation process. For modelling complex flow regions, such as recirculation bubbles, the Reynolds stress model has been found to be the most accurate model, and while the k-ε RNG model was designed specifically for recirculating regions, it has been found to overpredict the region significantly for very steep idealised terrain, and for flows over real topography. The most suitable turbulence model for use will depend on the results required, but for wind flow analyses over real terrain the author recommends the use of an advanced 2-equation model, unless cost is not an issue.

5. Turbulence characteristics have not been well predicted, and the errors can result from a number of sources. Full scale data was measured using a variety of equipment types, some of which are known to give inaccurate readings for turbulence data. Numerical issues are most likely to results from the simplifications incorporated into the flow regime. Stratification and buoyancy affect the flow turbulence significantly, and the level of grid sensitivity was not tested for turbulence values which are more difficult to simulate, so grid quality may result in error.

6. The automation of the CFD model while providing a good level of accuracy for wind flow modelling, allows these advanced numerical methods to be used alongside wind tunnel analyses to provide engineering

solutions. The level of accuracy involved in the mesh, and boundary condition representation has been examined and found to be acceptable. The level of error in the CFD simulations is equivalent to that found in wind tunnel studies, or indeed full scale experiments.

7. The computational requirements for the use of advanced numerical models are becoming available. All the work in this project has been performed on PC using a dual processor machine. Limitations in memory have limited the grid resolution, and is hence the main source of error. This usage of the PC shows how accessible CFD models are to general users, and the need for specialist workstations has effectively been removed

7.3. Future work

This work is far from an exhaustive study of atmospheric boundary layer flows over terrain regions and its continuation could follow a number of paths. The original subject area is for wind energy consideration, so real wind conditions must be recreated as much as possible, and the effects of wind farms on the atmospheric boundary layer should also be investigated. Any future work on CFD modelling using PCs should attempt to acquire extra memory and processing power to improve the grid resolution and reduce the solution cost.

The atmospheric boundary layer contains numerous characteristics which have not been considered in this study. Flow stratification results from the weather conditions and can be quite changeable. The effects of various stratification conditions could be investigated in any future study, and would involve using buoyancy models to simulate the more complicated atmospheric effects.

This study has also considered constant surface roughness over all terrains. This is rarely the case, and investigation of the changes on the ABL resulting from a roughness change should be investigated. Many wind farms are located in regions where forest and farmland are close together. The effects of different roughness were considered in Chapter 4 but the interaction of the two was not considered. The numerical approach to such a study would have to be carefully scrutinised as the mesh layout for each roughness would most likely vary.

Work could also consider the incorporation of a wind turbine or farm into the model. Published work is available on the effects of wind turbines on an idealised wind flow, and this could be incorporated into the real terrain model situation. A simple methodology would be to model the turbine as a momentum sink, though turbo machinery models are available which model the action of each rotating blade.

Finally, work may consider performing an unsteady analysis of the flow over both of the hills considered in this project, to analyse further the asymmetry in the recirculation regions.

References

Abe, K., Nagano, Y., Kondoh, T. (1993). '*Numerical prediction of separating and reattaching flows with a modified low-Reynolds-number k-ε model.*' Journal of Wind Engineering and Industrial Aerodynamics. Vol. 46-47, pp. 85-94.

Ackermann, T., Soder, L. (2002). '*An overview of wind energy-status 2002.*' Renewable and Sustainable Energy Reviews. Vol. 6, pp. 67-128.

AIAA (1998). '*Guide for the verification and validation of computational fluid dynamics simulations*'. Reston, Va, USA, American Institute of Aeronautics and Astronautics.

Allen, T., Brown, A.R. (2002). '*Large-eddy simulation of turbulent separated flow over rough hills.*' Boundary Layer Meteorology. Vol. 102, pp. 177-198.

Alm, L. K., Nygaard, T.A. (1993). '*Flow over complex terrain estimated by a general purpose Navier-Stokes solver*'. European Community Wind Energy Conference, Lubeck-Travemunde, Germany.

Antonia, R. A., Krogstad, P.-A. (2001). '*Turbulence structure in boundary layers over different types of surface roughness.*' Fluid Dynamics Research. Vol. 28, pp. 139-157.

Apsley, D. D. (1995). '*Numerical modelling of neutral and stably stratified flow and dispersion in complex terrain*'. Department of Mechanical Engineering, University of Surrey, UK.

Apsley, D. D., Castro, I.P. (1997). '*Flow and dispersion over hills: Comparison between numerical predictions and experimental data.*' Journal of Wind Engineering and Industrial Aerodynamics. Vol. 67-68, pp. 375-386.

Athanassiadou, M., Castro, I.P. (2001). '*Neutral flow over a series of rough hills: A laboratory experiment.*' Boundary Layer Meteorology. Vol. 101, pp. 1-30.

Atkinson, B. W. (1995). '*Diffusion and Transport of Pollutants in Atmospheric Mesoscale Flow Fields*', Kluwer Academic Publishers.

Aynsley, R. M., Melbourne, W., Vickery, B.J. (1977). '*Architectural Aerodynamics*', Applied Science.

Ayotte, K. W., Davy, R.J., Coppin, P.A. (2001). '*A simple temporal and spatial analysis of flow in complex terrain in the context of wind energy modelling.*' Boundary Layer Meteorology. Vol. 98, pp. 275-295.

Baetke, F., Werner, H. (1990). '*Numerical simulation of turbulent flow over surface-mounted obstacles with sharp edges and corners.*' Journal of Wind Engineering and Industrial Aerodynamics. Vol. 35, pp. 129-147.

Barth, T., Jesperson, D.C. (1989). '*The design and application of upwind schemes on unstructured meshes.*' AIAA.

Barthelmie, R. J. (2001). '*Evaluating the impact of wind induced roughness change and tidal range on extrapolation of offshore vertical wind speed profiles.*' Wind Energy. Vol. 4, pp. 99-105.

Barthelmie, R. J., Palutikof, J.P., Davies, T.D. (1993). '*Estimation of sector roughness lengths and the effect on prediction of the vertical wind speed profile.*' Boundary Layer Meteorology. Vol. 66, pp. 19-48

Baskaran, V., Smits, A.J., Joubert, P.N. (1987). '*A turbulent flow over a curved hill - Part 1. Growth of an internal boundary layer.*' Journal of Fluid Mechanics. Vol. 182, pp. 47-83.

Belcher, S. E., Hunt, J.C.R. (1998). '*Turbulent flow over hills and waves.*' Annual Review of Fluid Mechanics. Vol. 30, pp. 507-538.

Beljaars, A. C. M., Walmsley, J.L., Taylor, P.A. (1987). '*A mixed spectral finite-difference model for neutrally stratified boundary-layer flow over roughness changes and topography.*' Boundary Layer Meteorology. Vol. 38, pp. 273-303.

Bergeles, G. C. (1985). '*Numerical calculation of turbulent flow around two-dimensional hills.*' Journal of Wind Engineering and Industrial Aerodynamics. Vol. 21(3), pp. 307-321.

Besio, S., Mazzino, A., Ratto, C.F. (2003). '*Local log-law-of-the-wall in neutrally-stratified boundary-layer flows.*' Boundary Layer Meteorology. Vol. 107, pp. 115-142.

Botta, G. (1992). '*Wind Analysis on Complex Terrain - The case of Acqua Spruzza.*' Journal of Wind Engineering and Industrial Aerodynamics. Vol. 39(1-3), pp. 357-366.

Boussinesq (1877). '*Theorie de l'ecoulement tourbillant.*' Mem. Presentes par divers Savants Acad. Sci. Inst. Fr. Vol. 23, pp. 45-50.

Bowen, A. J., Lindley, D. (1977). '*A wind tunnel investigation of the wind speed and turbulence characteristics close to the ground over escarpment shapes.*' Boundary Layer Meteorology. Vol. 12, pp. 259-271.

Bradley, E. F. (1980). '*An experimental study of the profiles of wind speed, shearing stress and turbulence at the crest of a large hill.*' Quarterly Journal of the Royal Meteorological Society. Vol. 106, pp. 101-124.

Britter, R. E., Hunt, J.C.R., Richards, K.J. (1981). '*Air flow over a two-dimensional hill: Studies of velocity speed-up, roughness effects and turbulence.*' Quarterly Journal of the Royal Meteorological Society. Vol. 107, pp. 91-110.

Brutsaert, W. H. (1982). '*Evaporation into the Atmosphere*', D. Reidel.

Buschmann, M. H., Gad-el-Hak, M. (2003). '*Debate concerning the mean velocity profile of a turbulent boundary layer.*' AIAA. Vol. 41(4), pp. 565-572.

Byrne, C. E. I., Holdo, A.E. (1998). '*Effects of increased geometric complexity on the comparison between computational and experimental simulations.*' Journal of Wind Engineering and Industrial Aerodynamics. Vol. 73, pp. 159-179.

Calder, K. L. (1949). '*Eddy diffusion and evaporation in flow over aerodynamically smooth and rough surfaces: A treatment based on laboratory laws of turbulent flow with special reference to conditions in the lower atmosphere.*' Quarterly Journal of Mechanics and Applied Mathematics. Vol. 2(2), pp. 153-175.

Carpenter, P., Locke, N. (1999). '*Investigation of wind speeds over multiple two-dimensional hills.*' Journal of Wind Engineering and Industrial Aerodynamics. Vol. 83, pp. 109-210.

Castelli, S. T., Ferrero, E., Anfossi, D. (2001). '*Turbulence closures in neutral boundary layers over complex terrain.*' Boundary Layer Meteorology. Vol. 100, pp. 405-419.

Castro, F. A., Palma, J.M.L.M., Silva Lopes, A. (2003) '*Simulation of the Askervein flow. Part 1: Reynolds averaged Navier-Stokes equations (k-ε Turbulence model)*' Boundary Layer Meteorology. Vol. 107, pp. 501-530.

Castro, I. P., Apsley, D.D. (1997). '*Flow and dispersion over topography: A comparison between numerical and laboratory data for two-dimensional flows.*' Atmospheric Environment. Vol. 31(6), pp. 839-850.

Castro, I. P., Snyder, W.H. (1982). '*A wind tunnel study of dispersion from sources downwind of three-dimensional hills.*' Atmospheric Environment. Vol. 16, pp. 1869-1887.

Cermak, J. E., Cochran, L.S., Leffler, R.D. (1995). '*Wind-tunnel modelling of the atmospheric surface layer.*' Journal of Wind Engineering and Industrial Aerodynamics. Vol. 54-55, pp. 505-513.

CFX (2000). '*Private communications*'.

CFX (2003). '*CFX-5.6 Manual*'. Harwell, Oxfordshire, UK, CFX.

Chamberlain, A. C. (1965). '*Transport of gases to and from grass and grass-like surfaces.*'.

Charnock, H. (1955). '*Wind stress on a water surface.*' Quarterly Journal of the Royal Meteorological Society. Vol. 81, pp. 639-640.

Cheng, H., Castro, I.P. (2002). '*Near wall flow development after a step change in surface roughness.*' Boundary Layer Meteorology. Vol. 105, pp. 411-432.

Chien, K. Y. (1982). '*Prediction of channel and boundary layer flows with a low Reynolds number turbulence model.*' AIAA. Vol. 20, pp. 33-38.

Chung, T. J. (2002). '*Computational Fluid Dynamics*', Cambridge University Press.

Clarke, R. H., Hess, G.D. (1973). '*On the appropriate scaling for velocity and temperature in the planetary boundary layer.*' Journal of Atmospheric Science. Vol. 30, pp. 1346-1353.

Clarkson, J. (2003). '*What is that noise? It's a cat that's gone feral*'. The Sunday Times - 2nd March: 14-15.

Cockerill, T. T., Kuhn, M., van Bussel, G.J.W., Bierbooms, W., Harrison, R. (2001). '*Combined technical and economic evaluation of the Northern European offshore wind resource.*' Journal of Wind Engineering and Industrial Aerodynamics. Vol. 89, pp. 689-711.

Coelho, P. J., Pereira, J.C.F (1992). '*Finite volume computation of the turbulent flow over a hill employing 2D or 3D non-orthogonal collocated grid systems.*' International Journal for Numerical Methods in Fluids. Vol. 14, pp. 423-441.

Cook, N. J. (1997). '*The Deaves and Harris ABL model applied to heterogeneous terrain.*' Journal of Wind Engineering and Industrial Aerodynamics. Vol. 66, pp. 197-214.

Cook, N. J. (2003). '*Private communications*'. Anemos, UK.

Coppin, P. A., Bradley, E.F., Finnigan, J.J. (1994). '*Measurements of flow over and elongated ridge and its thermal stability dependence: the mean field.*' Boundary Layer Meteorology. Vol. 69, pp. 173-199.

Counihan, J. (1974). '*Flow over concatenated sinusoidal hills*'. Leatherhead, England, Central Electricity Research Laboratories.

Craft, T. J., Launder, B.E., Suga, K. (1996). '*Development of a cubic eddy-viscosity model of turbulence.*' International Journal of Heat and Fluid Flow. Vol. 17, pp. 108-115.

Cushman-Roisin, B. (1994). '*Introduction to Geophysical Fluid Dynamics*', Prentice-Hall.

Deaves, D. (1975). '*Wind over hills: A numerical approach.*' Journal of Wind Engineering and Industrial Aerodynamics. Vol. 1, pp. 371-391.

Deaves, D. (1980). '*Computations of wind flow over two-dimensional hills and embankments.*' Journal of Wind Engineering and Industrial Aerodynamics. Vol. 6, pp. 89-111.

Deaves, D. M., Harris, R.I. (1978). '*A mathematical model of the structure of strong winds*', Construction Industry Research and Information Association.

Derbyshire, S. H., Wood, N. (1994). '*The sensitivity of stable boundary layers to small slopes and other influences.*' Institute of mathematics and its applications conference series. Vol. 52, pp. 105-118.

Derickson, R. G., Peterka, J.A. (2004). '*Development of a powerful hybrid tool for evaluating wind power in complex terrain: Atmospheric numerical models and wind tunnels.*' AIAA.

Ding, L., Calhoun, R.J., Street, R.L. (2003). '*Numerical simulation of strongly stratified flow over a 3-D hill.*' Boundary Layer Meteorology. Vol. 107, pp. 81-114.

Durbin, P. A. (1991). '*Near wall turbulence without damping functions.*' Theoretical Computations of Fluid Dynamics. Vol. 3, pp. 1-13.

Durbin, P. A. (1993). '*A Reynolds stress model for near-wall turbulence.*' Journal of Fluid Mechanics. Vol. 249, pp. 465-498.

Durbin, P. A. (1996). '*Technical note: On the k-ε stagnation point anomaly.*' International Journal of Heat and Fluid Flow. Vol. 17, pp. 89-90.

Easom, G. (2000). '*Improved Turbulence models for Computational Wind Engineering*'. Civil Engineering. Nottingham, University of Nottingham.

Eidsvik, K. J., Utnes, T. (1997). '*Flow separation and hydraulic transitions over hills modelled by the Reynolds equations.*' Journal of Wind Engineering and Industrial Aerodynamics. Vol. 67-86, pp. 403-413.

Farell, C., Iyangar, A.K.S. (1999). '*Experiments on wind tunnel simulation of atmospheric boundary layers.*' Journal of Wind Engineering and Industrial Aerodynamics. Vol. 79, pp. 11-35.

Ferreira, A. D. (1995). '*Experimental and numerical simulation of wind flow around two-dimensional hills.*' Journal of Wind Engineering and Industrial Aerodynamics. Vol. 54/55, pp. 173-181.

Ferreira, A. D. (1995). '*Wind tunnel simulation of the adiabatic flow around a set of sinusoidal hill*'. 9th International Conference on Wind Engineering, New Delhi, India.

Ferreira, A. D. (1997). '*Wind tunnel simulation of the flow around two-dimensional hills.*' Journal of Wind Engineering and Industrial Aerodynamics. Vol. 38, pp. 109-122.

Ferziger, J. H. (1993). '*Simulation of complex turbulent flow: Recent advances and prospects in wind engineering.*' Journal of Wind Engineering and Industrial Aerodynamics. Vol. 46-48, pp. 195-212.

Finardi, S., Tinarelli, G., Faggian, P., Brusasca, G. (1998). '*Evaluation of different wind field modelling techniques for wind energy applications over complex topography.*' Journal of Wind Engineering and Industrial Aerodynamics. Vol. 74-76, pp. 283-294.

Finnigan, J. J., Neil, D., Lees, B.G., Croome, R.J., Woodgate, M. (1990) '*Modelling the wind flow pattern around a parabolic sand dune.*' Mathematics and Computers in Simulation. Vol. 32, pp. 89-94.

FLUENT (2002). '*Is my simulation converged?*' Fluent News. Spring 2002. pp. 21-23.

Gallego, M. C., Garcia, J.A., Cancillo, M.L. (2001). '*Characterisation of atmospheric turbulence by dynamical systems techniques.*' Boundary Layer Meteorology. Vol. 100, pp. 375-392.

Garratt, J. R. (1992). '*The Atmospheric Boundary Layer*', Cambridge University Press.

Garratt, J. R., Hess, G.D., Physick, W.L., Bougeault, P. (1996). '*The atmospheric boundary layer - Advances in knowledge and application.*' Boundary Layer Meteorology. Vol. 78, pp. 9-37.

Gatski, T. B., Hussaini, M.Y., Lumley, J.L. (1996). '*Simulation and modelling of turbulent flows*'. New York, Oxford University Press.

Gong, W., Ibbetson, A. (1989). '*A wind tunnel study of the turbulent flow over model hills.*' Boundary Layer Meteorology. Vol. 49, pp. 113-148.

Gosman, A. D. (1999). '*Developments in CFD for industrial and environmental application in wind engineering.*' Journal of Wind Engineering and Industrial Aerodynamics. Vol. 81, pp. 21-39.

Grotjans, H., Menter, F.R. (1998). '*Wall functions for general application CFD codes*'. Computational Fluid Dynamics - European Conference.

Hanjalic, K. (1994). '*Advanced turbulence closure models: a view of current status and future trends.*' International Journal of Heat and Fluid Flow. Vol. 15, pp. 178.

Hanjalic, K., Launder, B.E. (1972). '*A Reynolds stress model or turbulence and its application to thin shear flows.*' Journal of Fluid Mechanics. Vol. 52, pp. 609-638.

Hanna, S. R., Tehranian, S., Carissimo, B., Macdonald, R.W., Lohner, R. (2002). '*Comparison of model simulations with observations of mean flow and turbulence within simple obstacle arrays.*' Atmospheric Environment. Vol. 36, pp. 5067-5079.

Hinze, J. O. (1976). '*Turbulence: an introduction to its mechanism and theory*', McGraw Hill.

Hirsch, C. (1988). '*Numerical computation of Internal and External Flows. Volume 1: Fundamentals of Numerical Discretization*', John Wiley and Sons.

Hogstrom, U. (1996). '*Review of some basic characteristics of the atmospheric surface layer.*' Boundary Layer Meteorology. Vol. 78, pp. 215-246.

Hogstrom, U., Hunt, J.C.R., Smedman, A-S (2002). '*Theory and measurements for turbulence spectra and variances in the atmospheric neutral surface layer.*' Boundary Layer Meteorology. Vol. 103, pp. 101-124.

Hsieh, W. D., Chang, K.C. (1999). '*Two layer approach combining Reynolds stress and low Reynolds number k-ε models.*' AIAA. Vol. 37(2), pp. 283-287.

Hunt, J. C. R., Graham, J.M.R. (1978). '*Free stream turbulence near plane boundaries.*' Journal of Fluid Mechanics. Vol. 212, pp. 497-532.

Hunt, J. C. R., Leibovich, S., Richards, K.J. (1988). '*Turbulent shear flow over low hills.*' Quarterly Journal of the Royal Meteorological Society. Vol. 114, pp. 1435-1470.

Huser, A., Nilsen, P.J., Skatun, H. (1997). '*Application of the k-ε model to the stable ABL: Pollution in complex terrain.*' Journal of Wind Engineering and Industrial Aerodynamics. Vol. 67-68, pp. 425-436.

Ishihara, T., Hibi, K. (2002). '*Numerical study of turbulent wake flow behind a three-dimensional steep hill.*' Wind and Structures. Vol. 5, pp. 317-328.

Ishihara, T., Hibi, K. (2000). '*Numerical study of turbulent wake flow behind a three-dimensional steep hill.*' Computational Wind Engineering 2000.

Ishihara, T., Hibi, K., Oikawa, S. (1999). '*A wind tunnel study of turbulent flow over a three-dimensional steep hill.*' Journal of Wind Engineering and Industrial Aerodynamics. Vol. 83, pp. 95-107.

Iyengar, A. K. S., Farrell, C. (2001). '*Experimental issues in atmospheric boundary layer simulations: roughness length and integral length scale determination.*' Journal of Wind Engineering and Industrial Aerodynamics. Vol. 89, pp. 1059-1080.

Jackson, P. S., Hunt, J.C.R. (1975). '*Turbulent wind flow over a low hill.*' Quarterly Journal of the Royal Meteorological Society. Vol. 101, pp. 929-955.

Jacobsen, C. B. (1997). '*Large Eddy Simulation of confined swirling flow: numerical part*'. Institute of Energy Technology, Aalborg University.

Jensen, N. O., Petersen, E.L., Troen, I. (1984). '*Extrapolation of mean wind statistics with special regard to wind energy applications*'. Report WCP-86, World Meteorological Organisation, Geneva.

Jeong, U. Y., Koh, H-M., Lee, H.S (2002). '*Finite element formulation for the analysis of turbulent wind flow passing bluff structures using the RNG k-ε model.*' Journal of Wind Engineering and Industrial Aerodynamics. Vol. 90, pp. 151-169.

Kaimal, J. C., Finnigan, J.J. (1994). '*Atmospheric Boundary Layer Flows: Their structure and measurement*', Oxford University Press.

Kim, H. G., Lee, C.M., Lim, H.C., Kyong, N.H. (1997). '*An experimental and numerical study on the flow over two-dimensional hills.*' Journal of Wind Engineering and Industrial Aerodynamics. Vol. 66, pp. 17-33.

Kim, H. G., Patel, V.C., (2000). '*Test of turbulence models for wind flow over terrain with separation and recirculation.*' Boundary Layer Meteorology. Vol. 94, pp. 5-21.

Kim, H. G., Patel, V.C., Lee, C.M. (2000). '*Numerical simulation of wind flow over hilly terrain.*' Journal of Wind Engineering and Industrial Aerodynamics. Vol. 87, pp. 45-60.

Kim, S.-E., Boysan, F. (1999). '*Application of CFD to environmental flows.*' Journal of Wind Engineering and Industrial Aerodynamics. Vol. 81, pp. 145-158.

Kim, S. G., Yamaguchi, K., Kondo, A., Soda, S. (2003). '*A comparative study of the Mellor-Yamada and k-ε two-equation turbulence models in atmospheric application.*' Journal of Wind Engineering and Industrial Aerodynamics. Vol. 91, pp. 791-806.

Kobayashi, Y., Morinishi, Y., Togashi, S. (1993). '*Estimation of anisotropic k-ε model on the backward-facing step flow by LES data base.*' Journal of Wind Engineering and Industrial Aerodynamics. Vol. 46-47, pp. 77-84.

Kolmogorov (1941). '*The local structure of turbulence in incompressible viscous fluid for very large Reynolds numbers.*' Dokl. Akad. Nauk SSSR. Vol. 30, pp. 301-305.

Kustas, W. P., Brutsaert, W. (1986). '*Wind profile constants in a neutral atmospheric boundary layer over complex terrain.*' Boundary Layer Meteorology. Vol. 34, pp. 35-54.

Lam, C. K. G., Bremhorst, K. (1979). '*Prediction of turbulent heat fluxes and temperature fluctuations.*' International Communications in Heat and Mass Transfer. Vol. 6, pp. 489-501

Landberg, L., Myllerup, L., Rathman, O., Petersen, E.L., Jorgensen, B.H., Badger, J., Mortensen, N.G. (2003). '*Wind resource estimation - An overview.*' Wind Energy. Vol. 6, pp. 261-271.

Lange, B., Hojstrup, J. (2001). '*Evaluation of the wind resource estimation program WAsP for offshore applications.*' Journal of Wind Engineering and Industrial Aerodynamics. Vol. 89, pp. 271-291.

Launder, B. E., Reece, G.J., Rodi, W. (1975). '*Progress in the development of a Reynolds-stress turbulence closure.*' Journal of Fluid Mechanics. Vol. 68(3), pp. 537-566.

Launder, B. E., Sharma, B.I. (1974). '*Application of the energy-dissipation model of turbulence to the calculation of flow near a spinning disc.*' International Communications in Heat and Mass Transfer. Vol. 1, pp. 131-137.

Le, H., Moin, P., Kim, J. (1993). '*Direct numerical simulation of turbulent flow over a backward facing step.*' 9th Symposium on Turbulent Shear Flows. Vol., pp. 1-5

Lee, S.-J., Lim, H-C., Park, K-C. (2002). '*Wind flow over sinusoidal hilly obstacles located in a uniform flow.*' Wind and Structures. Vol. 5(6), pp. 515-526.

Leschziner, M. A. (1990). '*Modelling engineering flows with Reynolds stress turbulence closure.*' Journal of Wind Engineering and Industrial Aerodynamics. Vol. 35, pp. 21-47.

Lien, F. S., Leschziner, M.A. (1994). '*Assessment of turbulence-transport models including non-linear rng eddy-viscosity formulation and second-moment closure for flow over a backward-facing step.*' Computers and Fluids. Vol. 23, pp. 983-1004.

Lumley, J. (1970). '*Towards a turbulent constitutive relation.*' Journal of Fluid Mechanics. Vol. 41, pp. 413.

Lun, Y. F., Mochida, A., Murakami, S., Yoshino, H., Shirasawa, T. (2003). '*Numerical simulation of flow over topographic features by revised k-ε models.*' Journal of Wind Engineering and Industrial Aerodynamics. Vol. 91, pp. 231-245.

Manwell, J. F., Rogers, A.L., McGowan, J.G. (2000). '*Useful computer codes for wind engineering applications.*' Wind Engineering. Vol. 24(5), pp. 337-347.

Martano, P., Romanelli, A. (1997). '*A routine for the calculation of the time dependent height of the atmospheric boundary layer from surface-layer parameters.*' Boundary Layer Meteorology. Vol. 82, pp. 105-117.

Mason, P. J. (1986). '*Flow over the summit of an isolated hill.*' Boundary Layer Meteorology. Vol. 37, pp. 385-405.

Mason, P. J., King, J.C. (1984). '*Atmospheric flow over a succession of nearly two-dimensional ridges and valleys.*' Quarterly Journal of the Royal Meteorological Society. Vol. 110, pp. 821-845.

Mason, P. J., King, J.C. (1985). '*Measurements and prediction of flow and turbulence over and isolated hill of moderate slope.*' Quarterly Journal of the Royal Meteorological Society. Vol. 111, pp. 917-640.

Mason, P. J., Sykes, R.I. (1979). '*Flow over an isolated hill of moderate slope.*' Quarterly Journal of the Royal Meteorological Society. Vol. 105, pp. 383-395.

Maurizi, A. (2000). '*Numerical simulation of turbulent flows over 2-D valleys using three versions of the k-ε closure model.*' Journal of Wind Engineering and Industrial Aerodynamics. Vol. 85, pp. 59-73.

McNaughton, K. G., Brunet, Y. (2002). '*Townsend's hypothesis, coherent structures and Monin-Obukhov similarity.*' Boundary Layer Meteorology. Vol. 102, pp. 161-175.

Mellor, G. L., Yamada, T. (1974). '*A Hierarchy of Turbulence Closure Models for Planetary Boundary Layers.*' Journal of Atmospheric Science. Vol. 31, pp. 1791-1806.

Menter, F. (1992). '*Influence of freestream values on k-ω turbulence model predictions.*' AIAA. Vol. 30(6), pp. 1657-1659.

Menter, F. (1994). '*Two-equation eddy-viscosity turbulence models for engineering applications.*' AIAA. Vol. 32(8), pp. 1598-1605.

Meroney, R. N., Letchford, C.W., Sarkar, P.P. (2002). '*Comparison of numerical and wind tunnel simulation of wind loads on smooth, rough and dual domes immersed in a boundary layer.*' Wind and Structures. Vol. 5(2-4), pp. 347-358.

Mickle, R. E., Cook, N.J., Hoff, A.M., Jensen, N.O., Salmon, J.R., Taylor, P.A., Tetzlaff, G., Teunissen, H.W. (1988). '*The Askervein Hill Project: Vertical profiles of wind and turbulences.*' Boundary Layer Meteorology. Vol. 43, pp. 143-169.

Miller, C. A., Davenport, A.G. (1998). '*Guidelines for the calculation of wind speed-ups in complex terrain.*' Journal of Wind Engineering and Industrial Aerodynamics. Vol. 74-76, pp. 189-197.

Monin, A. S., Yaglom, A.M. (1975). '*Statistical Hydrodynamics: Vol 1 and 2*'. Cambridge, MA, MIT Press.

Montavon, C. (1998). '*Simulation of Atmospheric Flows over Complex Terrain for Wind Power Potential Assessment*'.

Mortensen, N. G., Landberg, L. (1993). '*Wind Atlas Analysis and Application Program (WAsP) User's Guide*'. Roskilde, Denmark, Riso National Laboratory: 133.

Morvan, H. P. (2003). '*Private communications*'. University of Nottingham, UK.

Murakami, S. (1997). '*Current status and future trends in computational wind engineering.*' Journal of Wind Engineering and Industrial Aerodynamics. Vol. 67-68, pp. 3-34.

Murakami, S. (1998). '*Overview of turbulence models applied in CWE-1997.*' Journal of Wind Engineering and Industrial Aerodynamics. Vol. 74-76, pp. 1-24.

Murakami, S., Mochida A. (1988). '*3-D numerical simulation of airflow around a cubic model by means of the k-ε model.*' Journal of Wind Engineering and Industrial Aerodynamics. Vol. 31(2-3), pp. 283-303.

Murayama, T. (1999). '*Surface and inlet boundary conditions for the simulation of turbulent boundary layer over complex rough surfaces.*' Journal of Wind Engineering and Industrial Aerodynamics. Vol. 81, pp. 311-322.

Murayama, T., Rodi, W., Murayama, Y., Hiraoka, H. (1999). '*Large eddy simulation of the turbulent boundary layer behind roughness elements using and artificially generated inflow.*' Journal of Wind Engineering and Industrial Aerodynamics. Vol. 83, pp. 381-392.

Nakanishi, M. (2001). '*Improvement of the Mellor-Yamuda turbulence closure model, based on large eddy simulation data.*' Boundary Layer Meteorology. Vol. 99, pp. 349-378.

Neff, D. E., Meroney, R.N. (1998). '*Wind-tunnel modelling of hill and vegetation influence on wind power availability.*' Journal of Wind Engineering and Industrial Aerodynamics. Vol. 74-76, pp. 335-343.

Nikuradse, J. (1932). '*Gesetzmässigkeit der turbulenten Strömung in glatten Rohren.*' VDI, Forschungsheft 356.

Nielsen, M. (1999). '*A method for spatial interpolation of wind climatologies.*' Wind Energy. Vol. 2, pp. 151-166.

Nieuwstadt, F. T. M., Duynkerke, P.G. (1996). '*Turbulence in the atmospheric boundary layer.*' Atmospheric Reseach. Vol. 40, pp. 111-142.

Ohya, Y. (2001). '*Wind tunnel study of the atmospheric stable boundary layer over a rough surface.*' Boundary Layer Meteorology. Vol. 98, pp. 57-82.

Paeschke, W. (1937). '*Experimentelle Untersuchungen zum Rauhigkeits- und stabilitatsproblem in der bodennahen Luftschicht.*' Beitrage z. Phys. d. freien. Atmos. Vol. 24, pp. 163-189.

Papadopoulos, K. H., Stefanatos, N.C., Paulsen, U.S., Morfiadakis, E. (2001). '*Effects of turbulence and flow inclination on the performance of cup anemometers in the field.*' Boundary Layer Meteorology. Vol. 101, pp. 77-107.

Parkinson, H. G. (1987). '*Measurements of wind flow over models of a hill*'. Oxford, University of Oxford.

Parkinson, G. V., Cook, N. (1992). '*Blockage tolerance of a boundary-layer wind tunnel.*' Journal of Wind Engineering and Industrial Aerodynamics. Vol. 42, pp. 873-884.

Patankar, S. V. (1980). '*Numerical heat transfer and fluid flow*'. New York, Hemisphere.

Patel, V. C., Rodi, W., Scheuerer, G. (1985). '*Turbulence models for near wall and low Reynolds number flows: A review.*' AIAA. Vol. 23, pp. 1308-1319.

Pearce, D. L., Ziesler, C.D. (2000). '*Using CFD modelling to improve the estimation of offshore wind resource.*' IMechE Seminar - Power Generation by Renewables. Vol., pp. 207-219.

Pearse, J. R. (1981). '*Wind flow over ridges is simulated in an atmospheric boundary layer.*' Boundary Layer Meteorology. Vol. 21, pp. 77-92.

Pearse, J. R. (1982). '*Wind flow over conical hills in a simulated atmospheric boundary layer.*' Journal of Wind Engineering and Industrial Aerodynamics. Vol. 10, pp. 303-313.

Petersen, E. L., Mortensen, N.G., Landberg, L., Hojstrup, J., Frank, H.P. (1998). '*Wind power meteorology. Part 1: Climate and Turbulence.*' Wind Energy. Vol. 1, pp. 2-22.

Petersen, E. L., Mortensen, N.G., Landberg, L., Hojstrup, J., Frank, H.P. (1998). '*Wind power meteorology. Part 2: Siting and models.*' Wind Energy. Vol. 1, pp. 55-72.

Piquet, J. (1999). '*Turbulent Flows: Models and Physics*'. Berlin, Springer-Verlag.

Plate, E. J. (1971). '*Aerodynamic characteristics of atmospheric boundary layers*'. Springfield, VA, US Atomic Energy Comm.

Pope, S. B. (1975). '*A more general effective-viscosity hypothesis.*' Journal of Fluid Mechanics. Vol. 72(2), pp. 331-340.

Prandtl, L. (1925). '*Uber die ausgebildete Turbulenz.*' ZAMM. Vol. 5, pp. 136-139.

Prandtl, L. (1945). '*Uber ein neues Formelsystem fur die ausgebildete Turbulenz.*' Nachr. Akad. Wiss. Gottinge, Math-Phys. Kl. Vol., pp. 6-19.

Prevezer, T. (2002). '*Bluff body asymmetric flow phenomemon - real effect or solver artefact?*' Wind and Structures. Vol. 5, pp. 359-368.

Pryor, S. C., Barthelmie, R.J. (2001). '*Comparison of potential power production at on- and offshore sites.*' Wind Energy. Vol. 4, pp. 173-181.

Rahman, M. M., Siikonen, T. (2002). '*Low Reynolds number k-ε model with enhanced near-wall dissipation.*' AIAA. Vol. 40(7), pp. 1462-1464.

Raithby, G. D., Stubley, G.D., Taylor, P.A. (1987). '*The Askervein hill project: A finite control volume prediction of three-dimensional flows over the hill.*' Boundary Layer Meteorology. Vol. 39, pp. 247-267.

Raw, M. (1995). '*A coupled algebraic multigrid method for the 3D Navier Stokes equations.*' Notes on Numerical Fluid Mechanics. Vol. 49, pp. 204-215.

Reynolds, O. (1895). '*On the dynamical theory of incompressible viscous fluids and the determination of the criterion.*' Proceedings of the Royal Society of London. Vol. 451.

Richards, P. J., Hoxey, R.P. (1993). '*Appropriate boundary conditions for computational wind engineering models using the k-ε turbulence model.*' Journal of Wind Engineering and Industrial Aerodynamics. Vol. 46-47, pp. 145-153.

Rodi, W. (1976). '*A new algebraic relation for calculating Reynolds stress.*' ZAMM. Vol. 56, pp. 219-221.

Rodi, W. (1997). '*Comparison of LES and RANS calculations of the flow around bluff bodies.*' Journal of Wind Engineering and Industrial Aerodynamics. Vol. 69-71, pp. 55-75.

Rodi, W., Mansour, N.N. (1993). '*Low Reynolds number k- modelling with the aid of direct simulation data.*' Journal of Fluid Mechanics. Vol. 250, pp. 509-529.

Rotta, J. C. (1951). '*Statistiche Theorie nichthomogener Turbulenz.*' Z. Phys. Vol. 129, pp. 547-572.

Saffman (1977). '*Results of a two equation model for turbulent flow and the development of a relaxation stress model for application to straining and rotating flows.*' Proceedings of Project SQUID workshop on turbulence in internal flows. Vol., pp. 191-231.

Salameh, M. G. (2003). '*Can renewable and unconventional energy sources bridge the global energy gap in the 21st century?*' Applied Energy. Vol. 75, pp. 33-42.

Salmon, J. R., Teunissen, H.W., Mickle, R.E., Taylor, P.A. (1988). '*The Kettles hill project: Field observations, wind-tunnel simulations and numerical model predictions for flow over a low hill.*' Boundary Layer Meteorology. Vol. 43, pp. 309-343.

Schlichting, H. (1955) '*Boundary Layer Theory*'. 1st Edition, McGraw Hill

Schlichting, H. (2000) '*Boundary Layer Theory*'. 8th Edition, Springer.

Schneider, G. E., Raw, M.J. (1987). '*Control volume finite-element method for heat transfer and fluid flow using collocated variables - 1. Computational procedure.*' Numerical Heat Transfer. Vol. 11, pp. 363-390.

Schneider, G. E., Raw, M.J. (1987). '*Control volume finite-element method for heat transfer and fluid flow using collocated variables - 2. Application and validation.*' Numerical Heat Transfer. Vol. 11, pp. 391-400.

Selvam, R. P. (1989). '*Computer simulation of wind flow over steep hills*'. 2nd Asia-Pacific Symposium on Wind Engineering, Beijing, China.

Shaw, C. T. (1992). '*Using Computational Fluid Dynamics*', Prentice Hall.

Shih, T. H., Lumley, J.L. (1993). '*Critical comparison of second order closures with direct numerical simulation of homogeneous turbulence.*' AIAA. Vol. 31(4), pp. 663-670.

Shih, T. H., Zhu, J., Lumley, J.L. (1995). '*A new Reynolds stress algebraic equation model.*' Computational Methods Applied to Mechanical Engineering. Vol. 125, pp. 287-302.

Smagorinsky, J. (1963). '*General circulation experiments with the primitive equations.*' Monthly Weather Review. Vol. 93, pp. 99-165.

Smith, G. D. (1985). '*Numerical solution of Partial Differential Equations: Finite difference methods*'. Oxford, Oxford University Press.

Snyder, W. H., Castro, I.P. (2002). '*The critical Reynolds number for rough-wall flows.*' Journal of Wind Engineering and Industrial Aerodynamics. Vol. 90, pp. 41-54.

So, R. M. C., Lai, Y.G., Zhang, H.S, Hwang, B.C. (1991). '*Second order near wall turbulence closures: A review.*' AIAA. Vol. 29(11), pp. 1819-1835.

Spalart, P. R. (2000) '*Strategies for turbulence modelling and simulations*' International Journal of Heat and Fluid Flow. Vol. 21, pp. 252-263.

Speziale, C. G. (1987). '*On non-linear k-ϑ and k-ε models of turbulence.*' Journal of Fluid Mechanics. Vol. 178, pp. 459-475.

Speziale, C. G. (1998). '*Turbulence modelling for time dependant RANS and VLES: A review.*' AIAA. Vol. 36(2), pp. 173-184.

Speziale, C. G., Gatski, T.B. (1994). '*Assessment of second order closure models in turbulent shear flows.*' AIAA. Vol. 32(10), pp. 2113-2115.

Stubley, G. D., Riopelle, G. (1988). '*The influence of the Earth's rotation on planetary boundary layer turbulence.*' Boundary Layer Meteorology. Vol. 45, pp. 307-324.

Stull, R. B. (1988). '*An Introduction to Boundary Layer Meteorology*', Kluwer Academic.

Suga, K. (1996). '*Development and application of a non-linear eddy-viscosity model sensitized to stress and strain invariants*'. Mechanical Engineering. Manchester, UMIST.

Sukoriansky, S., Galperin, B., Staroselsky, I. (2003). '*Cross-term and ε-expansion in RNG theory of turbulence.*' Fluid Dynamics Reseach. Vol. 33, pp. 319-331.

Sutton, O. G. (1953). '*Micrometeorology*', McGraw-Hill.

Takahashi, T., Ohtsu, T., Yassin, M.F., Kato, S., Murakami, S. (2002). '*Turbulence characteristics of wind over a hill with a rough surface.*' Journal of Wind Engineering and Industrial Aerodynamics. Vol. 90, pp. 1697-1706.

Tampieri, F., Mammarella, I., Maurizi, A. (2003). '*Turbulence in complex terrain.*' Boundary Layer Meteorology. Vol. 109, pp. 85-97.

Tamura, T. (2003). '*Current research by FDM.*' Journal of Wind Engineering and Industrial Aerodynamics. Vol. 46-47, pp. 893-896.

Tamura, T. (2003). '*Current researches by FEM.*' Journal of Wind Engineering and Industrial Aerodynamics. Vol. 46-47, pp. 897-898.

Taylor, G. I. (1921). Proceedings of the London Mathematical Society.

Taylor, G. I. (1938). '*The statistical theory of isotropic turbulence.*' Journal of Aeronautical Sciences. Vol. 4(8), pp. 311-315.

Taylor, P. A. (1998). '*Turbulent boundary-layer flow over low and moderate slope hills.*' Journal of Wind Engineering and Industrial Aerodynamics. Vol. 74-76, pp. 25-47.

Taylor, P. A. (2001). '*Private communications*'. York University, Toronto, Canada

Taylor, P. A., Mason, P.J., Bradley, E.F. (1987). '*Boundary-layer flow over low hills.*' Boundary Layer Meteorology. Vol. 39, pp. 107-132.

Taylor, P. A., Teunissen, H.W. (1983). '*ASKERVEIN '82: Report on the September/October 1982 Experiment to Study Boundary-Layer Flow over Askervein, South Uist*'. Ontario, Canada, Meteorological Services Research Branch.

Taylor, P. A., Teunissen, H.W. (1985). '*The Askervein Hill Project: Report on the Sept./Oct. 1983, Main Field Experiment*'. Ontario, Canada, Meteorological Services Research Branch.

Taylor, P. A., Teunissen, H.W. (1987). '*The Askervein Hill Project: Overview and background data.*' Boundary Layer Meteorology. Vol. 39, pp. 15-39.

Teunissen, H. W., Shokr, M.E., Wood, A.J. and Green, D.W.R. (1987). '*Askervein Hill Project: Wind tunnel simulations at three length scales.*' Boundary Layer Meteorology. Vol. 40, pp. 1-29.

Thivet, F., Daouk, H., Knight, D.D. (2002). '*Influence of the wall condition on k-ω turbulence model predictions.*' AIAA. Vol. 40(1), pp. 179-181.

Townsend, A. A. (1961). '*Equlibrium layers and wall turbulence.*' Journal of Fluid Mechanics. Vol. 11, pp. 97-120.

Tsuchiya, M., Murakami, S., Mochida, A., Kondo, K., Ishida, Y. (1997) '*Development of a new k-epsilon model for flow and pressure fields around bluff body.*' Journal of Wind Engineering and Industrial Aerodynamics. Vol. 67-68, pp. 169-182.

Uchida, T., Ohya, Y. (1999). '*Numerical simulation of atmospheric flow over complex terrain.*' Journal of Wind Engineering and Industrial Aerodynamics. Vol. 81, pp. 283-293.

Uchida, T., Ohya, Y. (2001). '*Numerical study of stably stratified flows over a two-dimensional fill in a channel of finite depth.*' Fluid Dynamics Reseach. Vol. 29, pp. 227-250.

Veersteeg, H. K., and Malalasekera, W. (1995). '*An introduction to Computational Fluid Dynamics*', Prentice Hall.

Vogelezang, D. H. O., Holtslag, A.A.M (1996). '*Evaluation and model impacts of alternative boundary layer height formulations.*' Boundary Layer Meteorology. Vol. 81, pp. 245-269.

Vu, T. C., Ashie, Y., Asaeda, T. (2002). '*A k-ε turbulence closure model for the atmospheric boundary layer including urban canopy.*' Boundary Layer Meteorology. Vol. 102, pp. 459-490.

Walmsley, J. L., Taylor, P.A., Keith, T. (1986). '*A simple model of neutrally stratified boundary-layer flow over complex terrain with surface roughness modulations.*' Boundary Layer Meteorology. Vol. 36, pp. 157-186.

Walmsley, J. L., Troen, I.B., Lalas, D.P., Mason, P.J. (1990). '*Surface-layer flow in complex terrain: Comparison of models and full scale observations.*' Boundary Layer Meteorology. Vol. 52, pp. 259-282.

Walshe, J. (2003). '*CFD modelling of wind flow over complex and rough terrain*'. Department of Electrical Engineering, Loughborough University.

Weng, W. (1997). '*Stably stratified boundary layer flow over low hills: A comparison of model results and field data.*' Boundary Layer Meteorology. Vol. 85, pp. 223-241.

Weng, W., Taylor, P.A. (2003). '*One dimensional atmospheric boundary layer modelling.*' Boundary Layer Meteorology. Vol. 107, pp. 371-400.

Wesseling, P. (2001). '*Principles of Computational Fluid Dynamics*', Springer.

White, F. M. (1979). '*Fluid Mechanics*'. 1st Edition, McGraw Hill.

White, F. M. (1991). '*Viscous Fluid Flow*', McGraw Hill.

White, F. M. (1999). '*Fluid Mechanics*'. 4th Edition, McGraw Hill.

Wieringa, J. (1993). '*Representative roughness parameters for homogeneous terrain.*' Boundary Layer Meteorology. Vol. 63, pp. 323-364.

Wieringa, J. (1996). '*Does representative wind information exist?*' Journal of Wind Engineering and Industrial Aerodynamics. Vol. 65, pp. 1-12.

Wilcox, D. C. (1994). '*Turbulence Modelling for CFD*'. La Canada, California, USA, DCW Industries Inc.

Wilczak, J. H., Oncley, S.P., Stage, S.A. (2001). '*Sonic anemometer tilt correction algorithm.*' Boundary Layer Meteorology. Vol. 99, pp. 127-150.

Wilson, J. D., Flesch, T.K. (2004). '*An idealized mean wind profile for the atmospheric boundary layer.*' Boundary Layer Meteorology. Vol. 110, pp. 281-299.

WMO (2003). '*www.wmo.ch*', World Meteorological Organisation.

Wood, N. (1995). '*The onset of separation in neutral turbulent flow over hills.*' Boundary Layer Meteorology. Vol. 76, pp. 137-164.

Wood, N. (2000). '*Wind flow over complex terrain: A historical perspective and the prospect for large eddy modelling.*' Boundary Layer Meteorology. Vol. 96, pp. 11-32.

Wright, S. D., Elliott, L., Ingham, D.B., Hewson, M.J.C. (1998). '*The adaption of the atmospheric boundary layer to a change in surface roughness.*' Boundary Layer Meteorology. Vol. 89, pp. 175-195.

Wu, G., Meroney, R.N. (1995). '*Impact of changes in surface roughness on surface layer winds, turbulence and plume dispersion*'. 9th International Conference on Wind Engineering, New Delhi.

Wyngaard, J. C. (1973). '*On surface layer turbulence*'. Workshop on Micrometeorology, American Meteorological Society.

Xian, X., Tao, W., Qingwei, S., Weimin, Z. (2002). '*Field and wind-tunnel studies of aerodynamic roughness length.*' Boundary Layer Meteorology. Vol. 104, pp. 151-163.

Xu, D., Taylor, P.A. (1997). '*On turbulence closure constants for atmospheric boundary layer modelling: Neutral stratification.*' Boundary Layer Meteorology. Vol. 84, pp. 267-287.

Yakhot, V., Orzag, S.A. (1986). '*Renormalisation Group analysis of turbulence: Basic theory*' Journal of Science and Computing Vol 1, pp 3-51

Yamaguchi, A., Ishihara, T., Fujino, Y (2003). '*Experimental study of the wind flow in a coastal region of Japan.*' Journal of Wind Engineering and Industrial Aerodynamics. Vol. 91, pp. 247-264.

Zeman, O., Jensen, N.O. (1987). '*Modification of turbulence characteristics in flow over hills.*' Quarterly Journal of the Royal Meteorological Society. Vol. 113, pp. 55-80.

Zervos, A. (2003). '*Developing wind energy to meet Kyoto targets in the European Union.*' Wind Energy. Vol. 6, pp. 309-319.

Zhang, C. X. (1994). '*Numerical predictions of turbulent recirculating flows with a k-ε model.*' Journal of Wind Engineering and Industrial Aerodynamics. Vol. 51(2), pp. 177-201.

Zienkiewicz, O. C., Taylor, R.L. (1989). '*The Finite Element Method*'. New York, McGraw-Hill.

Zilitinkevich, S., Baklanov, A. (2002). '*Calculation of the height of the stable boundary layer in practical applications.*' Boundary Layer Meteorology. Vol. 105, pp. 389-409.

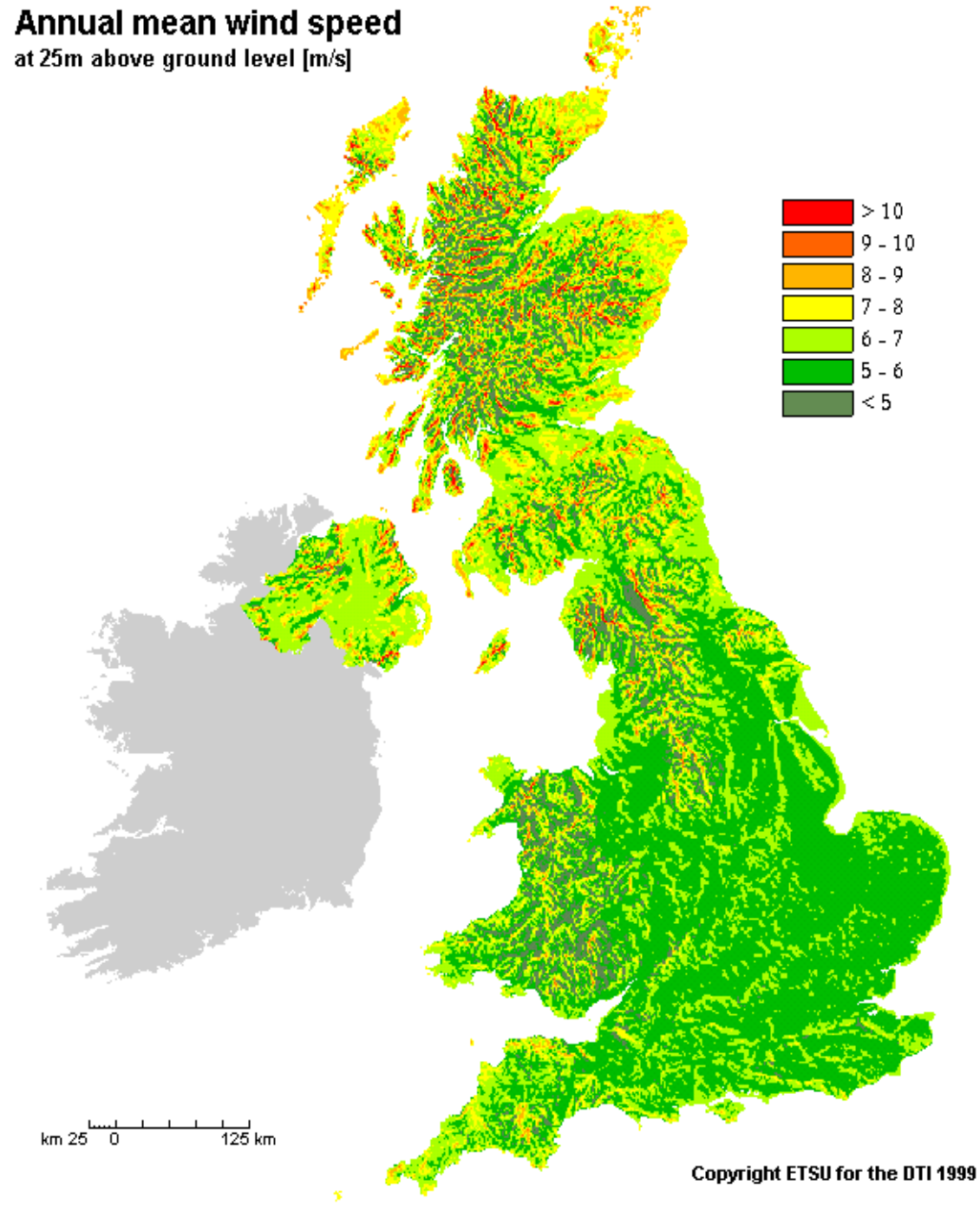

Figure 1.1 – Average wind speeds across the UK

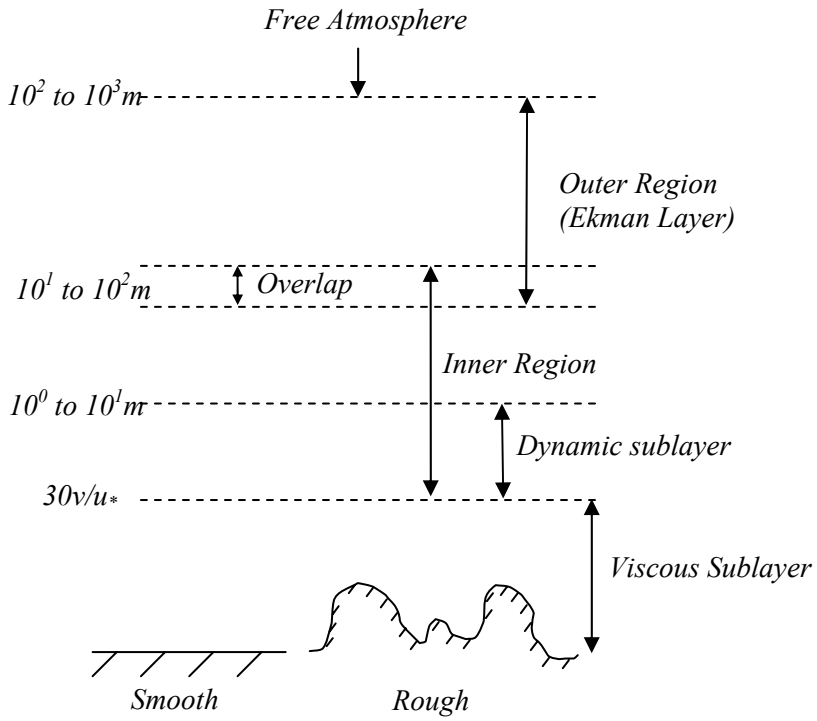

Figure 2.1 – Structure of the Atmospheric Boundary Layer
From Brutsaert (1982)

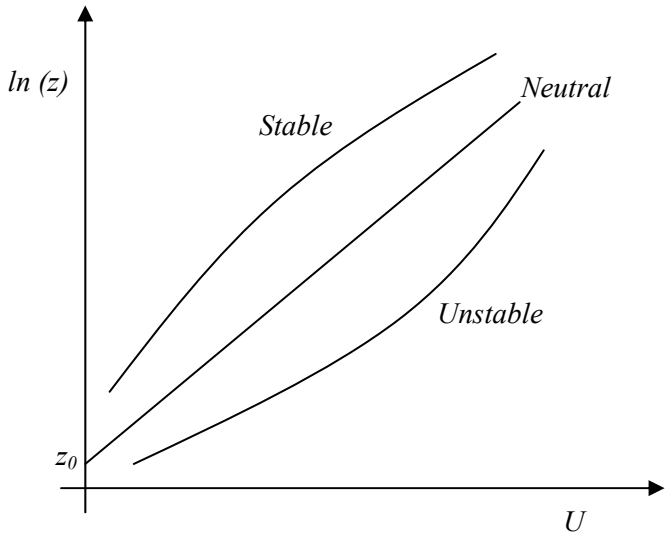

Figure 2.2 – Wind profile variation with stability

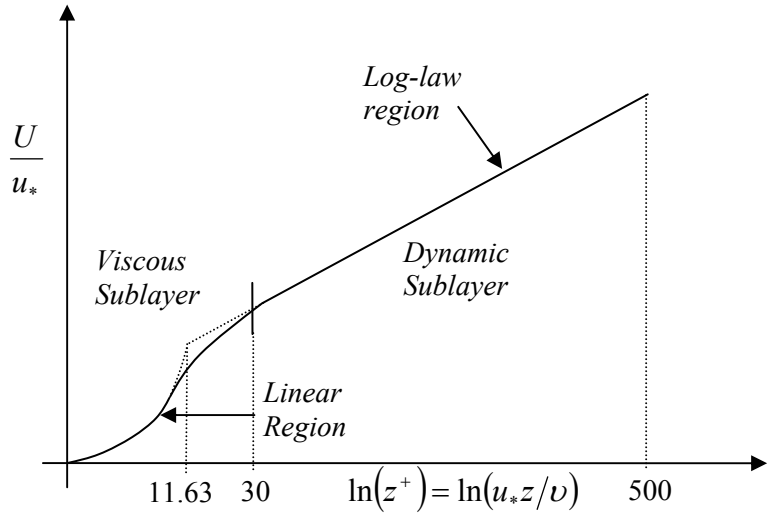

Figure 2.3 – Mean velocity profile in lower region of the ABL

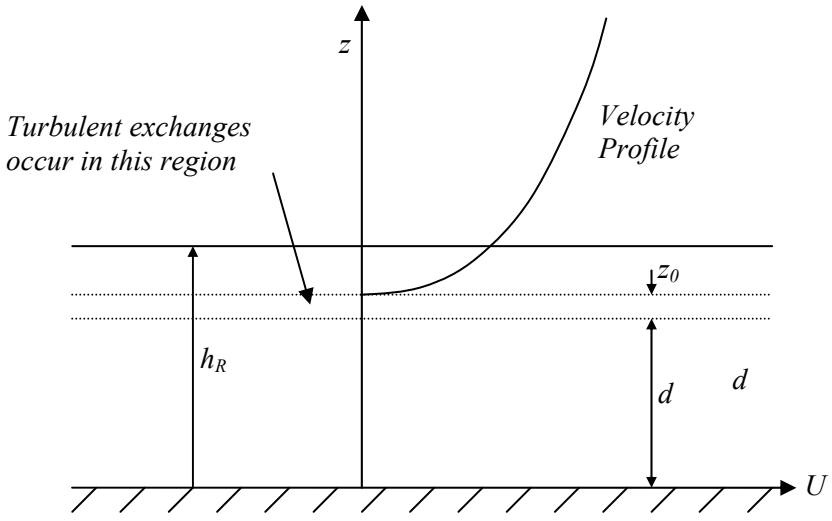

Figure 2.4 – Surface configuration close to the wall

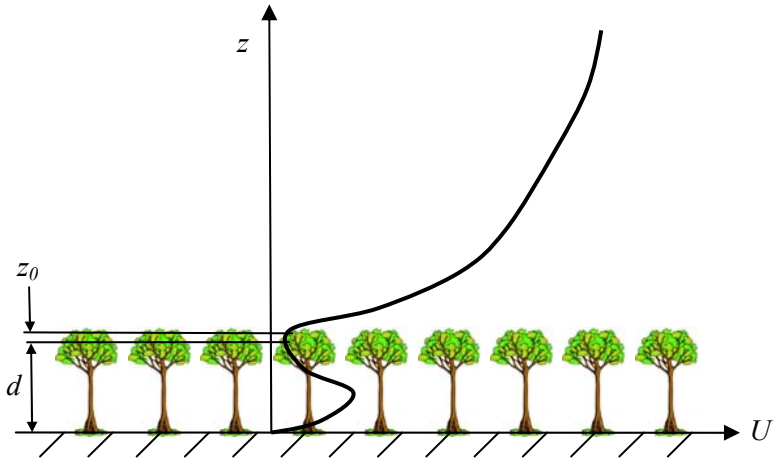

Figure 2.5 – Flow over a forest canopy

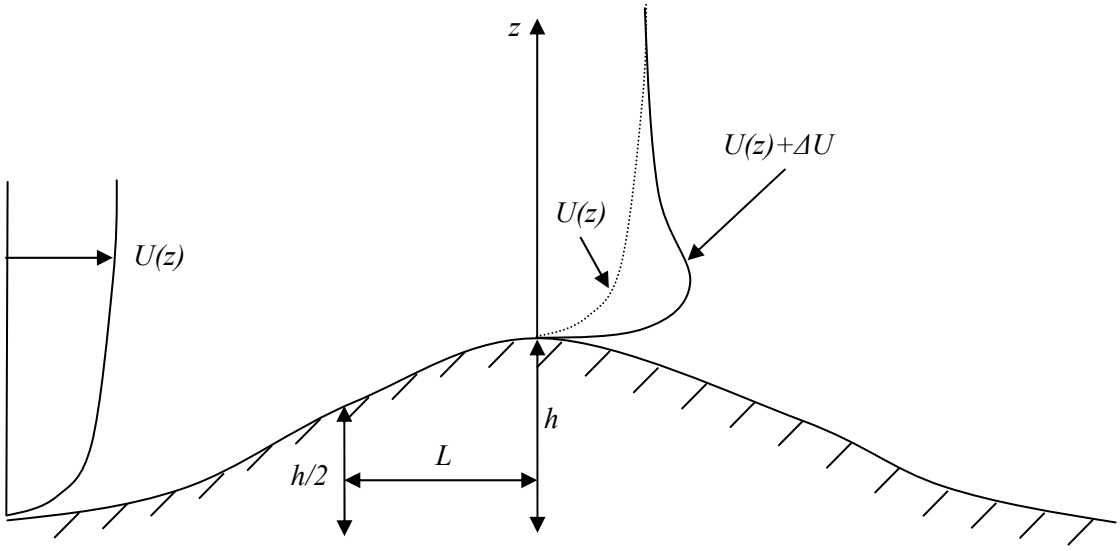

Figure 2.6 – Development of wind profile over a hill

Figure 2.7 – Typical cup anemometer combined with wind vane (Copyright – University of Virginia, Department of Environmental Science, 2003)

Figure 2.8 – Typical sonic anemometer (Copyright – The University of Colorado, National Centre for Atmospheric Research, 2003)

Figure 2.9 – Typical gill UVW anemometer
(Copyright – Novalynx Corporation)

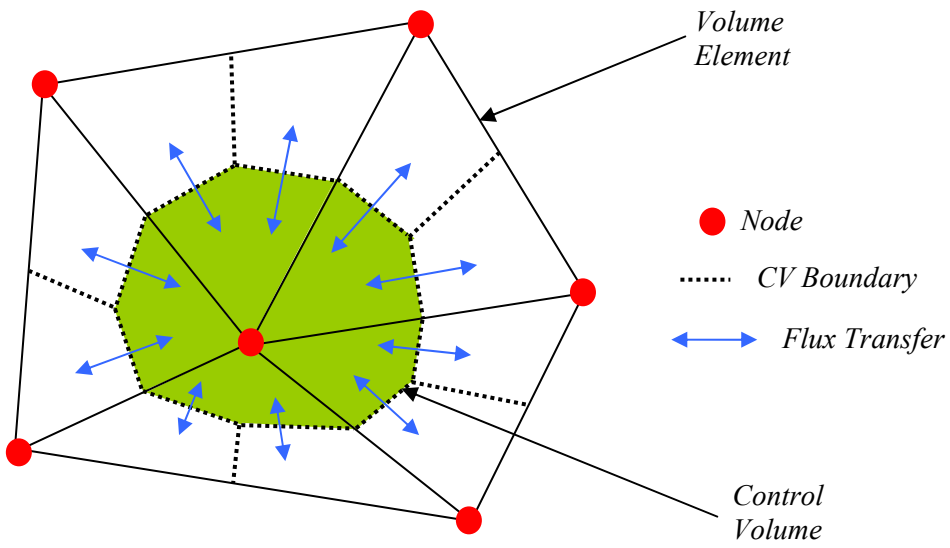

Figure 3.1 – Control volume showing node at centre and integration points on surfaces

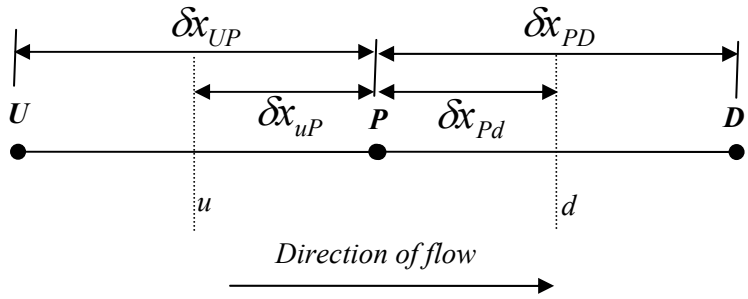

Figure 3.2 – 2D view of central, upwind and downwind nodes and faces

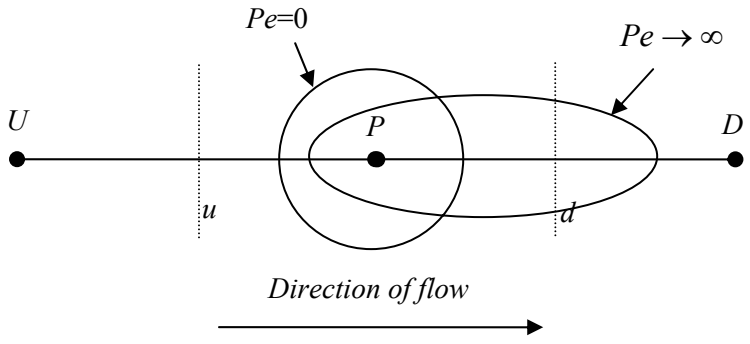

Figure 3.3 – Diffusion of a source for different Peclet numbers

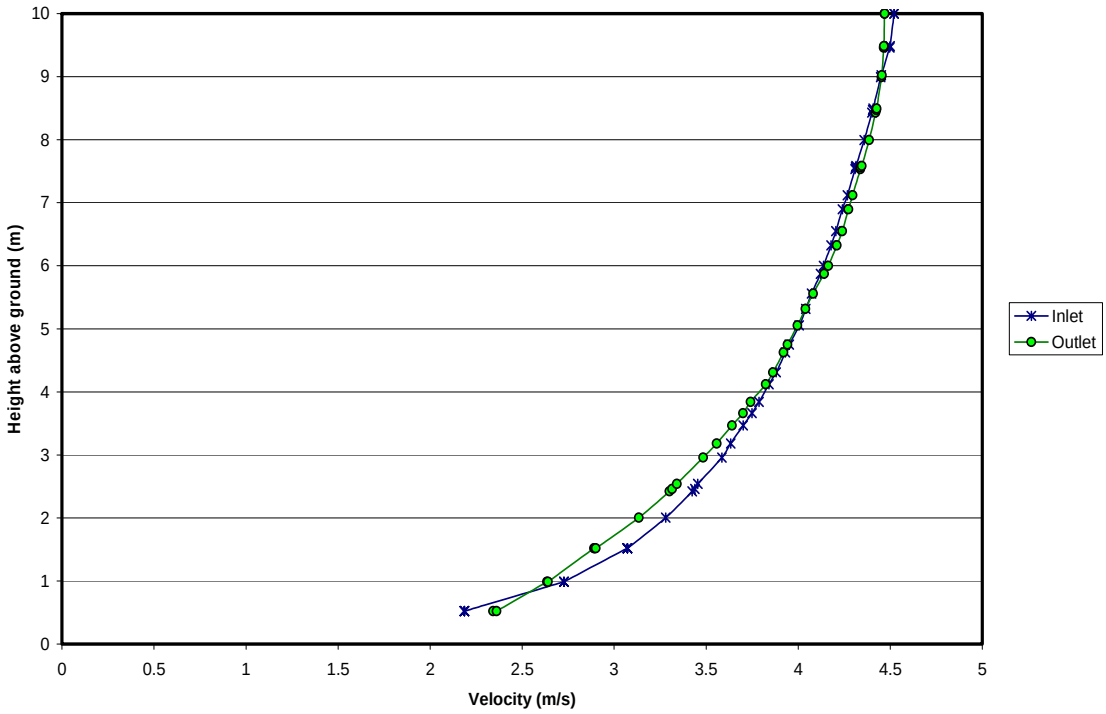

Figure 4.1 – Comparison of inlet and outlet profiles for flow over a flat grassy terrain

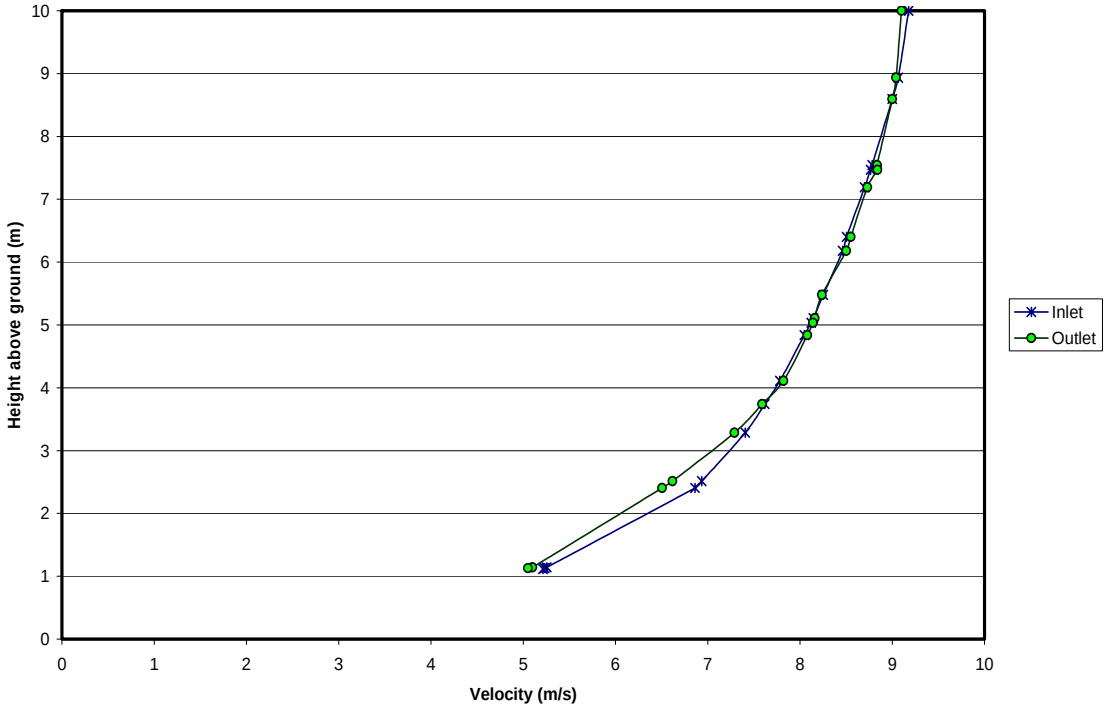

Figure 4.2 - Comparison of inlet and outlet profiles for flow over a flat forest terrain

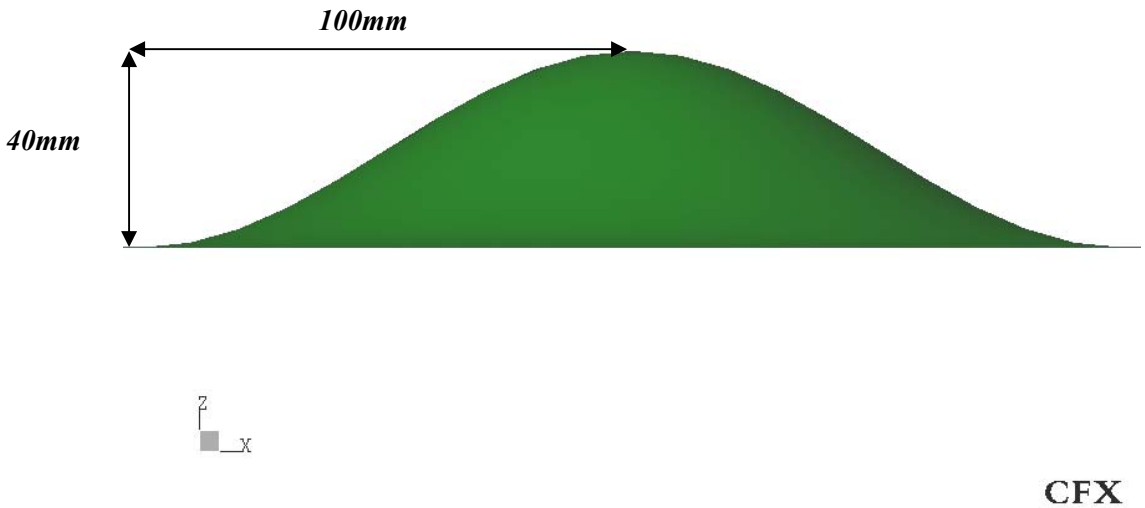

Figure 4.3 – Side view of 3D hill shape

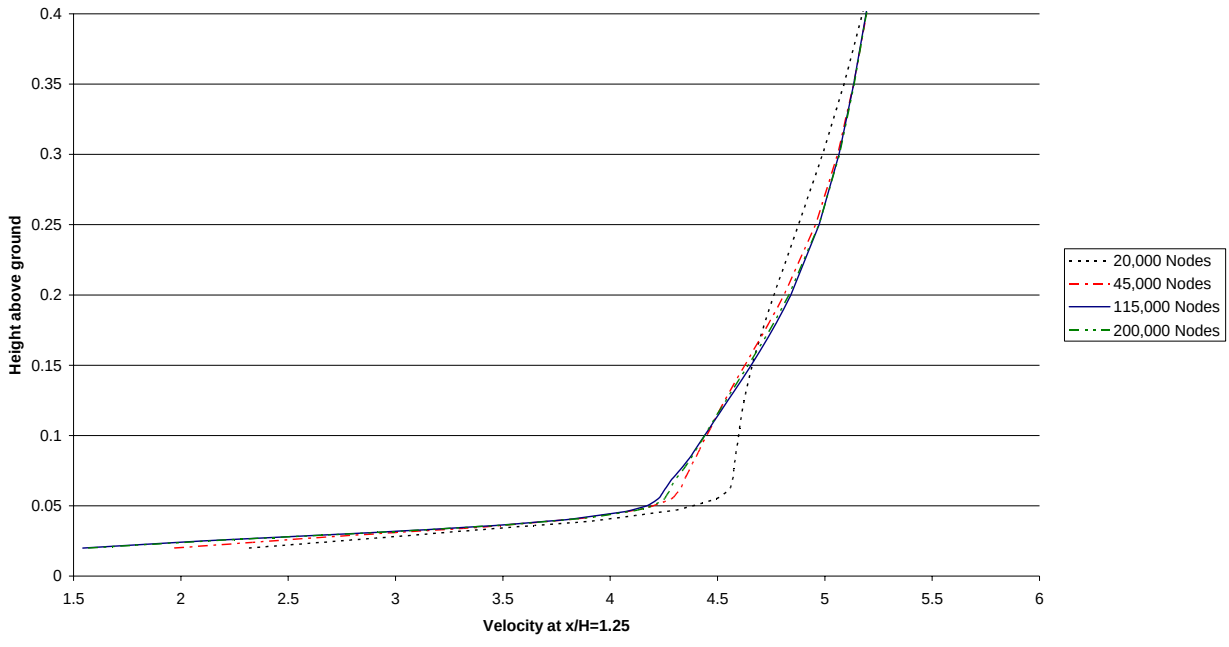

Figure 4.4 – Velocity profile comparison for different grids – 3D Hill

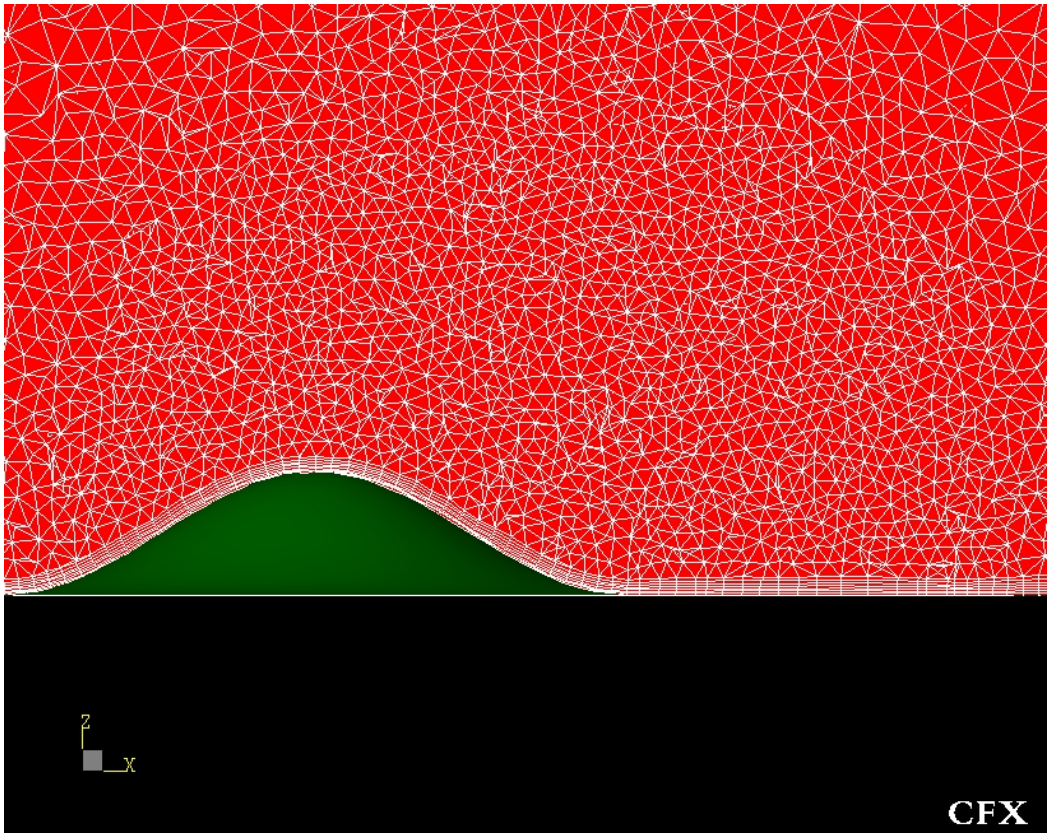

Figure 4.5 – Cross section of the mesh elements over the hill surface

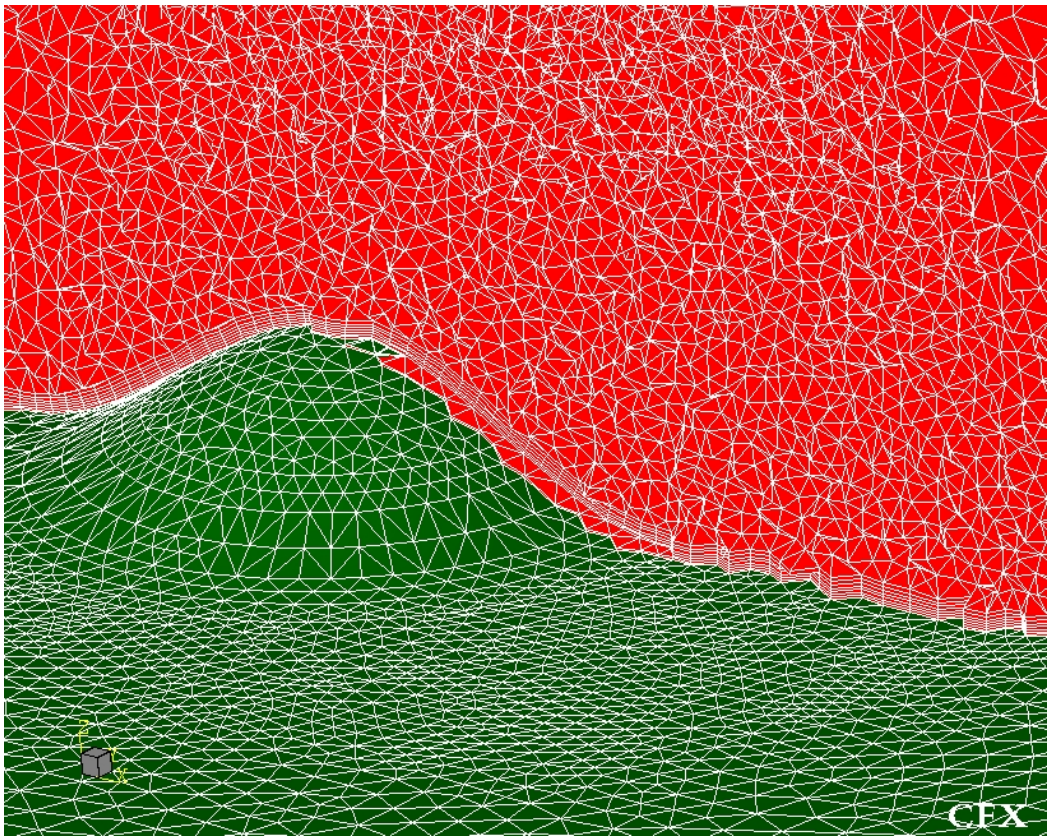

Figure 4.6- View of surface mesh and cross section mesh

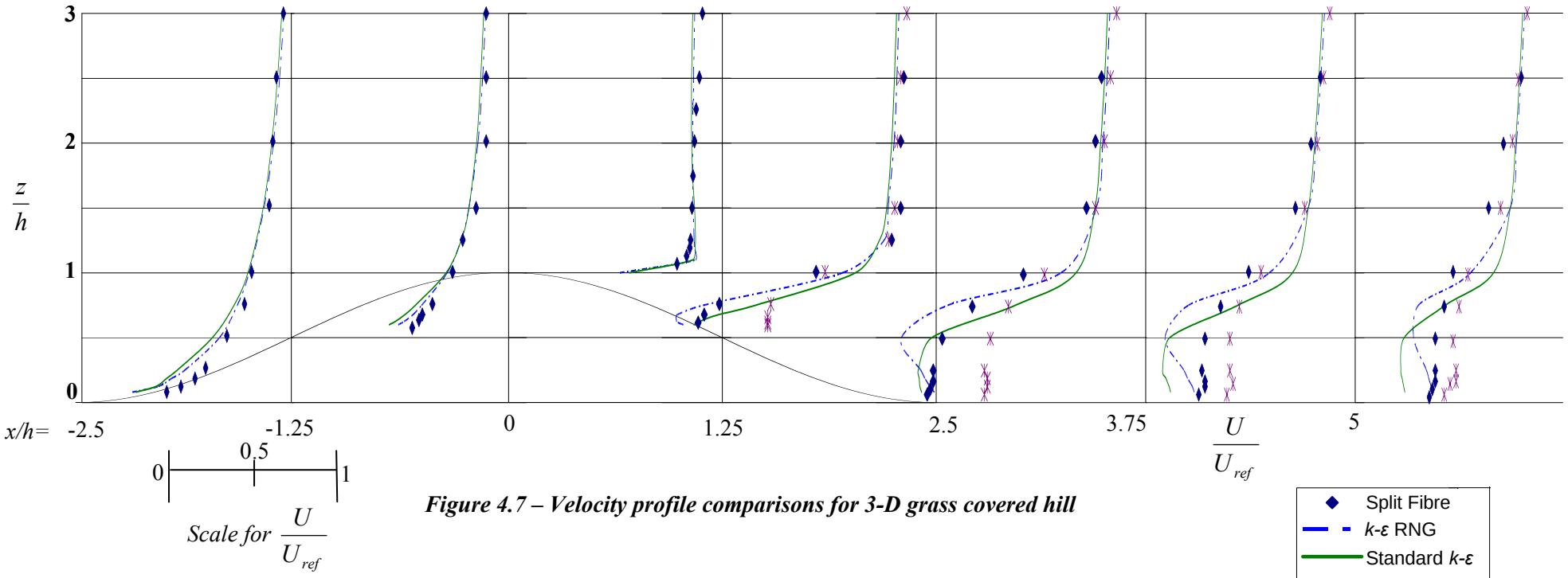

Figure 4.7 – Velocity profile comparisons for 3-D grass covered hill

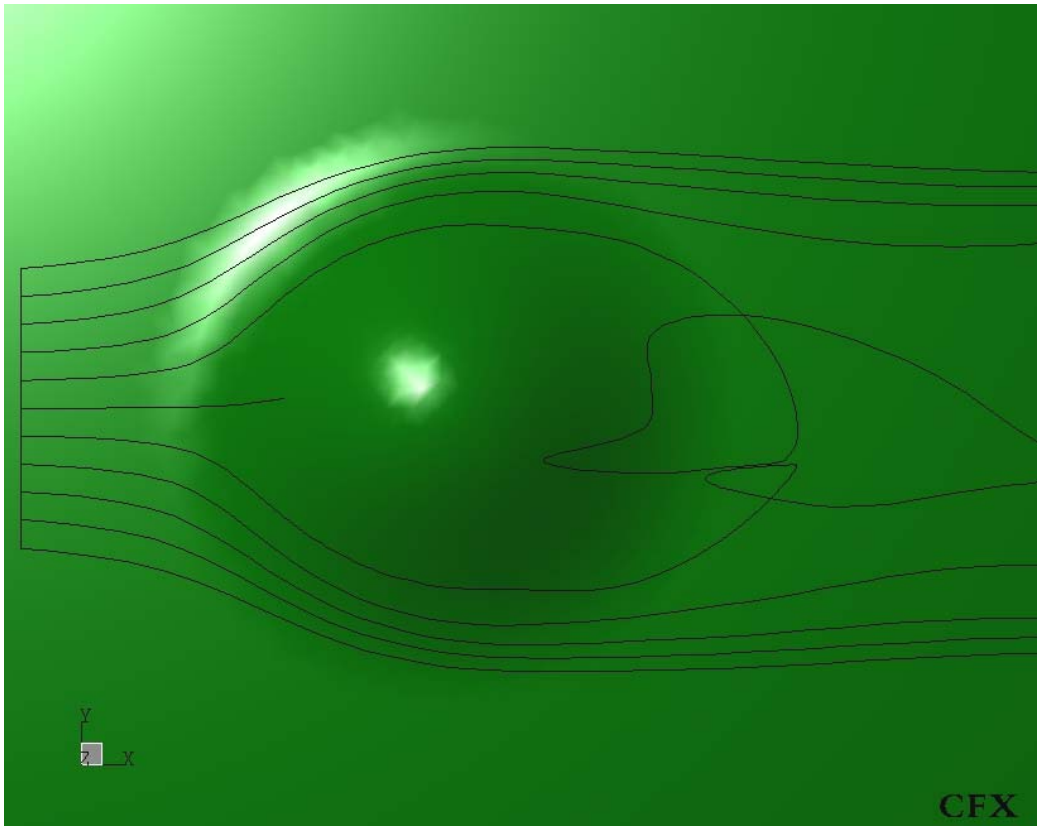

Figure 4.8a – Plan view of streamlines over grass covered hill

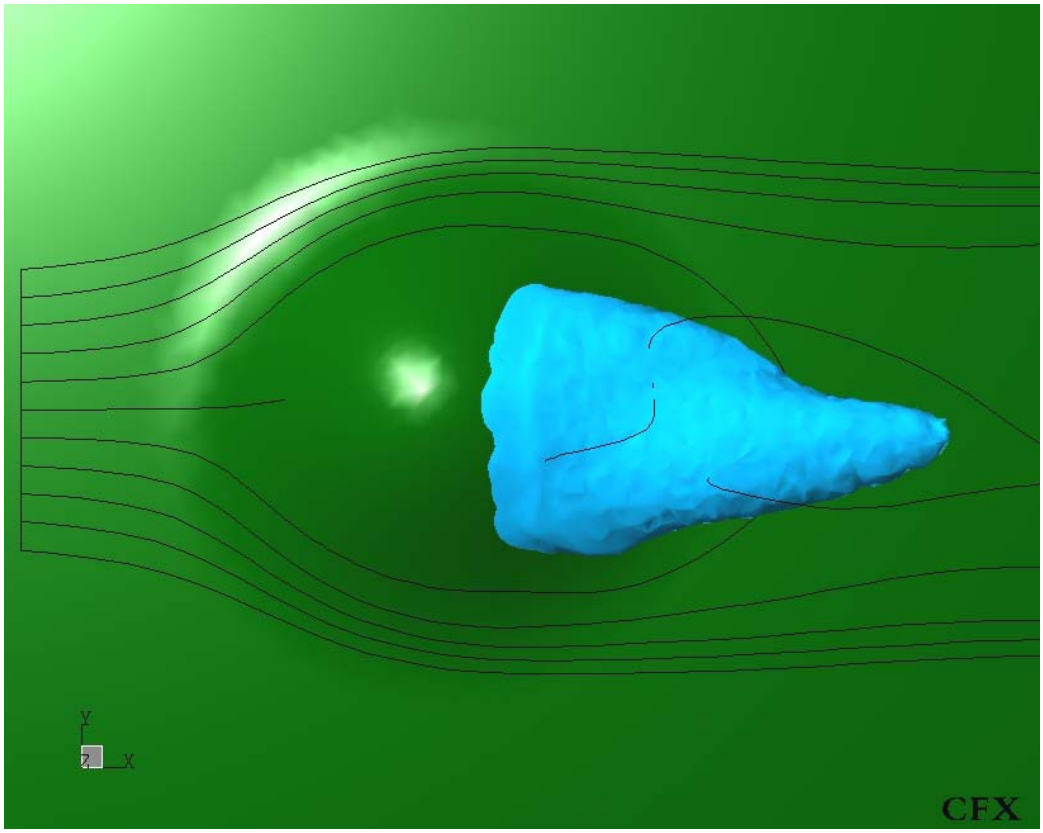

Figure 4.8b – Plan view of recirculation and streamlines over grass hill

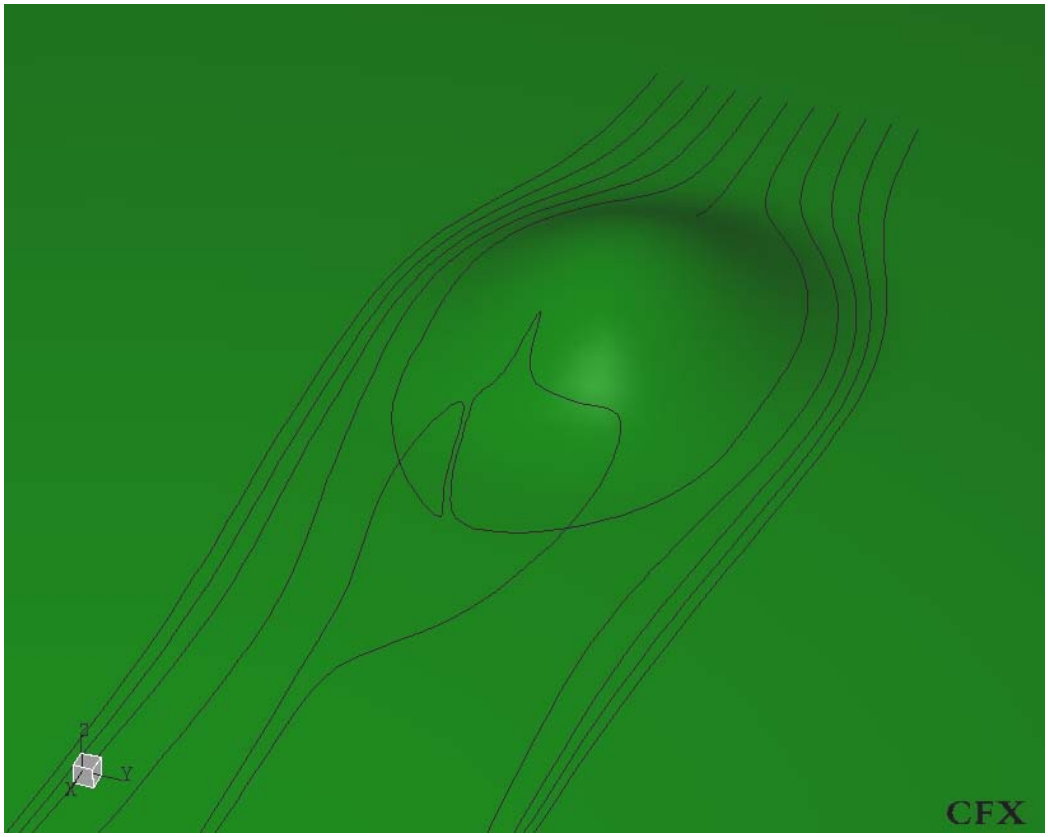

Figure 4.9a – View of streamlines over grass covered hill

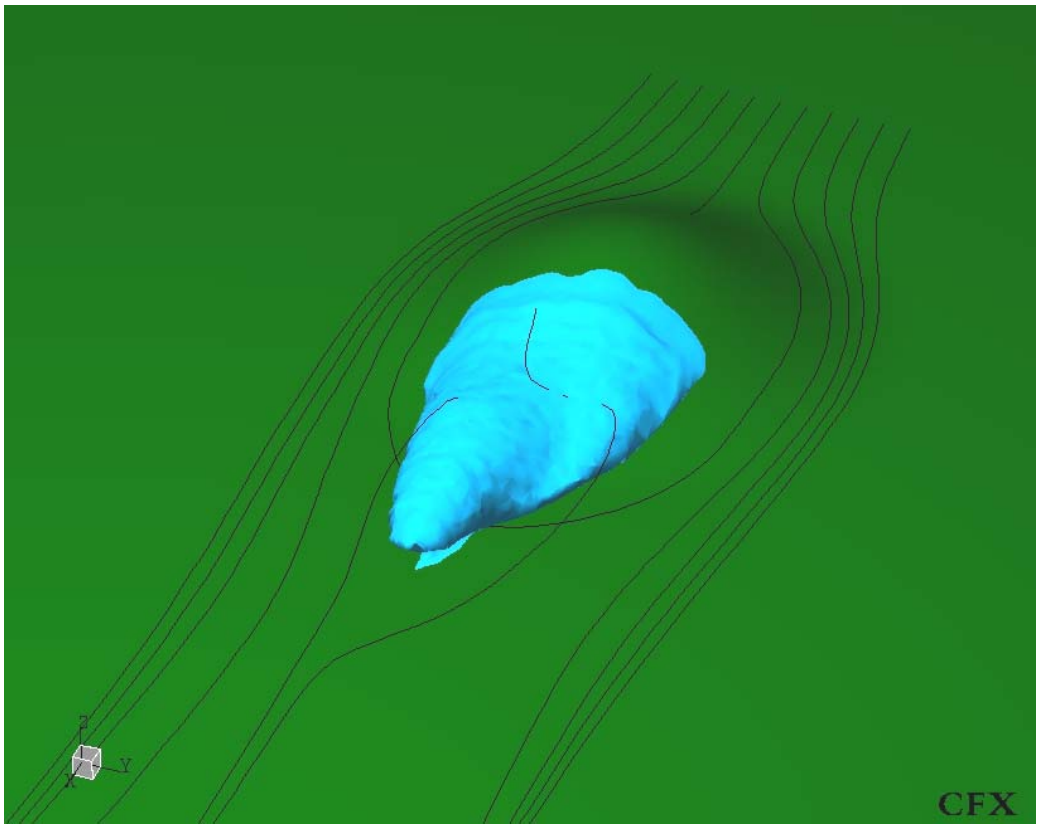

Figure 4.9b – Streamlines and recirculation over grass hill

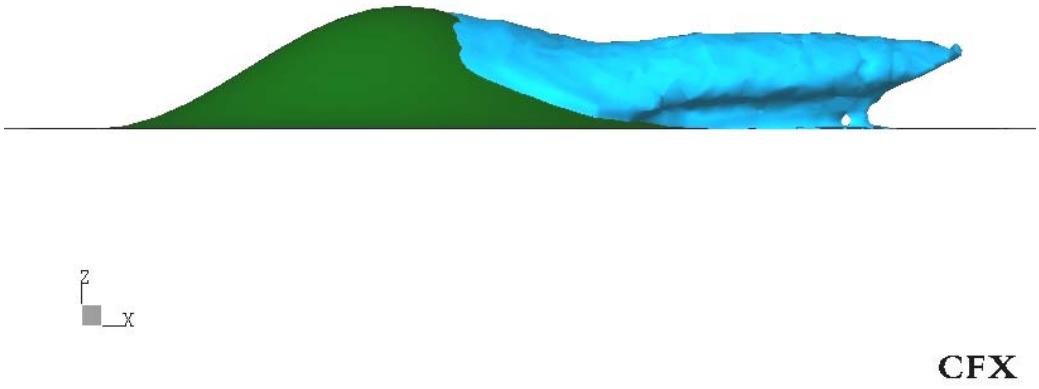

Figure 4.10 – Side view of grass hill with recirculation region

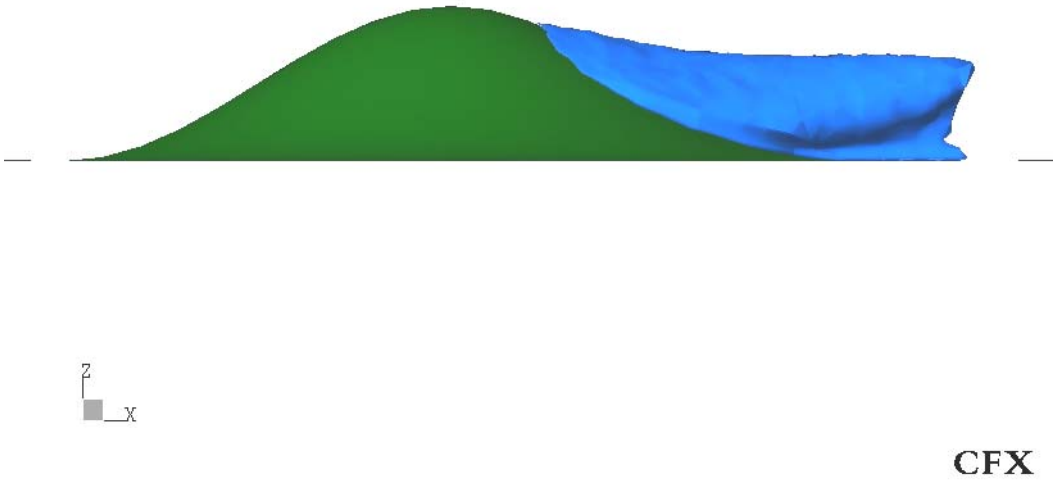

Figure 4.11 – Side view of forest hill with recirculation region

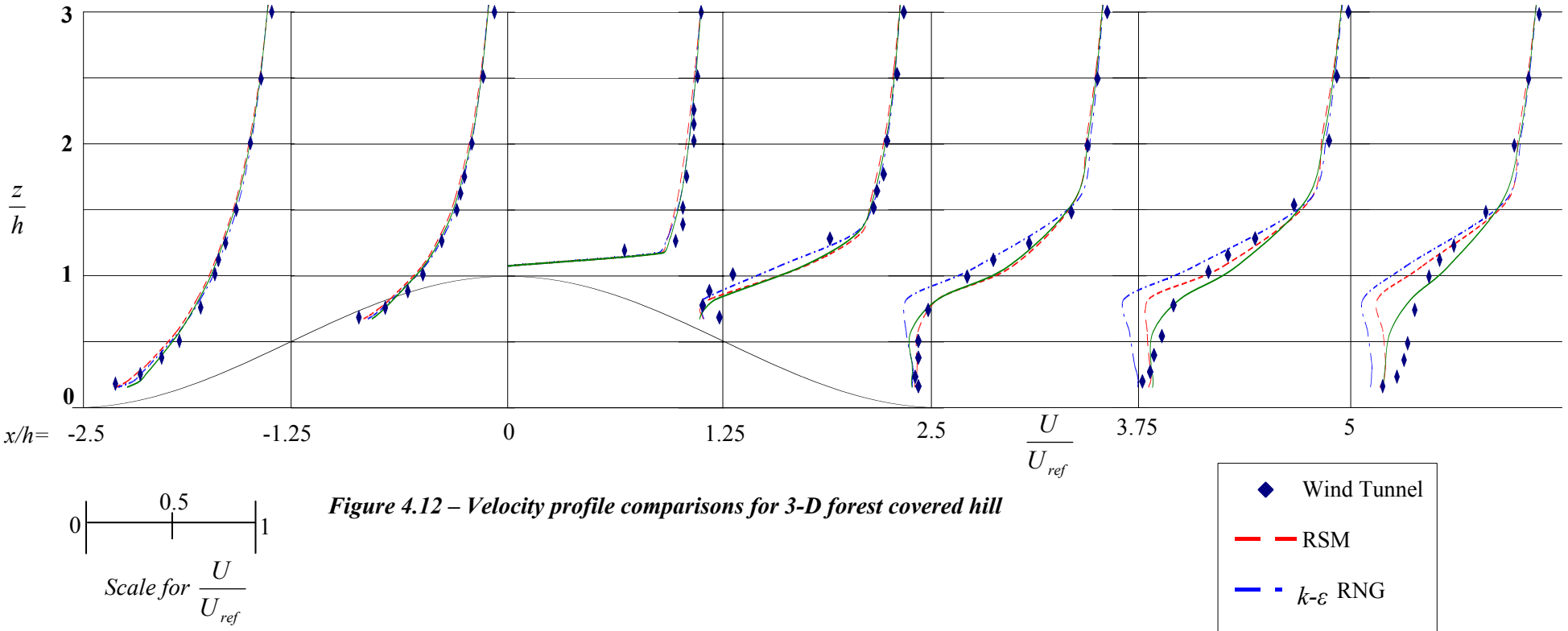

Figure 4.12 – Velocity profile comparisons for 3-D forest covered hill

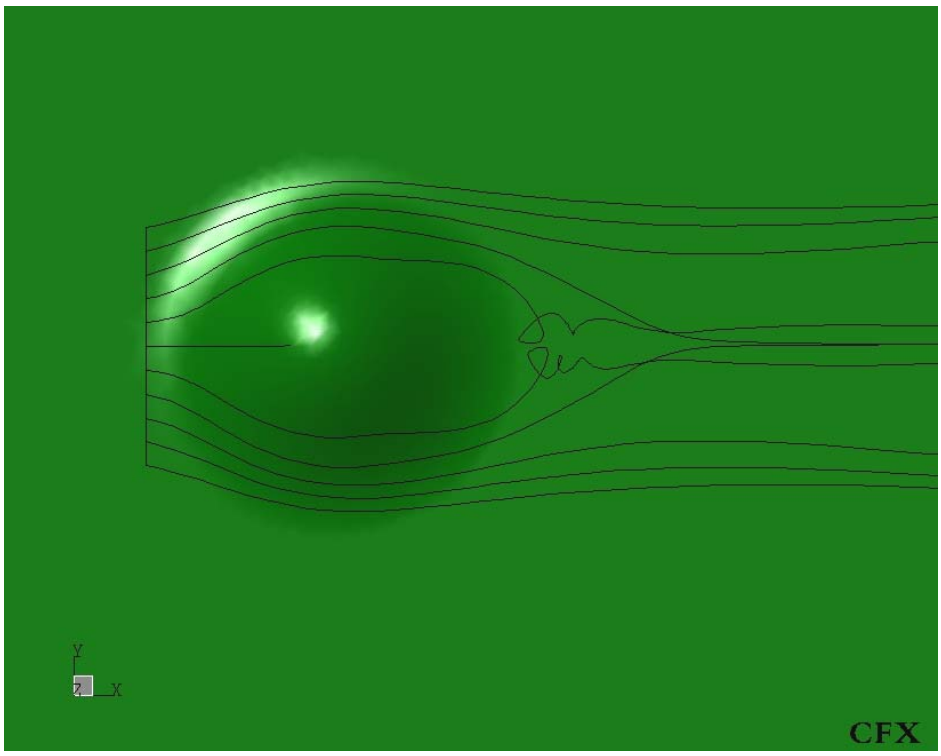

Figure 4.13a – Plan view of streamlines over forest hill

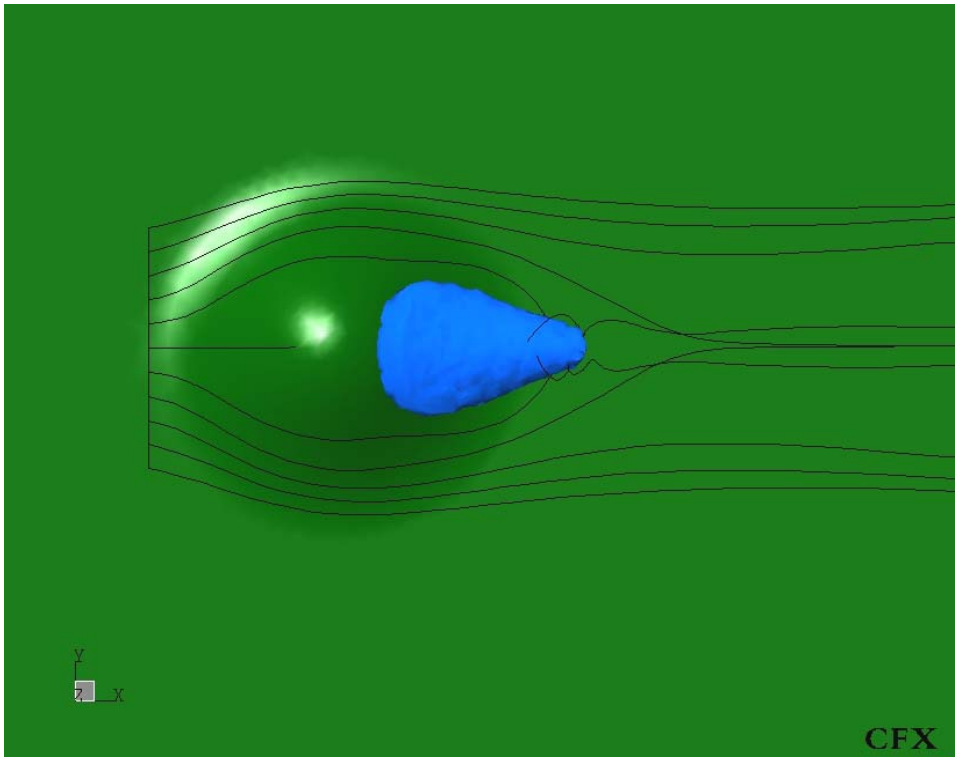

Figure 4.13b – Streamlines and recirculation over forest hill

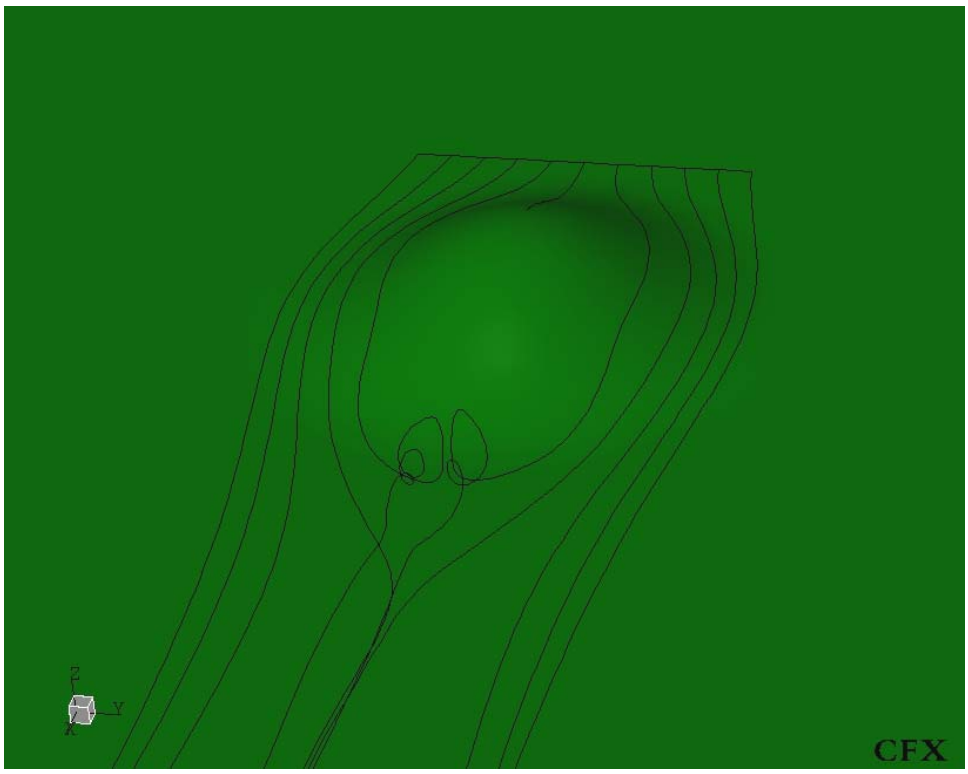

Figure 4.14a – View of streamlines over forest hill

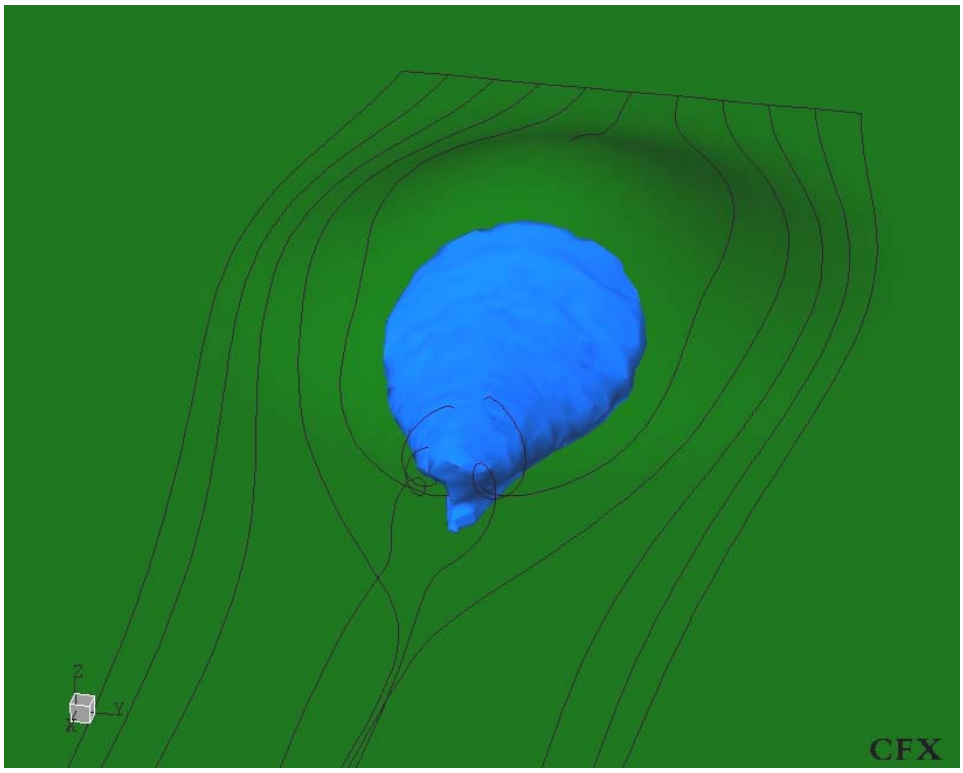

Figure 4.14b – Streamlines and recirculation over forest hill

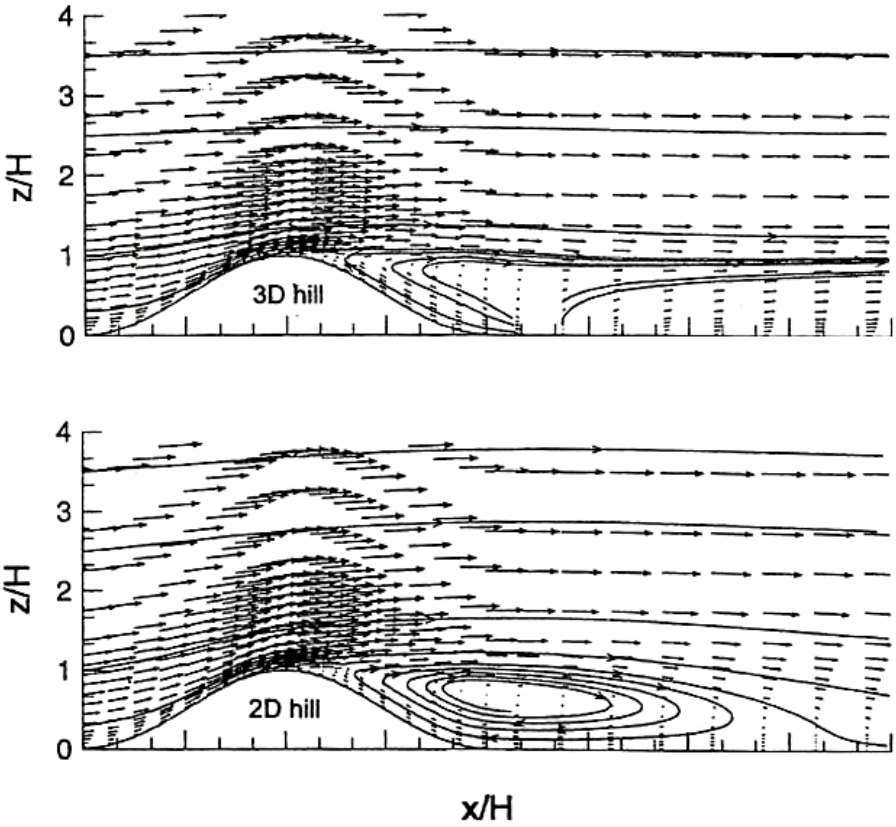

Figure 4.15 – Streamlines for 2D and 3D hills
From Ishihara and Hibi (2002)

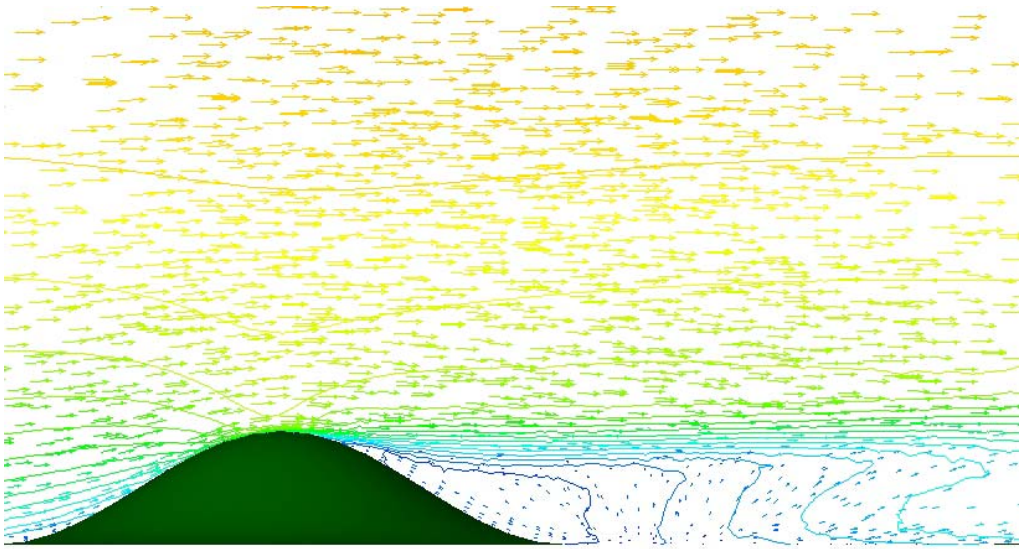

Figure 4.16 – Velocity contours and vectors over forest hill surface

Fig 5.1 Map of the UK showing location of Askervein
Image produced from the Ordnance Survey Get-a-map service. Image reproduced with kind permission of Ordnance Survey and Ordnance Survey of Northern Ireland.

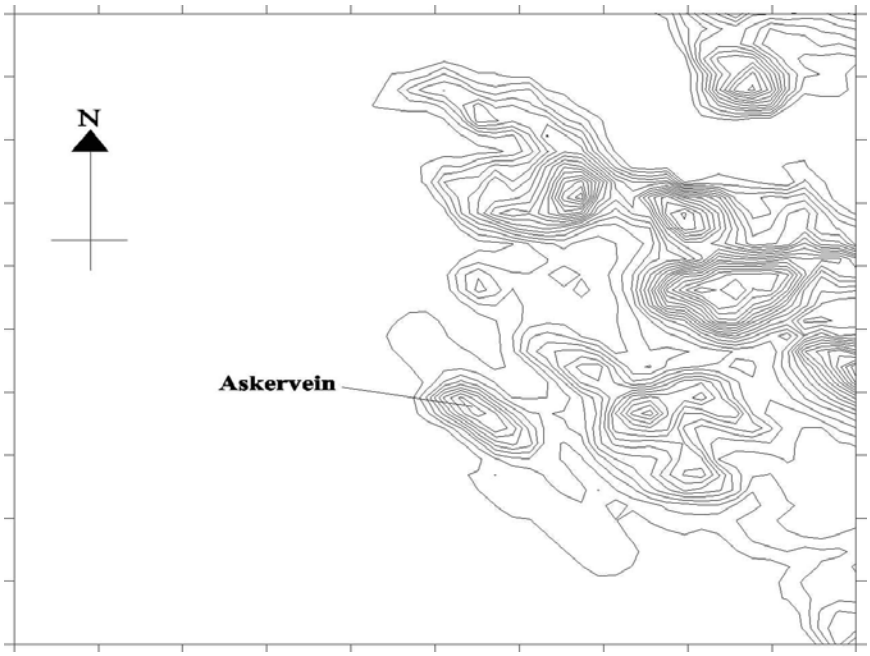

Fig 5.2 – Contour plot of Askervein and surrounding hills

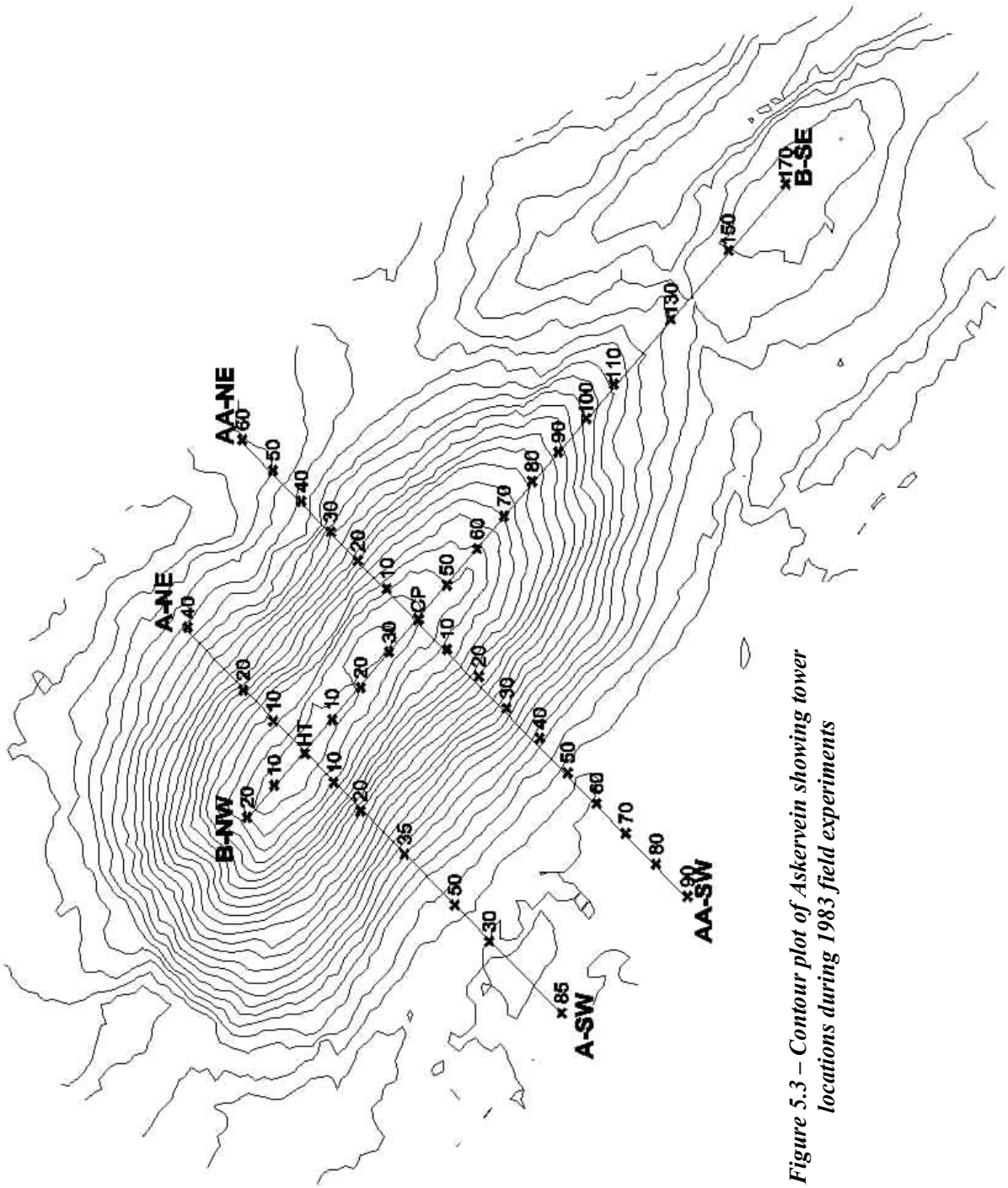

Figure 5.3 – Contour plot of Askervein showing tower locations during 1983 field experiments

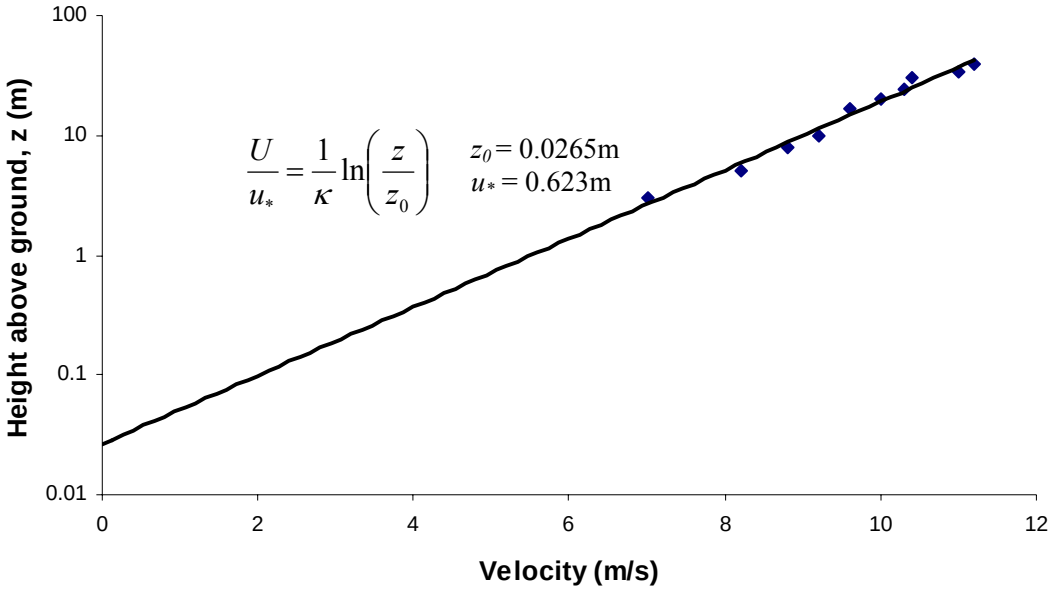

Figure 5.4 – Logarithmic velocity profile at RS for run MF01-D

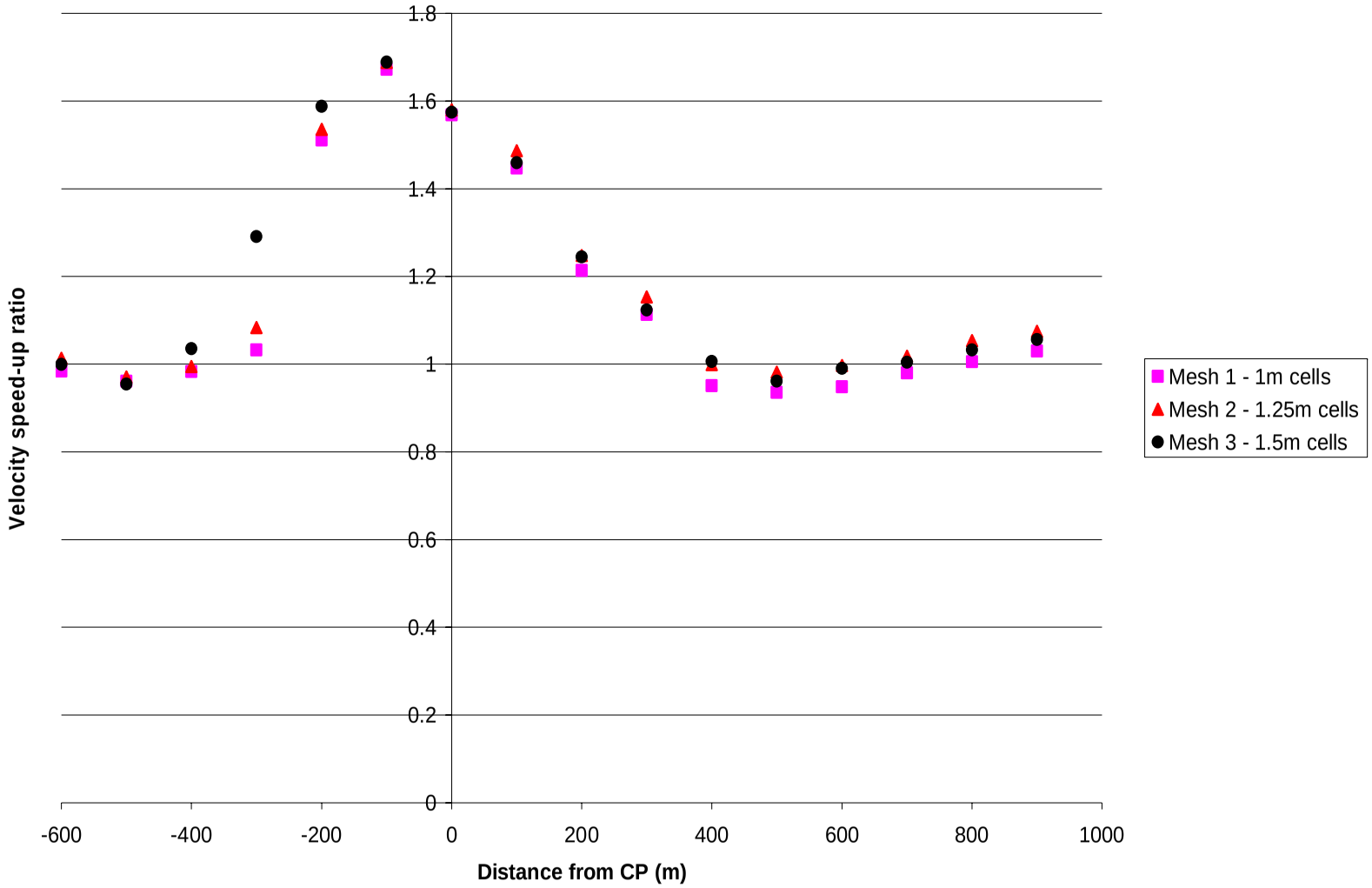

Figure 5.5a – Velocity speed-up ratios for each mesh type for 10m heights along tower line AA

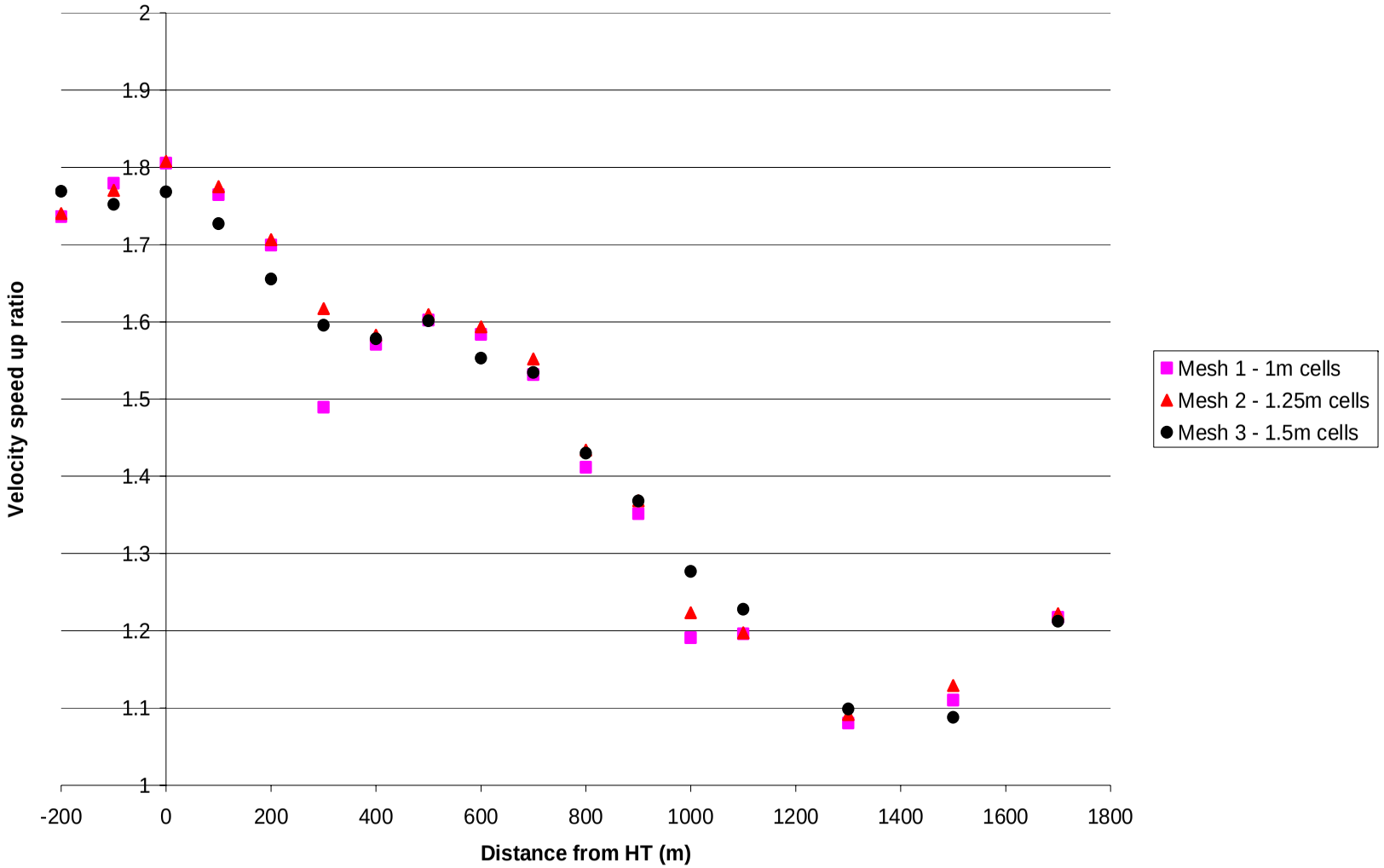

Figure 5.5b – Velocity speed-up ratios for each mesh type for 10m heights along tower line B

WIND ROSE FOR BENBECULAR
N.G.R: 0782E 8555N ALTITUDE: 6 metres a.m.s.l.

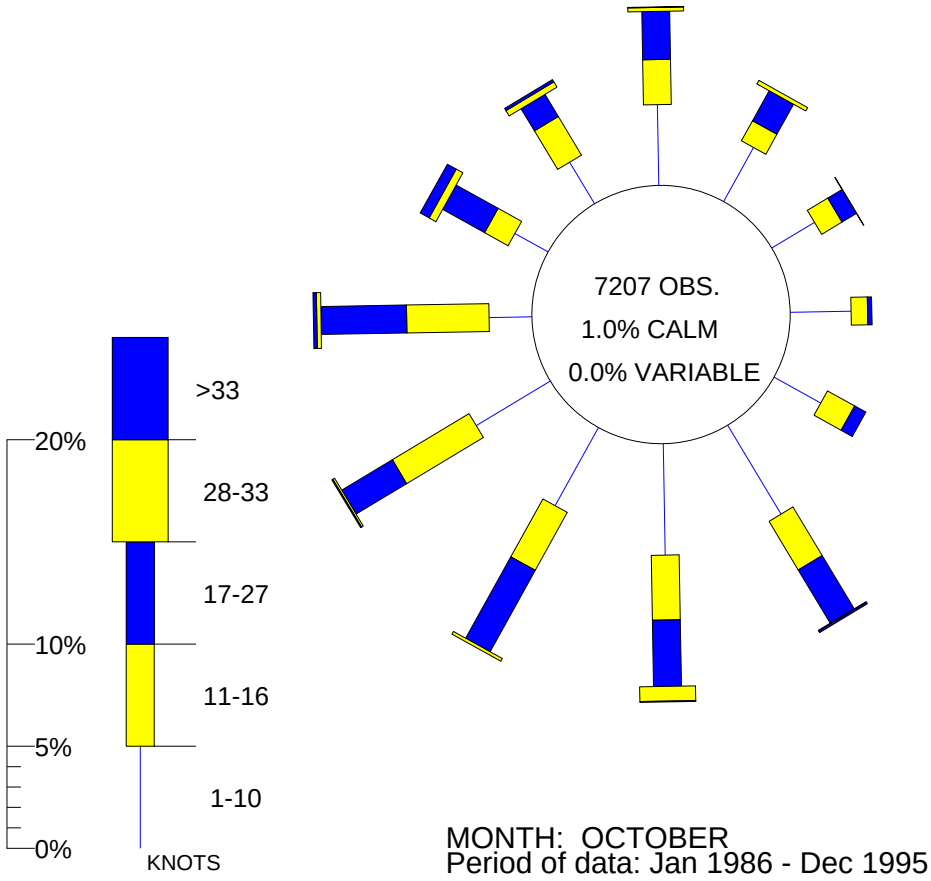

Figure 5.6 – The wind rose for Benbecula in October
Reproduced with kind permission from the Met. Office

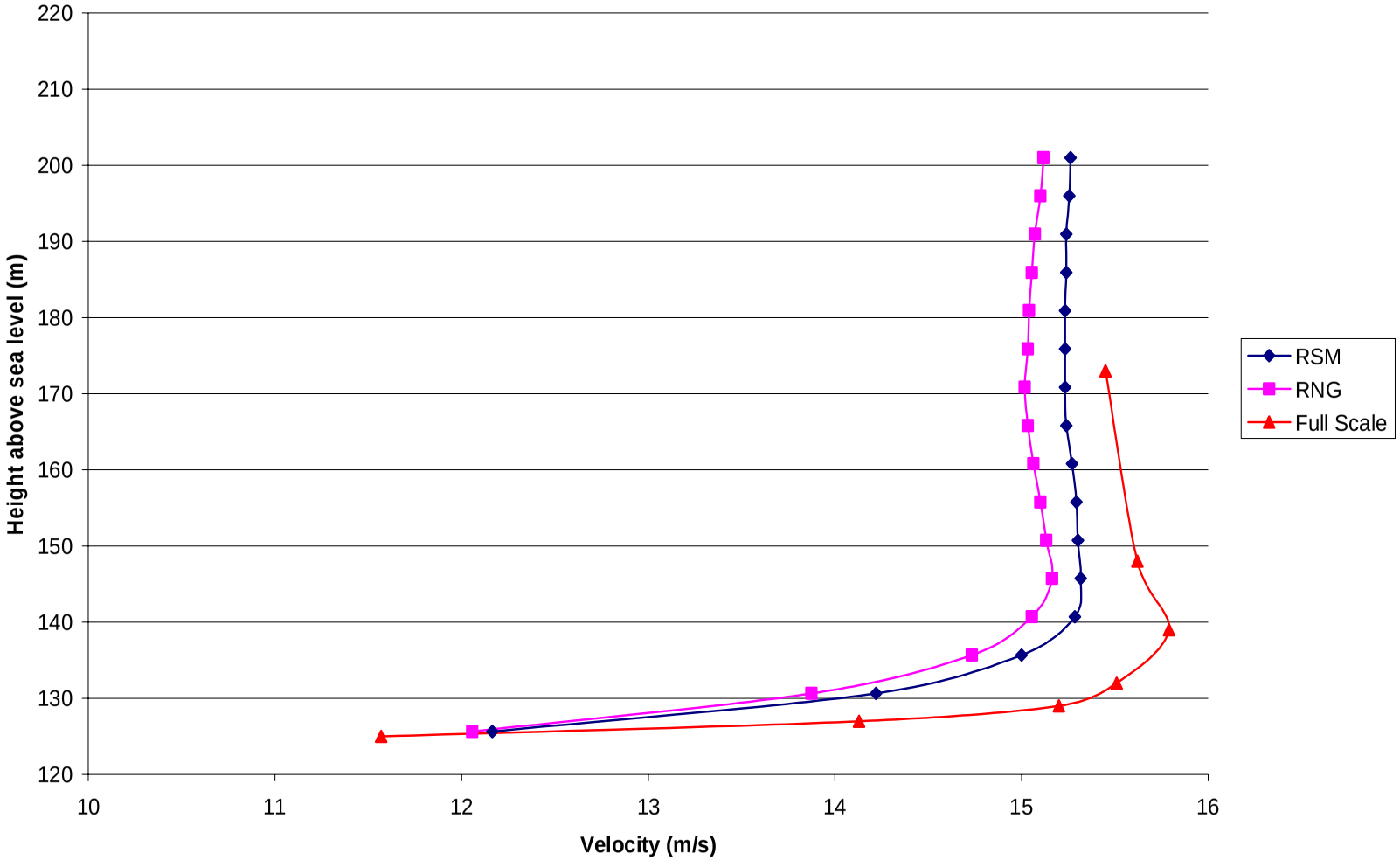

Figure 5.7a– Vertical profile of velocity at the hilltop (HT) for wind direction 180°

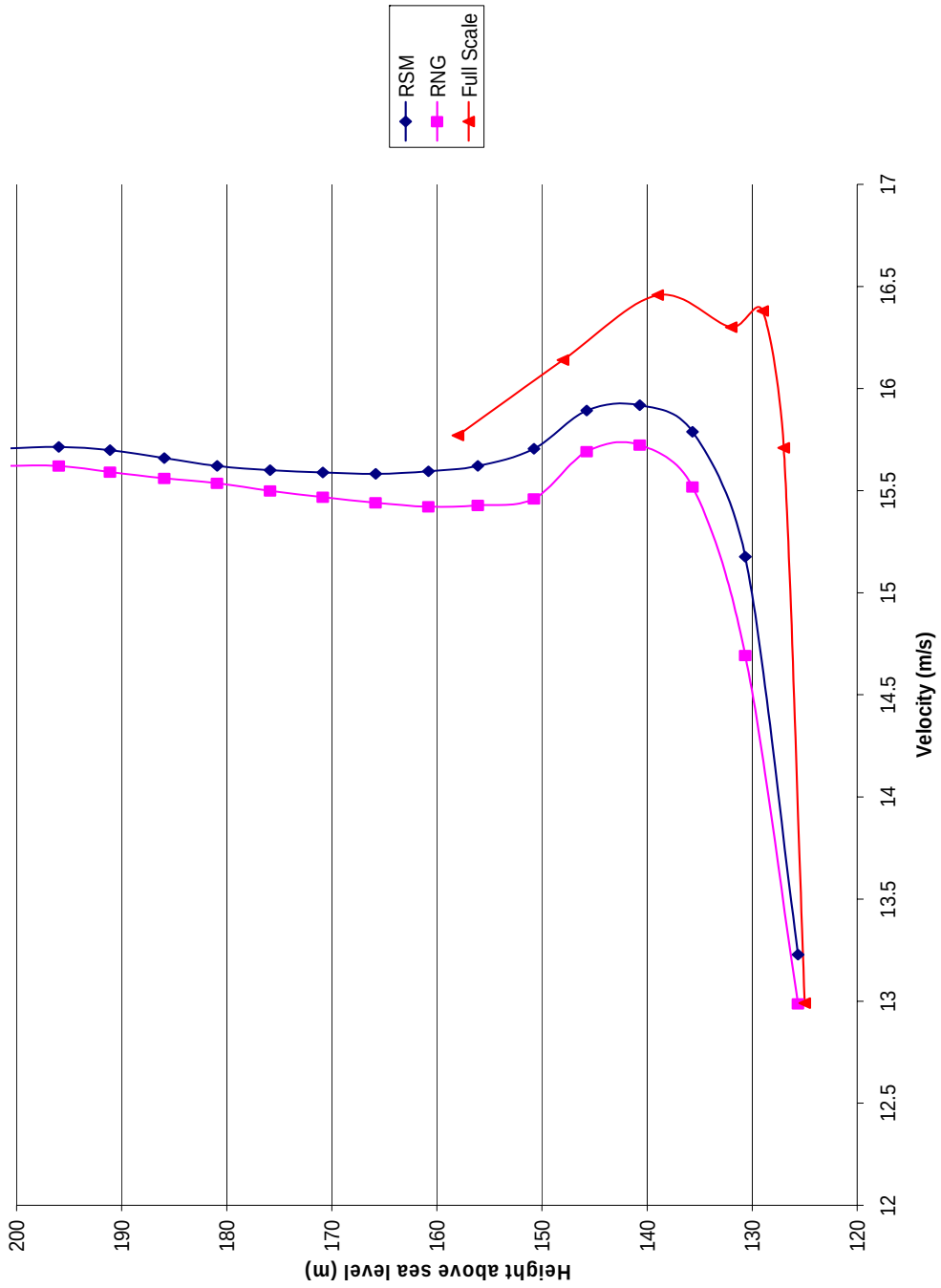

Figure 5.7b– Vertical profile of velocity at the hilltop (HT) for wind direction 210°

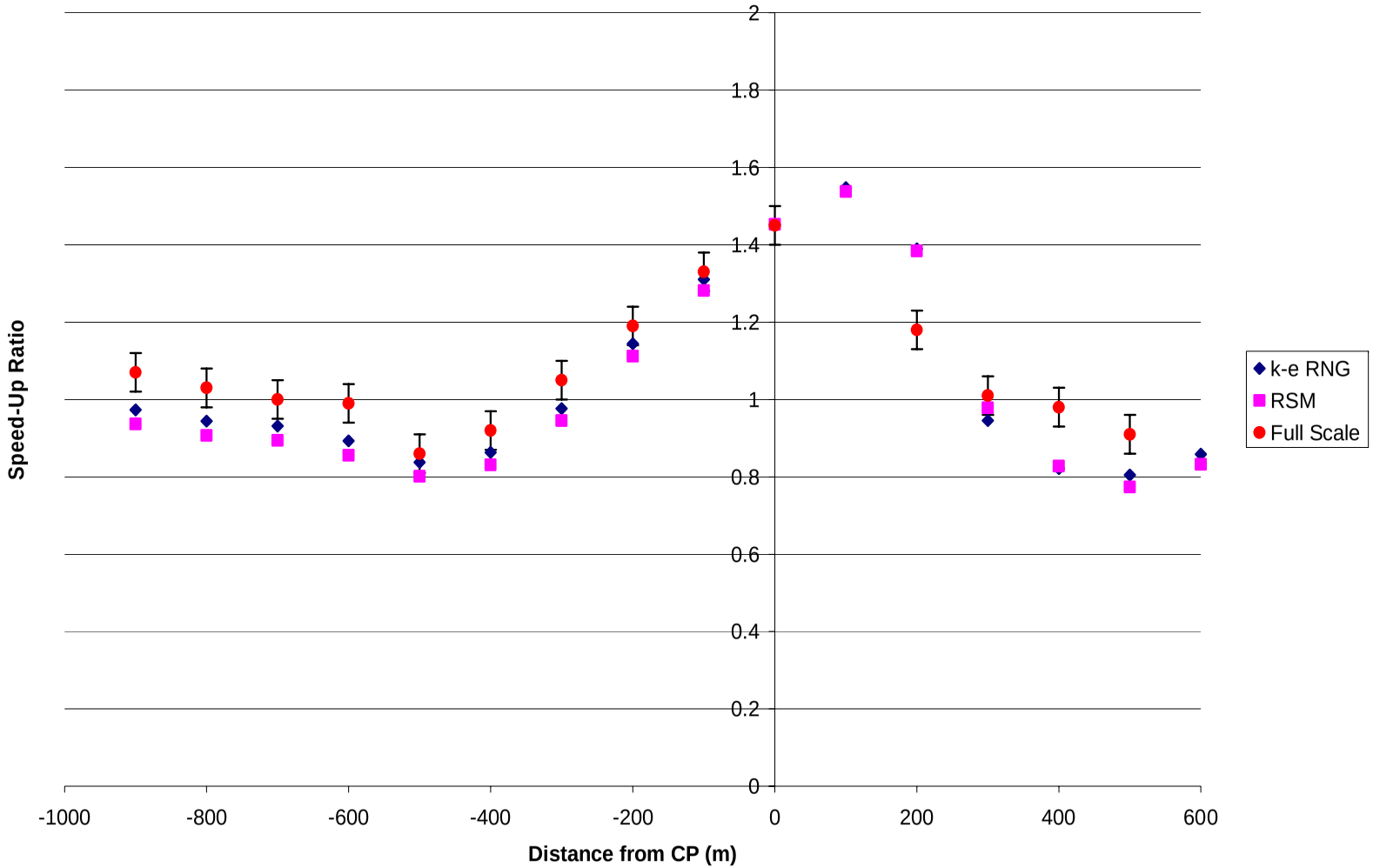

Figure 5.8a– Measurements of velocity speed up ratio at 10m along tower line AA for wind direction 180°

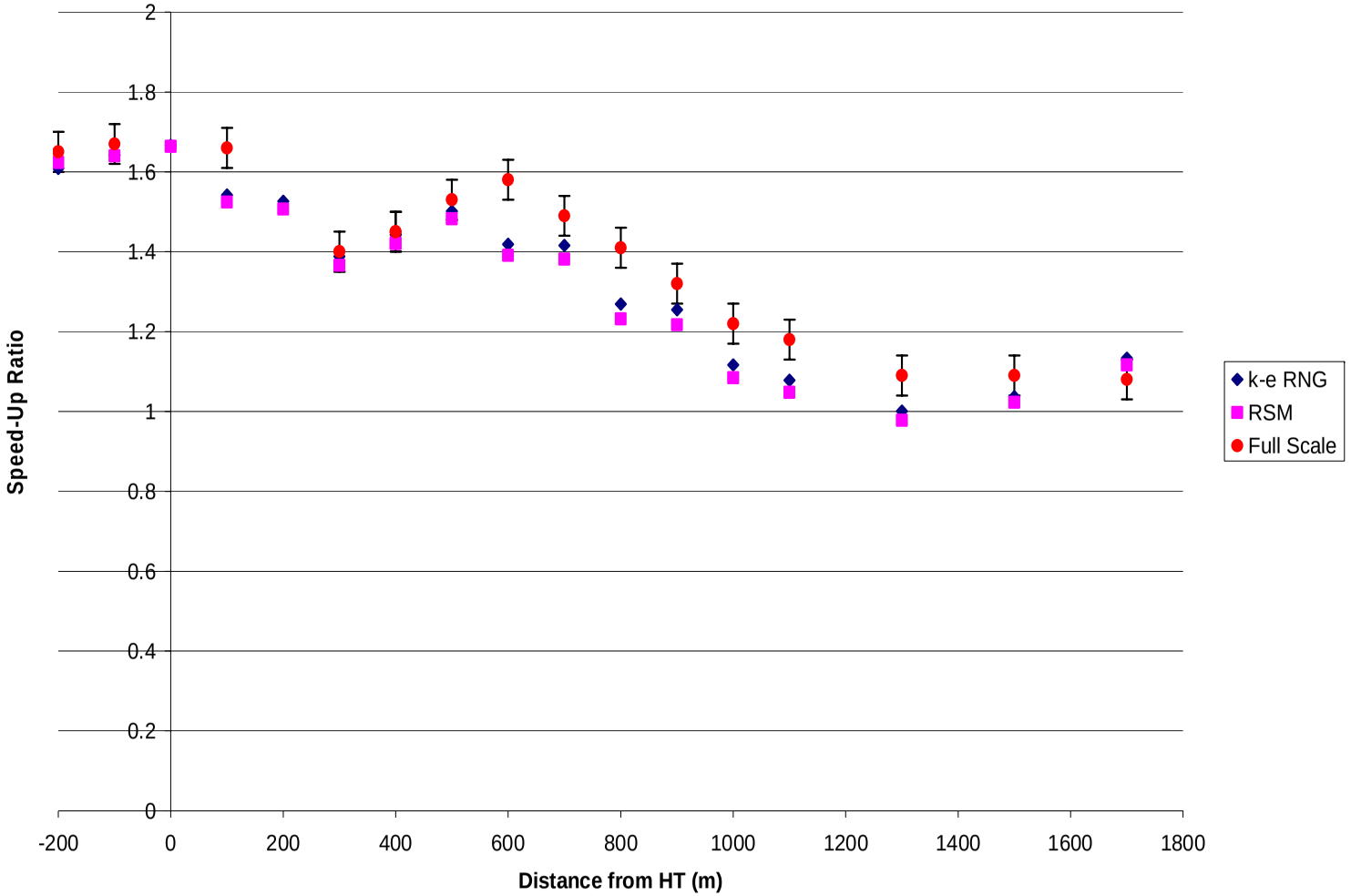

Figure 5.8b– Measurements of velocity speed up ratio at 10m along tower line B for wind direction 180°

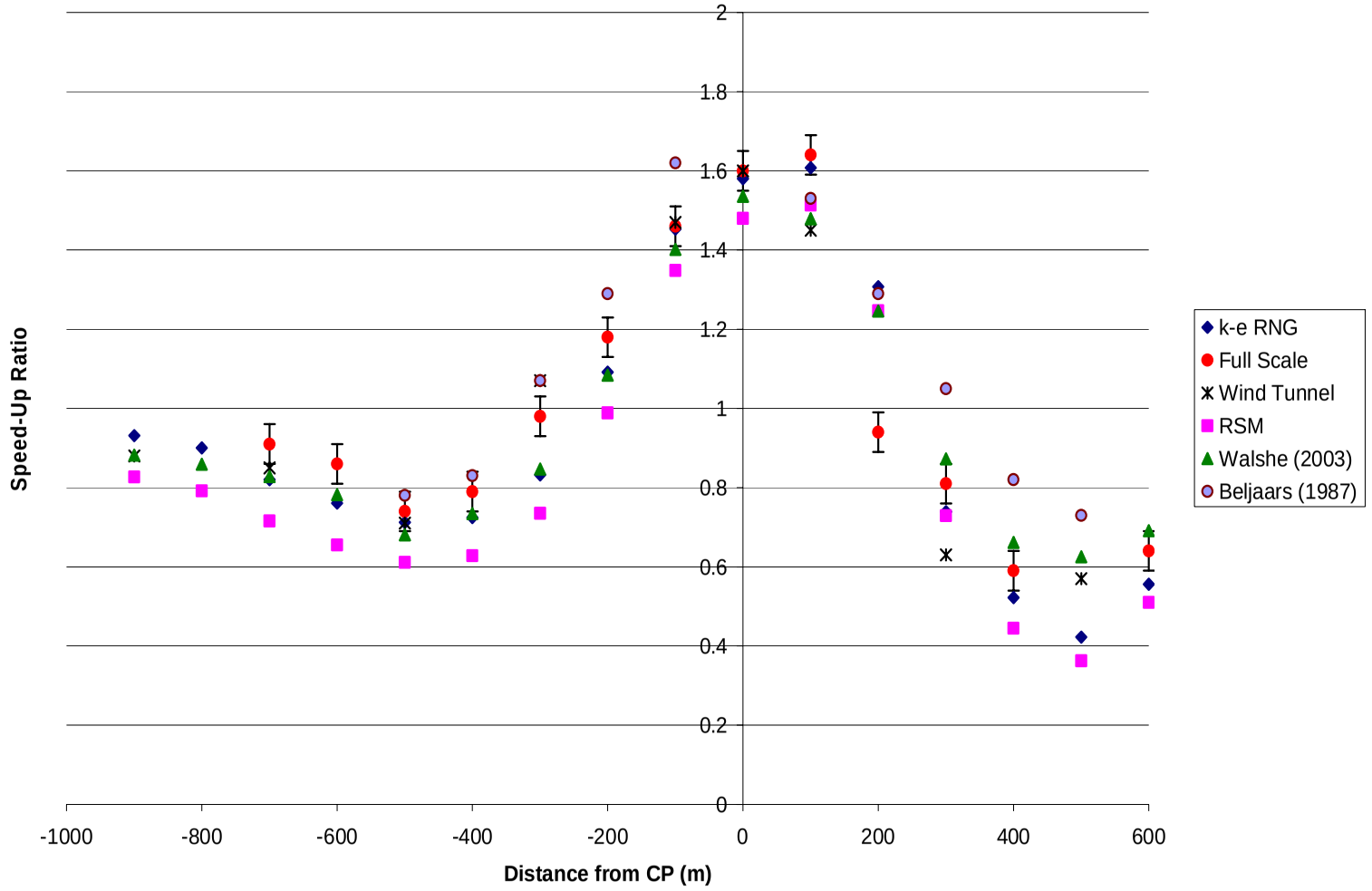

Figure 5.9a – Measurements of velocity speed up ratio at 10m along tower line AA for wind direction 210°

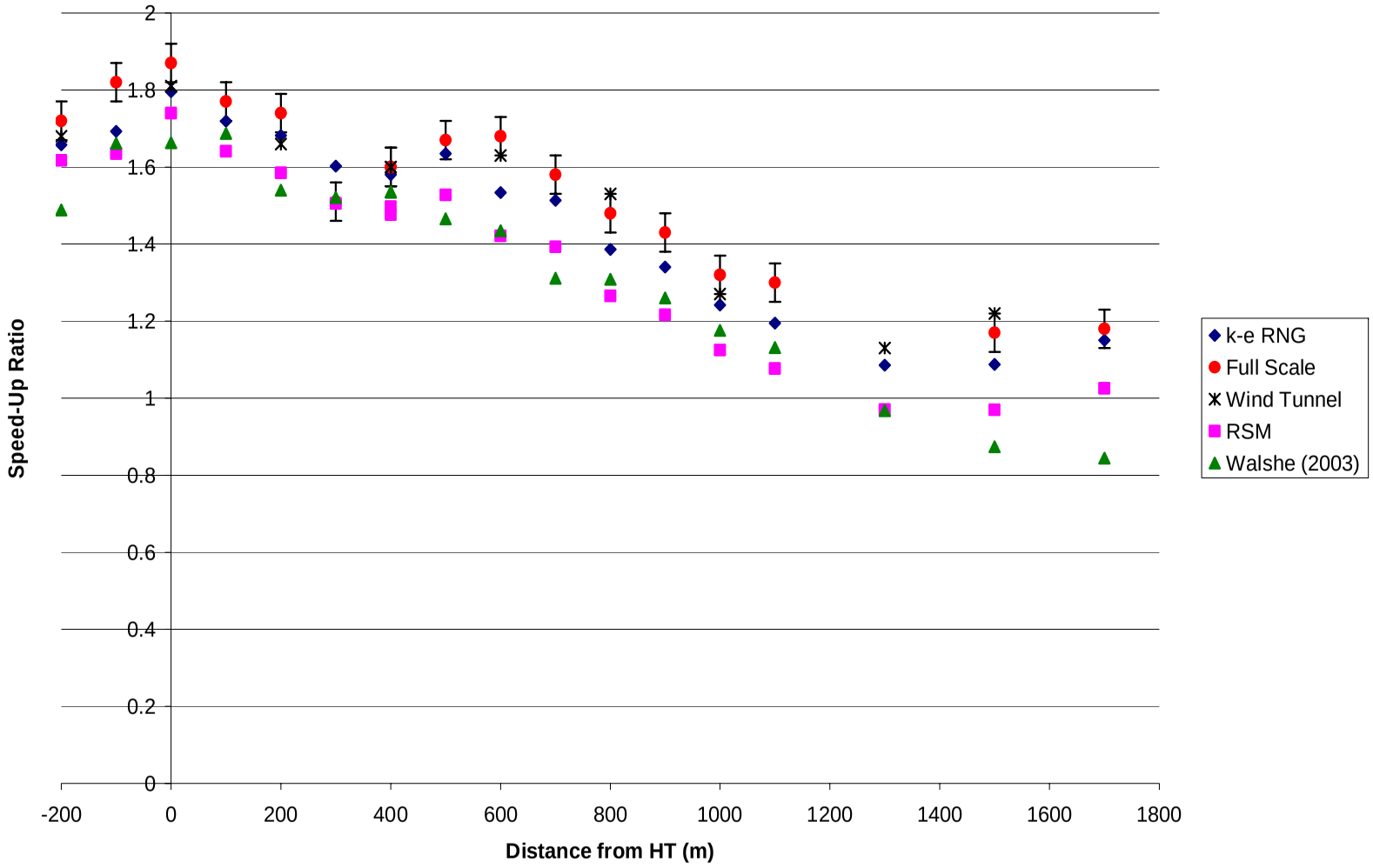

Figure 5.9b – Measurements of velocity speed up ratio at 10m along tower line B for wind direction 210°

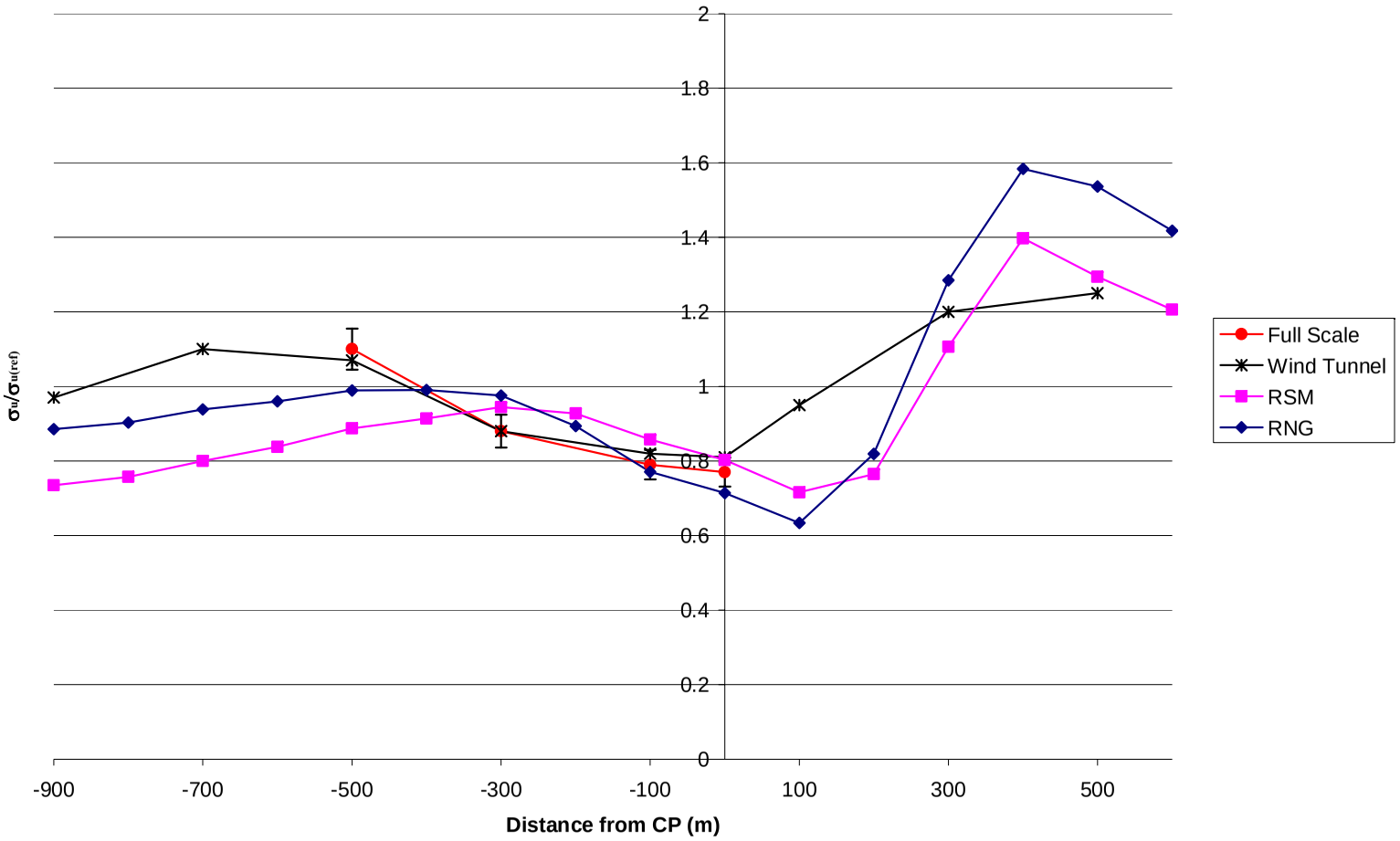

Figure 5.10a – Measurements of changes in σ_u at 10m along tower line AA for wind direction 210°

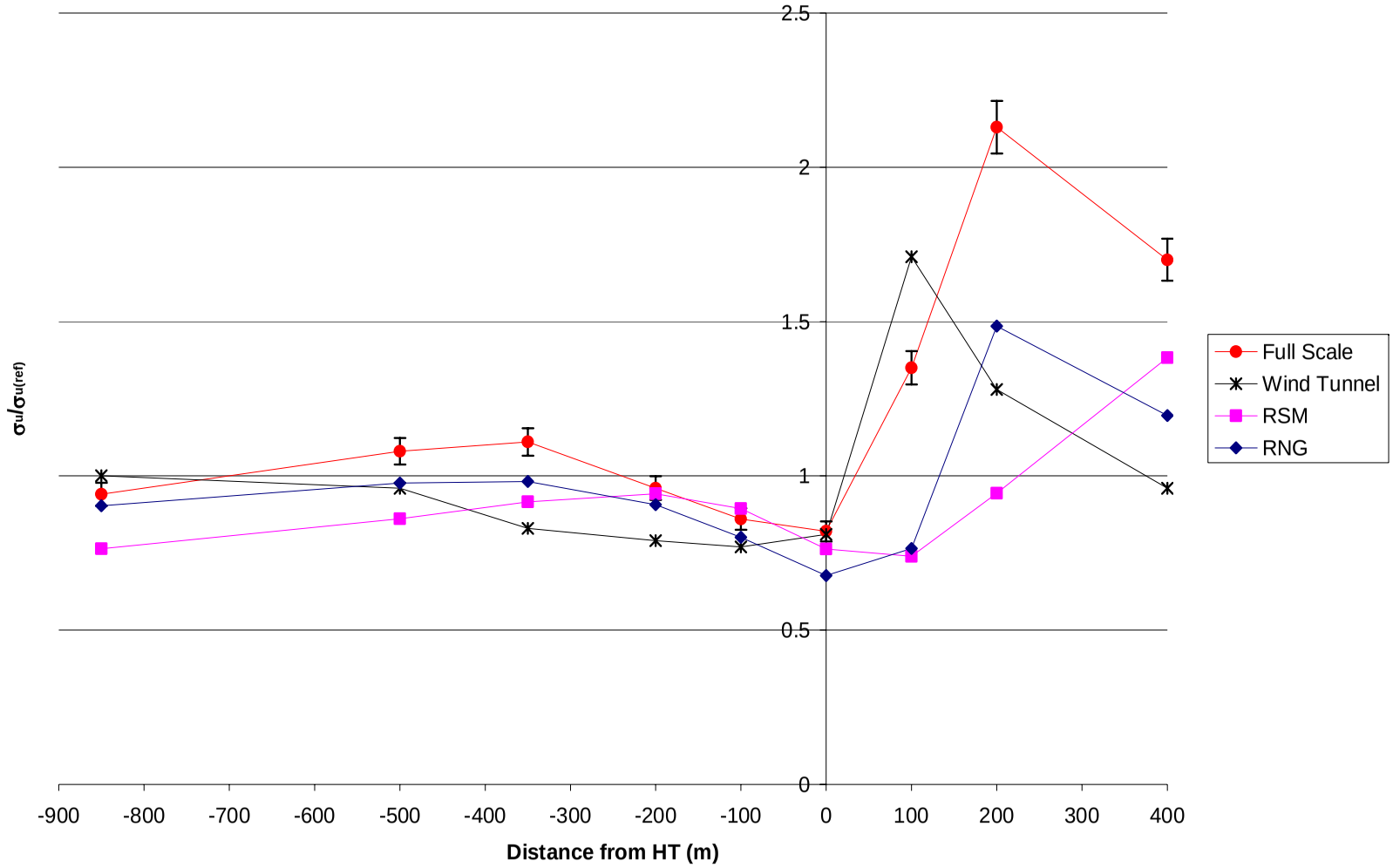

Figure 5.10b – Measurements of changes in σ_u at 10m along tower line A for wind direction 210°

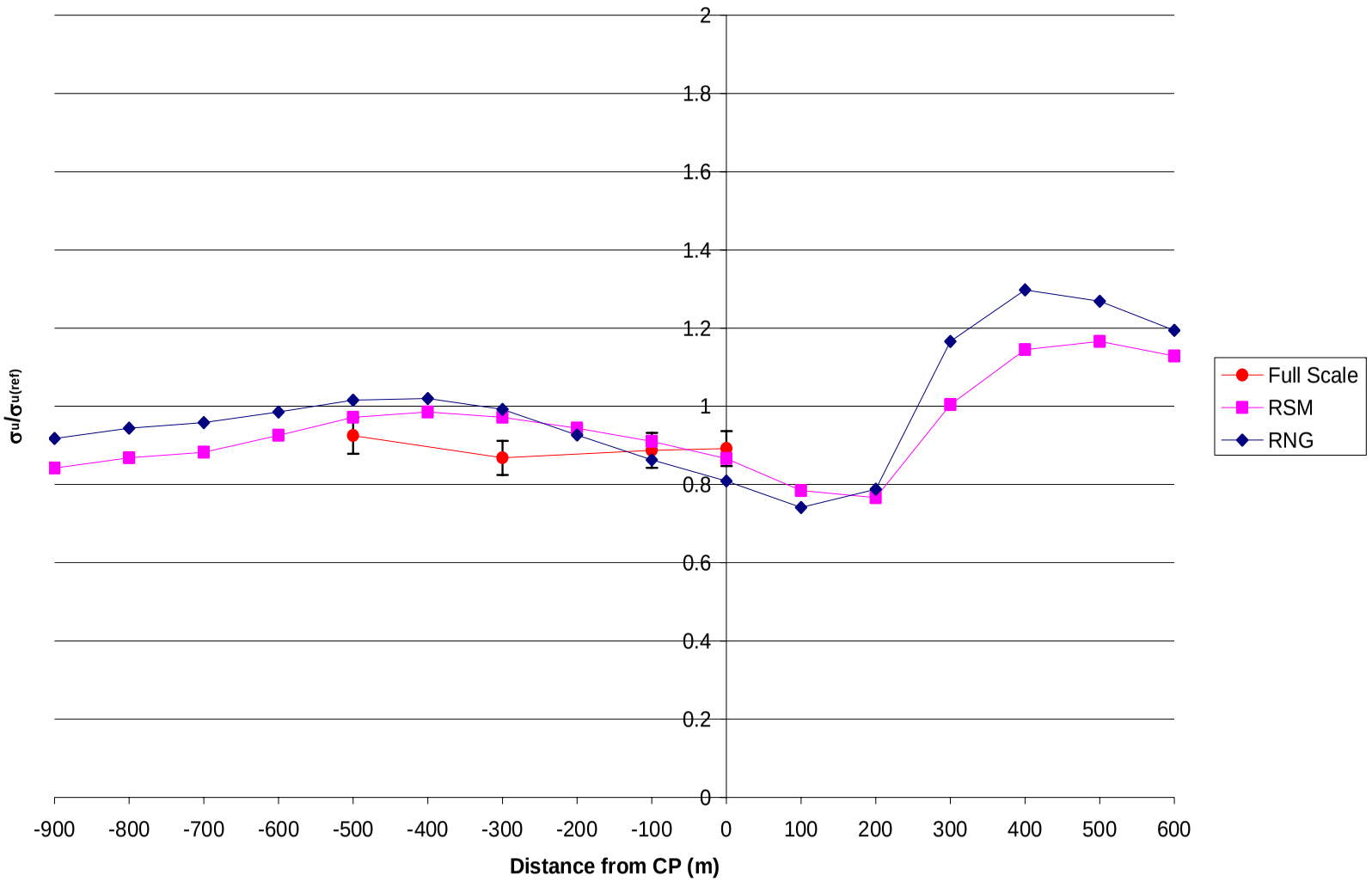

Figure 5.11a – Measurements of changes in σ_u at 10m along tower line AA for wind direction 180°

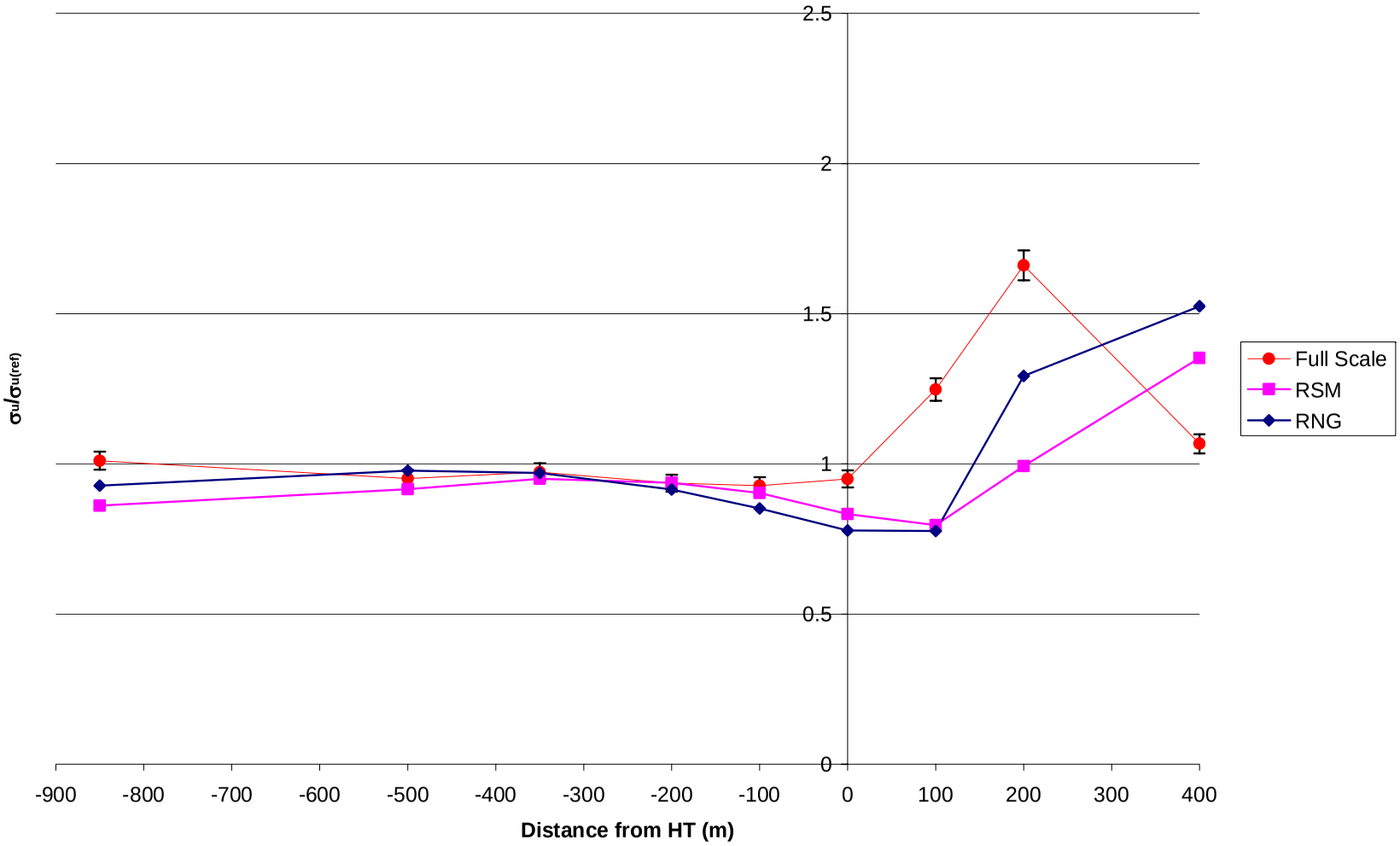

Figure 5.11 b– Measurements of changes in σ_u at 10m along tower line A for wind direction 180°

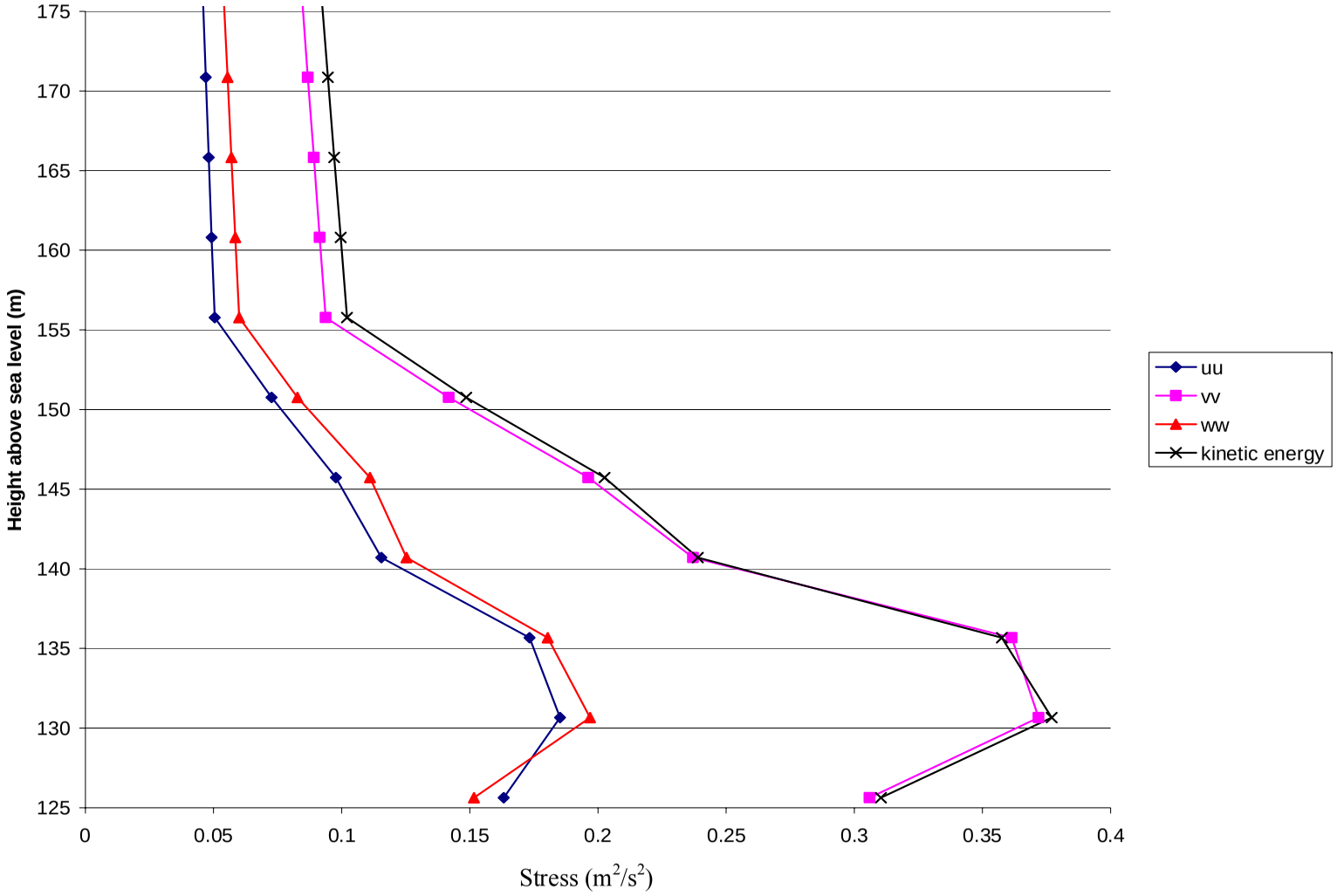

Figure 5.12 – Vertical profiles of Reynolds stress at HT

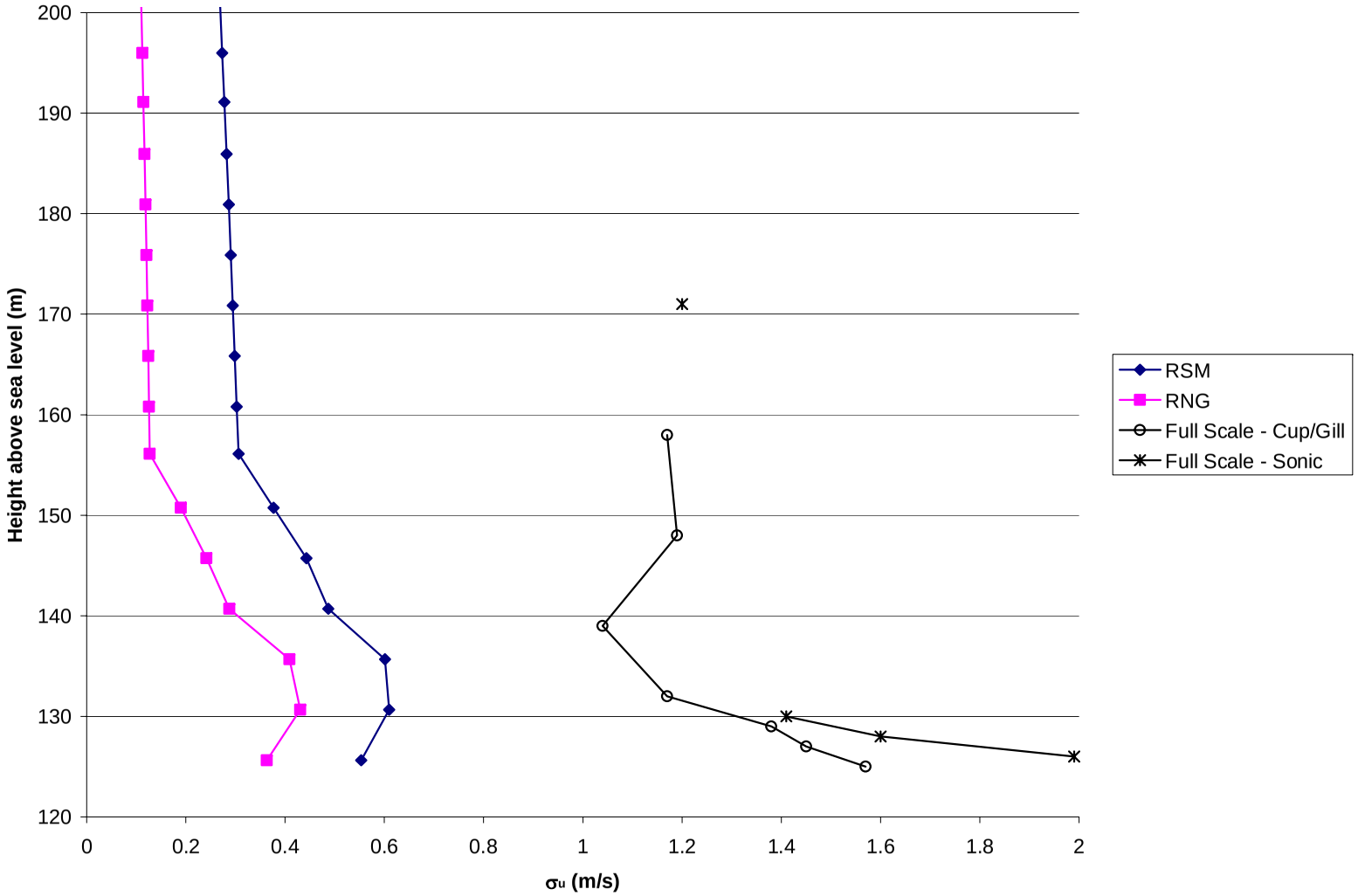

Figure 5.13a – Comparisons of RSM and RNG models, showing vertical profiles of σ_u at HT for wind direction 210°

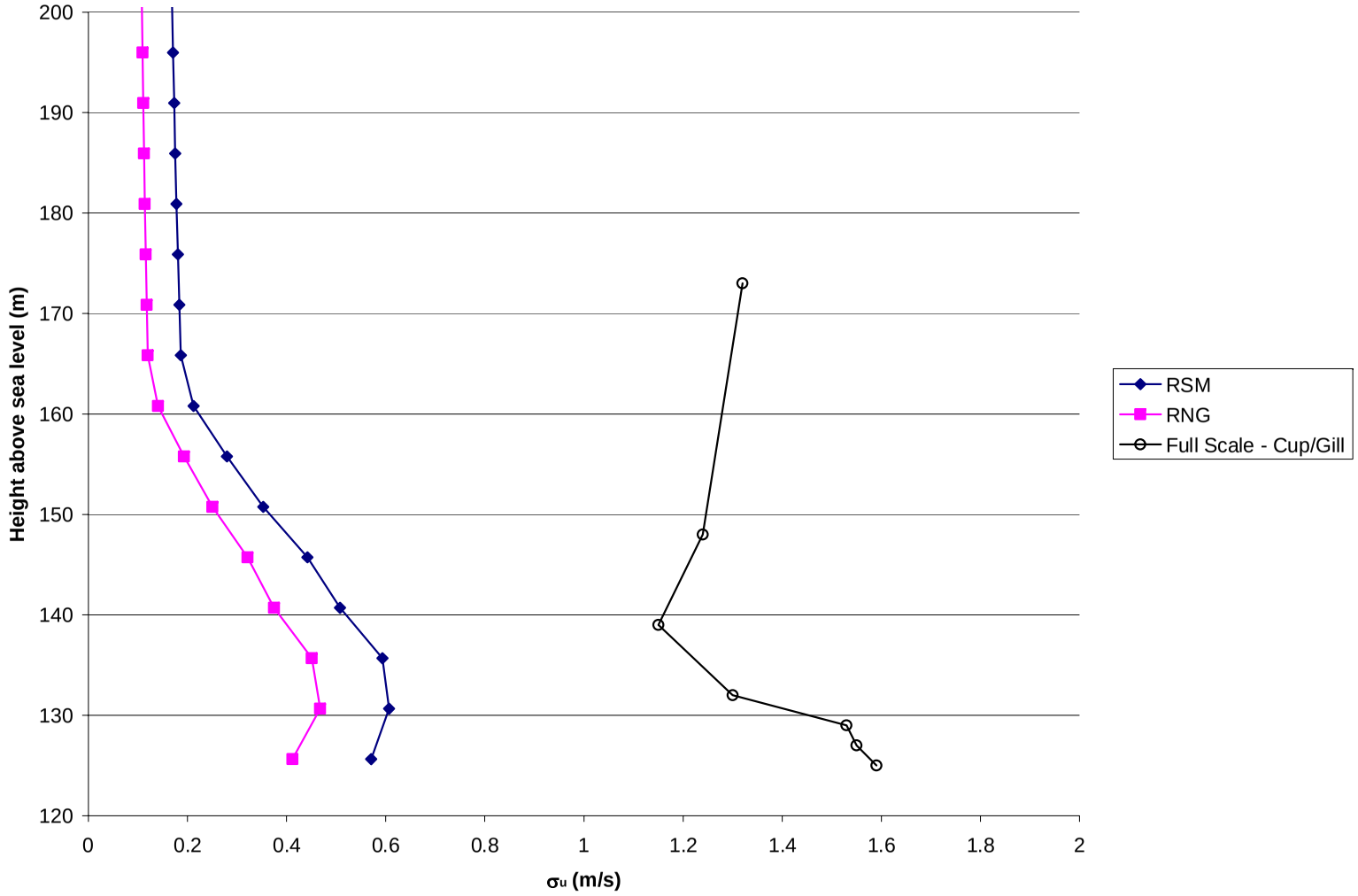

Figure 5.13b – Comparisons of RSM and RNG models, showing vertical profiles of σ_u at HT for wind direction 180°

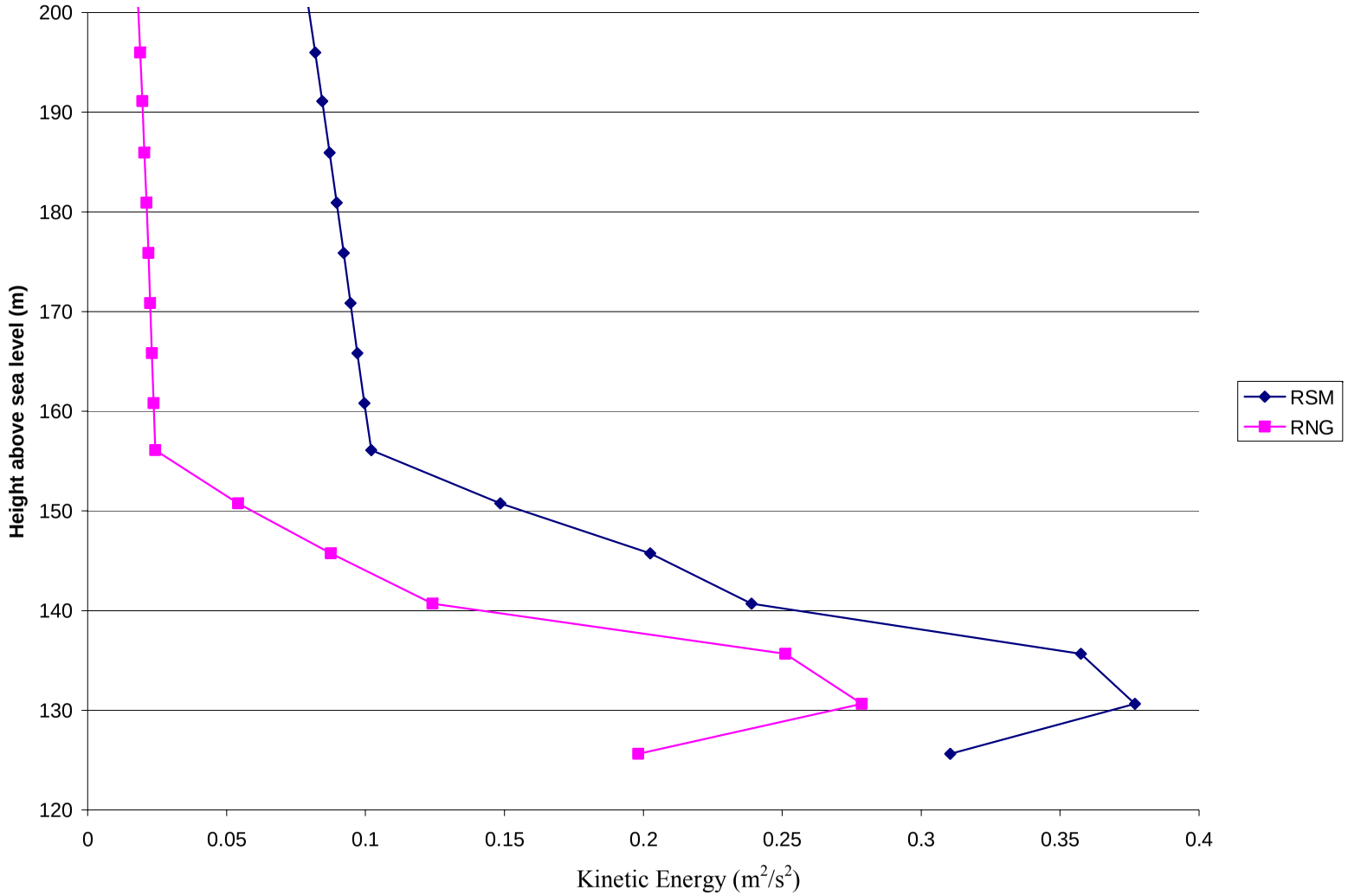

Figure 5.14a – Comparisons of RSM and RNG models, showing vertical profiles of Kinetic Energy at HT for wind direction 210°

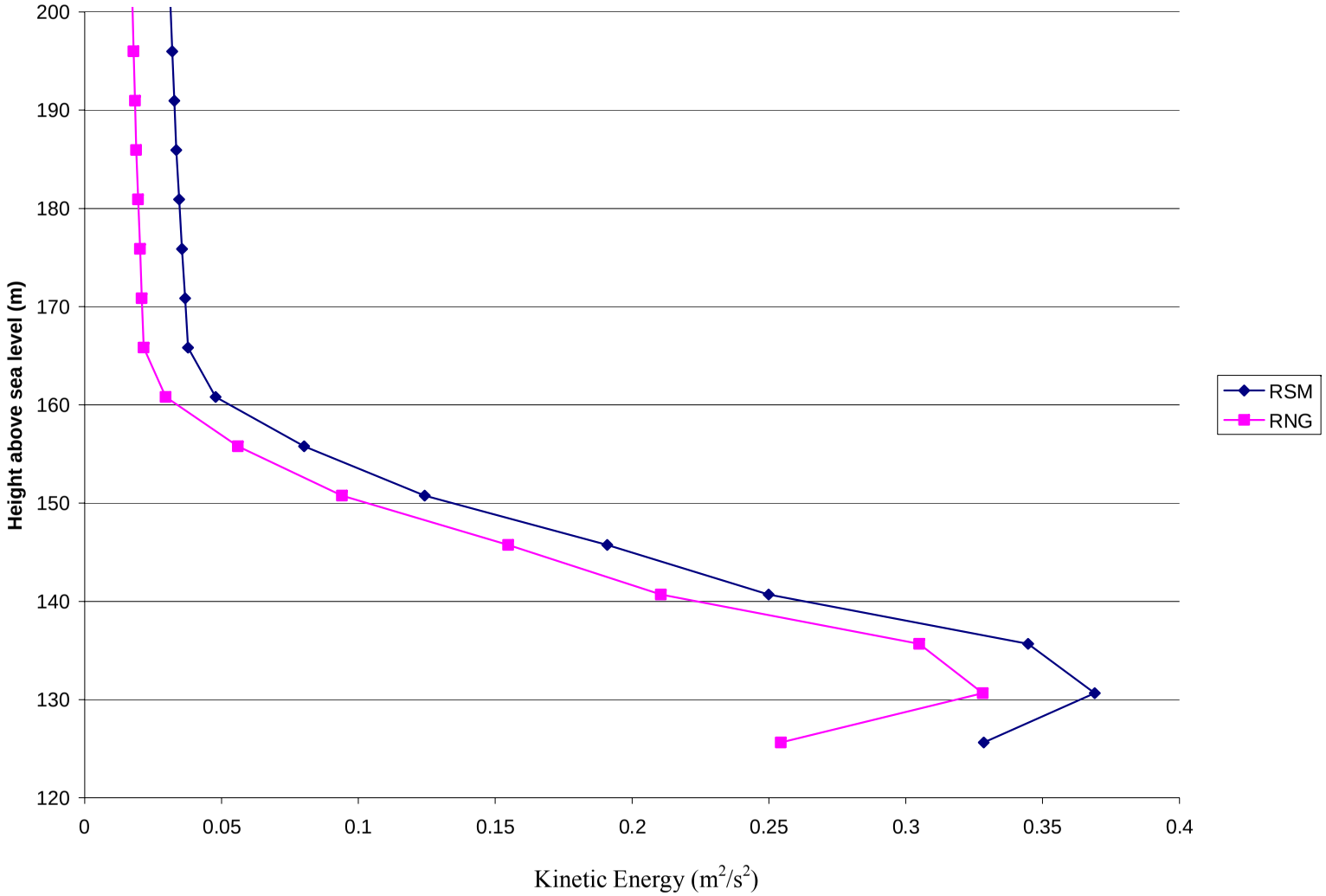

Figure 5.14b– Comparisons of RSM and RNG models, showing vertical profiles of Kinetic Energy at HT for wind direction 180°

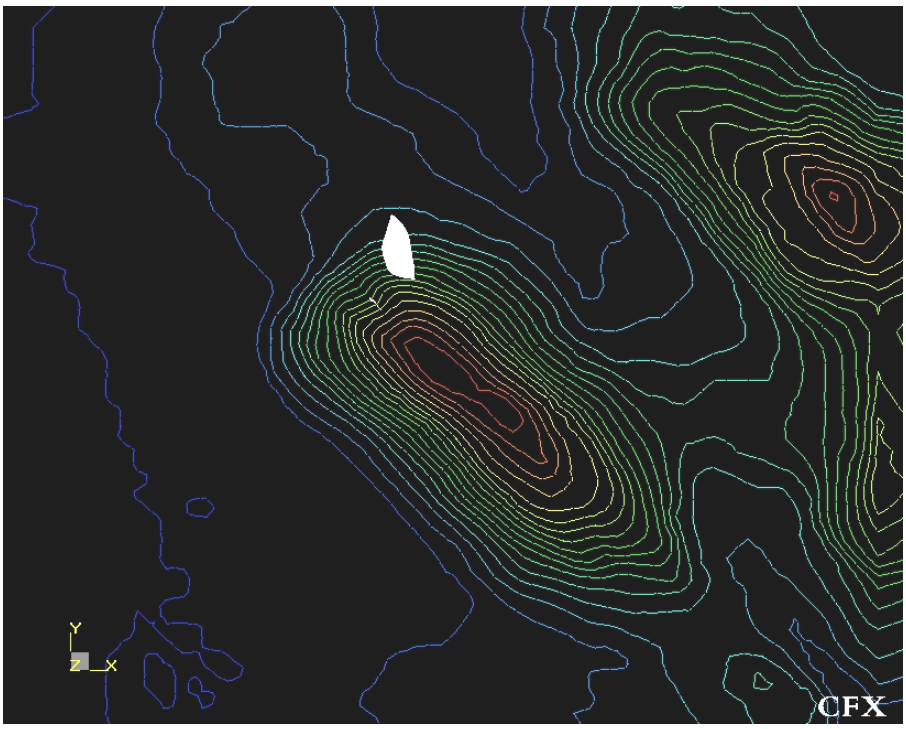

Figure 5.15a – Plan of Askervein showing flow separation (k-ε RNG model) – 180°

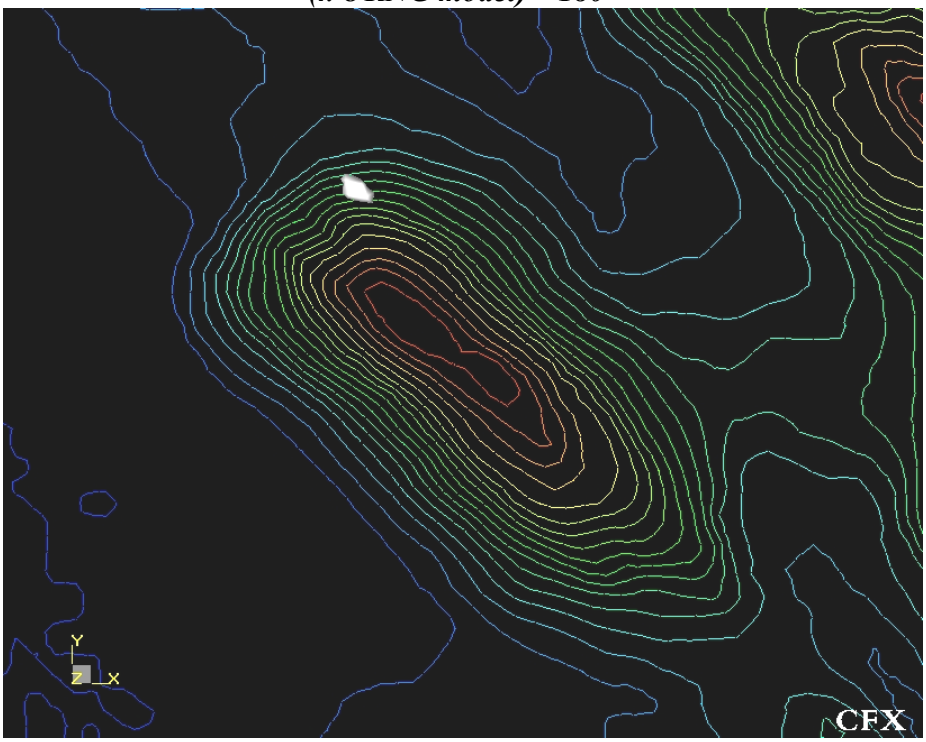

Figure 5.15b – Plan of Askervein showing flow separation (RSM) – 180°

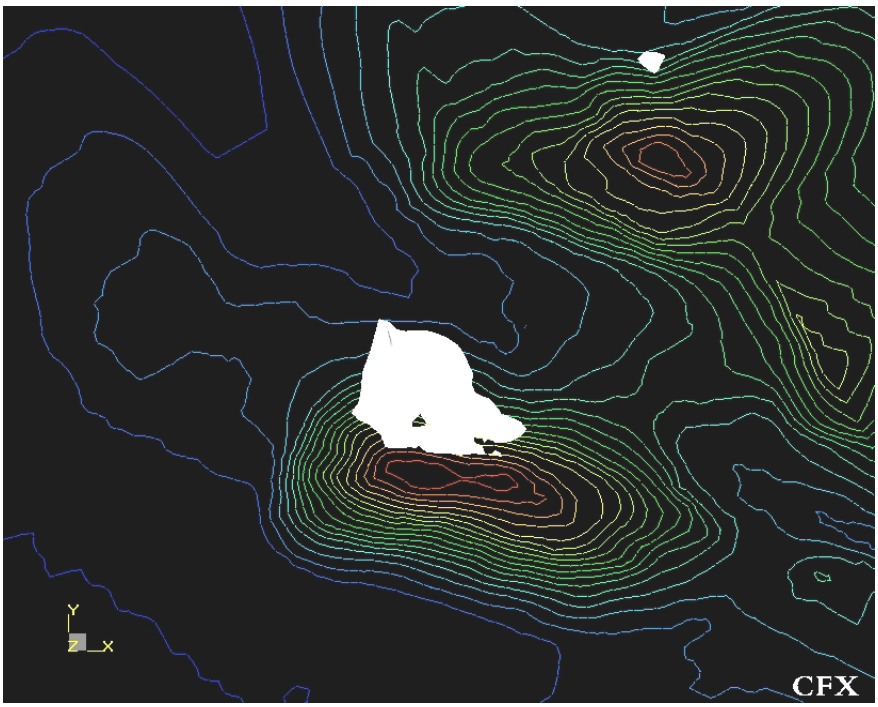

Figure 5.16a – Plan of Askervein showing flow separation (k-ε RNG model) – 210°

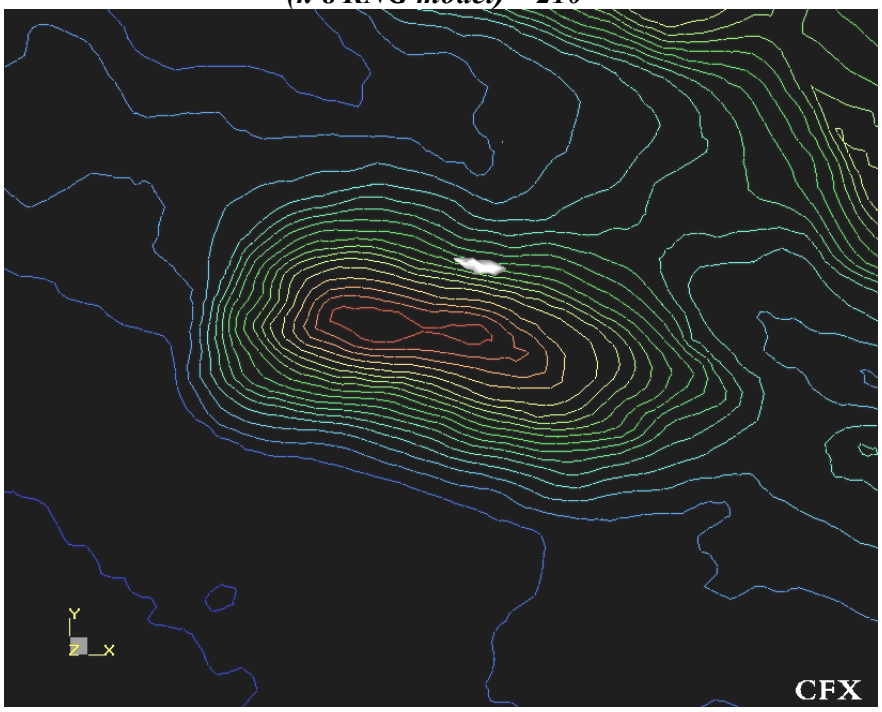

Figure 5.16b – Plan of Askervein showing flow separation (RSM) – 210°

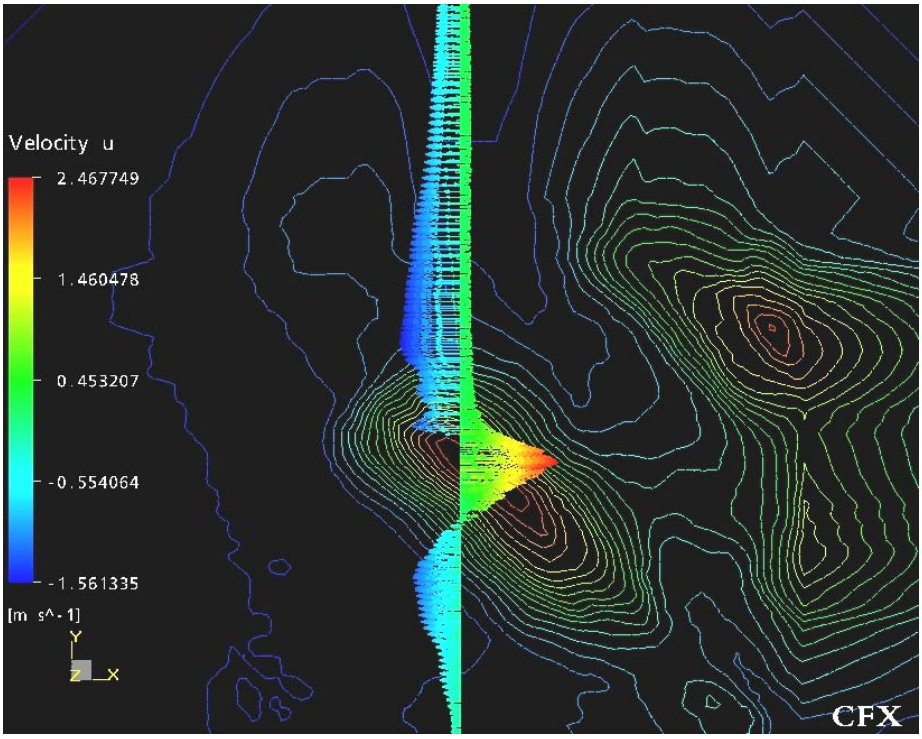

Figure 5.17a – Cross stream velocity through HT using k-ε RNG model - 180°

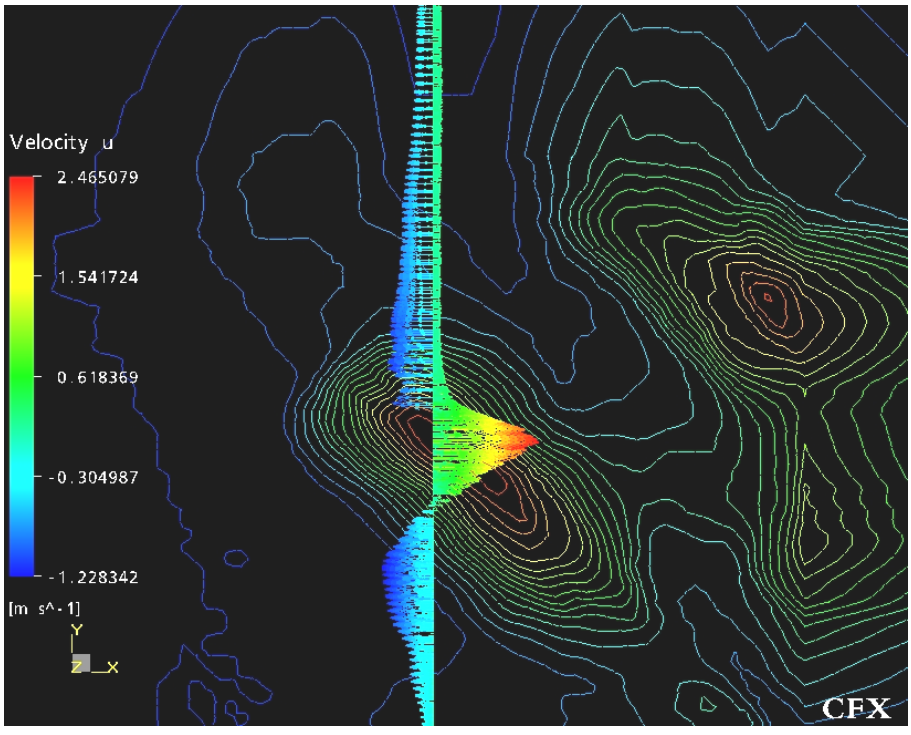

Figure 5.17b – Cross stream velocity through HT using RSM –180°

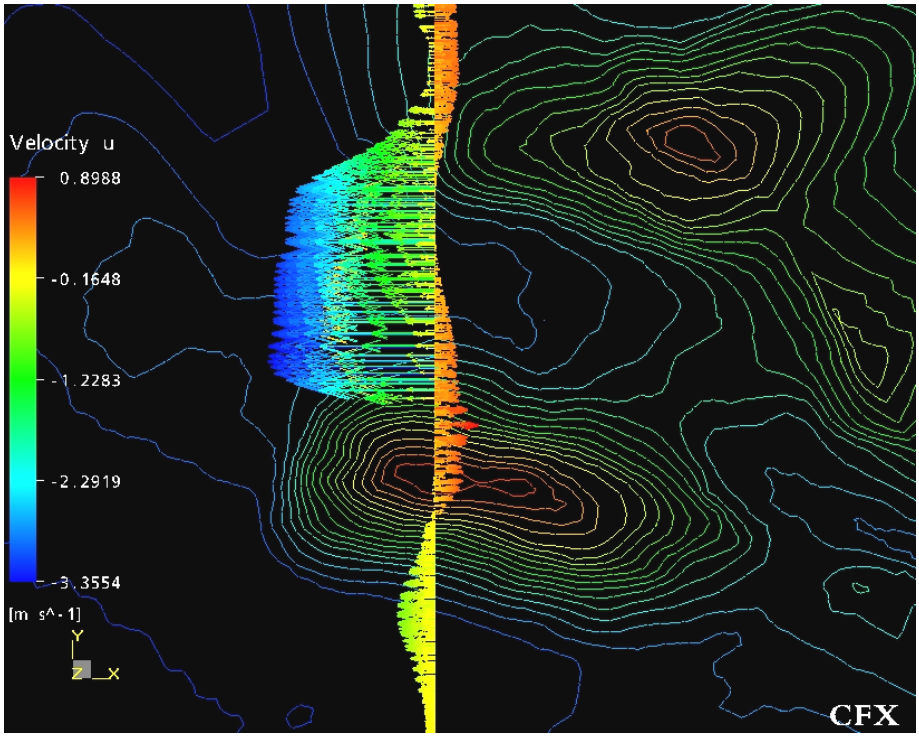

Figure 5.18a – Cross stream velocity through HT using k-ε RNG model – 210°

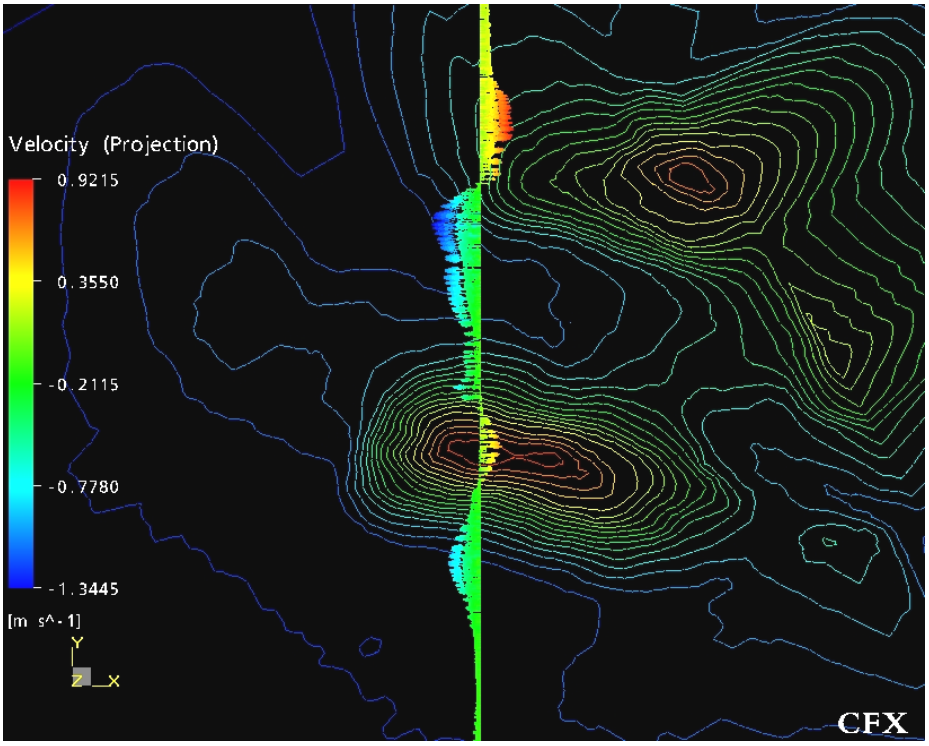

Figure 5.18b – Cross stream velocity through HT using RSM (1st order) – 210°

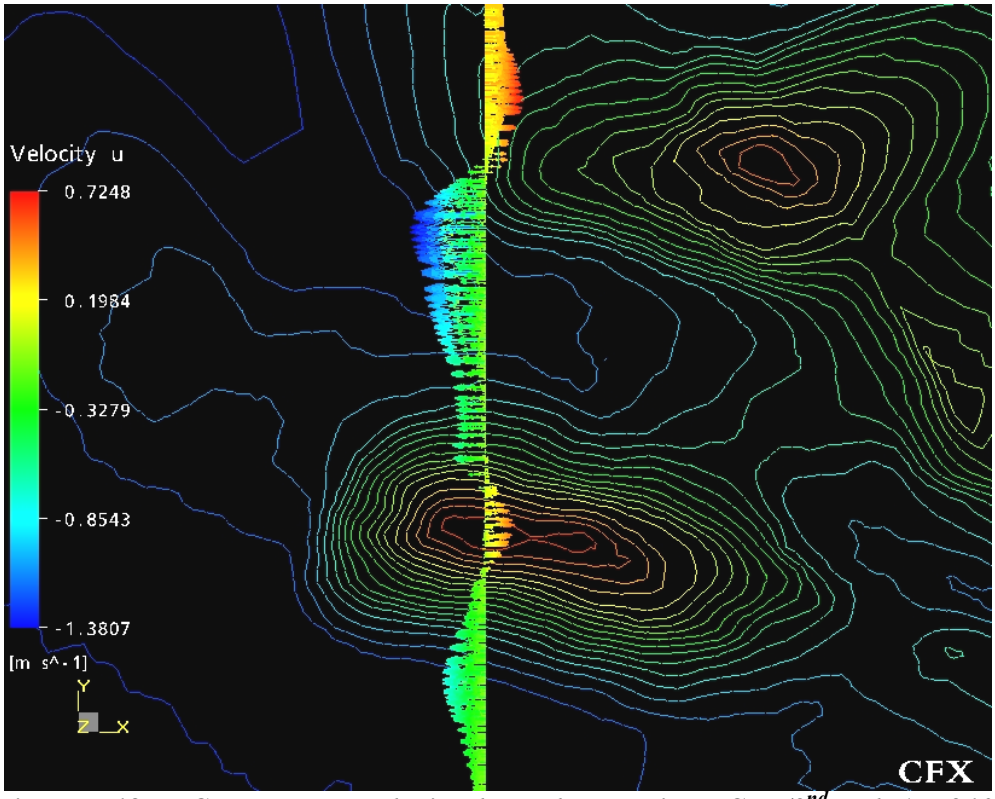

Figure 5.18c – Cross stream velocity through HT using RSM (2nd order) – 210°

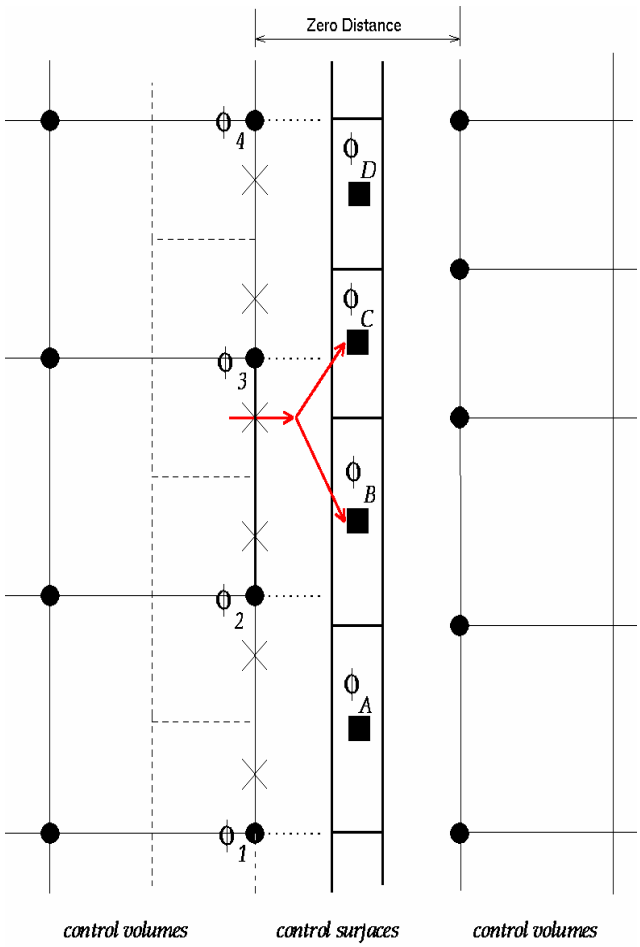

Figure 6.1- General Grid Interface layout (From CFX Ltd)

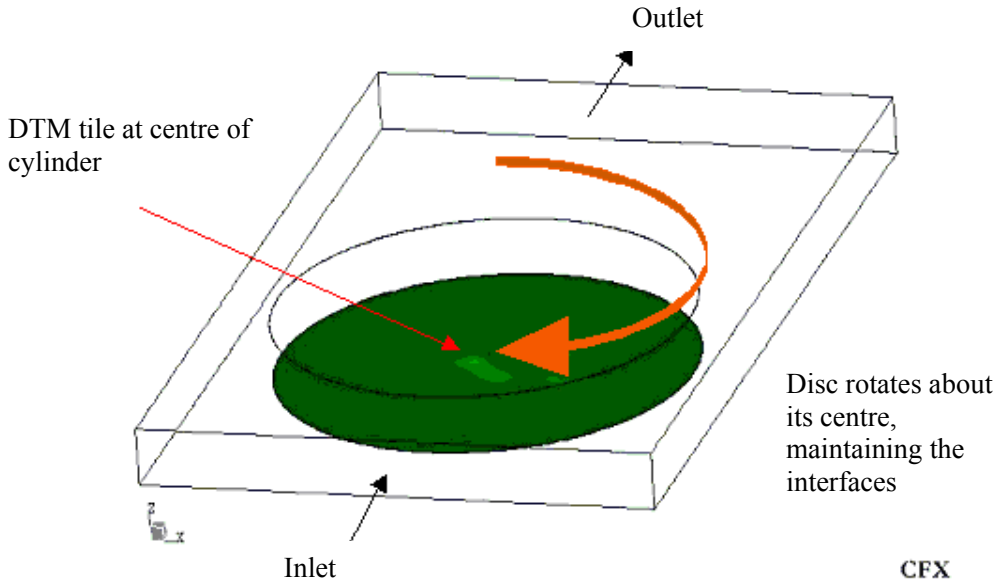

Figure 6.2 – Askervein setup for automation process

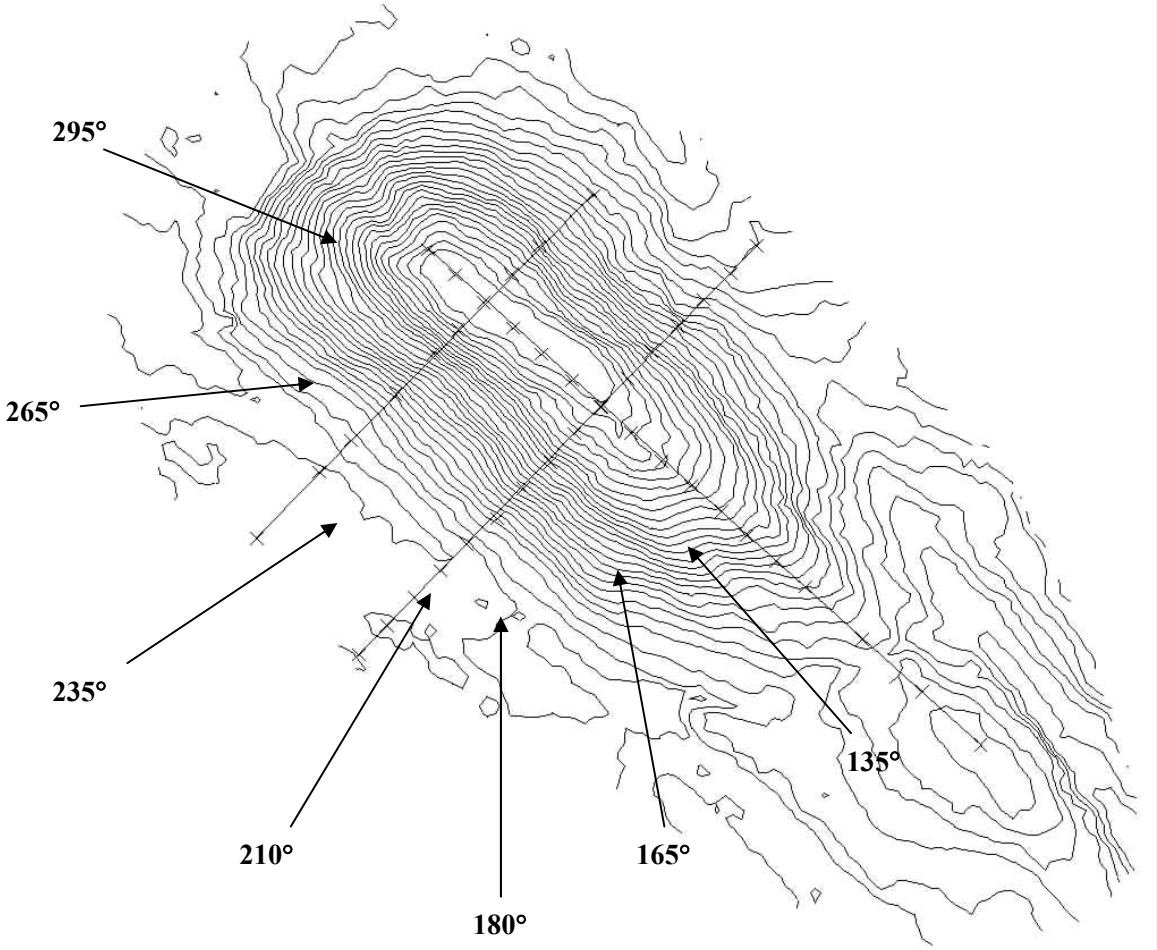

Figure 6.3 – Main wind directions over Askervein

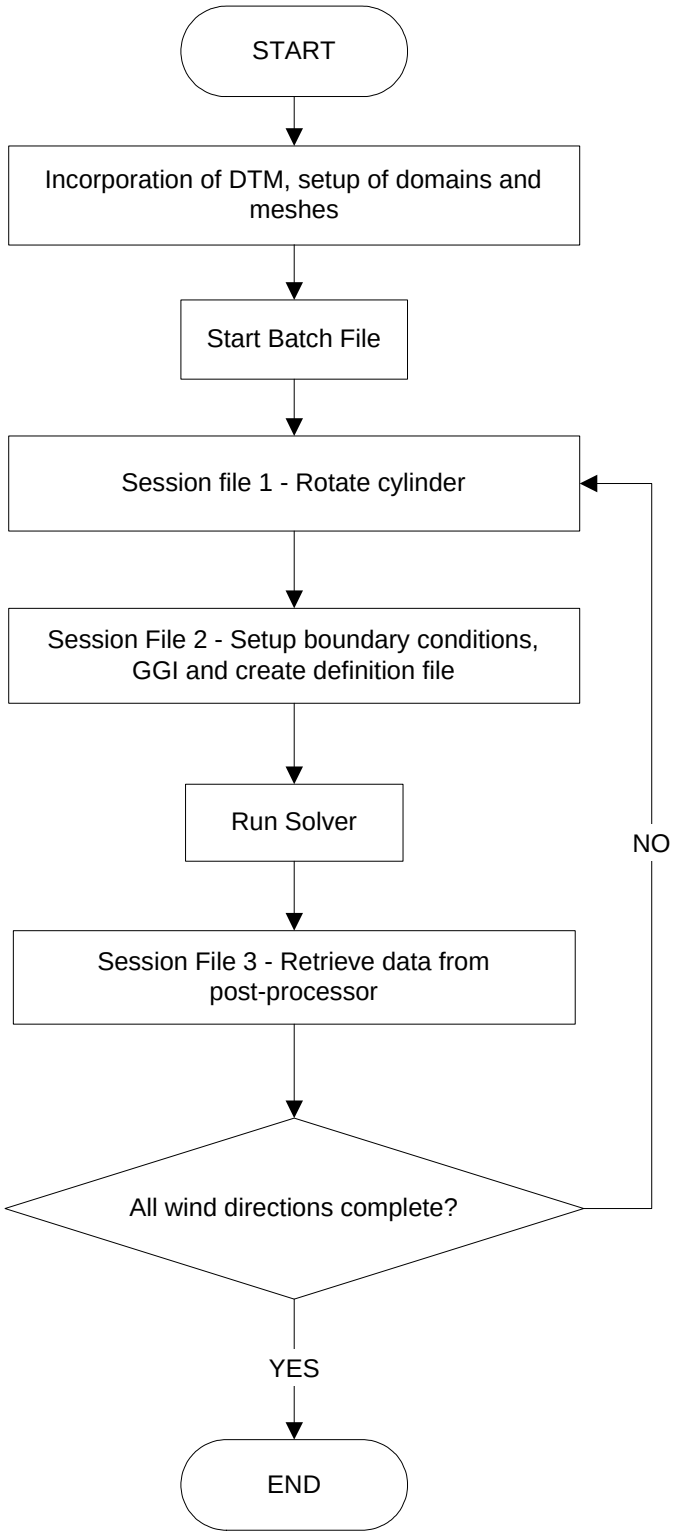

Figure 6.4 Flow chart of the automation process

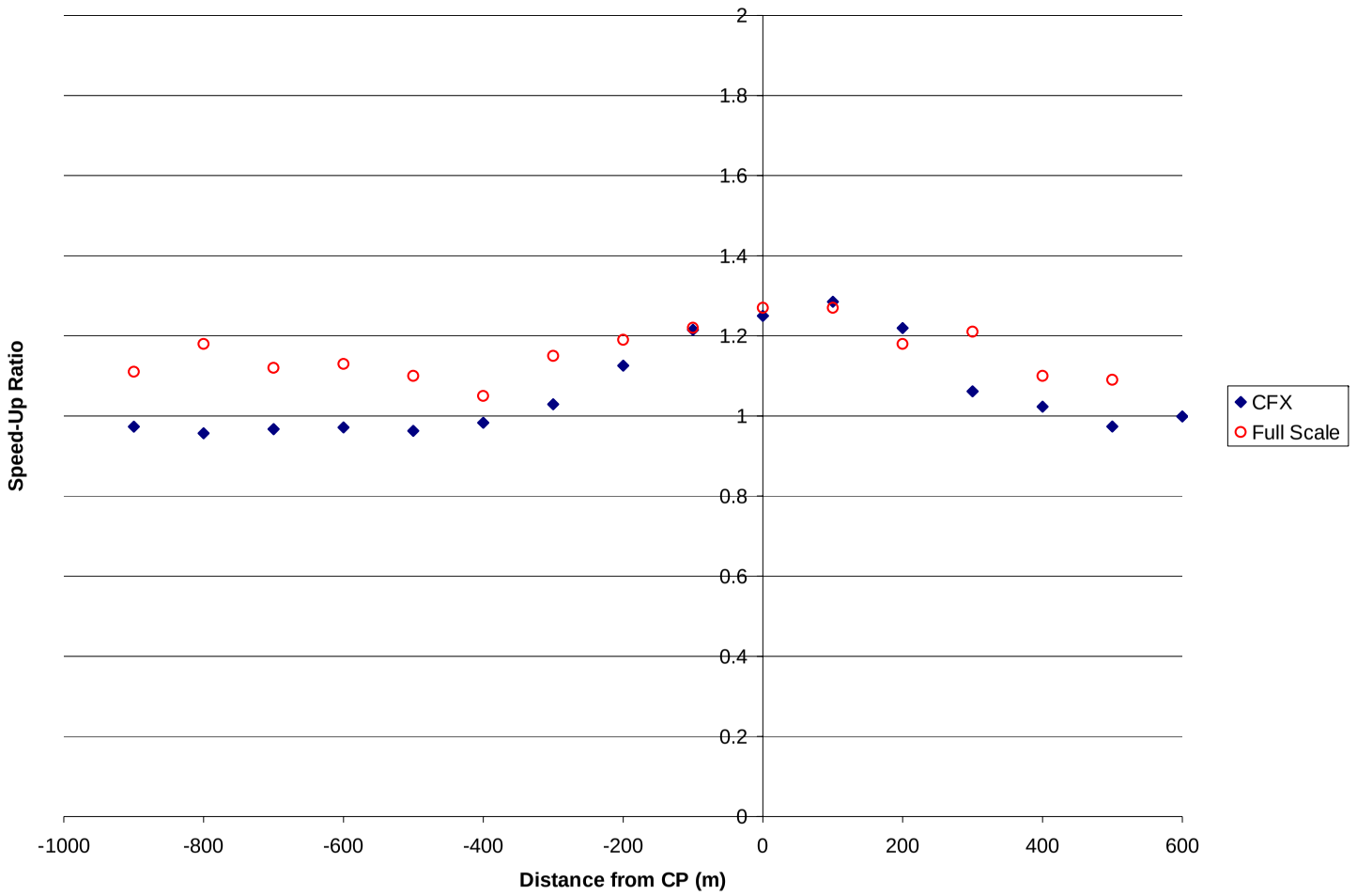

Figure 6.5 – Measurements of velocity ratio at 10m along tower line AA for wind direction 135°

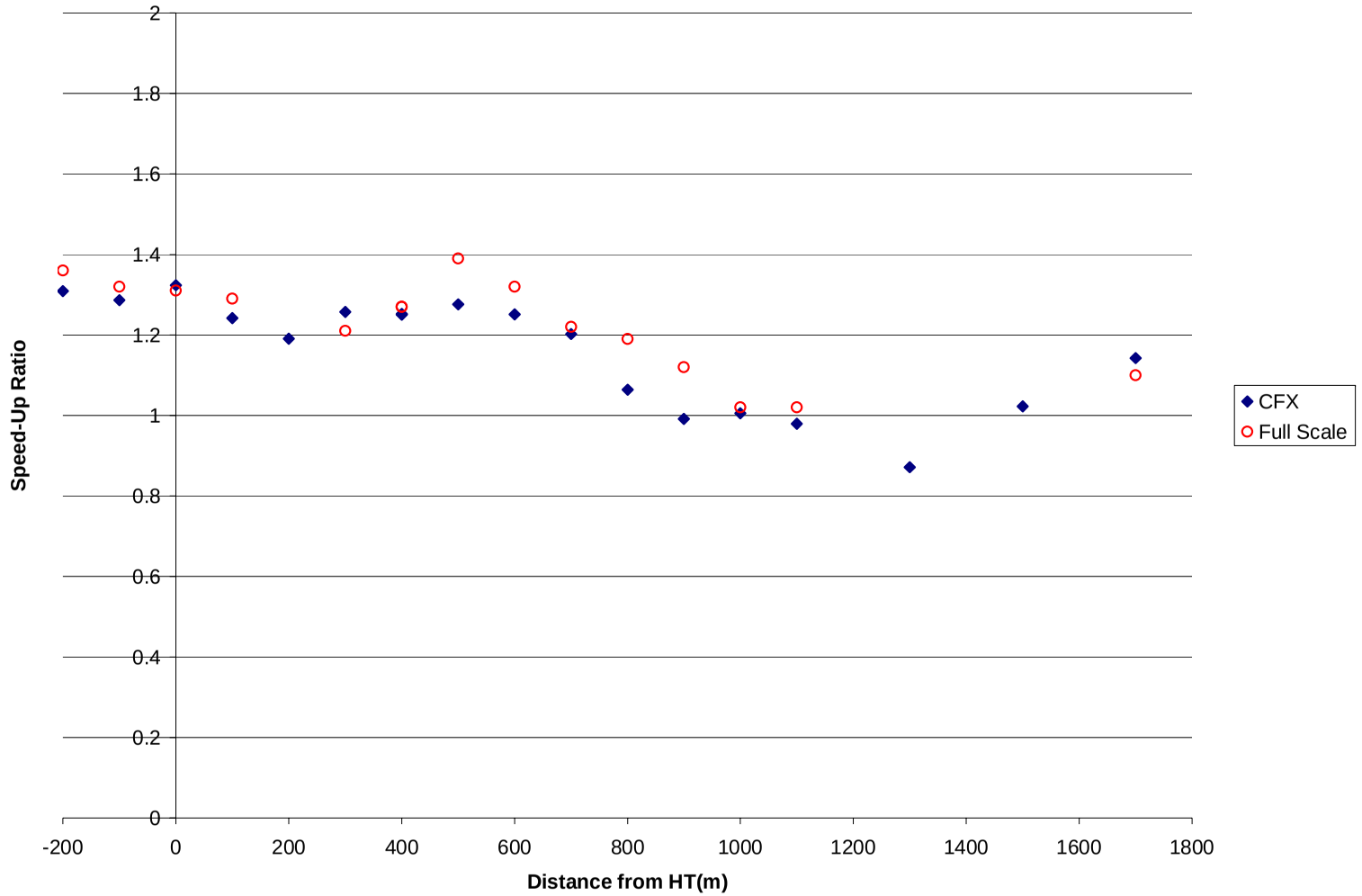

Figure 6.6 – Measurements of velocity ratio at 10m along tower line B for wind direction 135°

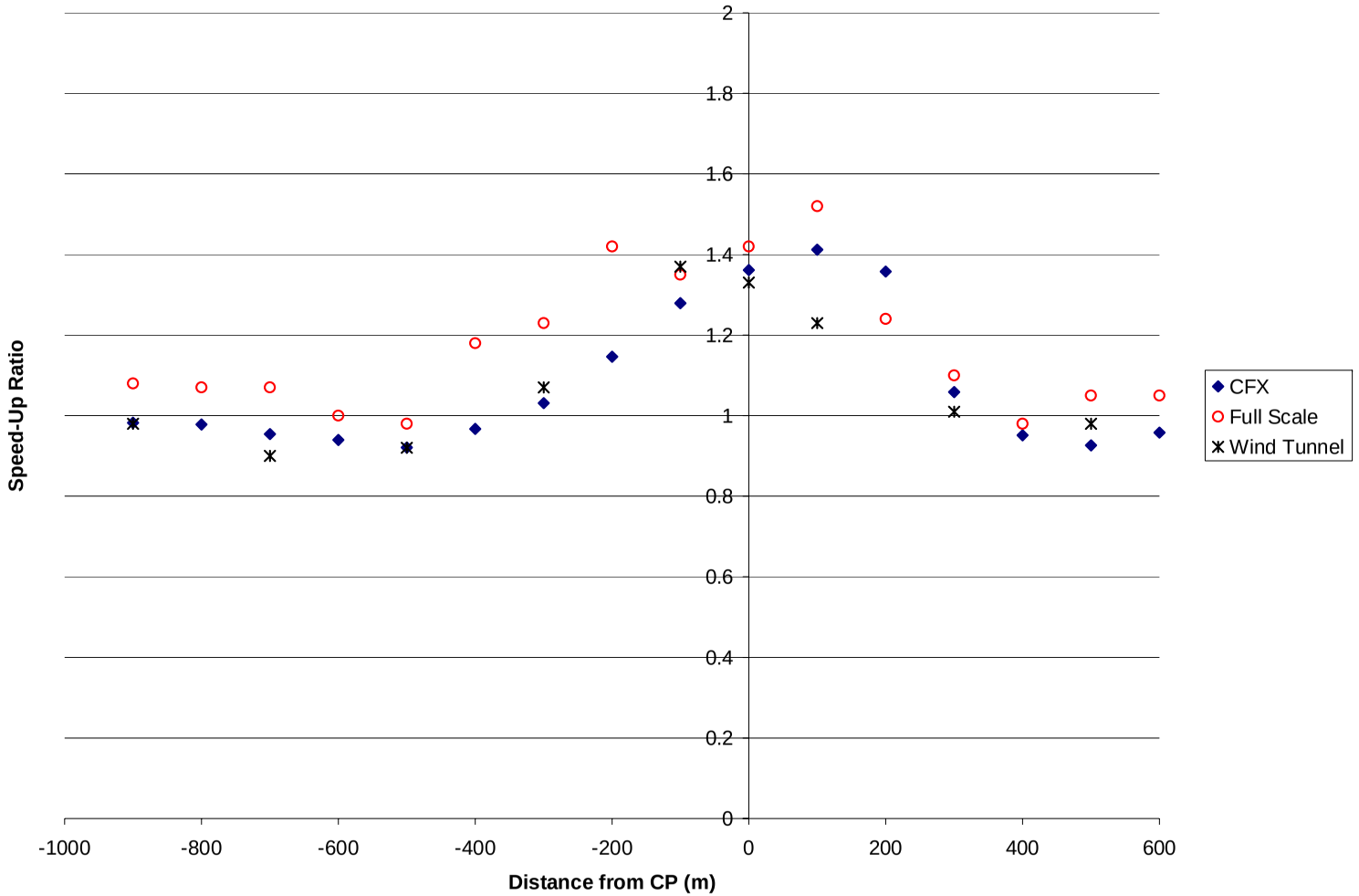

65°

Figure 6.7 – Measurements of velocity ratio at 10m along tower line AA for wind direction 165°

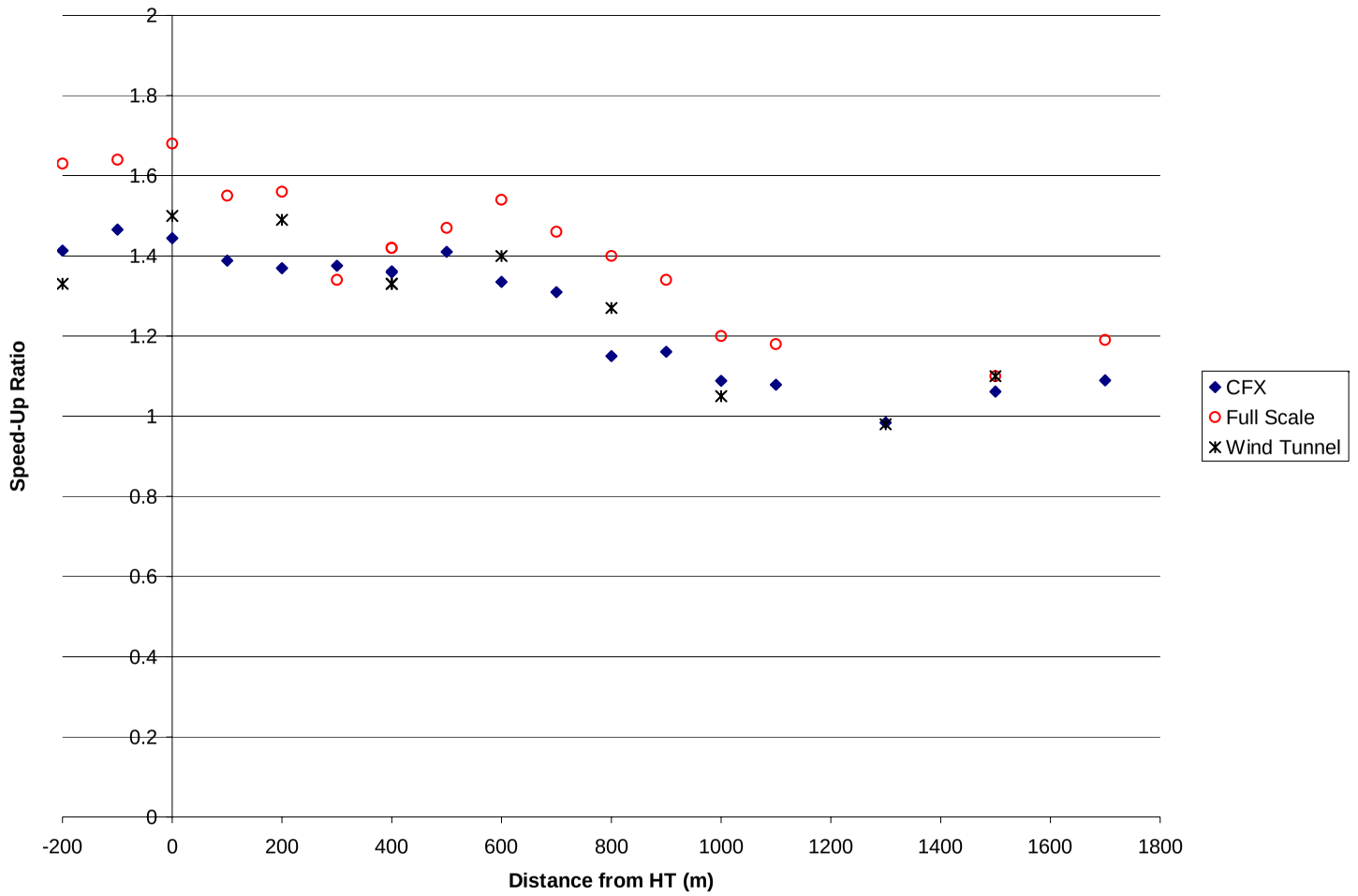

Figure 6.8 – Measurements of velocity ratio at 10m along tower line B for wind direction 165°

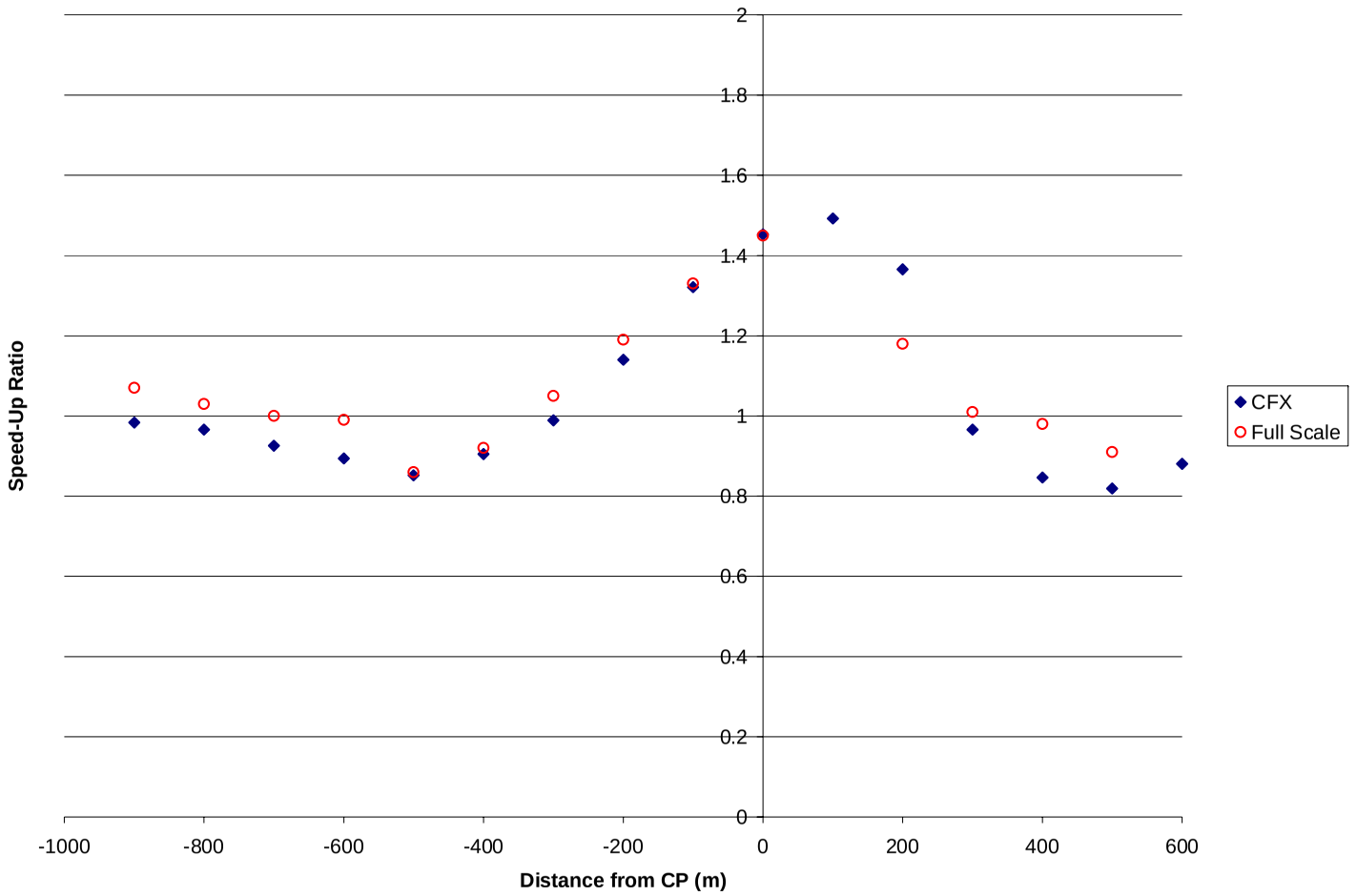

Figure 6.9 – Measurements of velocity ratio at 10m along tower line AA for wind direction 180°

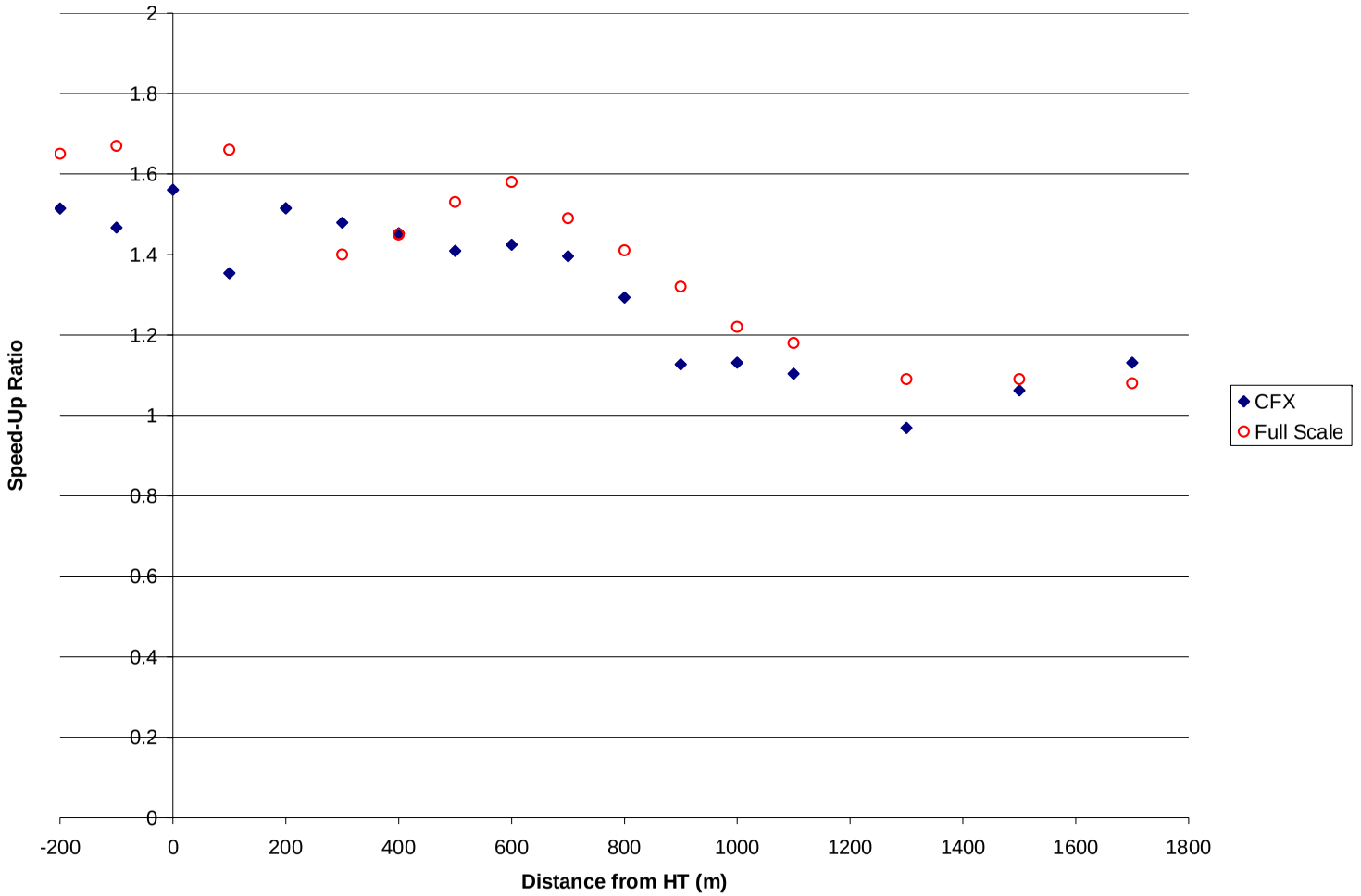

Figure 6.10 – Measurements of velocity ratio at 10m along tower line B for wind direction 180°

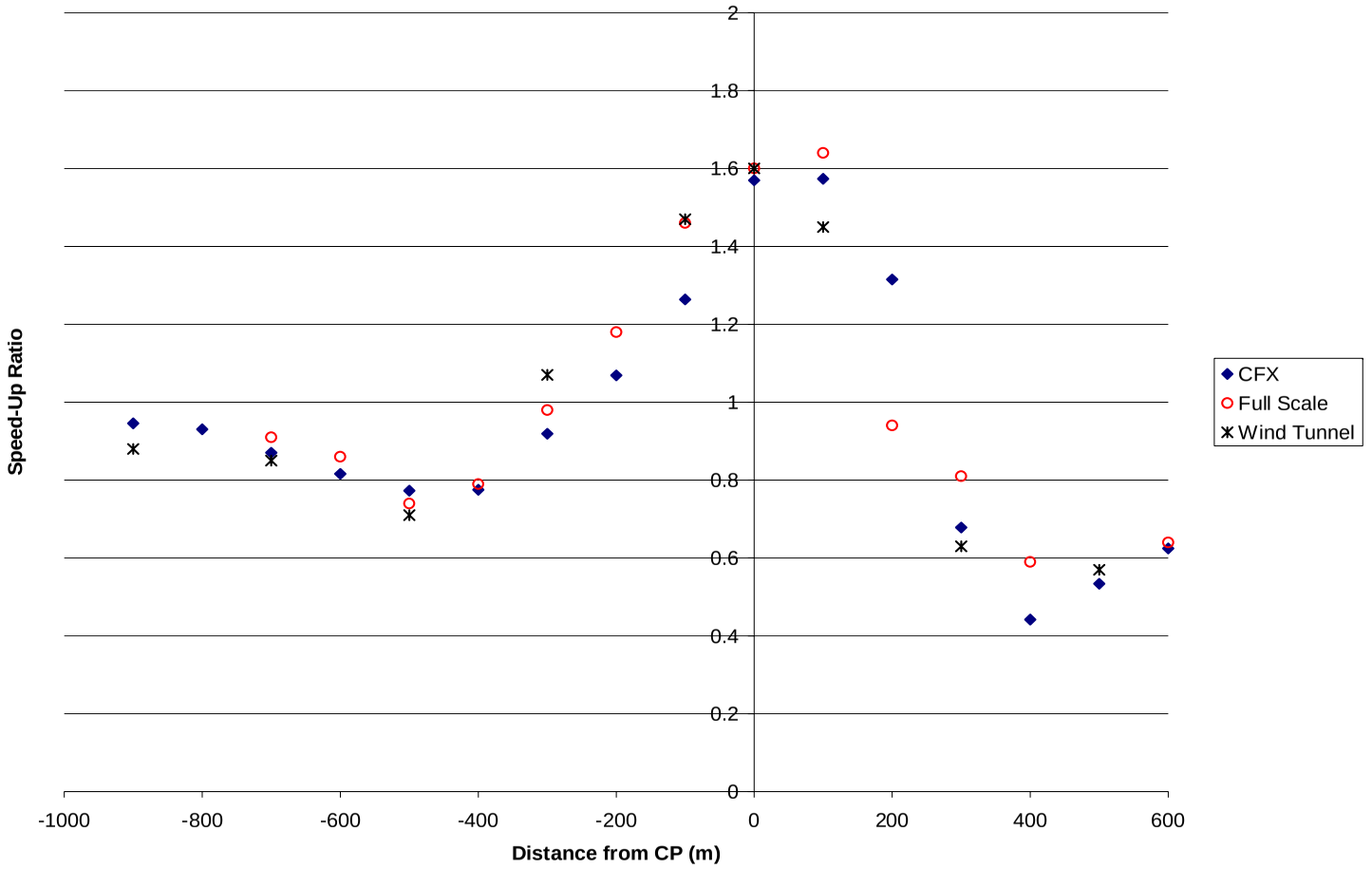

Figure 6.11 – Measurements of velocity ratio at 10m along tower line AA for wind direction 210°

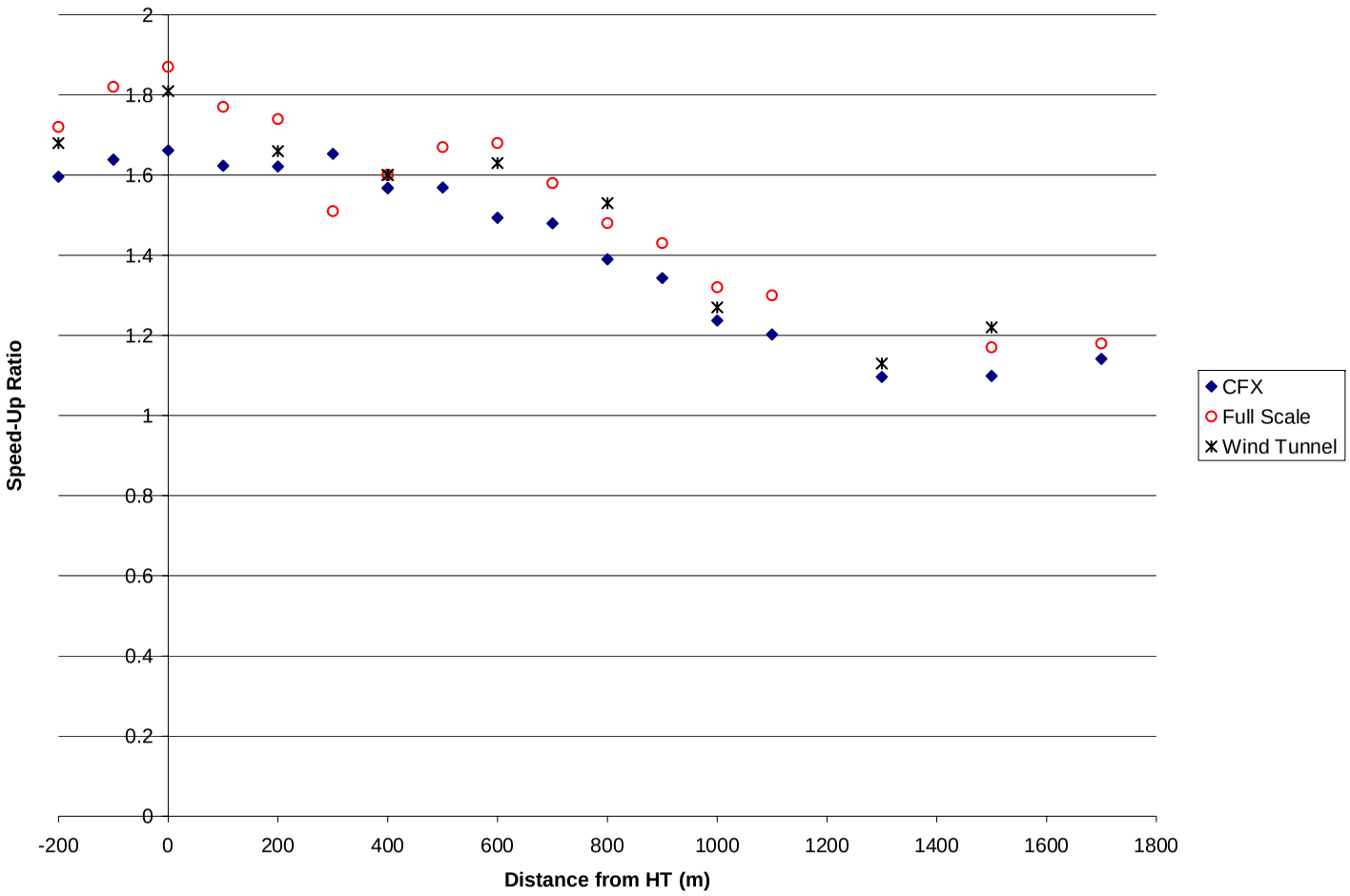

Figure 6.12 – Measurements of velocity ratio at 10m along tower line B for wind direction 210°

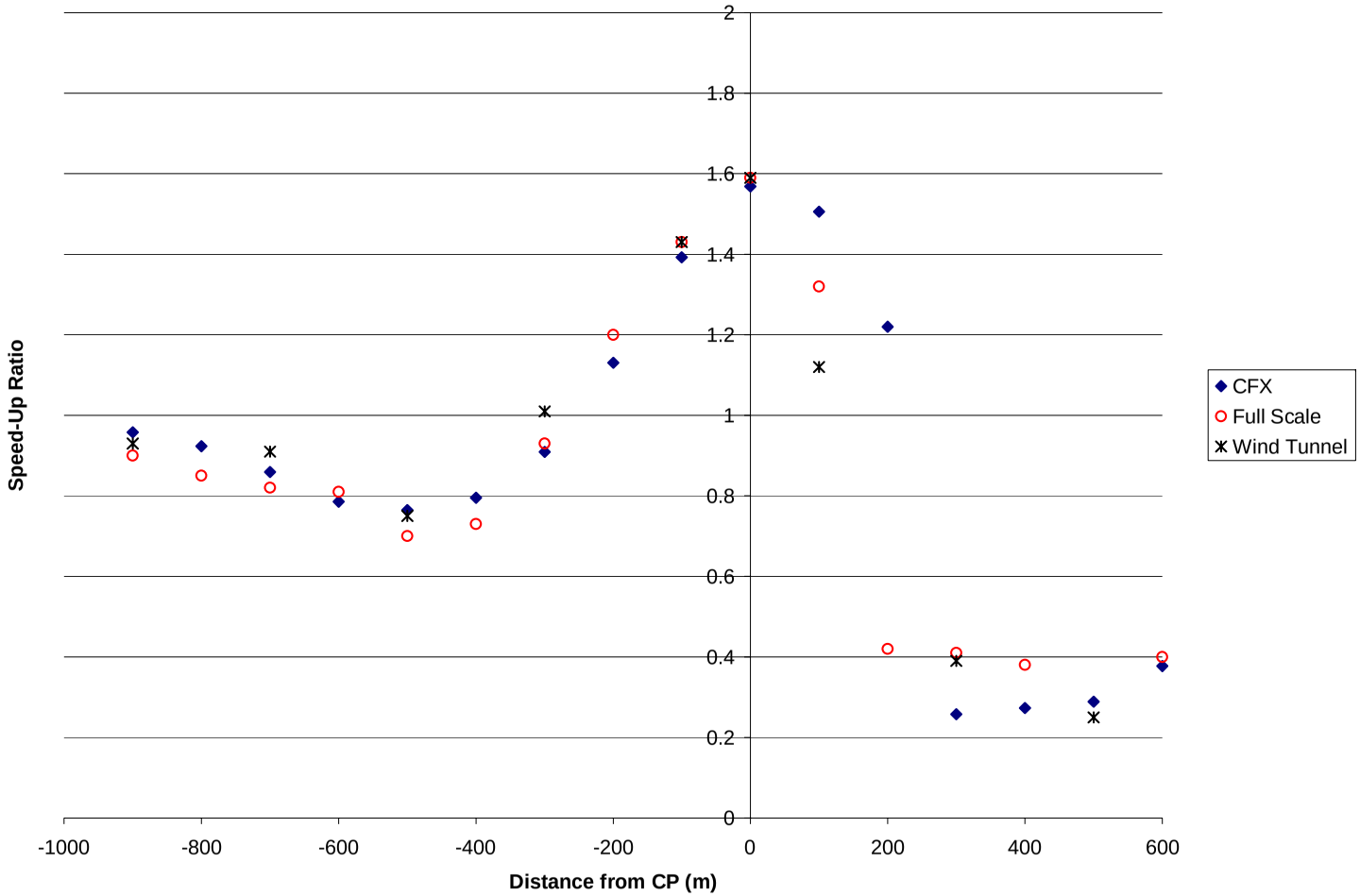

Figure 6.13 – Measurements of velocity ratio at 10m along tower line AA for wind direction 235°

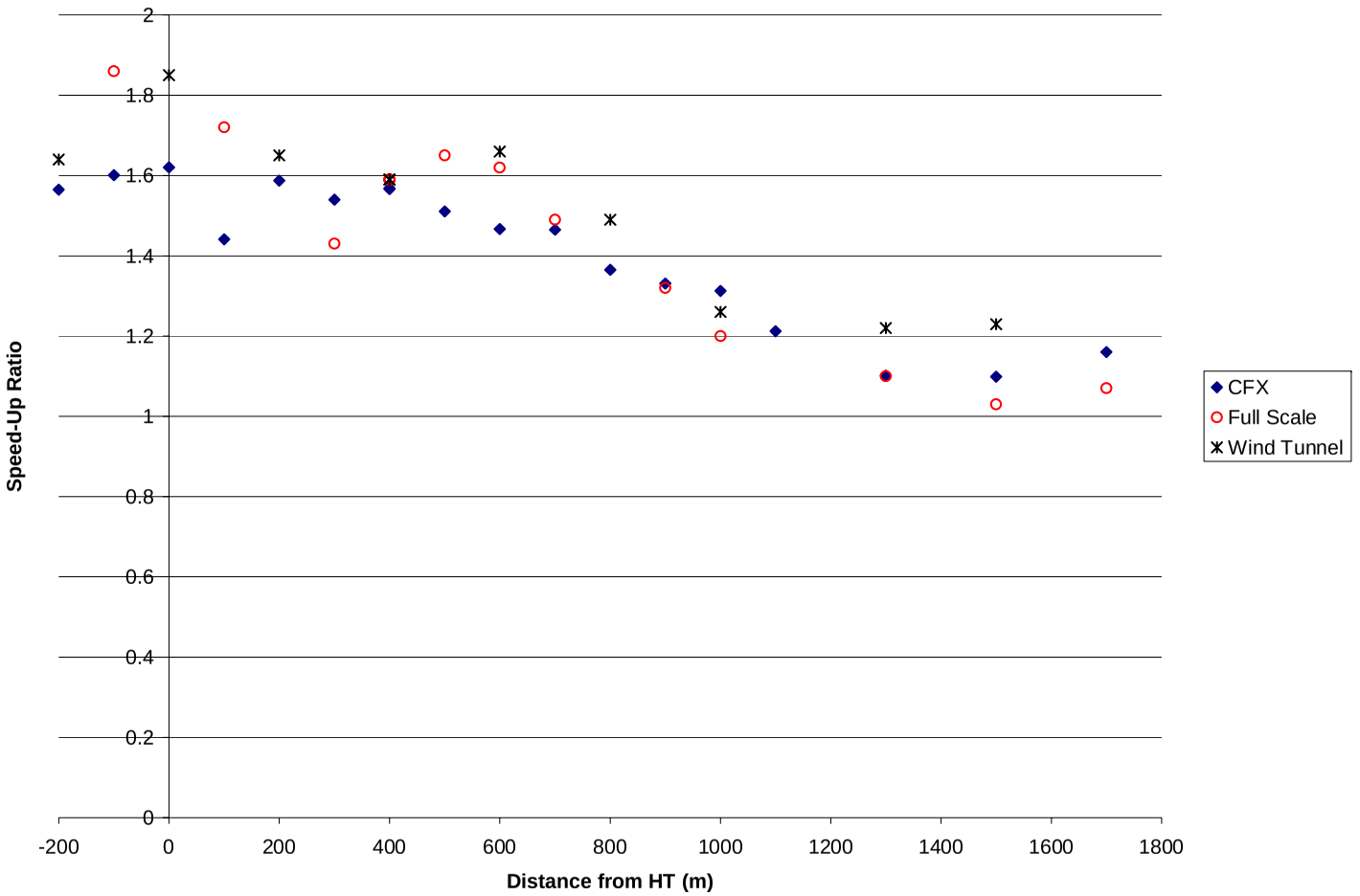

Figure 6.14 – Measurements of velocity ratio at 10m along tower line B for wind direction 235°

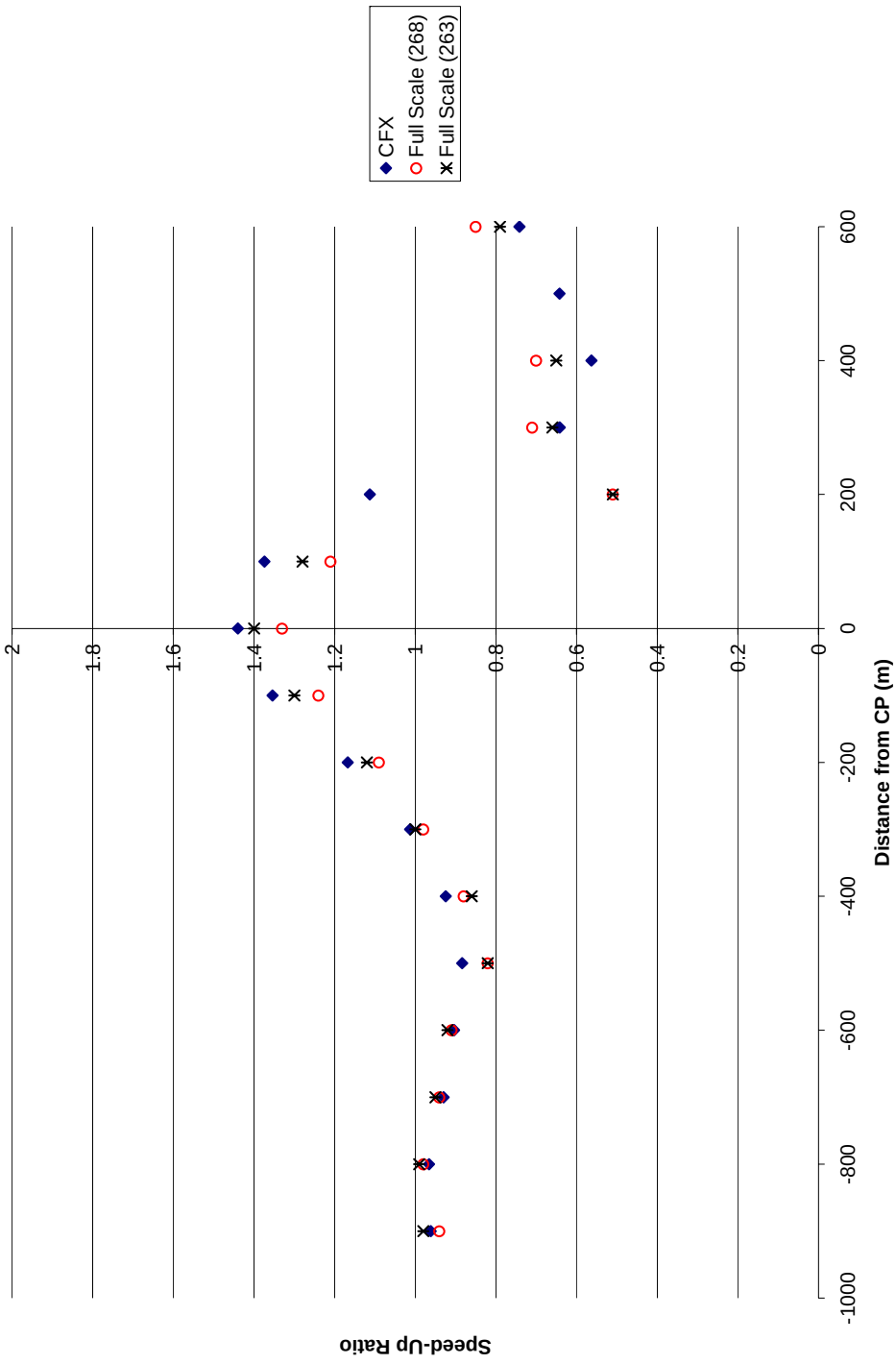

Figure 6.15 – Measurements of velocity ratio at 10m along tower line AA for wind direction 265°

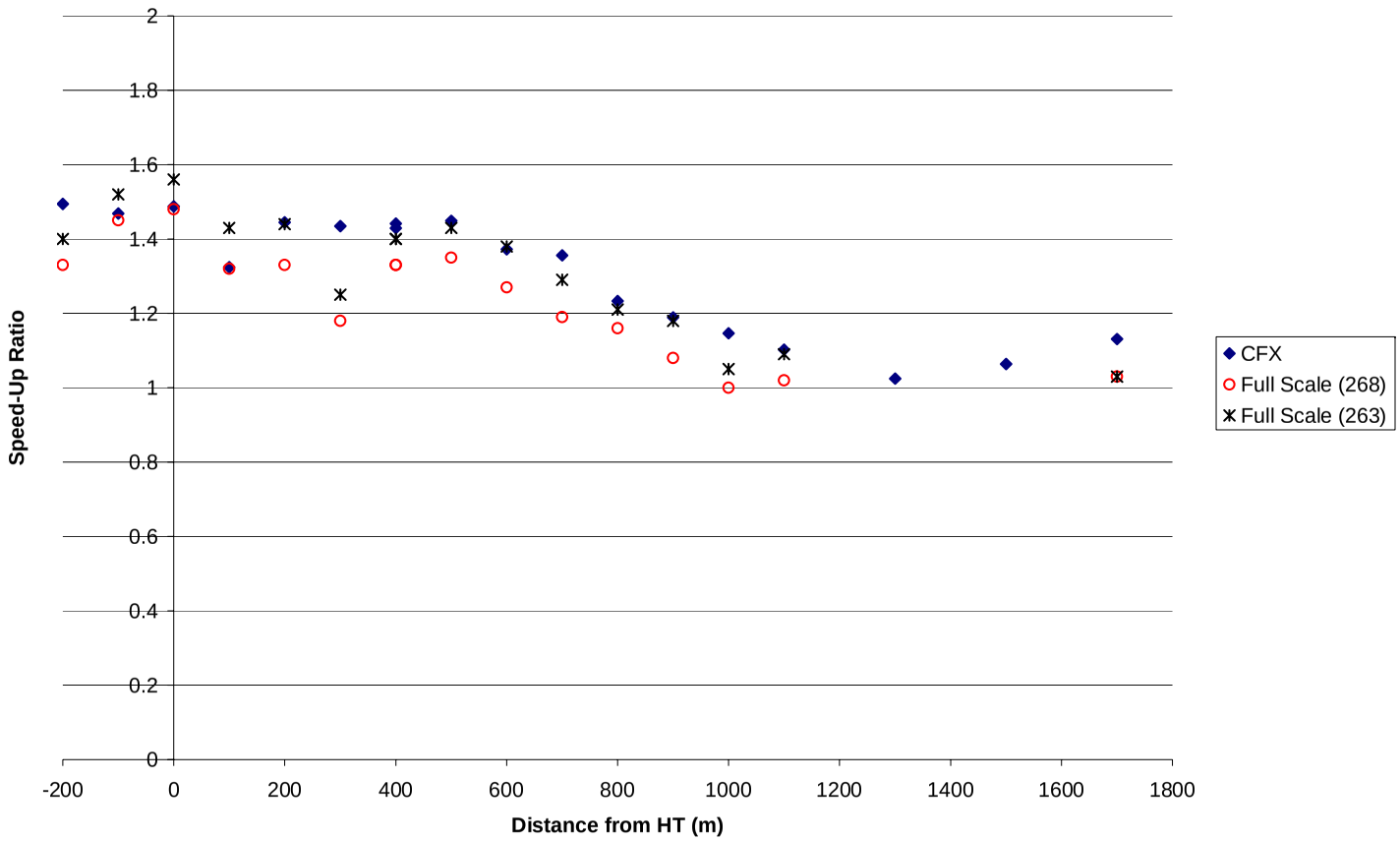

Figure 6.16 – Measurements of velocity ratio at 10m along tower line B for wind direction 265°

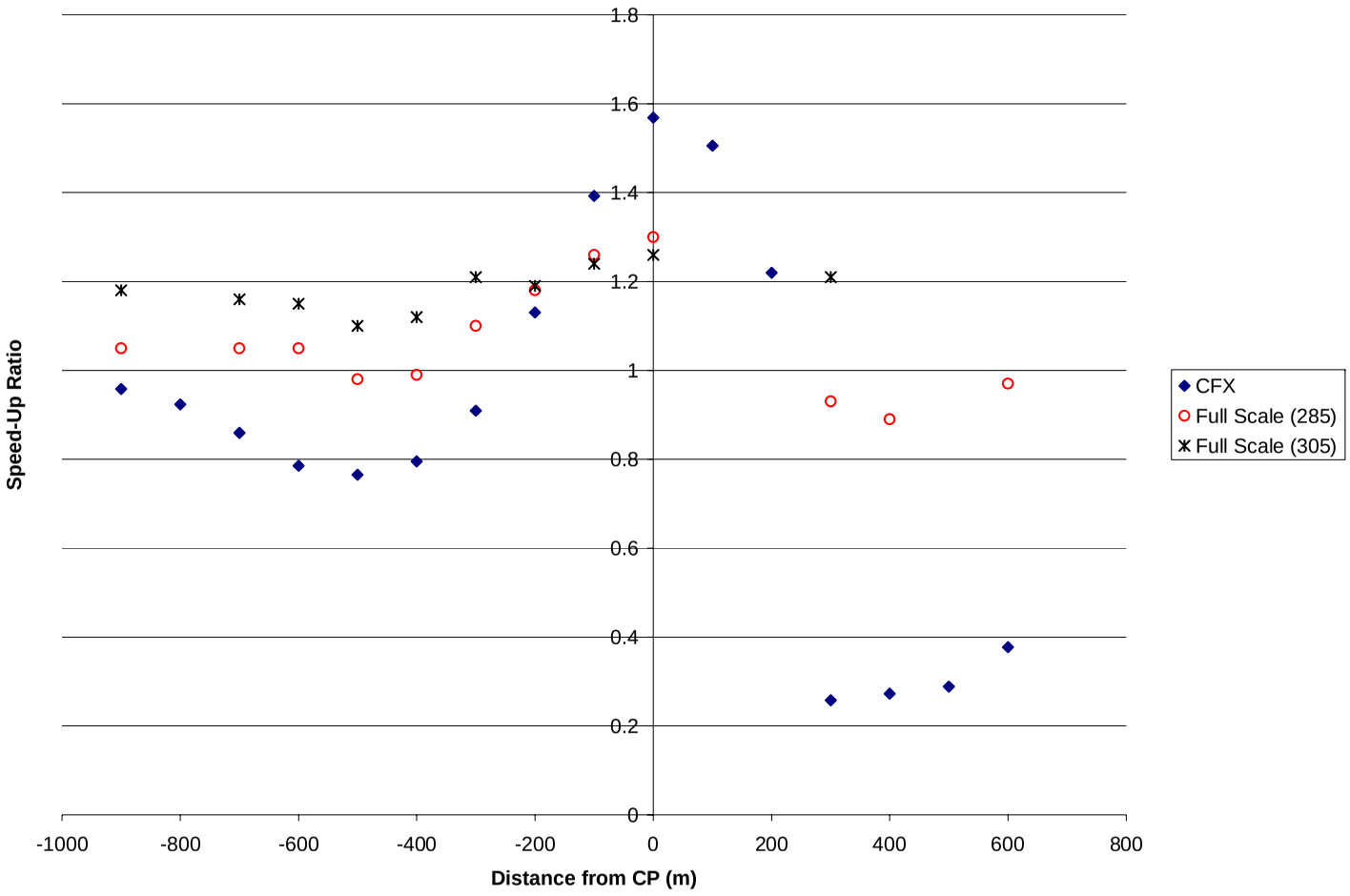

Figure 6.17 – Measurements of velocity ratio at 10m along tower line AA for wind direction 295°

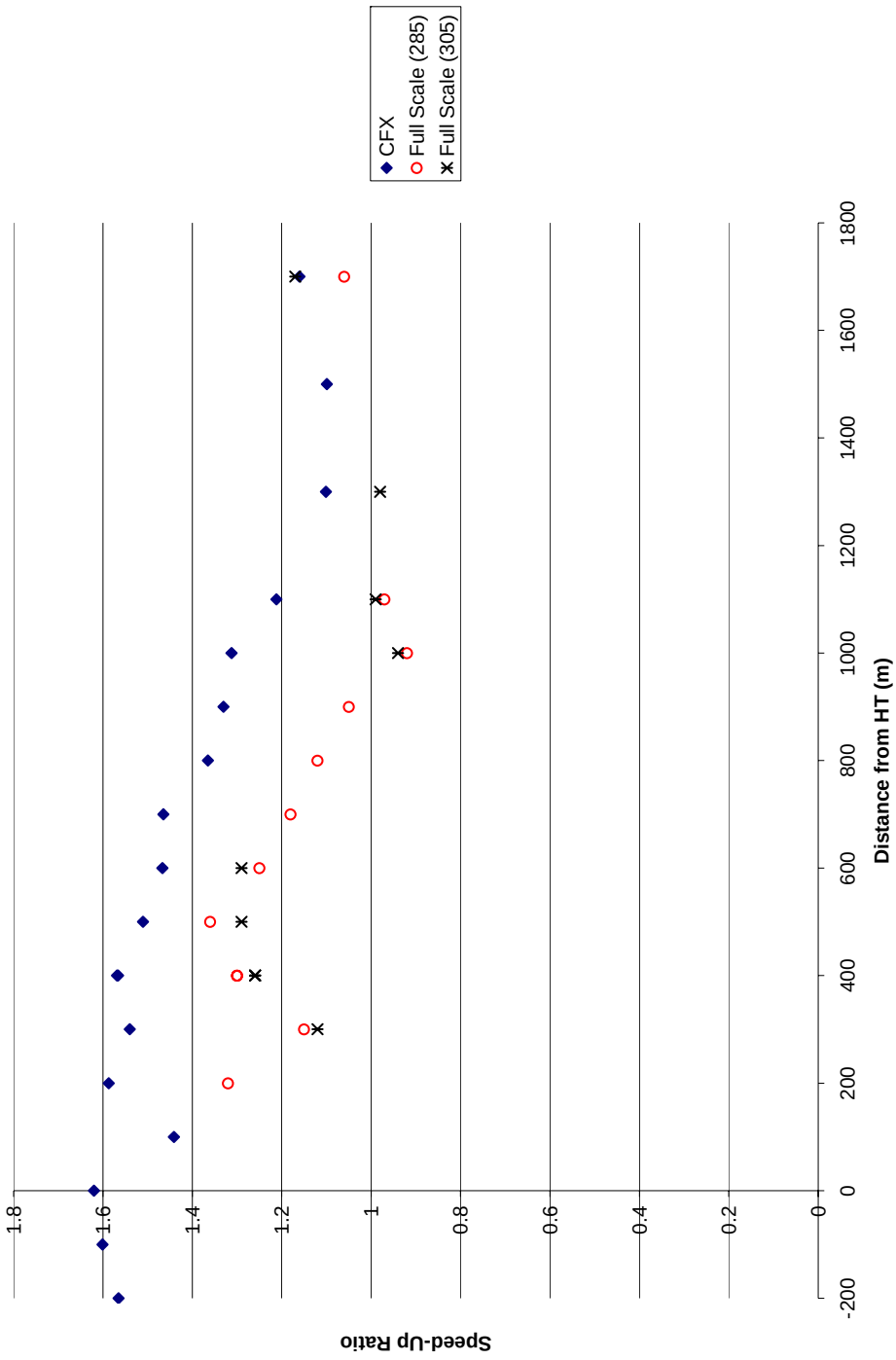

Figure 6.18 – Measurements of velocity ratio at 10m along tower line B for wind direction 295°

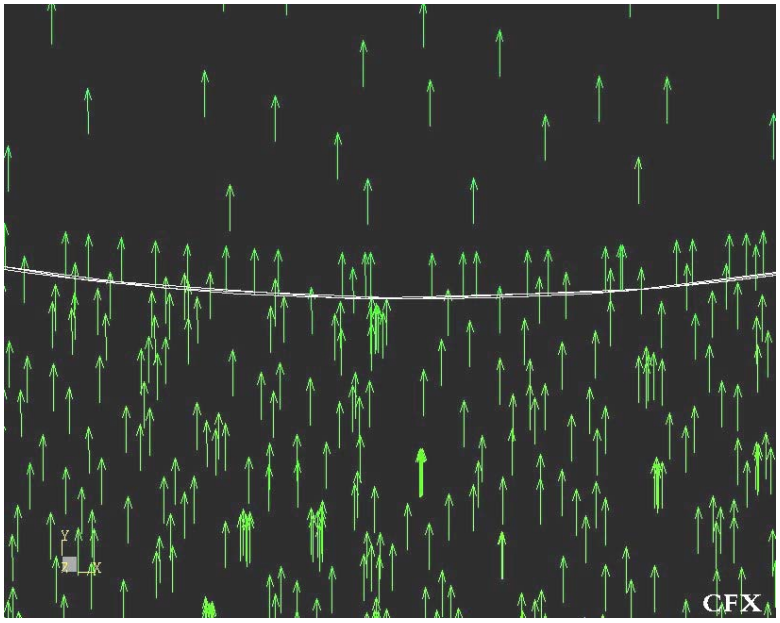

Figure 6.19a – Vector plot of the GGI – plan view

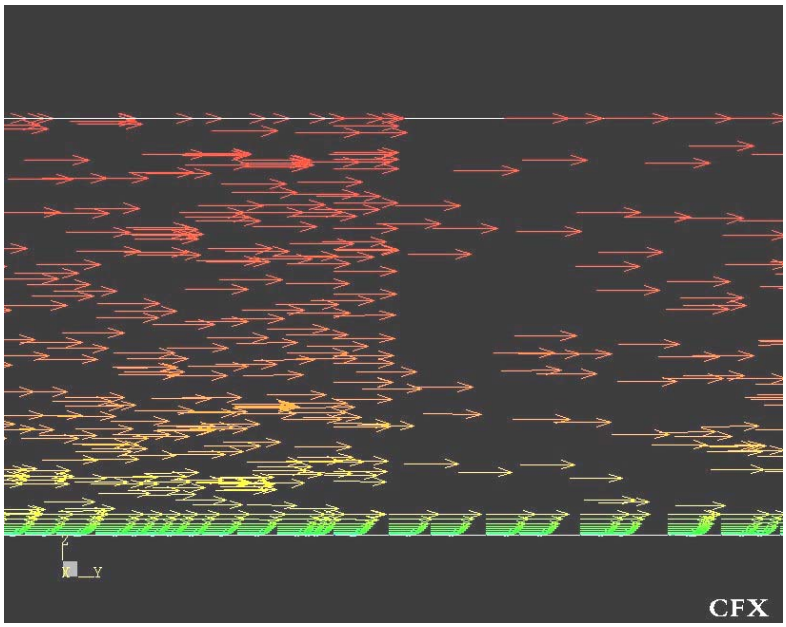

Figure 6.19b – Vector plots of the GGI – side view